

**Impact of deep-sea mining on
redox environment, biogeochemical processes and element fluxes
within and from sediments of the Clarion-Clipperton Zone,
Pacific Ocean**

Dissertation zur Erlangung des akademischen Doktorgrades
der Naturwissenschaften

Dr. rer. nat.
im Fachbereich Geowissenschaften
der Universität Bremen

vorgelegt von
Jessica B. Volz
Bremen, im Februar 2019
Kolloquium: 21. Juni 2019

Gutachter:

Frau Prof. Dr. Sabine Kasten
Universität Bremen
Fachbereich Geowissenschaften
Klagenfurter Straße 2
28359 Bremen

Herr Prof. Dr. Anton Eisenhauer
GEOMAR Helmholtz-Zentrum für Ozeanforschung Kiel
Wischhofstraße 1-3
24148 Kiel

PREFACE

This PhD project was conducted in the framework of the JPI Oceans (Joint Programming Initiative Healthy and Productive Seas and Oceans) pilot action “Ecological Aspects of Deep-Sea Mining (MiningImpact)”. The project was funded by the German Federal Ministry of Education and Research (BMBF) and received further funding from the Helmholtz Association at the Alfred Wegener Institute Helmholtz Centre for Polar and Marine Research. It was supervised by Prof. Dr. Sabine Kasten (AWI) and the outcome is submitted as cumulative doctoral thesis.

The dissertation opens with the motivation and objectives of the study and gives a scientific background (Chapter I). Hereafter, first authorship publications are presented, which are published (Chapter II) and under review (Chapter IV and V) in (ISI) peer-reviewed journals. The second authorship contribution to a publication published by project partners is presented in Chapter III. The dissertation closes with the main findings, conclusions and perspectives (Chapter VI).

All publications presented in this cumulative doctoral thesis are based on samples and data collected during RV SONNE cruise SO239 in 2015 in the framework of the JPI Oceans pilot action “Ecological Aspects of Deep-Sea Mining (MiningImpact)”. Most analyses were performed in the laboratories of the Alfred Wegener Institute Helmholtz Centre for Polar and Marine Research in Bremerhaven and at the Jacobs University Bremen in close collaboration with the MiningImpact project partners.

TABLE OF CONTENTS

| | |
|---|-----|
| THESIS SUMMARY | I |
| ZUSAMMENFASSUNG | IV |
| LIST OF FIGURES | i |
| LIST OF TABLES | vii |
| CHAPTER I: Introduction | 1 |
| 1.1 Motivation and objectives | 1 |
| 1.2 Deep-sea sediments | 2 |
| 1.3 (Bio)geochemical processes in deep-sea sediments | 3 |
| 1.4 Deep-sea mineral resources | 5 |
| 1.5 Formation of polymetallic nodules | 7 |
| 1.6 The Clarion-Clipperton Zone | 8 |
| 1.7 Resource management in the Clarion-Clipperton Zone | 11 |
| 1.8 Polymetallic nodule mining and potential environmental impacts | 12 |
| 1.9 Declaration of co-author contributions | 15 |
| References | 17 |
| CHAPTER II: Natural spatial variability of depositional conditions, biogeochemical processes and element fluxes in sediments of the eastern Clarion-Clipperton Zone, Pacific Ocean | 25 |
| CHAPTER III: Calcium phosphate control of REY patterns of siliceous-ooze-rich deep-sea sediments from the central equatorial Pacific | 60 |
| CHAPTER IV: Post-depositional manganese mobilization during the last glacial period in sediments of the eastern Clarion-Clipperton Fracture Zone, Pacific Ocean | 94 |
| CHAPTER V: Impact of small-scale disturbances on geochemical conditions, biogeochemical processes and element fluxes in sediments of the eastern Clarion-Clipperton Zone, Pacific Ocean | 121 |
| CHAPTER VI: Conclusions and Perspectives | 156 |
| APPENDIX | 160 |
| DANKSAGUNG | 187 |

THESIS SUMMARY

The economic interest in deep-sea mineral resources has grown in recent years mostly due to the increasing demand of metals and rare earth elements used in the high-tech industry. Deep-sea mineral resources of interest include polymetallic nodules, seafloor massive sulfides and cobalt-rich crust. One of the most extensive deposits of polymetallic nodules is found in the NE Pacific Ocean, namely the Clarion-Clipperton Zone (CCZ). In light of recent technological advances in mining equipment and metallurgical processes, the CCZ represents a prospective area for commercial deep-sea mining. In order to establish environmental regulations for the exploration, and ultimately, industrial exploitation of polymetallic nodules in the CCZ, baseline studies on the deep-sea ecosystem and the environmental impacts of deep-sea mining are essential.

Compared to other marine settings, the vast deep-sea environment remains insufficiently studied. In contrast to first suggestions that the deep seafloor is characterized by abyssal plains with mostly homogenous sedimentation, several studies have demonstrated that the seafloor within the CCZ is covered by numerous large seamounts, which highly influence the depositional conditions. It has been shown that distorted bottom-water currents in proximity to the seamounts cause variations in sediment composition and accumulation rates on the seafloor over several kilometers. These spatial variations in depositional conditions are expected to have strong implications for biogeochemical processes, redox zonation in the sediments of the CCZ and element fluxes across the sediment-water interface. In order to assess the impact of deep-sea mining on the sediment geochemistry in the CCZ, baseline studies are required addressing the natural spatial variations of depositional conditions as well as sediment biogeochemical processes, redox zonation and element fluxes across the sediment-water interface.

In the framework of this cumulative PhD thesis, surface sediments as well as long sediment cores of up to 10 m length from different areas within the CCZ were studied. The investigated areas include four different European contract areas for the exploration of polymetallic nodules in the CCZ and one of the protected Areas of Particular Environmental Interest (APEI) designated by the International Seabed Authority (ISA). Comprehensive pore-water and solid-phase analyses were performed on undisturbed sediments from the German BGR area (Bundesanstalt für Geowissenschaften und Rohstoffe), the Polish IOM area (InterOceanMetal), the Belgian GSR area (Global Sea Mineral Resources NV), the French IFREMER area (Institut Français de Recherche pour l'Exploitation de la Mer) and the APEI3 located north of the CCZ. In addition, disturbance tracks of small-scale experiments for the simulation of deep-sea mining

were investigated, which were created between 1 day and 37 years before sediment sampling in the different European contract areas. The acquired pore-water and solid-phase data of undisturbed and disturbed sediments were implemented in numerical transport-reaction models for the determination of the rates of biogeochemical processes and element fluxes as well as the evaluation of temporal changes in redox conditions in the sediments of the CCZ. Furthermore, transport-reaction modelling was performed in order to determine what time is required for the geochemical re-equilibration in the sediments after deep-sea mining experiments in the CCZ.

As a consequence of low surface water productivity in the NE Pacific Ocean, the seafloor within the CCZ receives small amounts of organic matter. Transport-reaction modelling performed as part of this PhD project revealed that aerobic respiration represents the dominant biogeochemical processes in the sediments while denitrification and manganese(IV) reduction only consume a fraction of the organic matter delivered to the seafloor. Oxygen usually penetrates several meters into the sediments of the CCZ while denitrification and manganese(IV) reduction usually coexist in the suboxic zone below. The oxidation of pore-water manganese at depth has been observed at several investigated sites, indicating that upward diffusing oxygen from the basaltic basement associated with low-temperature hydrothermal seawater circulation through crustal outcrops is a widespread phenomenon within the CCZ. Small- and large-scale natural spatial variations in redox conditions are associated with a lateral gradient in the flux of organic matter to the seafloor as well as regional differences in sediment composition and accumulation rates caused by bottom-water currents. The spatial variability in sediment composition is also reflected in the depth distribution of rare earth elements in the sediments, which are mostly bound to calcium phosphates. Due to significantly lower organic carbon burial rates in the sediments of the protected APEI3 area, the geochemical conditions do not represent the conditions found in the studied European contract areas.

Solid-phase manganese maxima have been observed in the surface sediments at most of the sites investigated in this PhD project. Transport-reaction modelling showed that postulated lower bottom-water oxygen concentrations during the last glacial period could have caused a much more condensed redox zonation than observed today during which diagenetically mobilized manganese precipitated at a shallow oxic-suboxic redox boundary at the sediment surface. The solid-phase manganese peak was continuously mixed into subsequently depositing Holocene sediments by bioturbation causing the observed manganese enrichment in the surface sediments. As the solid-phase manganese maximum was not observed in the sediments of the APEI3 area, the redox zonation was most likely not as compressed during the last glacial period in the APEI3 area due to considerably lower carbon burial rates. This provides further evidence

that the APEI3 area does not represent the geochemical conditions found in the European contract areas.

The investigation of surface sediments from disturbance tracks of small-scale deep-sea mining experiments confirmed the findings of an earlier study, suggesting that the depth distribution of solid-phase manganese provides a reliable tool for monitoring the disturbance depth. As the labile fraction of organic matter driving early diagenetic processes in the sediments is restricted to the surface sediment layer, it is mostly removed by the disturbance. As a consequence, the upper oxic zone extends up to tenfold deeper into the sediments with significantly reduced fluxes of oxygen into the sediments while denitrification and manganese(IV) reduction are inhibited. While bioturbation is crucial for the establishment of a new geochemical equilibrium, the disturbance depth as well as the burial rate of organic carbon ultimately determine the recovery of the geochemical system in the sediments. Due to slow sediment accumulation rates and low fluxes of organic matter to the seafloor within the CCZ, the new geochemical equilibrium in the sediments is expected to be established 10,000 to 100,000 years after deep-sea mining activities.

This PhD thesis advances the understanding of small- and large-scale heterogeneities of depositional conditions, biogeochemical processes and redox zonation in deep-sea sediments. Furthermore, temporal changes in the sediment redox zonation associated with climatically-induced changes in bottom-water conditions provide new insights for paleoceanographic aspects of the Pacific Ocean. The assessment of the impact of deep-sea mining on the geochemical system in the sediments contribute data crucial for further deep-sea impact assessment studies. They may be used for the establishment of environmental regulations for the exploration, and ultimately, exploitation of polymetallic nodules in the CCZ.

ZUSAMMENFASSUNG

Steigende Rohstoffpreise durch die wachsende Nachfrage nach Metallen und Seltenen Erden stärken seit einigen Jahren das Interesse an kommerziellen Tiefseebergbau. Mineralische Vorkommen aus der Tiefsee, die für zukünftigen kommerziellen Tiefseebergbau in Frage kommen, umfassen Manganknollen, Massivsulfide und Kobaltkrusten. Die Clarion-Clipperton Zone (CCZ) im NE Pazifik wird als „Manganknollen-Gürtel“ bezeichnet und ist durch eines der größten Vorkommen an Manganknollen auf dem Meeresboden gekennzeichnet. Neueste technologische Fortschritte könnten den großskaligen, kommerziellen Abbau von Manganknollen in der CCZ in naher Zukunft ermöglichen. Für die Erstellung von Richtlinien, die die Erkundung und den Abbau von Manganknollen in der CCZ regulieren, sind Grundlagenstudien des Tiefsee-Ökosystems und der potentiellen ökologischen Auswirkungen von Tiefseebergbau nötig.

Im Gegensatz zu anderen Regionen der Meere ist die Tiefsee bis heute weitestgehend unerforscht. Entgegen der Annahme, dass der Meeresboden in der Tiefsee von flachen Tiefsee-Ebenen dominiert ist, haben neuere Studien gezeigt, dass der Meeresboden in der CCZ zahlreiche große Tiefseeberge aufweist. Diese stellen ein natürliches Hindernis für Bodenwasser-Strömungen dar und lenken diese ab, was zur Folge hat, dass die Zusammensetzung und Ablagerungsrate der Sedimente über mehrere Kilometer variieren kann. Diese lateralen Unterschiede in den Ablagerungsbedingungen beeinflussen biogeochemische Prozesse und Redoxbedingungen in den Sedimenten, sowie die Stoffflüsse über die Sediment/Wasser-Grenzfläche. Um mögliche Folgen von Tiefseebergbau auf das geochemische Milieu der Sedimente zu untersuchen, sind Grundlagenstudien nötig, welche die natürlichen lateralen Unterschiede in den Ablagerungsbedingungen, biogeochemischen Prozessen, Redoxbedingungen und Stoffflüssen aufzeigen.

Im Rahmen dieser kumulativen Dissertation wurden Oberflächensedimente und lange Sedimentkerne mit einer Länge von maximal 10 m aus der CCZ untersucht. Diese Sedimente stammen aus vier europäischen Erkundungsgebieten für Manganknollen in der CCZ und einem der Schutzgebiete (APEI), die von der Internationalen Meeresbodenbehörde (ISA) designiert wurden. Im Rahmen dieser Studie wurden umfangreiche Porenwasser- und Festphase-Analysen an ungestörten Sedimenten aus dem deutschen BGR (Bundesanstalt für Geowissenschaften und Rohstoffe) Gebiet, dem polnischen IOM (InterOceanMetal) Gebiet, dem belgischen GSR (Global Sea Mineral Resources NV) Gebiet, dem französischen IFREMER (Institut Français de Recherche pour l'Exploitation de la Mer) Gebiet und dem Schutzgebiet APEI3 nördlich der

CCZ durchgeführt. Zudem wurden bis zu 37 Jahre alte Störungsspuren von verschiedenen Störungsexperimenten in den Erkundungsgebieten der CCZ untersucht. Die gewonnenen Porenwasser- und Festphase-Daten von ungestörten und gestörten Sedimenten wurden in Transport-Reaktionsmodelle implementiert, um biogeochemische Prozesse und Stoffflüsse zu quantifizieren, sowie zeitliche Variationen in Redoxbedingungen in den Sedimenten der CCZ zu untersuchen. Des Weiteren wurde ein Transport-Reaktionsmodell angewendet, um zu bestimmen, wie lange es dauert, bis ein neues geochemisches Gleichgewicht nach den Störungsexperimenten in den Sedimenten der CCZ hergestellt ist.

Aufgrund der geringen Produktivität im Oberflächenwasser des NE Pazifiks erreichen nur geringe Mengen an organischem Material den Meeresboden in der CCZ. Transport-Reaktionsmodellierungen, die im Rahmen dieser Arbeit durchgeführt wurden, zeigten, dass aerobische Respiration als biogeochemischer Prozess dominiert, während Denitrifikation und Mangan(IV)-Reduktion nur einen Bruchteil des organischen Materials verbraucht. Sauerstoff diffundiert meist mehrere Meter in die Sedimente, während Denitrifikation und Mangan(IV)-Reduktion gleichzeitig in der darunterliegenden suboxischen Zone auftreten. An einigen Stationen wird Porenwasser-Mangan in der Tiefe durch Sauerstoff, welches von der basaltischen Kruste ins Sediment diffundiert, aufgebraucht. Diese Beobachtung zeigte, dass die Zirkulation von Seewasser durch die ozeanische Kruste ein weitverbreitetes Phänomen in der CCZ ist. Klein- und großskalige laterale Unterschiede in den Redoxbedingungen der Sedimente hängen weiterhin mit dem lateralen Produktivitäts-Gradienten und regionalen Unterschieden in Sediment-Zusammensetzung und Sedimentationsrate durch den Einfluss von Bodenwasser-Strömungen zusammen. Die laterale Variabilität in der Zusammensetzung der Sedimente zeigte sich auch anhand der Tiefenverteilung von Seltenen Erden, die hauptsächlich in Calciumphosphat-Mineralen gebunden sind. Im APEI3-Schutzgebiet treten deutlich geringere Ablagerungsraten von organischem Material auf, sodass die geochemischen Bedingungen in den Sedimenten nicht denen der vier europäischen Erkundungsgebieten für Manganknollen in der CCZ entsprechen.

Die Oberflächensedimente an fast allen untersuchten Stationen zeigten eine Anreicherung von Mangan(IV) in der Festphase. Die Transport-Reaktionsmodellierung ergab, dass postulierte geringere Sauerstoff-Gehalte im Bodenwasser des Pazifiks während des letzten Glazials eine komprimierte Redoxzonierung in den Sedimenten der CCZ verursacht haben könnte. Dadurch konnte mobilisiertes Mangan im Porenwasser bis zur Sedimentoberfläche diffundieren, wo es als Mangan(IV) an der oxisch-suboxischen Redoxgrenze ausgefällt wurde. Anschließend wurde die Mangan(IV)-Anreicherung durch Bioturbation in Sedimente der Holozäns vermenget.

Die Mangan(IV)-Anreicherung trat nicht in den Sedimenten des APEI3-Schutzgebiets auf, was weiterhin impliziert, dass das APEI3 nicht repräsentativ für die untersuchten vier europäischen Erkundungsgebiete ist.

Die geochemischen Untersuchungen an Sedimenten der Störungsspuren in der CCZ bestätigten eine vorherige Studie, die zeigte, dass die Gehalte von Mangan in der Festphase für die Bestimmung der Störungstiefe im Sediment geeignet sind. Die Verfügbarkeit von labilen organischen Komponenten, welche die frühdiagenetischen Prozesse im Sediment antreiben, beschränkt sich auf die obere Sedimentschicht. Da dieses labile organische Material durch Störungen überwiegend entfernt wird, dehnt sich die obere oxische Zone nach unten aus, während die Sauerstoff-Flüsse ins Sediment nach der Störung deutlich abnehmen und Denitrifikation und Mangan(IV)-Reduktion inhibiert sind. Die Wiederherstellung eines neuen geochemischen Gleichgewichts in den Sedimenten der CCZ nach Störungsexperimenten ist hauptsächlich von der Störungstiefe und der Ablagerungsrate von organischem Material in den Sedimenten abhängig. Aufgrund der geringen Sedimentationsraten und Flüsse von organischem Material zum Meeresboden, ist ein neues geochemisches Gleichgewicht in den Sediments der CCZ nach 10.000–100.000 Jahren erreicht.

Diese kumulative Dissertation erweitert das Verständnis von klein- und großskaligen Unterschieden in Ablagerungsbedingungen, biogeochemischen Prozessen und Redoxzonierung in Tiefsee-Sedimenten. Änderungen der Redoxzonierung in den Sedimenten der CCZ können durch klimatisch-bedingte geringere Sauerstoffkonzentrationen im Bodenwasser verursacht worden sein, was neue Erkenntnisse bezüglich paleozeanografischer Aspekte im Pazifik liefert. Weiterhin liefert diese Studie wichtige Daten zur Beurteilung der Auswirkungen von Tiefseebergbau und zur Erstellung von Regularien für potentiellen Tiefseebergbau in der CCZ.

LIST OF FIGURES

CHAPTER I: Introduction

Figure 1: Schematic graph of the geochemical zonation with the classification of the redox zones after Froelich et al. (1979) and Berner (1981) as well as zones of mineral dissolution and authigenic mineral precipitation in marine sediments (Kasten et al., 2003).

Figure 2: World map showing the occurrence of the main marine minerals: polymetallic nodules (blue), seafloor massive sulfides (orange) and cobalt-rich ferromanganese crusts (yellow) (Miller et al., 2018). The DISCOL area is located in the Peru Basin, where the Disturbance and Recolonization experiment (DISCOL) has been carried out in 1989 (Thiel and Schriever, 1989).

Figure 3: (A) Typical discoidal shape of a polymetallic nodule with a smooth texture on the upper surface and a rough, coarse-grained surface at the bottom. (B) Vertical section of a typical polymetallic nodule showing the layered growth structure around a nucleus (Kuhn et al., 2017a). Both figures: © BGR

Figure 4: Bathymetric map showing the seafloor of the CCZ in the NE Pacific Ocean.

Figure 5: Schematic illustration of the geochemical zonation in the sediments of the CCZ and conceptual model of ridge-flank low hydrothermal circulation facilitated by seamount after Wheat and Fisher (2008) and Versteegh et al. (in prep.). Inset figure shows the hydrogenetic and oxic-diagenetic accretion of metals onto the surface of polymetallic nodules (modified after Kuhn et al., 2017b), which currently dominate the nodule growth in the CCZ.

Figure 6: Contract areas for the exploration of polymetallic nodules granted by the International Seabed Authority (ISA) within the CCZ (white areas) surrounded by nine Areas of Particular Environmental Interest (APEIs, green shaded squares), which are excluded from any mining activities (Geographical data provided by the International Seabed Authority).

Figure 7: (A) Concept of deep-sea mining with the (1) mining platform, (2) lift pipe, (3) nodule collector and (4) discharge system (e.g., Oebius et al., 2001). Figure modified after Gollner et al. (2017). (B) Small-scale deep-sea mining experiments performed in the area of the CCZ (Jones et al., 2017).

CHAPTER II: Natural spatial variability of depositional conditions, biogeochemical processes and element fluxes in sediments of the eastern Clarion-Clipperton Zone, Pacific Ocean

Figure 1: Maps of the study area during RV SONNE cruise SO239 showing (a) the four investigated exploration areas in the CCZ, the APEI3 and the sampling stations (white circles). The background colors indicate the estimated upper limit in POC flux [$\text{mg C}_{\text{org}} \text{m}^{-2} \text{d}^{-1}$] to the seafloor by Lutz et al. (2007) (modified after Vanreusel et al., 2016). Detailed hydroacoustic maps created with the multibeam system EM122 (Martínez Arbizu and Haeckel, 2015; Greinert, 2016) show the locations of the sampling stations with b: IOM; c: BGR; d: IFREMER; e: GSR; f: APEI3. The maps were produced with GMT5 (Wessel et al., 2013).

Figure 2: Pore-water profiles of oxygen, dissolved Mn(II) and nitrate of the APEI3, IFREMER, GSR, IOM and BGR sites. The inset plot for the IFRE-1 site show oxygen (black dots) and dissolved Mn(II) concentrations (open circles) on separate axes (upper axis: oxygen; lower axis: Mn(II)) between 2.5 and 7.5 m sediment depth. Bottom-water oxygen concentrations measured by CTD are indicated (grey crosses).

Figure 3: Solid-phase profiles of TOC of the APEI3, IFREMER, GSR, IOM and BGR sites.

Figure 4: $^{230}\text{Th}/^{231}\text{Pa}$ -derived sedimentation rates for the uppermost 50 cm of the sediments of the APEI3, IFREMER, GSR and IOM sites.

Figure 5: Model results for all sites including the biogeochemical processes of aerobic respiration, Mn(IV) reduction, denitrification, Mn^{2+} oxidation, nitrification and Mn-annamox (R₁–R₆).

Figure 6: Comparison of the TOC contents of surface sediments (upper 30 cm) within the different contract areas CCZ. The data for the BGR sites A1-1-MN, A1-2-NN, A5-2-SN, A5-1-BN from cruise SO205 are taken from Mewes et al. (2014). The range of TOC contents comprises the lowest to highest measured contents throughout MUC cores taken at the individual sites. The highest TOC content at each site was determined at the sediment surface, i.e. in the uppermost centimeter of the sediment.

Figure 7: Correlation between the oxygen penetration depth (OPD) and the POC fluxes used as boundary conditions for the diagenetic model. Based on interpolation of the oxygen profile at the APEI3 site, oxygen may be consumed at 11.5 m. The linear regression through the BGR (blue), IOM (yellow), *IFRE-1 (red), +IFRE-2 (red) and APEI3 (grey) sites shows a coefficient of determination of $r^2 = 0.85$.

CHAPTER III: Calcium phosphate control of REY patterns of siliceous-ooze-rich deep-sea sediments from the central equatorial Pacific

Figure 1: REY_{SN} patterns of fish debris, fossil fish teeth, marine phosphorite, hydrogenetic Fe-Mn crust, and seawater (PAAS from Taylor and McLennan, 1985, except Dy from McLennan, 1989). (See above-mentioned references for further information.)

Figure 2: Core sampling locations of 87GC and 165GC in the CCZ and of 194GC north of the Clarion Fracture Zone. The map was created using GeoMapApp.

Figure 3: Top: Depth profiles of selected major elements and three representative REY (Ce, Nd, Yb). Yb concentrations were multiplied by 10 to fit the scale of the figure. Core pictures depict that the sediment gets darker with depth in all cores and has thin dark layers throughout. Oxygen data from Volz et al. (2018). Bottom: Depth profiles of REY parameters HREE/LREE, MREE/MREE*, Ce/Ce*, and Y/Ho for bulk sediment, the sequential extraction solutions (Na-dithionite only for HREE/LREE and MREE/MREE* for 194GC-561 cm), and pore water (Y/Ho only for 194GC-511 cm).

$$\text{HREE/LREE} = (\text{Ho} + \text{Er} + \text{Tm} + \text{Yb} + \text{Lu}) / (\text{La} + \text{Ce} + \text{Pr} + \text{Nd}).$$

$$\text{MREE/MREE}^* = (\text{Sm} + \text{Eu} + \text{Gd} + \text{Tb} + \text{Dy}) / ((\text{La} + \text{Ce} + \text{Pr} + \text{Nd} + \text{Ho} + \text{Er} + \text{Tm} + \text{Yb} + \text{Lu}) * 2).$$

Figure 4: REY_{SN} patterns of selected sediment layers of the three cores investigated in this study (PAAS from Taylor and McLennan, 1985, except for Dy from McLennan, 1989). All cores and layers show a slight enrichment of MREY and HREY and most layers display a negative Ce_{SN} anomaly.

Figure 5: Increase of negative Ce_{SN} anomaly with depth and with increasing P concentration. See equation (1) in chapter 2.3 for the calculation of the Ce_{SN} anomaly.

Figure 6: Left: REY_{SN} patterns of pore waters from 194GC (PAAS from Taylor and McLennan, 1985, except Dy from McLennan, 1989). All patterns show an enrichment of the MREY and a pronounced negative Ce_{SN} anomaly. Right: Bulk sediment and Ca phosphate phase normalized to pore water.

Figure 7: REY_{SN} patterns of sequential leaching solutions of selected sediment layers from the three cores (PAAS from Taylor and McLennan, 1985, except Dy from McLennan, 1989). From each core one sample from an upper and lower part of the core was selected. Some data points are missing for the Na-dithionite and NH₄-oxalate patterns due to concentrations below the LOQ.

Figure 8: Scanning electron microscopy (SEM) images of particles rich in phosphorus and calcium; examples from layers 165GC-792 cm (left and middle) and 165GC-812 cm (right).

Figure 9: Left: P vs. Ca plot. Right: P vs. Nd plot. Nd represents the REY. Linear regression lines for the cores in both graphs and Pearson R correlation coefficients in the legend. All cores show positive correlations of P and Ca and P and Nd. The deepest layers in 165GC (792–912 cm) and 194GC (521–561 cm) deviate from the linear regression due to a lower Nd/P ratio (for further discussion see text).

Figure 10: Nd/P ratio of bulk sediment at different depths for cores 87GC, 165GC and 194GC. Nd represents the REY. Similar values with depth suggest that the ratio of REY to P stays the same except in the deep layers (165GC 792–912 cm and 194GC 521–561 cm) where lower Nd/P values suggest that P is more enriched than the REY. The relative uncertainty of Nd/P based on NIST-2702 digestions (n = 12 for P and n = 10 for Nd) and measurements is 6.27%.

Figure 11: Ce/Ce* values for each layer. Ce/Ce* was calculated according to equation (1) in the text. Yellow star symbols denote no Ce_{SN} anomaly. Values decrease with depth in all three cores, starting with different Ce/Ce* values at the top of the sediment cores.

CHAPTER IV: Post-depositional manganese mobilization during the last glacial period in sediments of the eastern Clarion-Clipperton Zone, Pacific Ocean

Figure 1: Map of the investigated sampling sites (open circles, star and triangle) in the different European contract areas for the exploration of polymetallic nodules and in the APEI3. The IFRE-1 and IFRE-2 sites are both located in the IFREMÉR area (open circle). The BGR area includes the BGR-RA (open circle), BGR-PA (open star) and SO205-65 (open triangle; Rühlemann et al., 2010; Mewes et al., 2016) sites. Background colors indicate the maximum POC flux [$\text{mg C}_{\text{org}} \text{m}^{-2} \text{d}^{-1}$] to the seafloor estimated by Lutz et al. (2007). Map is modified after Volz et al. (2018).

Figure 2: Method test of the leaching protocols after (A) Koschinsky et al. (2001) and (B) Poulton and Canfield (2005) separately applied on sediment samples from MUC core SO205-65 (Fig. 1; Table 1). Sequentially leached percentages of Mn and Fe oxides after the protocol by Koschinsky et al. (2001) (Mn_{carb} , Fe_{carb} ; Mn_{mobil} , Fe_{mobil} ; Mn_{ox} , Fe_{ox}) and Poulton and Canfield (2005) (Mn_{carb} , Fe_{carb} ; Mn_{ox1} , Fe_{ox1} ; Mn_{ox2} , Fe_{ox2} ; Mn_{mag} , Fe_{mag}) are shown with respect to bulk sediment contents of Mn and Fe (Mn_{total} ; Fe_{total}).

Figure 3: Bulk sediment contents of Mn and Fe (Mn_{total} ; Fe_{total}), total leachable contents of Mn and Fe ($Mn_{leachable}$; $Fe_{leachable}$) using the combined leaching protocol (Table 2) and Mn_{total}/Al_{total} and Fe_{total}/Al_{total} ratios (black dots) for all investigated sites. Average values for the upper continental crust (diamond) and mid-ocean ridge basalts (circle) are taken from Rudnick and Gao (2004) and Klein (2004), respectively.

Figure 4: Total leachable contents of Mn and Fe ($Mn_{leachable}$; $Fe_{leachable}$) and contents of sequentially leached Mn oxides (Mn_{mobil} , Mn_{ox1}) and Fe oxides (Fe_{ox1} (including Fe_{mobil}); Fe_{ox2} ; Fe_{mag}) using the combined leaching protocol (Table 2) for all investigated sites. Black arrows indicate the location of the LGM sediment surface based on $^{230}Th/^{231}Pa$ -derived sedimentation rates (Table 1).

Figure 5: Model results for the BGR-RA site (A), the IFRE-2 site (B) and the APEI3 site (C) including the steady state transport-reaction simulations (left) and the transient transport-reaction simulations (right). Concentrations of oxygen (grey dots) and Mn^{2+} (black dots) for 10-m-long GC cores were taken from Volz et al. (2018). Left: Simulations were performed for bottom-water oxygen concentrations (O_2^{bw}) of 120 μM for the BGR-RA site (solid line), 150 μM for the IFRE-2 site (solid line), 160 μM for the APEI3 site (solid line) and glacial O_2^{bw} of 35 μM (dashed line). Right: Simulations for the depth distribution of Mn_{mobil} after linearly increasing O_2^{bw} from 35 μM to 120 μM (BGR-RA), 150 μM (IFRE-2) and 160 μM (APEI3) between 14–15 kyr. Measured contents of mobilizable Mn(IV) (Mn_{mobil}) are indicated (black dots).

Figure 6: Conceptual model for the depth distribution of authigenic Mn(IV) (Mn_{mobil}) since the last glacial maximum (LGM) 21 kyr before present (BP) and under current geochemical conditions in the sediments of the CCZ. During the last glacial termination (LGT) between 14–15 kyr BP, bottom-water oxygen concentrations O_2^{bw} increase from 35 μM to $\sim 150 \mu M$ within 1000 years.

CHAPTER V: Impact of small-scale disturbances on geochemical conditions, biogeochemical processes and element fluxes in sediments of the eastern Clarion-Clipperton Zone, Pacific Ocean

Figure 1: Sampling sites (black circles, black star) in various European contract areas for the exploration of manganese nodules within the Clarion-Clipperton Fracture Zone (CCZ). Investigated stations are located in the German BGR area (blue), eastern European IOM area (yellow), Belgian GSR area (green) and French IFREMER area (red). The two stations within the German BGR area are located in the “prospective area” (BGR-PA, black star) and in the “reference area” (BGR-RA, black circle). The contract areas granted by the International Seabed Authority (ISA) are surrounded by nine Areas of Particular Environmental Interest (APEI), which are excluded from any mining activities (green shaded squares). Geographical data provided by the ISA.

Figure 2: Examples of undisturbed reference sediments in the German BGR-PA area and the French IFREMER area and pictures of small-scale disturbances for the simulation of deep-sea mining within the CCZ, which are investigated in the framework of this study (years: yr; months: mth; days: d). Copyright: ROV KIEL 6000 Team, GEOMAR Helmholtz Centre for Ocean Research Kiel, Germany.

Figure 3: Solid-phase Mn and TOC contents for all disturbed sites investigated in the framework of this study.

Figure 4: Correlation of solid-phase Mn and TOC contents between the disturbed sites and the respective undisturbed reference sediments (grey shaded profiles) using the disturbance depths determined with the Pearson correlation coefficient (compare Table 3). For the undisturbed reference sediments, solid-phase Mn contents are taken from Volz et al. (under review) and TOC contents are taken from Volz et al. (2018).

Figure 5: Model results of the transient transport-reaction model for (a) EBS disturbance in the German BGR-RA area and (b) the IOM-BIE disturbance in the eastern European IOM area.

Figure 6: Detailed model results of the transient transport-reaction model for the upper 1 m of the sediments for (a) EBS disturbance in the German BGR-RA area and (b) the IOM-BIE disturbance in the eastern European IOM area.

Figure 7: Pore-water fluxes of oxygen (O_2), nitrate (NO_3^{2-}) and ammonia (NH_4^+) at the sediment-water interface obtained by the application of the transient transport-reaction model. Oxygen fluxes into the sediment and fluxes of nitrate and ammonia towards the sediment surface are shown as a function of time after the EBS and IOM-BIE disturbances in the German BGR-RA area (blue) and in the eastern European IOM area (black), respectively.

Figure 8: Conceptual model for time-dependent pore-water fluxes of oxygen (O_2), nitrate (NO_3^{2-}) and ammonia (NH_4^+) at the sediment-water interface after the removal of the upper 7–10 cm of the sediments. The re-establishment of bioturbation, the maximum oxygen penetration depth (OPD) as well as the re-establishment of the surface sediment layer dominated by the reactive labile organic matter fraction are indicated as a function of time after the sediment removal.

CHAPTER VI: Conclusions and perspectives

Figure 1: Schematic illustration of the geochemical conditions in the sediments of the CCZ before (A) and after (B, C) anthropogenic disturbances (compare Figure 5 in CHAPTER I: Introduction). (A): Undisturbed sediment redox zonation and solid-phase Mn and TOC maxima in the surface sediments. The uppermost 15 cm of the sediments are most likely removed by anthropogenic disturbances. (B) Redox zonation in the sediments 10^3 years after the surface sediment removal with an extended upper oxic zone and a compressed suboxic zone below. (C) Pre-disturbance redox conditions and the removed sediment surface layer are re-established 10^4 – 10^5 years after the disturbance (Depth distribution of Mn(IV) is roughly estimated).

LIST OF TABLES

CHAPTER II: Natural spatial variability of depositional conditions, biogeochemical processes and element fluxes in sediments of the eastern Clarion-Clipperton Zone, Pacific Ocean

Table 1: MUC and GC cores investigated in this study including information on geographic position, water depth and core length. Nodule coverage shows the density and size of nodules recovered from the sediment surface at the box corer (BC) station nearest to MUC and GC locations. Nodule sampling area is 0.25 m², the length of scale (■□) corresponds to 10 cm.

Table 2: Fluxes of POC and oxygen into the sediment and depth-integrated rates of the predominant biogeochemical processes derived from the diagenetic model.

Table 3: Oxygen gradients calculated from oxygen profiles for the uppermost 0.4–1 cm of sediment. Negative gradients indicate the oxygen flux into the sediment. The data from SO205 were taken from Mewes et al. (2014). Note that the oxygen gradient at the GSR site is biased due to miscalibration of the sensor.

CHAPTER III: Calcium phosphate control of REY patterns of siliceous-ooze-rich deep-sea sediments from the central equatorial Pacific

Table 1: Overview of GC sampling sites.

Table 2: Leaching scheme for the sequential extraction of Mn- and Fe-(oxyhydr)oxides (adapted from Köster, 2017).

Table 3: Pearson R correlation coefficients of Nd, representing the REY, with various major elements of the bulk sediment digestions. Data correlated for the completely analyzed core sections.

CHAPTER IV: Post-depositional manganese mobilization during the last glacial period in sediments of the eastern Clarion-Clipperton Zone, Pacific Ocean

Table 1: Investigated MUC sampling sites with geographic position and water depth. If not indicated otherwise, sampling station characteristics, such as sedimentation rate (Sed. rate), flux of particulate organic carbon (POC) to the seafloor, bioturbation depth (Bioturb. depth), oxygen penetration depth (OPD) and nodule size are taken from Volz et al. (2018). Information for site SO205-65 is taken from Rühlemann et al. (2010) and Mewes et al. (2016). For the BGR-PA site, information is taken from an adjacent site (A5-2-SN; 11°57.22'N, 117°0.42'W) studied by Mewes et al. (2014) and Mogollón et al. (2016).

Table 2: Protocol for the optimized leaching scheme combining the methods after Koschinsky et al. (2001) and Poulton and Canfield (2005).

Table 3: Model-derived downward O₂ fluxes and upward Mn²⁺ fluxes [μmol cm⁻² yr⁻¹] at the sediment-water interface for glacial bottom-water oxygen concentrations (O₂^{bw}) of 35 μM (e.g., Hoogakker et al., 2018; Anderson et al., 2019) and current O₂^{bw} of 120 μM at the BGR-RA site, 150 μM at the IFRE-2 site and 160 μM at the APEI3 site (Volz et al., 2018).

CHAPTER V: Impact of small-scale disturbances on geochemical conditions, biogeochemical processes and element fluxes in sediments of the eastern Clarion-Clipperton Zone, Pacific Ocean

Table 1: MUC and PC cores investigated in this study including information on geographic position, water depth, type and age of the disturbances (years: yr; months: mth; days: d).

Table 2: Information of sedimentation rate (Sed. rate), flux of particulate organic carbon (POC) to the seafloor, bioturbation depth (Bioturb. depth), oxygen penetration depth (OPD) based on GC cores from the investigated sites and determined in the study by Volz et al. (2018). Information for the BGR-PA area is taken from an adjacent site (A5-2-SN; 11°57.22'N, 117°0.42'W) studied by Mewes et al. (2014) and Mogollón et al. (2016).

Table 3: Calculated Pearson correlation coefficients r_{Mn} and r_{TOC} for the determination of the disturbance depth of various small-scale disturbances investigated in the framework of this study (compare Table 1).

CHAPTER I:

Introduction

1.1 Motivation and objectives

The resource potential of the deep sea was discovered during the first global marine research voyage conducted by the *HMS Challenger* in the 1870s. During the *Challenger* expedition, numerous unknown marine species of flora and fauna were collected as well as deep-sea mineral deposits, such as polymetallic nodules (Murray and Renard, 1891). Based on considerable metal quantities concentrated within these nodules, their potential use as an economic resource was first raised in the 1960s, via the extension of terrestrial and shallow-water mining activities into the deep (Mero, 1965). At time of writing this thesis, there has been no commercial exploitation of polymetallic nodules and other deep-sea mineral resources. However, mineral prices for some of the high-tech metals found in these deep-sea mineral resources have been increasing within the past years due to recent technological advances and the growing demand for modern electronics. Thus, deep-sea mining may be economically viable in the near future (e.g., Halfar and Fujita, 2002; Wedding et al., 2015).

The commercial interest in polymetallic nodules from one of the most extensive deposits located in the Clarion-Clipperton Zone (CCZ) in the NE Pacific Ocean has led to comprehensive resource exploration campaigns and environmental baseline studies in the CCZ since the 1970s. Several states have temporal contracts with the International Seabed Authority (ISA) since the 2000s, which stipulate that the contractors explore polymetallic nodules in designated contract areas within the CCZ, test mining equipment and assess potential environmental impacts of deep-sea mining activities. These baseline studies are pivotal for the development of a regulative environmental framework for potential future deep-sea mining activities in the CCZ (Lodge et al., 2014; Madureira et al., 2016). In 2015, the Joint Programming Initiative Healthy and Productive Seas and Oceans (JPI Oceans) launched the European project “Ecological Aspects of Deep-Sea Mining (MiningImpact)” during which a multidisciplinary European scientific community studied the impacts of deep-sea mining activities on deep-sea ecosystems. The presented cumulative PhD thesis was carried out in the framework of this European JPI Oceans project.

The first aim of the PhD project was to investigate the natural spatial and temporal variability of biogeochemical processes and redox conditions in the sediments as well as element fluxes across the sediment-water interface in different European contract areas for the exploration of

polymetallic nodules within the CCZ and one of the protected Areas of Particular Environmental Interest (APEI). The investigated European contract areas include the German BGR area (Bundesanstalt für Geowissenschaften und Rohstoffe), the Polish IOM area (InterOceanMetal), the Belgian GSR area (Global Sea Mineral Resources NV) and the French IFREMER area (Institut Français de Recherche pour l'Exploitation de la Mer). These baseline data are crucial in order to assess the potential impact of deep-sea mining on the sediment geochemical system.

The second aim of this PhD project was to assess the impact of deep-sea mining on the geochemical system of the sediments within the CCZ. As there has been no deep-sea mining trails on a commercial scale until today, the impact assessment of small-scale disturbances for the simulation of deep-sea mining provide the only approximation to the environmental consequences of potential future large-scale deep-sea mining activities.

The following section will give a scientific background for biogeochemical processes in deep-sea sediments, present the formation processes and the occurrence of polymetallic nodules and introduce the study area within the CCZ. In addition, mining trials and disturbance experiments carried out in the CCZ as well as the resource management in the area by the ISA are outlined.

1.2 Deep-sea sediments

The seafloor in the ocean basins is covered by sediments of different types, origin and thickness (e.g., Berger, 1974; Davies and Gorsline, 1976). Pelagic sediments accumulate on the seafloor of the open ocean, far from the coast as a result of particle settling. These particles consist mostly of a mixture of microscopic calcareous or siliceous shells as well as terrigenous clay-size siliciclastic particles, which were transported from land to the open ocean mostly by air, i.e. aeolian transport (e.g., Blank et al., 1985; Rea, 1994; Fütterer, 2006). Traces of meteoric dust and different concentrations of volcanic debris are also found in pelagic sediments (e.g., Müller et al., 1988; Uścińowicz, 2012). Pelagic sediments, which consist of at least 30% calcareous or siliceous shell detritus are classified as calcareous and siliceous biogenic oozes, respectively (e.g., Berger, 1974). Calcareous oozes dominate the world ocean's floor and generally accumulate above the carbonate compensation depth (CCD) at 4–5 km water depth, at sedimentation rates of roughly a few centimeters per thousand years (e.g., Berger, 1974; Fütterer, 2006). Siliceous oozes commonly precipitate below the CCD at slower rates of just a few millimeters per thousand years.

1.3 (Bio)geochemical processes in deep-sea sediments

Produced in the zone of primary production in the surface ocean, organic matter is sinking down through the water column to the seafloor and subsequently incorporated into seafloor sediments. Froelich et al. (1979) and Berner (1981) were amongst the first to describe early diagenetic processes in marine sediments as a vertical succession of microbially utilized electron acceptors during the degradation of organic matter, resulting in the development of a distinct geochemical redox zonation in the sediments (Fig. 1). The redox zonation in marine sediments is determined by the flux of organic matter to the seafloor, the sedimentation rate and the availability of thermodynamically favorable electron acceptors (e.g., Froelich et al., 1979; Berner, 1981). The general sequence of terminal electron acceptors includes dissolved oxygen (O_2) and nitrate (NO_3^-), solid-phase manganese(IV) (oxyhydr)oxides (MnO_2) and iron(III) (oxyhydr)oxides, such as ferrihydrite ($Fe(OH)_3$), lepidocrocite ($FeOOH$), hematite (Fe_2O_3) and magnetite (Fe_3O_4) as well as dissolved sulfate (SO_4^{2-}). The last step during the degradation of organic matter is the fermentation of methane (CH_4). This general succession of electron acceptors is determined by the yield of free energy gained by microorganisms during the respective redox reaction (e.g., Froelich et al., 1979; Jørgensen, 2006). The oxidation of organic matter is associated with the release of reduced pore-water species such as manganese (Mn^{2+}), iron (Fe^{2+}) and hydrogen sulfide (H_2S). The availability of pore-water Mn^{2+} , Fe^{2+} as well as H_2S and methane (CH_4) define the suboxic and sulfidic/anoxic redox zones in the sediments, respectively (Fig. 1; Froelich et al., 1979; Berner, 1981). Once released into the pore water, the constituents diffuse up- and downwards until they are consumed during aerobic or anaerobic (i.e. absence of oxygen) oxidation processes and precipitate as secondary authigenic mineral phases at redox boundaries (Fig. 1). The dissolution of solid-phase components during the oxidation of organic matter and the formation of authigenic minerals alters the primary sediment composition and properties, such as magnetic susceptibility (Fig. 1; e.g., Riedinger et al., 2005). Dissolved Mn^{2+} , for example, is released during the dissimilatory reduction of MnO_2 and precipitates as authigenic MnO_2 at the oxic-suboxic redox boundary during the reaction with O_2 (e.g., Lynn and Bonatti, 1965; Froelich et al., 1979; Burdige and Gieskes, 1983). Pore-water profiles of reactants (O_2 , NO_3^- , SO_4^{2-}) and products (NH_4^+ , Mn^{2+} , Fe^{2+} , H_2S) during organic matter degradation can be used to infer dominant (bio)geochemical processes in the sediments and to assess the present depth of reaction fronts (e.g., oxic-suboxic boundary).

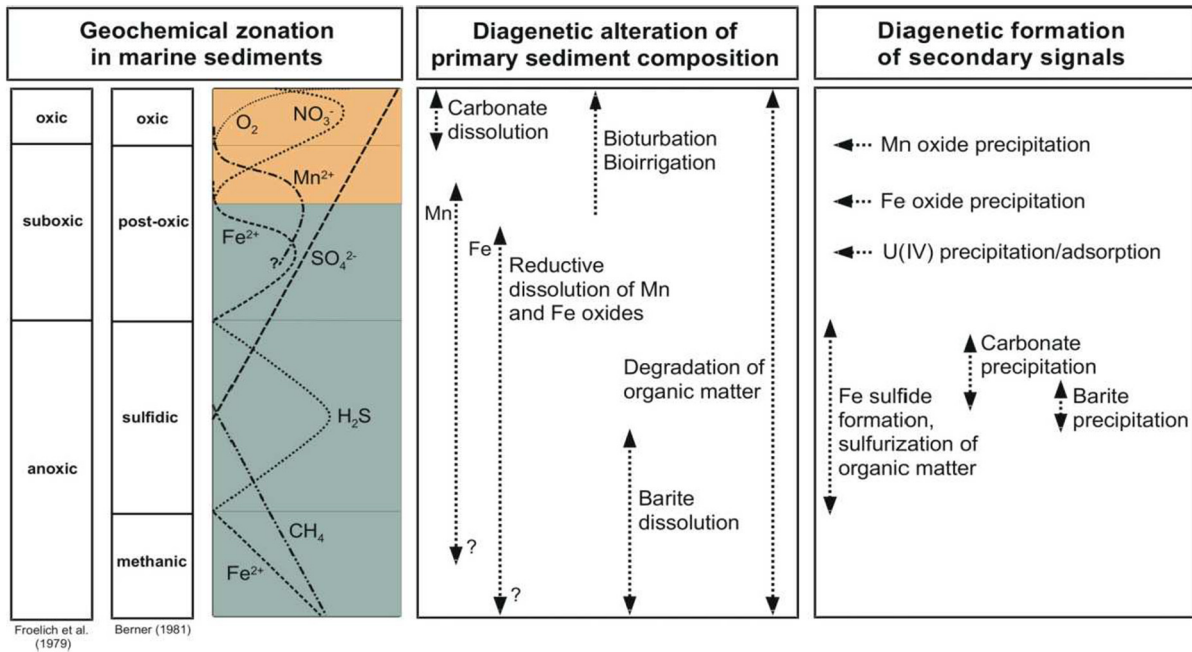


Figure 1: Schematic graph of the geochemical zonation with the classification of the redox zones after Froelich et al. (1979) and Berner (1981) as well as zones of mineral dissolution and authigenic mineral precipitation in marine sediments (Kasten et al., 2003).

Oxygen is usually rapidly consumed during aerobic respiration in the uppermost centimeters of the sediments underlying productive surface waters, particularly in areas of coastal upwelling (e.g., Glud et al., 1994; Holby and Riess, 1996). In contrast, sediments underlying carbon-starved surface waters, such as oceanic gyre systems are characterized by meter-scale oxygen penetration depths (OPD; Fischer et al., 2009; Ziebis et al., 2012; Røy et al., 2012). For example, the sediments in the Peru Basin in the SE Pacific Ocean are characterized by organic matter inputs from the southern border of the equatorial Pacific high-productivity belt as well as the Peruvian coastal upwelling system (e.g., Weber et al., 2000). In these sediments, oxygen is consumed in the upper 5–25 cm of the sediments, while denitrification and dissimilatory Mn(IV) reduction takes place at greater depths (Haeckel et al., 2001; Paul et al., 2018). In pelagic sediments in the central Pacific Ocean, oxygen penetrates several meters into the sediments, mostly as a consequence of the low fluxes of organic matter to the seafloor (e.g., Røy et al., 2012; Ziebis et al., 2012; Mewes et al., 2014). The redox zonation of the study area investigated in the framework of this PhD thesis project will be discussed in more detail in section 1.6 The Clarion-Clipperton Zone.

It should be noted that the idealized succession of (bio)geochemical processes by Froelich et al. (1979) and Berner (1981) can be more complex in natural settings once secondary autotrophic redox reactions become significant for microbial metabolic processes. For example, studies have suggested that the nitrogen (N) and Mn cycles may be coupled in Mn-rich sediment

deposits (> 0.05 wt%), such as pelagic sediments of the Pacific Ocean (Mogollón et al., 2016). The N-Mn coupling occurs in the suboxic zone of the sediments by (1) the oxidation of pore-water Mn^{2+} by nitrate and (2) the oxidation of pore-water ammonia generated during organic matter degradation by MnO_2 (Mn-annamox; Luther et al., 1997). Furthermore, studies on sediments from the Peru Basin have reported that Fe(II) bound in the clay mineral crystal lattice is oxidized to Fe(III) in the presence of pore-water nitrate in the suboxic zone, which is associated with a color transition from green to brown in the sediments (e.g., Lyle, 1983; Drodt et al., 1997).

(Bio)geochemical processes in the sediments occur under steady state or non-steady state conditions (e.g., Kasten et al., 2003; Schulz, 2006). Steady state conditions are defined by a constant composition of the depositing sediment, as well as fixed sedimentation rates and fluxes of organic matter and dissolved constituents into/from the sediments. Changes in depositional and/or bottom-water conditions induce non-steady state conditions during which pore-water constituents adjust by the migration of diagenetic reaction fronts. The classification of depositional settings into steady state or non-steady state diagenetic conditions is highly dependent on the time scale considered. Although steady state diagenetic conditions may not actually persist, the assumption of steady state diagenetic conditions in slowly accumulating depositional settings, such as the deep sea allows the application of simplified numerical models in order to quantify (bio)geochemical processes in marine sediments (e.g., Boudreau, 1997).

1.4 Deep-sea mineral resources

Most marine mineral deposits throughout the world ocean occur on the seabed beyond the borders of the national jurisdiction of littoral states (Fig. 2). Each state adjacent to the sea owns sovereign rights over natural resources in its exclusive economic zone (EEZ), which extends 200 nautical miles from the state's coast into the sea. Economically viable deep-sea mineral resources include seafloor massive sulfides (SMS) associated with hydrothermal vents (e.g., Boschen et al., 2013), cobalt-rich ferromanganese crusts at seamounts (e.g., Hein et al., 2009) and polymetallic nodules (e.g., Hein et al., 2013). During the last few years, the Canadian company *Nautilus Minerals Inc.* has been actively exploring SMS in the EEZ of Papua New Guinea with the goal of commencing commercial mining operations at the mining site *Solwara 1* in 2019 (Fig. 2; Nautilus Minerals, 2017). Besides concerns over the potential severe long-term environmental consequences of mining operations (e.g., Steiner, 2009), financial and technical issues have caused a recent “fall back” in the progress of the *Solwara 1* project (Nautilus Minerals, 2018a; 2018b; 2019). Compared to these

SMS deposits found at water depths of less than 2000 m, cobalt-rich ferromanganese crusts and polymetallic nodules have received less attention due to (1) usually greater water depth of up to 5000 m, (2) relatively low metal prices and (3) less advanced mining and metallurgical processing technologies (e.g., Randhawa et al., 2016).

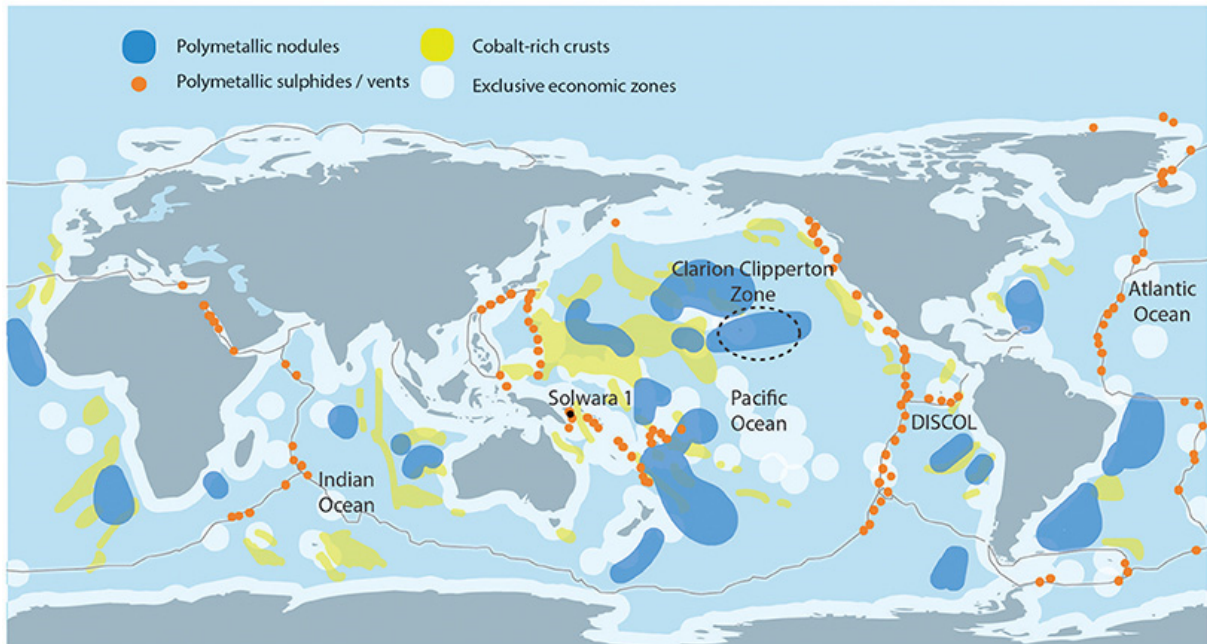


Figure 2: World map showing the occurrence of the main marine minerals: polymetallic nodules (blue), seafloor massive sulfides (orange) and cobalt-rich ferromanganese crusts (yellow) (Miller et al., 2018). The DISCOL area is located in the Peru Basin, where the Disturbance and Recolonization experiment (DISCOL) has been carried out in 1989 (Thiel and Schriever, 1989).

Polymetallic nodules were initially attractive economically, due to their relatively high base metal contents, such as Fe, Al, Ni, Cu, Co (e.g., Mero, 1965; McKelvey et al., 1983; Halbach et al., 1988). Recent studies have shown that the nodules also host large quantities of other critical metals, such as Mo, Zr, Li, Y and rare earth elements (REEs), needed for high-tech and green-tech energy applications (Hein et al., 2013). Polymetallic nodules are found throughout the world ocean at water depths between 3500–6500 m (e.g., Kuhn et al., 2017a; Miller et al., 2018). The occurrence of polymetallic nodules on the seafloor depends on various environmental factors, such as the location of the CCD in the water column, water depth, primary productivity in the surface water and subsequent transport pathways to the deep ocean, sedimentation rates, sediment type, benthic activity, seafloor topography and bottom-water currents (e.g., Halbach et al., 1988; Kuhn et al., 2017a). The most extensive deposits occur in the Pacific Ocean, notably the Clarion-Clipperton Zone (CCZ), the Peru Basin and the Penrhyn-Samoa Basin (Fig. 2; Glasby, 1976; Reyss et al., 1985; von Stackelberg and Beiersdorf, 1987). Average nodule abundances of 15 kg m^{-2} and 10 kg m^{-2} have been estimated

for the CCZ and the Peru Basin, respectively (Hein et al., 2013) while surface sediment nodule abundances of 30 kg m⁻² have been reported for the Penrhyn Basin (Cronan et al., 2010).

1.5 Formation of polymetallic nodules

Deep-sea polymetallic nodules have been known to science for more than 150 years, following their discovery during the global *Challenger* expedition (Murray and Renard, 1891). Ever since, numerous investigations have been conducted to better understand the origin of polymetallic nodules, and to evaluate their resource potential (e.g., Cronan, 1980; McKelvey, 1983). Polymetallic nodules are mineral concretions, which form on the seafloor from hydrothermal fluids (e.g., Moorby et al., 1984) or during hydrogenetic, diagenetic (e.g., Halbach et al., 1988) and microbial-mediated accretion (e.g., Blöthe et al., 2015).

The formation of these polymetallic nodules requires nuclei, i.e. growth cores, which can be fragments of sediments, rocks or biogenic material such as shark's teeth or clam shell pieces (Fig. 3; e.g., Burns and Burns, 1975; Sorem and Fewkes, 1979; Halbach et al., 1988). Under normal seawater Eh and pH conditions (Eh > 0.5 V; pH ~ 8), dissolved Mn²⁺ and Fe²⁺ tend to oxidize to Mn(IV) and Fe(III)(oxyhydr)oxide phases, which are insoluble under oxic conditions (Kuhn et al., 2017a). Amphoteric properties of hydrolyzed (oxyhydr)oxide phases cause a pH-dependent surface charge with strongly negative charged MnO₂ and a slightly positive charged δ-FeOOH. As a consequence, dissolved cations, such as Co²⁺, Ni²⁺, Zn²⁺, Tl⁺ and anionic complexes such as carbonates (REE(CO₃)₂⁻), hydroxides (Hf(OH)₅⁻) and oxyanion (MoO₄²⁻) adsorb onto the MnO₂ and δ-FeOOH surfaces, respectively (Koschinsky and Halbach, 1995; Koschinsky and Hein, 2003; Hein et al., 2013; Blöthe et al., 2015; Kuhn et al., 2017a). Dissolved components accumulate onto the growing nodule either from the overlying seawater, i.e. hydrogenetic, or from the interstitial pore water in the underlying sediment, i.e. diagenetic (e.g., Halbach and Özkara, 1979; von Stackelberg and Marchig, 1987). Hydrogenetic nodules grow about 2 mm Myr⁻¹ and have a predominantly spheroidal shape while diagenetic nodules grow at rates between 10 and 250 mm Myr⁻¹ and usually display a cauliflower shape (e.g., Koschinsky and Hein, 2003 and references therein; von Stackelberg, 2000; Glasby, 2006; Kuhn et al., 2017a). The accretion of dissolved constituents onto the nodule surface results in the formation of concentric bands around the growth core (e.g., Halbach et al., 1988; Wegorzewski and Kuhn, 2014; Wegorzewski et al., 2015). The majority of nodules are discoidal-shaped and consist of irregular bands of differing composition, which are associated with the alternation of hydrogenetic and diagenetic accretion (Fig. 3; e.g., Dymond et al., 1984; Wegorzewski and Kuhn, 2014; Kuhn et al., 2017a). Hydrogenetically grown layers have Mn/Fe

ratios ≤ 5 and are dominated by the mineral vernadite ($\delta\text{-MnO}_2$) whereas concentric layers of diagenetic origin have Mn/Fe ratios > 5 and mainly consist of todorokite (10 Å manganate) and birnessite (7 Å manganate) (e.g., Burns and Burns 1978a, 1978b; Halbach et al., 1981; Halbach et al., 1988). The diagenetic nodule growth processes can be divided into the oxic-diagenetic and suboxic-diagenetic pathways (e.g., Halbach and Özkara, 1979; Dymond et al., 1984; Reyss et al., 1985; Halbach et al., 1988). During the oxic-diagenetic formation, dissolved constituents accumulate from oxic pore water during the degradation of organic matter at the sediment surface, while the suboxic-diagenetic accretion requires the upward diffusion of pore-water Mn^{2+} from deeper sediments towards the sediment surface.

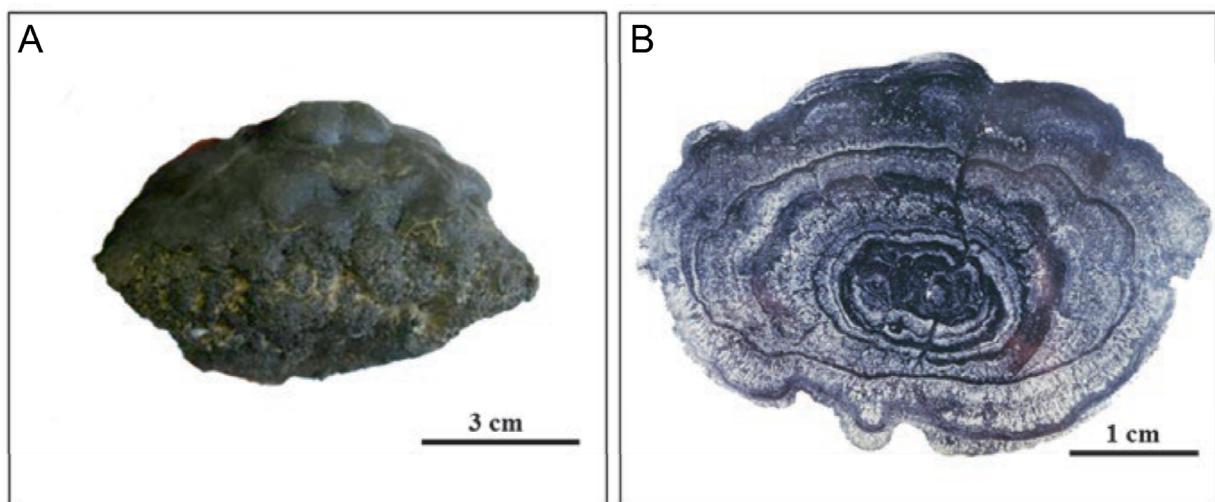


Figure 3: (A) Typical discoidal shape of a polymetallic nodule with a smooth texture on the upper surface and a rough, coarse-grained surface at the bottom. (B) Vertical section of a typical polymetallic nodule showing the layered growth structure around a nucleus (Kuhn et al., 2017a). Both figures: © BGR

1.6 The Clarion-Clipperton Zone

The Clarion-Clipperton Zone (CCZ) comprises a seabed area of about 6 million km^2 at water depths of 4000–5000 m in the NE Pacific Ocean (Fig. 4). The CCZ is defined by two major transform faults, the Clarion Fracture Zone in the north and the Clipperton Fracture Zone in the south. Both fracture zones have been formed at the East Pacific Rise (EPR) and stretch perpendicular to the mid-ocean ridge. The vast seafloor within the CCZ is characterized by numerous seamounts as well as NNE-SSW oriented horst and graben structures, which are relics of the oceanic crust formation at the EPR about 20 Myr ago (e.g., Macdonald et al., 1996; Barckhausen et al., 2013; Mewes et al., 2016; Kuhn et al., 2017b).

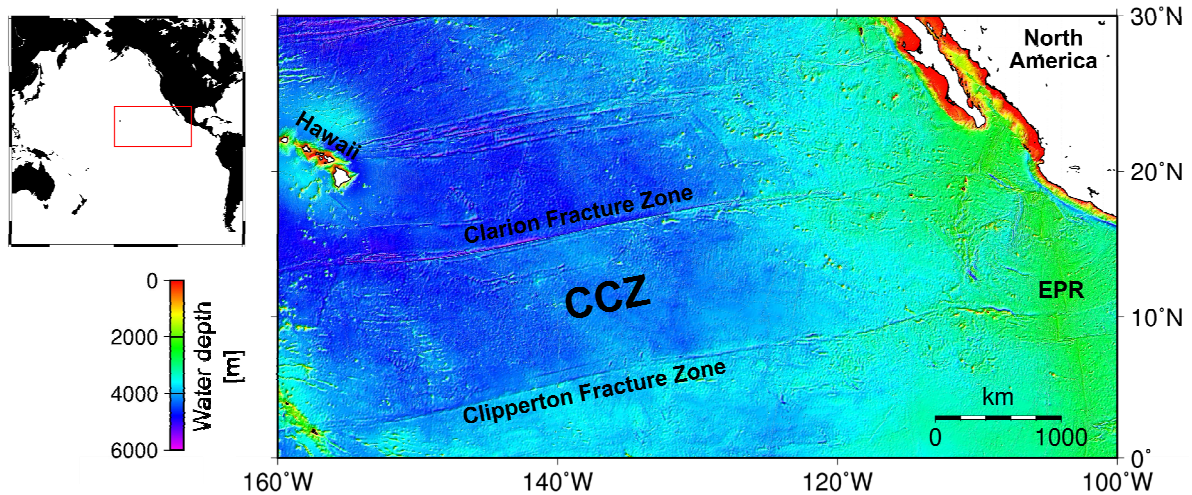


Figure 4: Bathymetric map showing the seafloor of the CCZ in the NE Pacific Ocean.

The CCZ is located north of the equatorial Pacific high-productivity belt, where the upwelling of cold, nutrient-rich waters in the eastern boundary current and along the equator fuels the surface water productivity (e.g., Barber and Chavez, 1991). In the surface waters overlying the CCZ, the productivity is lower when compared to the equatorial Pacific high-productivity belt due to warm, nutrient-poor surface waters (e.g., Murray et al., 1989). As a function of surface water productivity, there is an east-to-west and south-to-north gradient in the POC fluxes to the seafloor in the CCZ, within the range of 1–2 mg C_{org} $m^{-2} d^{-1}$ (e.g., Lutz et al., 2007; Vanreusel et al., 2016). As the abyssal seafloor within the CCZ is mostly situated below the modern CCD at 4–5 km, the pelagic sediments are dominated by siliceous oozes (e.g., Berger et al., 1974; Pälike et al., 2012).

The widespread occurrence of polymetallic nodules at the seafloor is mostly facilitated by low sedimentation rates of less than 1 cm kyr^{-1} throughout the CCZ (Müller and Mangini, 1980; Mewes et al., 2014). The distribution of nodules at the seafloor varies strongly throughout the CCZ, mostly associated with spatial variations in sediment composition and accumulation rate (e.g., Halbach et al., 1988; Peukert et al., 2018). Both environmental factors, sediment composition and accumulation rate, are greatly influenced by the POC flux to the seafloor, benthic biological activity in the sediment, i.e. bioturbation, as well as seafloor topography and bottom-water currents (e.g., Mewes et al., 2014; Kuhn et al., 2017a). The complex system of bottom-water currents in the CCZ is tidally influenced, controlled by latitudinal and seasonal variations and locally diverse (e.g., Juan et al., 2018). Moreover, abundant large seamounts are found within the CCZ, which rise up to 3000 m from the abyssal seafloor and can affect bottom-water currents (e.g., Gould et al., 1981; Rühlemann et al., 2011; Xu and Lavelle, 2017). In the proximity of seamounts, bottom-water currents can be intensified, attenuated and

deflected, causing variations in sediment composition and accumulation rates on the seafloor over several kilometers (Turnewitsch et al., 2004; Mewes et al., 2014; Turnewitsch et al., 2015). Well oxygenated bottom waters, low POC fluxes to the seafloor and low sedimentation rates in the CCZ are associated with a broad upper oxic zone of more than 1 m in the sediments (Fig. 5; Røy et al., 2012; Mewes et al., 2014; 2016; Kuhn et al., 2017b). Due to this meter-scale oxygen penetration depth (OPD) in the sediments, the nodule growth in the CCZ is currently dominated by hydrogenetic, oxic-diagenetic and microbial-mediated accretion (Fig. 5; Mewes et al., 2014; Wegorzewski et al., 2014; Blöthe et al., 2015; Heller et al., 2018; Menendez et al., 2018). Aerobic respiration is the dominant biogeochemical process in the sediments of the CCZ, which consumes most of the organic matter delivered to the seafloor (Müller et al., 1988; Mewes et al., 2016; Mogollón et al., 2016). Below the oxic zone, denitrification and the dissimilatory reduction of Mn(IV) co-occur in the suboxic zone, where oxygen and sulfide are absent (Fig. 5; e.g., Mewes et al., 2014; Mogollón et al., 2016; Kuhn et al., 2017b). Depending on the concentration of pore-water Mn^{2+} in the suboxic zone, the N-Mn redox cycling is linked via Mn^{2+} oxidation by nitrate and Mn-annamox (Luther et al., 1997; Mogollón et al., 2016).

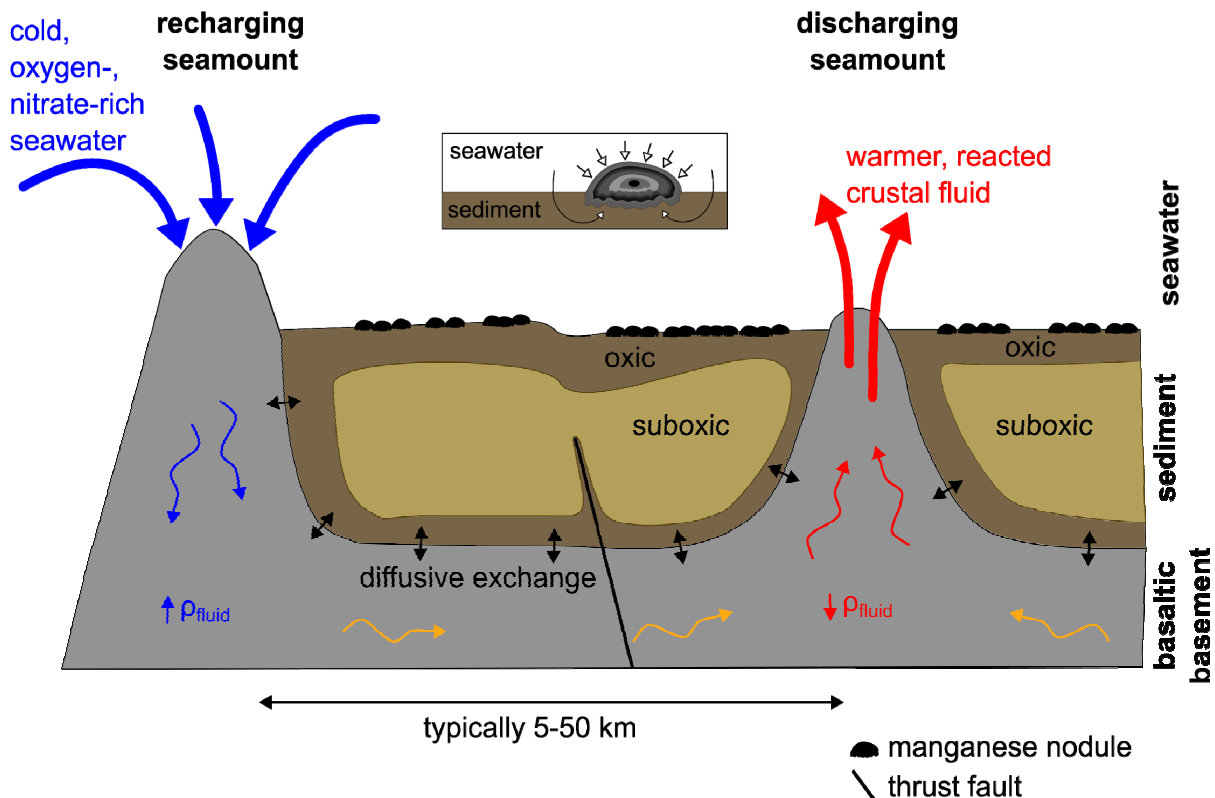


Figure 5: Schematic illustration of the geochemical zonation in the sediments of the CCZ and conceptual model of ridge-flank low hydrothermal circulation facilitated by seamount after Wheat and Fisher (2008) and Versteegh et al. (in prep.). Inset figure shows the hydrogenetic and oxic-diagenetic accretion of metals onto the surface of polymetallic nodules (modified after Kuhn et al., 2017b), which currently dominate the nodule growth in the CCZ.

Based on downward increasing oxygen concentrations and/or the oxidation of pore-water Mn^{2+} in the sediments at several sites within the CCZ at depth, studies have suggested that upward diffusing oxygen is supplied from the basaltic basement below (Fig. 5; Mewes et al., 2016; Kuhn et al., 2017b; Versteegh, in prep.). The supply of oxygen from the basaltic basement has been demonstrated to be associated with the existence of low-temperature hydrothermal seawater circulation through crustal outcrops, extracting a significant fraction of heat from the oceanic lithosphere (Fig. 5; e.g., Wheat and Fisher, 2008; Kuhn et al., 2017b). The hydrothermal circulation of seawater through the basaltic basement is mainly driven by small pressure gradients (ρ_{fluid}) on the ridge flanks (Fig. 5; e.g., Wheat and Fisher, 2008). The permeability of the basaltic crust determines the rate at which the seawater recharges at a seamount, flows laterally through the basement, ascends and discharges at another seamount (Fig. 5; e.g., Wheat and Fisher, 2008). As marine sediments have much lower permeability than the basaltic crust (e.g., Spinelli et al., 2004), only a small fraction of the lateral fluid flow in the basement diffuses vertically into the overlying sediments (e.g., Wheat and Fisher, 2008). The “reversed” redox zonation resulting from upward diffusing oxygen from the basaltic crust has been reported for several sites within the CCZ and may be a large-scale phenomenon (Mewes et al., 2016; Kuhn et al., 2017b; Versteegh, in prep.).

1.7 Resource management in the Clarion-Clipperton Zone

Since the concept of deep-sea mining was first introduced by Mero (1965), the global interest in deep-sea mining thrived in the 1970s. In 1967, the need for international environmental protection regulations was urged by Malta’s Ambassador Arvid Pardo in a speech to the First Committee of United Nations General Assembly, where the Ambassador referred to deep-sea mineral deposits as the “common heritage of mankind”. Under the United Nations convention on the Law of the Sea (UNCLOS) in 1982, the International Seabed Authority (ISA) was established as an autonomous organization responsible for the protection and conservation of marine mineral resources in the area beyond the EEZs (Article 145 UNCLOS; Fig. 2). The ISA has granted contract areas in the central Pacific Ocean to sixteen national governments and consortia of states for the exploration of polymetallic nodules, including technology tests and the assessment of the environmental impacts of mining activities (Lodge et al., 2014; Madureira et al., 2016). In 2012, the ISA approved an Environmental Management Plan (EMP) for the central Pacific Ocean, which represents the first regulatory framework for the exploitation and the environmental management of deep-sea mining (ISA, 2011). The EMP includes assigned contract areas for the exploration of polymetallic nodules with a network of nine protected areas, namely Areas of Particular Interest (APEIs),

which surround the contract areas (Fig. 6). These APEIs each cover an area of 400 x 400 km² and are excluded from any mining activities (ISA, 2011). For the ongoing development of the EMP, the ISA is depending on all contract holders to conduct and report on environmental studies (Lodge et al., 2014).

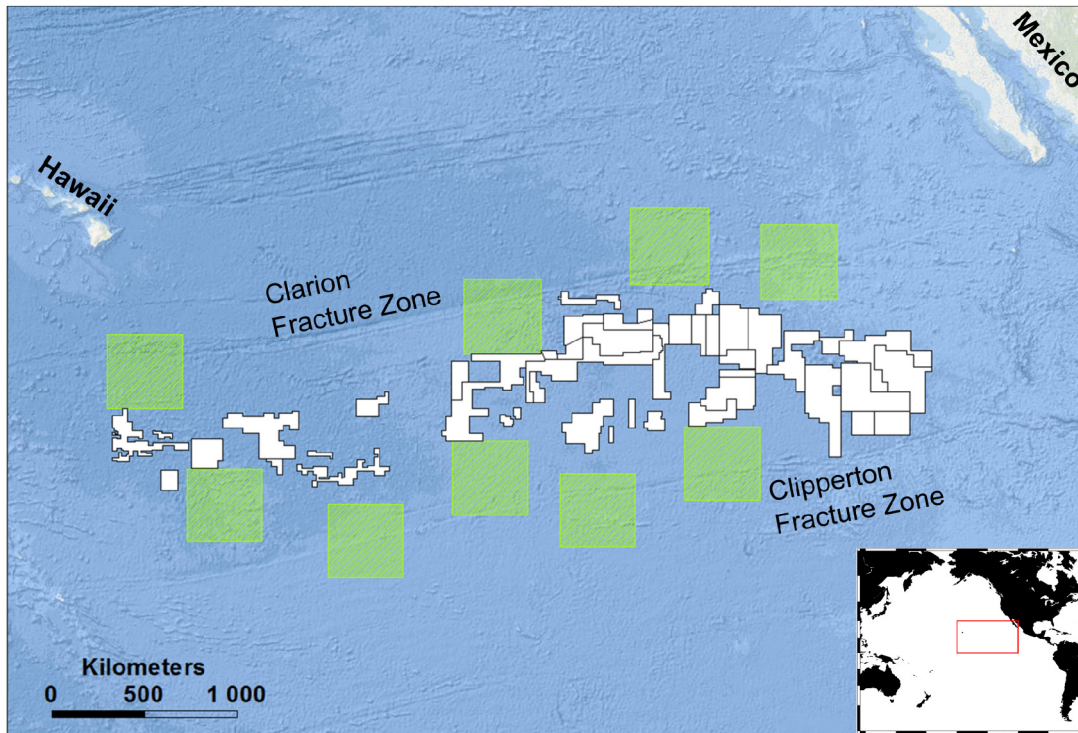


Figure 6: Contract areas for the exploration of polymetallic nodules granted by the International Seabed Authority (ISA) within the CCZ (white areas) surrounded by nine Areas of Particular Environmental Interest (APEIs, green shaded squares), which are excluded from any mining activities (Geographical data provided by the International Seabed Authority).

1.8 Polymetallic nodule mining and potential environmental impacts

The recent rise in prices for some of the high-tech metals found within polymetallic nodules has made deep-sea mining attractive again and with the high resource potential of polymetallic nodules in the NE Pacific Ocean, future commercial deep-sea mining will probably target the CCZ (e.g., Halbach et al., 1988; Hein et al., 2013; Kuhn et al., 2017a). Despite recent significant advances in deep-sea mining technology, a clear consensus on the most suitable mining technique at great water depths is still lacking (e.g., Oebius et al., 2001; Jones et al., 2017; Gollner et al., 2017). Several concepts have been proposed and prototypes have been built, which generally consist of four components (Fig. 7): (1) the mining platform as operational control and pre-processing plant for the nodules, (2) the lift pipe for conveying the nodules, (3) the nodule collector at the seafloor and (4) the discharge system for waste water containing nodules, re-suspended sediment and particles after pre-processing the nodules on the

platform (e.g., Oebius et al., 2001). Nodule collectors are proposed to plough tens of centimeters into the sediments, from which the nodules are mechanically or hydraulically removed from the seafloor (Fig. 7; e.g., Gollner et al., 2017).

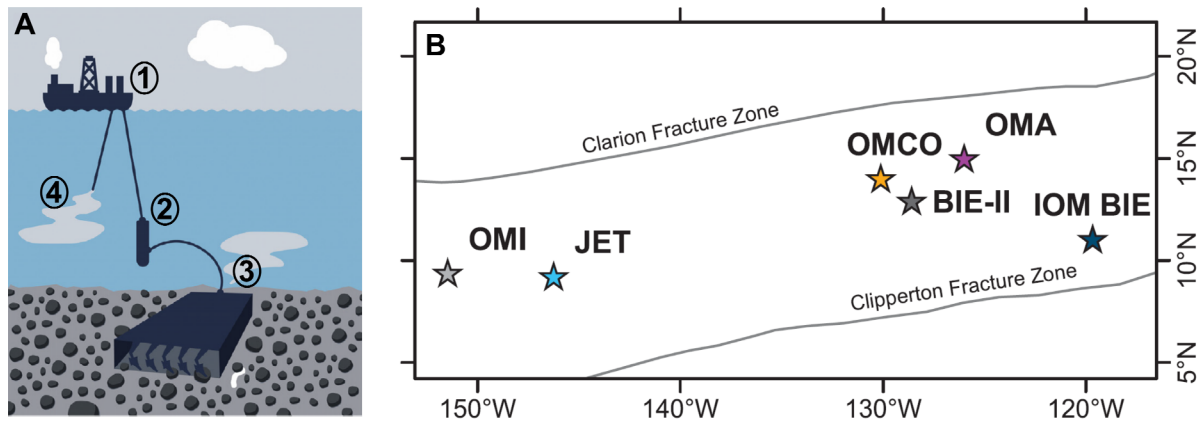


Figure 7: (A) Concept of deep-sea mining with the (1) mining platform, (2) lift pipe, (3) nodule collector and (4) discharge system (e.g., Oebius et al., 2001). Figure modified after Gollner et al. (2017). (B) Small-scale deep-sea mining experiments performed in the area of the CCZ (Jones et al., 2017).

Several mining tests have been performed in the area of the CCZ (Fig. 7). Furthermore, small-scale deep-sea mining simulations have been conducted using different devices in order to assess the potential environmental consequences in the CCZ and in the Peru Basin (Figs. 2 and 7; e.g., Jones et al., 2017). The first nodule mining attempt in the CCZ was carried out in 1976 by the Ocean Mining Associates (OMA) consortium, which was followed by three further tests in 1978. These mining trials were undertaken by Ocean Management Inc. (OMI), Deepsea Ventures Inc. for OMA and by a consortium of several U.S. industry groups merged as the Ocean Minerals Company (OMCO). The environmental impacts of the mining tests were studied during the comprehensive Deep Ocean Mining Environmental Study (DOMES; Burns, 1980) project. During the *Nautilus* and *Nodinaut* cruises in 1988 and 2004 lead by the French institute IFREMER, the disturbance tracks created during the mining trials by OMCO in 1978 were re-visited (e.g., Khripounoff et al., 2006). With focus on the environmental impact assessment of small-scale deep-sea mining simulations, the Japan Deep Sea Impact Experiment (JET; Fukushima, 1995) was conducted in 1994. The Benthic Impact Experiment (BIE) was performed in two phases between 1993 (BIE-II) and 1995 (IOM-BIE) (e.g., Trueblood and Ozturgut, 1997; Radziejewska, 2002). In the framework of environmental protection activities, the German Disturbance and Recolonization Experiment (DISCOL) was conducted in 1989 in Peru Basin (Fig. 2; Thiel and Schriever, 1989; Thiel et al., 2001). The DISCOL area was re-visited several years after the disturbance during the ATESEPP (Impacts of potential

technical interventions on the deep-sea ecosystem in the southeast Pacific) project (Schriever et al., 1997; Thiel et al., 2001). As part of the EU-funded MIDAS partnership (Managing Impacts of Deep-Sea resources exploitation), the recovery of benthic habitats and communities at the OMCO site in the CCZ was studied 26 years after the initial disturbance (Fig. 7; e.g., Miljutin et al., 2011). In 2015, the JPI Oceans (Joint Programming Initiative Healthy and Productive Seas and Oceans) pilot action “Ecological Aspects of Deep-Sea Mining (MiningImpact)” was launched during which the disturbance tracks of several mining trials and small-scale deep-sea mining simulations were re-visited in the CCZ (OMCO and IOM-BIE; Fig 7; Martínez Arbizu and Haeckel, 2015). In addition, several new small-scale deep-sea mining simulations were performed in different European contract areas in the CCZ (Martínez Arbizu and Haeckel, 2015). The DISCOL area in the Peru Basin was also re-visited in the framework of the JPIO pilot action “Ecological Aspects of Deep-Sea Mining (MiningImpact)” in order to assess the recovery state 26 years after the initial deep-sea mining experiment (Boetius, 2015; Greinert, 2015).

The environmental consequences of deep-sea mining activities include the removal of nodules and sediments as well as the development of a re-suspended particle plume in the water column due to sediment stirring (Fig. 7; Oebius et al., 2001; Jankowski and Zielke, 2001; Thiel et al., 2001; Cuvelier et al., 2018; Gillard et al., 2019). Depending on the nodule collector, sediments may also be mixed and compacted due to the weight of the operating nodule collector (e.g., Paul et al., 2018; Cuvelier et al., 2018; Hauquier et al., 2019). Further potential environmental impacts of deep-sea mining activities on the deep-sea ecosystem include (1) the loss of sessile and mobile fauna (e.g., Purser et al., 2016; Jones et al., 2017), (2) the destruction of seafloor habitats (e.g., Gollner et al., 2017), (3) the alteration of (bio)geochemical processes and redox zonation (e.g., König et al., 2001), (4) the release of possibly toxic metals from the pore water into the overlying bottom water (e.g., Koschinsky et al., 2003) and (5) sediment blanketing due to re-settling particles from the re-suspended particle plume on a kilometer-scale around the disturbed area (e.g., Fukushima, 1995; Gillard et al., 2019). The recolonization of the benthic fauna after deep-sea mining activities is expected to take several centuries, while pre-mining benthic communities may never be restored due to the removal of seafloor habitats (e.g., Miljutin et al., 2011; Vanreusel et al., 2016; Gollner et al., 2017).

1.9 Declaration of co-author contributions

All manuscripts presented in this dissertation were produced in close collaboration of all co-authors. In this section, the individual contributions to the scientific articles as well as the manuscript statuses are expounded.

CHAPTER II: Natural spatial variability of depositional conditions, biogeochemical processes and element fluxes in sediments of the eastern Clarion-Clipperton Zone, Pacific Ocean

Jessica B. Volz (JBV), José M. Mogollón (JMM), Walter Geibert (WG), Pedro Martínez Arbizu (PMA), Andrea Koschinsky (AK), Sabine Kasten (SK)

Status: Published in *Deep-Sea Research Part I*, doi:10.1016/j.dsr.2018.08.006; published online August, 14th 2018

The study was conceived by JBV, SK and AK. JBV carried out the sampling and analyses on board during RV SONNE cruise SO239, the analytical work in the laboratories at AWI in Bremerhaven and evaluated the data with the support of WG. JMM produced the numerical transport-reaction model and provided the depth-integrated rates of the modeled biogeochemical processes. JBV prepared the manuscript with substantial contributions from JMM, WG, PMA and SK. The personal contribution is estimated to 80%.

CHAPTER III: Calcium phosphate control of REY patterns of siliceous-ooze-rich deep-sea sediments from the central equatorial Pacific

Sophie A. L. Paul (SALP), Jessica B. Volz (JBV), Michael Bau (MB), Male Köster (MK), Sabine Kasten (SK), Andrea Koschinsky (AK)

Status: Published in *Geochimica et Cosmochimica Acta*; doi:10.1016/j.gca.2019.02.019; published online February, 16th 2019

The study was conceived by SALP and AK. JBV conducted parts of the analytical work in the laboratories at AWI in Bremerhaven and supervised the optimized leaching experiments carried out by MK. SALP conducted further analyses and wrote the manuscript with substantial contributions from MB, JBV, SK and AK. The personal contribution is estimated to 10%.

CHAPTER IV: Post-depositional manganese mobilization during the last glacial period in sediments of the eastern Clarion-Clipperton Zone, Pacific Ocean

Jessica B. Volz (JBV), Bo Liu (BL), Male Köster (MK), Susann Henkel (SH), Andrea Koschinsky (AK), Sabine Kasten (SK)

Status: Revised manuscript submitted to *Earth and Planetary Science Letters* on September, 23rd 2019

The study was conceived by JBV, MK and SK. MK developed the optimized sequential leaching method and carried out the analytical work in the laboratories at AWI in Bremerhaven under supervision of SK, SH and JBV. MK developed and applied the optimized sequential leaching in the framework of the master thesis. JBV carried out parts of the analytical work and produced the bulk sediment data. BL modified the numerical transport-reaction model presented in the 1st manuscript and provided the scenario modelling results. JBV wrote the manuscript with substantial contributions from MK, BL, AK and SK. The personal contribution is estimated to 70%.

CHAPTER V: Impact of small-scale disturbances on geochemical conditions, biogeochemical processes and element fluxes in sediments of the eastern Clarion-Clipperton Zone, Pacific Ocean

Jessica B. Volz (JBV), Laura Haffert (LH), Matthias Haeckel (MH), Andrea Koschinsky (AK), Sabine Kasten (SK)

Status: Under review at *Biogeosciences* since August, 20th 2019

The study was conceived by JBV, SK, AK and MH. JBV carried out the sampling and analyses on board during RV SONNE cruise SO239 and the analytical work in the laboratories at AWI in Bremerhaven. LH modified the numerical transport-reaction model presented in the 1st manuscript and provided model results for the long-term effects of small-scale disturbances on geochemical conditions and biogeochemical processes. JBV prepared the manuscript with substantial contributions from LH, MH, AK and SK. The personal contribution is estimated to 70%.

References

- Barber, R.T., Chavez, F.P., 1991. Regulation of primary productivity rate in the equatorial Pacific. *Limnol. Oceanogr.* 36, 1803–1815.
- Barckhausen, U., Bage, M., Wilson, D.S., 2013. Seafloor spreading anomalies and crustal ages of the Clarion-Clipperton zone. *Mar. Geophys. Res.* 34, 79–88.
- Berger, W.H., 1974. Deep-sea sedimentation. In: *The Geology of Continental Margins* (eds. Burk, C.A., Drake, C.L.). Springer, New York, 213–241.
- Berner, R.A., 1981. A new geochemical classification of sedimentary environments. *J. Sediment. Petrol.* 51, 359–365.
- Blank, M., Leinen, M., Prospero, J.M., 1985. Major Asian aeolian inputs indicated by the mineralogy of aerosols and sediments in the western North Pacific. *Nature* 314, 84–86.
- Blöthe, M., Wegorzewski, A., Müller, C., Simon, F., Kuhn, T., Schippers, A., 2015. Manganese-Cycling Microbial Communities Inside Deep-Sea Manganese Nodules. *Environ. Sci. Technol.* 49, 7692–7700.
- Boetius, A., 2015. RV Sonne Fahrtbericht / Cruise Report SO242-2: JPI OCEANS Ecological Aspects of Deep-Sea Mining, DISCOL Revisited, Guayaquil-Guayaquil (Equador), 28.08.–01.10.2015, Kiel: Helmholtz-Zentrum für Ozeanforschung.
- Boschen, R.E., Rowden, A.A., Clark, M.R., Gardner, J.P.A., 2013. Mining of deep-sea seafloor massive sulfides: A review of the deposits, their benthic communities, impacts from mining, regulatory frameworks and management strategies. *Ocean Coast. Manag.* 84, 54–67.
- Boudreau, B.P., 1997. A one-dimensional model for bed-boundary layer particle exchange. *J. Mar. Syst.* 11, 279–303.
- Burdige, D.J., Gieskes, J.M., 1983. A pore water/solid phase diagenetic model for manganese in marine sediments. *Am. J. Sci.* 283, 29–47.
- Burns, R.E., 1980. Assessment of environmental effects of deep ocean mining of manganese nodules. *Helgoländer Meeresunters.* 33, 433–442.
- Burns, V.M., Burns, R.G., 1978b. Post-depositional metal enrichment processes inside manganese nodules from the north equatorial Pacific. *Earth Planet. Sci. Lett.* 39, 341–348.
- Burns, V.M., Burns, R.G., 1978a. Authigenic todorokite and phillipsite inside deep-sea manganese nodules. *Am. Mineral.* 63, 827–831.
- Burns, R.G., Burns, V.M., 1975. Mechanisms for nucleation and growth of manganese nodules. *Nature* 255, 130–131.
- Cronan, D.S., Rothwell, G., Croudace, I., 2010. An ITRAX geochemical study of ferromanganiferous sediments from the Penrhyn basin, South Pacific Ocean. *Mar. Georesour. Geotechnol.* 28, 207–221.
- Cronan, D.S., 1980. Underwater minerals. Academic Press, London.
- Cuvelier, D., Gollner, S., Jones, D.O.B., Kaiser, S., Arbizu, P. M., Menzel, L., Mestre, N.C., Morato, T., Pham, C., Pradillon, F., Purser, A., Raschka, U., Sarrazin, J., Simon-Lledó, E., Stewart, I.M., Stuckas, H., Sweetman, A.K., Colaço, A., 2018. Potential Mitigation and Restoration Actions in Ecosystems Impacted by Seabed Mining. *Front. Mar. Sci.* 5. doi:10.3389/fmars.2018.00467.
- Davies, T.A., Gorsline, D.S., 1976. Oceanic sediments and sedimentary processes. In: *Chemical oceanography 5* (eds. Riley, J.P., Chester, R.). Academic Press, London, New York, San Francisco, pp 1–80.

- Drodt, M., Trautwein, A.X., König, I., Suess, E., Bender Koch, C., 1997. Mössbauer spectroscopic studies on the iron forms of deep-sea sediments. *Phys. Chem. Miner.* 24, 281–293.
- Dymond, J., Lyle, M.W., Finney, B.P., Piper, D.Z., Murphy, K., Conard, R., Pisias, N., 1984. Ferromanganese nodules from MANOP Sites H, S, and R – Control of mineralogical and chemical composition by multiple accretionary processes. *Geochim. Cosmochim. Acta* 48, 931–949.
- Fischer, J.P., Ferdelman, T.G., D'Hondt, S., Roy, H., Wenzhöfer, F., 2009. Oxygen penetration deep into the sediment of the South Pacific gyre. *Biogeosciences* 6, 1467–1478.
- Froelich, P.N., Klinkhammer, G.P., Bender, M.L., Luedke, L.A., Heath, G.R., Cullen, C., Dauphin, P., Hammond, D., Hartmann, B., Maynard, V., 1979. Early oxidation of organic matter in pelagic sediments of the Eastern Equatorial Pacific, suboxic diagenesis. *Geochim. Cosmochim. Acta* 43, 1075–1090.
- Fütterer, D.K., 2006. The Solid Phase of Marine Sediments. In: *Marine geochemistry* (eds. Schulz, H.D., Zabel, M.). Springer Berlin Heidelberg, 73–124.
- Fukushima, T., 1995. Overview "Japan Deep-Sea Impact Experiment = JET", ISOPE-M-95-008, ISOPE.
- Gillard, B., Purkiani, K., Chatzievangelou, D., Vink, A., Iversen, M.H., Thomsen, L., 2019. Physical and hydrodynamic properties of deep sea mining-generated, abyssal sediment plumes in the Clarion Clipperton Fracture Zone (eastern-central Pacific). *Elem. Sci. Anth.* 7.
- Glasby, G.P., 2006. Manganese: Predominant Role of Nodules and Crusts. In: *Marine geochemistry* (eds. Schulz, H.D., Zabel, M.). Springer Berlin Heidelberg, 371–427.
- Glasby, G.P., 1976. Manganese nodules in the South Pacific: A review. *N.Z. Jl. Geol. Geophys.* 19, 707–736.
- Glud, R.N., Gundersen, J.K., Jørgensen, B.B., Revsbech, N.P., Schulz, H.D., 1994. Diffusive and total oxygen uptake of deep-sea sediments in the eastern South Atlantic Ocean: in situ and laboratory measurements. *Deep-Sea Res.* 41, 1767–1788.
- Gollner, S., Kaiser, S., Menzel, L., Jones, D.O.B., Brown, A., Mestre, N.C., van Oevelen, D., Menot, L., Colaço, A., Canals, M., Cuvelier, D., Durden, J.M., Gebruk, A., Eghe, G.A., Haeckel, M., Marcon, Y., Mevenkamp, L., Morato, T., Pham, C.K., Purser, A., Sanchez-Vidal, A., Vanreusel, A., Vink, A., Arbizu, P.M., 2017. Resilience of benthic deep-sea fauna to mining activities. *Mar. Environ. Res.* 129, 76–101.
- Gould, W.J., Hendry, R., Huppert, H.E., 1981. An abyssal topographic experiment. *Deep-Sea Res.* 28A, 409–440.
- Greinert, J., 2015. RV Sonne Fahrtbericht / Cruise Report SO242-1: JPI OCEANS Ecological Aspects of Deep-Sea Mining, DISCOL Revisited, Guayaquil-Guayaquil (Ecuador), 28.07.–25.08.2015, Kiel: Helmholtz-Zentrum für Ozeanforschung.
- Haeckel, M., König, I., Riech, V., Weber, M.E., Suess, E., 2001. Pore water profiles and numerical modelling of biogeochemical processes in Peru Basin deep-sea sediments. *Deep. Res. Part II Top. Stud. Oceanogr.* 48, 3713–3736.
- Halbach, P., Friedrich, G., von Stackelberg, U. (eds.), 1988. The manganese nodule belt of the Pacific Ocean. Enke, Stuttgart.
- Halbach, P., Scherhag, C., Hebisch, U., Marchig, V., 1981. Geochemical and mineralogical control of different genetic types of deep-sea nodules from the Pacific Ocean. *Mineral. Deposita* 16, 59–84.

- Halbach, P., Özkara, M., 1979. Morphological and geochemical classification of deep-sea ferromanganese nodules and its genetical interpretation. *La Genese des Nodules de Manganese* 289, 77–88.
- Halfar, J., Fujita, R.M., 2002. Precautionary management of deep-sea mining. *Mar. Pol.* 26, 103–106.
- Hauquier, F., Macheriotou, L., Bezerra, T.N., Egho, G., Martínez Arbizu, P., Vanreusel, A., 2019. Geographic distribution of free-living marine nematodes in the Clarion-Clipperton Zone: implications for future deep-sea mining scenarios. *Biogeosciences* 16, 3475–3489.
- Hein, J.R., Mizell, K., Koschinsky, A., Conrad, T.A., 2013. Deep-ocean mineral deposits as a source of critical metals for high- and green-technology applications: comparison with land-based resources. *Ore Geol. Rev.* 51, 1–14.
- Hein, J.R., Conrad, T.A., Dunham, R.E., 2009. Seamount characteristics and mine-site model applied to exploration- and mining-lease-block selection for cobalt-rich ferromanganese crusts. *Mar. Geores. Geotech.* 27, 160–176.
- Heller, C., Kuhn, T., Versteegh, G.J., Wegorzewski, A.V., Kasten, S., 2018. The geochemical behavior of metals during early diagenetic alteration of buried manganese nodules. *Deep-Sea Res. Part I* 142, 16–33.
- Holby, O., Riess, W., 1996. In Situ Oxygen Dynamics and pH-Profiles. In: *Report and preliminary results of Meteor cruise M34/2 Walvis Bay-Walvis Bay, 29.01.1996–18.02.1996* (eds. Schulz, H.D. and cruise participants). Berichte, Fachbereich Geowissenschaften, Univ. Bremen, 78: 85–87.
- International Seabed Authority (ISA), 2011. Environmental Management Plan for the Clarion-Clipperton Zone. Legal and Technical Commission. <https://www.isa.org.jm/documents/isba17l7tc7>.
- Jankowski, J.A., Zielke, W., 2001. The mesoscale sediment transport due to technical activities in the deep sea. *Deep. Res. Part II Top. Stud. Oceanogr.* 48, 3487–3521.
- Jørgensen B.B., 2006. Bacteria and marine biogeochemistry. In: *Marine geochemistry* (eds. Schulz, H.D., Zabel, M.). Springer Berlin Heidelberg, 173–207.
- Jones, D.O.B., Kaiser, S., Sweetman, A.K., Smith, C.R., Menot, L., Vink, A., and 11 others, 2017. Biological response to disturbance from simulated deep-sea polymetallic nodule mining. *PLoS ONE* 12(2):e0171750.
- Juan, C., Van Rooij, D., De Bruycker, W., 2018. An assessment of bottom current controlled sedimentation in Pacific Ocean abyssal environments. *Mar. Geol.* 403, 20–33.
- Kasten S., Zabel M., Heuer V., Hensen C., 2003. Processes and Signals of Nonsteady-State Diagenesis in Deep-Sea Sediments and their Pore Waters. In: *The South Atlantic in the Late Quaternary* (eds. Wefer, G., Mulitza, S., Ratmeyer, V.). Springer Berlin Heidelberg, 431–459.
- Khripounoff, A., Caprais, J.-C., Crassous, P., Etoubleau, J., 2006. Geochemical and biological recovery of the disturbed seafloor in polymetallic nodule fields of the Clipperton-Clarion Fracture Zone (CCFZ) at 5,000-m depth. *Limnol. Oceanogr.* 51, 2033–2041. doi:10.4319/lo.2006.51.5.2033, 2006.
- König, I., Haeckel, M., Lougear, A., Suess, E., Trautwein, A.X., 2001. A geochemical model of the Peru Basin deep-sea floor – and the response of the system to technical impacts. *Deep. Res. Part II Top. Stud. Oceanogr.* 48, 3737–3756.

- Koschinsky, A., Winkler, A., Fritsche, U., 2003. Importance of different types of marine particles for the scavenging of heavy metals in the deep-sea bottom water. *Appl. Geochemistry* 18, 693–710.
- Koschinsky, A., Hein, J.R., 2003. Uptake of elements from seawater by ferromanganese crusts: solid-phase associations and seawater speciation. *Mar. Geol.* 198, 331–351.
- Koschinsky, A., Halbach, P., 1995. Sequential leaching of marine ferromanganese precipitates: Genetic implications. *Geochim. Cosmochim. Acta* 59, 5113–5132.
- Kuhn, T., Versteegh, G.J.M., Villinger, H., Dohrmann, I., Heller, C., Koschinsky, A., Kaul, N., Ritter, S., Wegorzewski, A.V., Kasten, S., 2017b. Widespread seawater circulation in 18–22 Ma oceanic crust: Impact on heat flow and sediment geochemistry. *Geology* 45, 799–802.
- Kuhn, T., Wegorzewski, A., Rühlemann, C., Vink, A., 2017a. Composition, Formation, and Occurrence of Polymetallic Nodules. In: *Deep Sea Mining* (ed. Sharma, R.). Springer, Cham.
- Lodge, M., Johnson, D., Le Gurun, G., Wengler, M., Weaver, P., Gunn, V., 2014. Seabed mining: International Seabed Authority environmental management plan for the Clarion-Clipperton Zone. A partnership approach. *Mar. Pol.* 49, 66–72.
- Luther, G.W., Sundby, B., Lewis, B.L., Brendel, P.J., Silverberg, N., 1997. Interactions of manganese with the nitrogen cycle: Alternative pathways to dinitrogen. *Geochim. Cosmochim. Acta* 61, 4043–4052.
- Lutz, M.J., Caldeira, K., Dunbar, R.B., Behrenfeld, M.J., 2007. Seasonal rhythms of net primary production and particulate organic carbon flux to depth describe the efficiency of biological pump in the global ocean. *J. Geophys. Res. Ocean.* 112.
- Lyle, M.W., 1983. The brown-green color transition in marine sediments: A marker of the Fe(III) - Fe(II) redox boundary. *Limnol. Oceanogr.* 28, 1026–1033.
- Lynn, D.C., Bonatti, E., 1965. Mobility of manganese in diagenesis of deep-sea sediments. *Mar. Geol.* 3, 457–474.
- Macdonald, K.C., Fox, P.J., Alexander, R.T., Pockalny, R., Gente, P., 1996. Volcanic growth faults and the origin of Pacific abyssal hills. *Nature* 380, 125–129.
- Madureira, P., Brekke, H., Cherkashov, G., Rovere, M., 2016. Exploration of polymetallic nodules in the Area: Reporting practices, data management and transparency. *Mar. Pol.* 70, 101–107. doi:10.1016/j.marpol.2016.04.051.
- Martínez Arbizu, P., Haeckel, M., 2015. RV SONNE Fahrtbericht / Cruise Report SO239: EcoResponse Assessing the Ecology, Connectivity and Resilience of Polymetallic Nodule Field Systems, Balboa (Panama) – Manzanillo (Mexico,) 11.03.–30.04.2015 (Report No. doi:10.3289/GEOMAR_REP_NS_25_2015), GEOMAR Helmholtz-Zentrum für Ozeanforschung, Kiel, Germany.
- McKelvey, V.E., Wright, N.A., Bowen, R.W., 1983. Analysis of the world distribution of metal-rich subsea manganese nodules. *U.S. Geol. Surv. Circ.* 886, 55 pp.
- Menendez, A., James, R.H., Lichtschlag, A., Connelly, D., Peel, K., 2018. Controls on the chemical composition on ferromanganese nodules in the Clarion-Clipperton Fracture Zone, eastern equatorial Pacific. *Mar. Geol.* 409, 1–14.
- Mero, J.L., 1965. *The Mineral Resources of the Sea*. Elsevier, Amsterdam.
- Mewes, K., Mogollón, J.M., Picard, A., Rühlemann, C., Eisenhauer, A., Kuhn, T., Ziebis, W., Kasten, S., 2016. Diffusive transfer of oxygen from seamount basaltic crust into overlying sediments: An example from the Clarion-Clipperton Fracture Zone. *Earth Planet. Sci. Lett.* 433, 215–225.

- Mewes, K., Mogollón, J.M., Picard, A., Rühlemann, C., Kuhn, T., Nöthen, K., Kasten, S., 2014. Impact of depositional and biogeochemical processes on small scale variations in nodule abundance in the Clarion-Clipperton Fracture Zone. *Deep-Sea Res. Part I: Oceanogr. Res. Pap.* 91, 125–141.
- Miljutin, D.M., Miljutina, M.A., Martínez Arbizu, P., Galeron, J., 2011. Deep-sea nematode assemblage has not recovered 26 years after experimental mining of polymetallic nodules (CCFZ, Pacific). *Deep-Sea Res. Part I: Oceanogr. Res. Pap.* 58, 885–897.
- Miller, K.A., Thompson, K.F., Johnston, P., Santillo, D., 2018. An Overview of Seabed Mining Including the Current State of Development, Environmental Impacts, and Knowledge Gaps. *Front. Mar. Sci.* 4, 418.
- Mogollón, J.M., Mewes, K., Kasten, S., 2016. Quantifying manganese and nitrogen cycle coupling in manganese-rich, organic carbon-starved marine sediments: Examples from the Clarion-Clipperton fracture zone. *Geophys. Res. Lett.* 43, 2016GL069117.
- Moorby, S.A., Cronan, D.S., Glasby, G.P., 1984. Geochemistry of hydrothermal Mn-oxide deposits from the S.W. Pacific island arc. *Geochim. Cosmochim. Acta* 48, 433–441.
- Müller, P.J., Hartmann, M., Suess, E., 1988. The chemical environment of pelagic sediments. In: *The Manganese Nodule Belt of the Pacific Ocean: Geological Environment, Nodule Formation, and Mining Aspects* (eds. Halbach, P., Friedrich, G., von Stackelberg, U.). Enke, Stuttgart, 70–90.
- Müller, P.J., Mangini, A., 1980. Organic carbon decomposition rates in sediments of the pacific manganese nodule belt dated by ^{230}Th and ^{231}Pa . *Earth Planet. Sci. Lett.* 51, 94–114.
- Murray, J.W., Downs, J.N., Strom, S., Wei, C.-L., Jannasch, H.W., 1989. Nutrient assimilation, export production and ^{234}Th scavenging in the eastern equatorial Pacific. *Deep-Sea Res. Part I: Oceanogr. Res. Pap.* 36, 1471–1489.
- Murray, J., Renard, A.F., 1891. Deep-sea deposits (based on the specimens collected during the voyage of HMS Challenger in the years 1872 to 1876). Report on the scientific results of the voyage of H.M.S. Challenger during the years 1873–76; John Menzies and Co., Edinburgh, United Kingdom.
- Nautilus Minerals, 2019. Nautilus provides Corporate Update. Press release January 8, 2019. http://www.nautilusminerals.com/irm/PDF/2074_0/NautilusProvidesCorporateUpdate (Accessed January 29, 2019)
- Nautilus Minerals, 2018b. Nautilus provides Corporate Update. Press release December 2, 2018. http://www.nautilusminerals.com/irm/PDF/2072_0/NautilusProvidesCorporateUpdate (Accessed January 29, 2019)
- Nautilus Minerals, 2018a. Nautilus Minerals announces departure of President and CEO Michael Johnston. Press release August 7, 2018. http://www.nautilusminerals.com/irm/PDF/2053_0/NautilusMineralsannouncesdepartureofPresidentandCEO (Accessed January 29, 2019)
- Nautilus Minerals, 2017. Nautilus provides project update. Press release October 12, 2017. http://www.nautilusminerals.com/irm/PDF/1930_0/Nautilusprovidesprojectupdate (Accessed January 29, 2019)
- Oebius, H.U., Becker, H.J., Rolinski, S., Jankowski, J.A., 2001. Parametrization and evaluation of marine environmental impacts produced by deep-sea manganese nodule mining. *Deep-Sea Res. Part II Top. Stud. Oceanogr.* 48, 3453–3467.

- Pälike, H., Lyle, M.W., Nishi, H., Raffi, I., Ridgwell, A., Gamage, K., Klaus, A., and 57 others, 2012. A new Cenozoic record of equatorial Pacific carbonate accumulation rates and compensation depth. *Nature* 488, 609–615.
- Paul, S.A.L., Gaye, B., Haeckel, M., Kasten, S., Koschinsky, A., 2018. Biogeochemical Regeneration of a Nodule Mining Disturbance Site: Trace Metals, DOC and Amino Acids in Deep-Sea Sediments and Pore Waters. *Front. Mar. Sci.* 5.
- Peukert, A., Schoening, T., Alevizos, E., Köser, K., Kwasnitschka, T., Greinert, J., 2018. Understanding Mn-nodule distribution and evaluation of related deep-sea mining impacts using AUV-based hydroacoustic and optical data. *Biogeosciences* 15, 2525–2549.
- Purser, A., Marcon, Y., Hoving, H.J.T., Vecchione, M., Piatkowski, U., Eason, D., Bluhm, H., Boetius, A., 2016. Association of deep-sea incirrate octopods with manganese crusts and nodule fields in the Pacific Ocean. *Curr. Biol.* 26, R1268–R1269.
- Radziejewska, T., 2002. Response of deep-sea meiobenthic communities to sediment disturbance simulating effects of polymetallic nodule mining. *Int. Rev. Hydrobiol.* 87, 457–477.
- Randhawa, N.S., Hait, J., Jana, R.K., 2016. A brief overview on manganese nodules processing signifying the detail in the Indian context highlighting the international scenario. *Hydrometallurgy* 165, 166–181.
- Rea, D.K., 1994. The paleoclimatic record provided by eolian deposition in the deep-sea: The geological history of wind. *Rev. Geophys.* 32, 159–195.
- Reyss, J.L., Lemaître, N., Ku, T.L., Marching, V., Southon, J.R., Nelson, D.E., Vogel, J.S., 1985. Growth of a manganese nodule from Peru Basin: A radiochemical anatomy. *Geochim. Cosmochim. Acta* 49, 2401–2408.
- Riedinger N., Pfeifer K., Kasten S., Garming J.F.L., Vogt C., Hensen C., 2005. Diagenetic alteration of magnetic signals by anaerobic oxidation of methane related to a change in sedimentation rate. *Geochim. Cosmochim. Acta* 69, 4117–4126.
- Røy, H., Kallmeyer, J., Adhikari, R.R., Pockalny, R., Jørgensen, B.B., D'Hondt, S., 2012. Aerobic Microbial Respiration in 86-Million-Year-Old Deep-Sea Red Clay. *Science* 336, 922–925.
- Rühlemann, C., Kuhn, T., Wiedicke, M., Kasten, S., Mewes, K., Picard, A., 2011. Current status of manganese nodule exploration in the German license area. *Proc. of the 9th ISOPE Conference*, Maui, 168–173.
- Schriever, G., Ahnert, A., Bluhm, H., Borowski, C., Thiel, H., 1997. Results of the large-scale deep-sea environmental impact study DISCOL during eight years of investigation. *Proc. of the 7th ISOPE Conference*, Honolulu, Hawaii.
- Schulz, H.D., 2006. Quantification of Early Diagenesis: Dissolved Constituents in Pore Water and Signals in the Solid Phase. In: *Marine geochemistry* (eds. Schulz, H.D., Zabel, M.). Springer Berlin Heidelberg, 73–124.
- Sorem, R.K., Fewkes, R.H., 1979. Internal characteristics of marine manganese nodules. In: *Marine manganese deposits* (ed. Glasby, G.P.). Elsevier Oceanogr. Ser. 15. Elsevier Amsterdam, 147–1183.
- Spinelli, G.A., Giambalvo, E.G., Fisher, A.T., 2004. Hydrologic properties and distribution of sediments. In: *Hydrogeology of the Oceanic Lithosphere* (eds. Davis, E.E., Elderfield, H.). Cambridge University Press, Cambridge, UK.

- Steiner, R., 2009. Independent Review of the Environmental Impact Statement for the proposed Nautilus Minerals Solwara 1 Seabed Mining Project, Papua New Guinea. Bismarck-Solomon Seas Indigenous Peoples Council.
- Thiel, H., and Forschungsverband Tiefsee-Umweltschutz, 2001. Evaluation of the environmental consequences of polymetallic nodule mining based on the results of the TUSCH Research Association. *Deep-Sea Res. Part II Top. Stud. Oceanogr.* 48, 3433–3452.
- Thiel, H., Schriever, G., 1989. Cruise Report DISCOL 1, Sonne – cruise 61. Berichte aus dem Zentrum für Meeres- und Klimaforschung 3. Zentrum für Meeres- und Klimaforschung der Universität Hamburg, Institut für Hydrobiologie und Fischereiwissenschaft, 75 pp.
- Trueblood, D.D., Ozturgut, E., 1997. The benthic impact experiment: A study of the ecological impacts of deep seabed mining on abyssal benthic communities. *Proc. of the 7th ISOPE Conference*, Honolulu, Hawaii.
- Turnewitsch, R., Reyss, J.-L., Chapman, D.C., Thomson, J., Lampitt, R.S., 2004. Evidence for a sedimentary fingerprint of an asymmetric flow field surrounding a short seamount. *Earth Planet. Sci. Lett.* 222, 1023–1036.
- Turnewitsch, R., Lahajnar, N., Haeckel, M., Christiansen, B., 2015. An abyssal hill fractionates organic and inorganic matter in deep-sea surface sediments. *Geophys. Res. Lett.* 42.
- Uścińowicz, G., 2012. Spherical, magnetic grains of extraterrestrial origin, isolated from Pacific sediments. *Ocean and Hydro.* 41, 48–53.
- Vanreusel, A., Hilario, A., Ribeiro, P.A., Menot, L., Arbizu, P.M., 2016. Threatened by mining, polymetallic nodules are required to preserve abyssal epifauna. *Sci. Rep.* 6, 26808.
- Versteegh, G.J.M., Koschinsky, A., Kuhn, T., Dohrmann, I., Filmsair, C., Fronzek, J., Hartmann, J.F., Kleint, C., Preuss, I., Ritter, S., Kasten, S., in preparation. Widespread diffusion of oxygen from oceanic crust into overlying sediments in the NE Pacific Ocean – geochemical consequences and significance for biogeochemical cycles (RV Sonne Cruise SO240 - FLUM).
- von Stackelberg, U., 2000. Manganese nodules of the Peru Basin. In: *Handbook of marine mineral deposits* (ed. Cronan, D.S.). CRC Press, Boca Raton, pp 197–238.
- von Stackelberg, U., Beiersdorf, H., 1987. Manganese nodules and sediments in the equatorial North Pacific Ocean, “Sonne” Cruise SO25, 1982. *Geol. Jahrb.* D87, 403 pp.
- von Stackelberg, U., Marching, V., 1987. Manganese nodule from the equatorial North Pacific Ocean. *Geol. Jahrb.* D87, 123–227.
- Weber, M.E., von Stackelberg, U., Marchig, V., Wiedicke, M., Grupe, B., 2000. Variability of surface sediments in the Peru basin: Dependence on water depth, productivity, bottom water flow, and seafloor topography. *Mar. Geol.* 163, 169–184.
- Wedding, L.M., Reiter, S.M., Smith, C.R., Gjerde, K.M., Kittinger, J.N., Friedlander, A.M., Gaines, S.D., Clark, M.R., Thurnherr, A.M., Hardy, S.M., Crowder, L.B., 2015. Managing mining of the deep seabed. *Science* 349, 144–145.
- Wegorzewski, A.V., Kuhn, T., Dohrmann, R., Wirth, R., Grangeon, S., 2015. Mineralogical characterization of individual growth structures of Mn-Nodules with different Ni+Cu content from central Pacific Ocean. *Am. Mineral.* 100, 2497–2508.
- Wegorzewski, A.V., Kuhn, T., 2014. The influence of suboxic diagenesis on the formation of manganese nodules in the Clarion Clipperton nodule belt of the Pacific Ocean. *Mar. Geol.* 357, 123–138.

- Wheat, C.G., Fisher, A.T., 2008. Massive, low-temperature hydrothermal flow from a basaltic outcrop on 23 Ma seafloor of the Cocos Plate: chemical constraints and implications. *Geochem. Geophys. Geosyst.* 9.
- Xu, G., Lavelle, J.W., 2017. Circulation, hydrography, and transport over the summit of Axial Seamount, a deep volcano in the Northeast Pacific. *J. Geophys. Res. Oceans* 122, 5404–5422.
- Ziebis, W., McManus, J., Ferdelman, T., Schmidt-Schierhorn, F., Bach, W., Muratli, J., Edwards, K.J., Villinger, H., 2012. Interstitial fluid chemistry of sediments underlying the North Atlantic gyre and the influence of subsurface fluid flow. *Earth Planet. Sci. Lett.* 323, 79–91.

CHAPTER II:

Natural spatial variability of depositional conditions, biogeochemical processes and element fluxes in sediments of the eastern Clarion-Clipperton Zone, Pacific Ocean

Jessica B. Volz^{a,*}, José M. Mogollón^{b,c,d}, Walter Geibert^a, Pedro Martínez Arbizu^e, Andrea Koschinsky^f, Sabine Kasten^{a,g}

^a Alfred Wegener Institute Helmholtz Centre for Polar and Marine Research, Bremerhaven, Germany (corresponding author: jessica.volz@awi.de, Tel.: +49 471 4831 1842)

^b Department of Marine Organic Biogeochemistry, NIOZ Royal Netherlands Institute for Sea Research, P.O. Box 59, Den Burg, The Netherlands

^c Department of Earth Sciences – Geochemistry, Utrecht University, P.O. Box 80.021, 3508TA Utrecht, The Netherlands

^d Institute of Environmental Sciences (CML), Leiden University, Einsteinweg 2, 2333CC, Leiden, The Netherlands

^e Senckenberg am Meer, DZMB, Wilhelmshaven, Germany

^f Jacobs University Bremen, Department of Physics and Earth Sciences, Bremen, Germany

^g University of Bremen, Faculty of Geosciences, Klagenfurter Strasse, Bremen, Germany

Manuscript published in *Deep-Sea Research Part I* 140 (2018) 159–172.
doi:10.1016/j.dsr.2018.08.006

Abstract

The manganese nodule belt within the Clarion and Clipperton Fracture Zones (CCZ) in the abyssal NE Pacific Ocean is characterized by numerous seamounts, low organic matter (OM) depositional fluxes and meter-scale oxygen penetration depths (OPD) into the sediment. The region hosts contract areas for the exploration of polymetallic nodules and Areas of Particular Environmental Interest (APEI) as protected areas. In order to assess the impact of potential mining on these deep-sea sediments and ecosystems, a thorough determination of the natural spatial variability of depositional and geochemical conditions as well as biogeochemical processes and element fluxes in the different exploration areas is required. Here, we present a comparative study on (1) sedimentation rates and bioturbation depths, (2) redox zonation of the sediments and element fluxes as well as (3) rates and pathways of biogeochemical reactions at six sites in the eastern CCZ. The sites are located in four European contract areas and in the APEI3. Our results demonstrate that the natural spatial variability of depositional and (bio)geochemical conditions in this deep-sea sedimentary environment is much larger than previously thought. We found that the OPD varies between 1 and 4.5 m, while the sediments at two sites are oxic throughout the sampled interval (7.5 m depth). Below the OPD, manganese and nitrate reduction occur concurrently in the suboxic zone with pore-water Mn^{2+} concentrations of up to 25 μM . The thickness of the suboxic zone extends over depth intervals of less than 3 m to more than 8 m. Our data and the applied transport-reaction model suggest that the extension of the oxic and suboxic zones is ultimately determined by the (1) low flux of particulate organic carbon (POC) of 1–2 $\text{mg C}_{\text{org}} \text{m}^{-2} \text{d}^{-1}$ to the seafloor, (2) low sedimentation rates between 0.2 and 1.15 cm kyr^{-1} and (3) oxidation of pore-water Mn^{2+} at depth. The diagenetic model reveals that aerobic respiration is the main biogeochemical process driving OM degradation. Due to very low POC fluxes of 1 $\text{mg C}_{\text{org}} \text{m}^{-2} \text{d}^{-1}$ to the seafloor at the site investigated in the protected APEI3 area, respiration rates are twofold lower than at the other study sites. Thus, the APEI3 site does not represent the (bio)geochemical conditions that prevail in the other investigated sites located in the European contract areas. Lateral variations in surface water productivity are generally reflected in the POC fluxes to the seafloor across the various areas but deviate from this trend at two of the study sites. We suggest that the observed spatial variations in depositional and (bio)geochemical conditions result from differences in the degree of degradation of OM in the water column and heterogeneous sedimentation patterns caused by the interaction of bottom water currents with seafloor topography.

1. Introduction

Vast deep-sea regions of the open Pacific Ocean are characterized by low fluxes of organic carbon to the seafloor (Lutz et al., 2007). The discovery of high abundances of polymetallic nodules in these carbon-starved environments in the equatorial Pacific Ocean during the *HMS Challenger* expedition (Murray and Renard, 1891) has driven the global economic interest in deep-sea mining (Mero, 1965) and has triggered several comprehensive studies in the area of the Clarion-Clipperton Zone (CCZ) (e.g., Chun, 1908; Bischoff and Piper, 1979; Bender, 1983; von Stackelberg and Beiersdorf, 1987; Lodge et al., 2014). Most geochemical studies on CCZ sediments have focused on polymetallic manganese nodules, more precisely their chemical and mineralogical composition as well as pathways of formation (e.g., Calvert and Price, 1977; Jeong et al., 1994; Wegorzewski and Kuhn, 2014). Only a few studies that combine pore-water and sediment geochemistry have been performed on sediments of the CCZ (e.g., Bischoff and Piper, 1979; Jahnke et al., 1982; Müller et al., 1988; Mewes et al., 2014; Mogollón et al., 2016). The upper few centimeters of the sediments in the CCZ are generally characterized by organic carbon (OC) contents of < 0.5 wt% (e.g., Arrhenius, 1952; Heath et al., 1977; Khripounoff et al., 2006). Below 30 cm, a residual OC fraction of ~0.1 wt% remains in the deeply buried sediments (Müller and Mangini, 1980; Müller et al., 1988; Mewes et al., 2014; Mogollón et al., 2016). Müller and Mangini (1980) have reported a sedimentation rate of 0.15–0.4 cm kyr⁻¹ for the western CCZ. Slightly higher rates between 0.35 and 0.6 cm kyr⁻¹ were determined by Mewes et al. (2014) for the eastern CCZ. In the framework of the MANOP (Manganese Nodule Project) study, sediments and associated pore water underlying the Pacific equatorial upwelling area between 0° and 10°N were analyzed (e.g., Emerson et al., 1980; Klinkhammer, 1980). The relatively high POC flux to the seafloor in this area (Lutz et al., 2007) causes a compressed redox zonation in the sediments with the occurrence of Mn²⁺ in the absence of oxygen and sulfide in the pore water after nitrate is consumed below 10 cm (Emerson et al., 1980; Klinkhammer, 1980; Jahnke et al., 1982). The study by Røy et al. (2012) was performed along a sampling transect at 0°N in the eastern Pacific Ocean and shows that the oxygen penetration depth (OPD) is generally 10 cm. Oxygen depletion in combination with the absence of sulfate reduction allows manganese reduction to extend over sediment intervals of up to 100 m (D'Hondt et al., 2004). Studies performed by Mewes et al. (2014) and Mogollón et al. (2016) in the German contract area “East” for the exploration of polymetallic nodules show that oxygen typically penetrates 1.8–3 m into the sediments between 11°–12°N and 117°–120°W. Below the oxic zone, manganese and nitrate reduction occur concurrently over depth intervals between 6 m to more than 12 m depth. In

contrast, sediments underlying the carbon-starved waters of the North Pacific Gyre (NPG) are deeply oxygenated at least 30 m below the seafloor due to low respiration rates (Røy et al., 2012).

Considering that abyssal benthic communities are limited by low carbon export from the euphotic zone (e.g., Smith et al., 2008), biodiversity in the CCZ is surprisingly high (e.g., Glover et al., 2002). Vanreusel et al. (2016) have recently performed a comparative study of benthic faunal composition and densities in five areas in the CCZ over a distance of approximately 1300 km. This biological study revealed (1) lowest densities of both sessile and mobile fauna in the area with lowest POC fluxes to the seafloor, (2) a strong dependency of local biodiversity on manganese nodule abundance and (3) a reduction of the mobile fauna by at least 50% in areas where controlled anthropogenic disturbances were created 37 and 20 years ago. As these simulated deep-sea mining experiments cause the removal or alteration of top sediment layers, and the formation of large sediment plumes in the water column, the recovery of benthic communities after anthropogenic impacts is expected to be very slow (e.g., Miljutin et al., 2011; Jones et al., 2017; Boetius and Haeckel, 2018).

Due to the economic interest in the exploitation of deep-sea manganese nodules, the International Seabed Authority (ISA) has adopted an Environmental Management Plan (EMP) for the CCZ, which includes temporal contracts for the exploration of manganese nodules (ISA, 2010; Lodge et al., 2014; Madureira et al., 2016). In addition to this, nine areas have been designated for the conservation of natural resources, which are excluded from any mining activities and declared as “Areas of Particular Environmental Interest” (APEI). For the further development of an efficient EMP, Lodge et al. (2014) emphasize the necessity of environmental baseline studies including the determination of chemical parameters before and after anthropogenic disturbances.

In order to assess the natural spatial variability of geochemical conditions, biogeochemical processes, and element fluxes in the CCZ as needed for such baseline studies, we present a comparative study on (1) sedimentation rates and bioturbation depths, (2) redox zonation of sediments and oxygen fluxes, and (3) rates and pathways of biogeochemical reactions driving the degradation of organic matter in these deep-sea deposits. We have studied sediments of four European contract areas including the German BGR area “East” (Bundesanstalt für Geowissenschaften und Rohstoffe), the area of the eastern European consortium IOM (InterOceanMetal), the Belgian GSR area (Global Sea Mineral Resources NV), the French IFREMER area (Institut Français de Recherche pour l'Exploitation de la Mer) and one of the

nine APEIs which is located north of the CCZ and referred to as the APEI3. Our work includes *ex situ* oxygen measurements, comprehensive pore-water and solid-phase analyses on the upper 10 m of sediment and the application of a one-dimensional steady-state reaction transport model.

2. Geological and oceanographic setting

The CCZ comprises an area of about 6 million km² in the equatorial Pacific Ocean defined by two major transform faults, the Clarion Fracture Zone in the north and the Clipperton Fracture Zone in the south (Halbach et al., 1988). The fracture zones are formed at the East Pacific Rise, stretch perpendicular to the spreading center, and enclose a vast seafloor covered by numerous seamounts and NNE-SSW oriented horst and graben structures (Johnson, 1972; ISA, 2010). The abyssal deep-sea pelagic sediments at 4–5 km water depth between 116°–155°W and 5°–15°N are dominated by biogenic sediments, notably siliceous oozes (Berger, 1974). The CCZ sedimentary records commonly have hiatuses caused by (1) erosion and redeposition of sediment elsewhere or (2) nondeposition (Johnson, 1972; Craig, 1979; von Stackelberg and Beiersdorf, 1991; Mewes et al., 2014). Average deep-water flow velocities of < 10 cm s⁻¹ refute significant contemporary erosion, but distinct hiatuses in the Eocene to Quaternary sediments may have resulted from relatively higher current velocities (Craig, 1979; Theyer et al., 1985; von Stackelberg and Beiersdorf, 1987).

Average particulate organic carbon (POC) fluxes to the seafloor in the eastern CCZ are 1.5–1.8 mg C_{org} m⁻² d⁻¹ between 10° and 15°N and decline to 1.3 mg C_{org} m⁻² d⁻¹ north of 15°N (Lutz et al., 2007; Fig. 1a). As a consequence of microbial respiration in the water column and weak ocean ventilation, a pronounced oxygen minimum zone (OMZ) persists in the eastern equatorial Pacific (e.g., Wishner et al., 1995; Kalvelage et al., 2015). Oxygen measurements throughout the water column in the CCZ show a well-oxygenated upper mixed layer with a sharp oxycline particularly in the BGR and IOM areas (Martínez Arbizu and Haeckel, 2015). Below the oxycline, the OMZ extends over 100–1000 m and 100–800 m, respectively, with concentrations below 3 µM. The GSR and IFREMER areas show similar extents of the OMZ, however, lowest oxygen concentrations range between 3 and 16 µM. In the APEI3, the OMZ is located at 300–900 m water depth with minimum oxygen concentrations of 6–16 µM (Martínez Arbizu and Haeckel, 2015).

3. Material and methods

As part of the BMBF-EU JPI Oceans pilot action “Ecological Aspects of Deep-Sea Mining (MiningImpact)” sediment cores were taken at five sites in the CCZ during RV SONNE cruise SO239 in March/April 2015 (Fig. 1; Martínez Arbizu and Haeckel, 2015). For the recovery of sediment cores, two different sampling devices were deployed in all investigated areas. A multiple corer (MUC) equipped with twelve 60 cm long tubes with an inner diameter of 9.4 cm was used for the retrieval of undisturbed surface sediments. For the recovery of long sediment cores of up to 10 m length a gravity corer (GC) with a 12 cm wide plastic liner was deployed (Table 1).

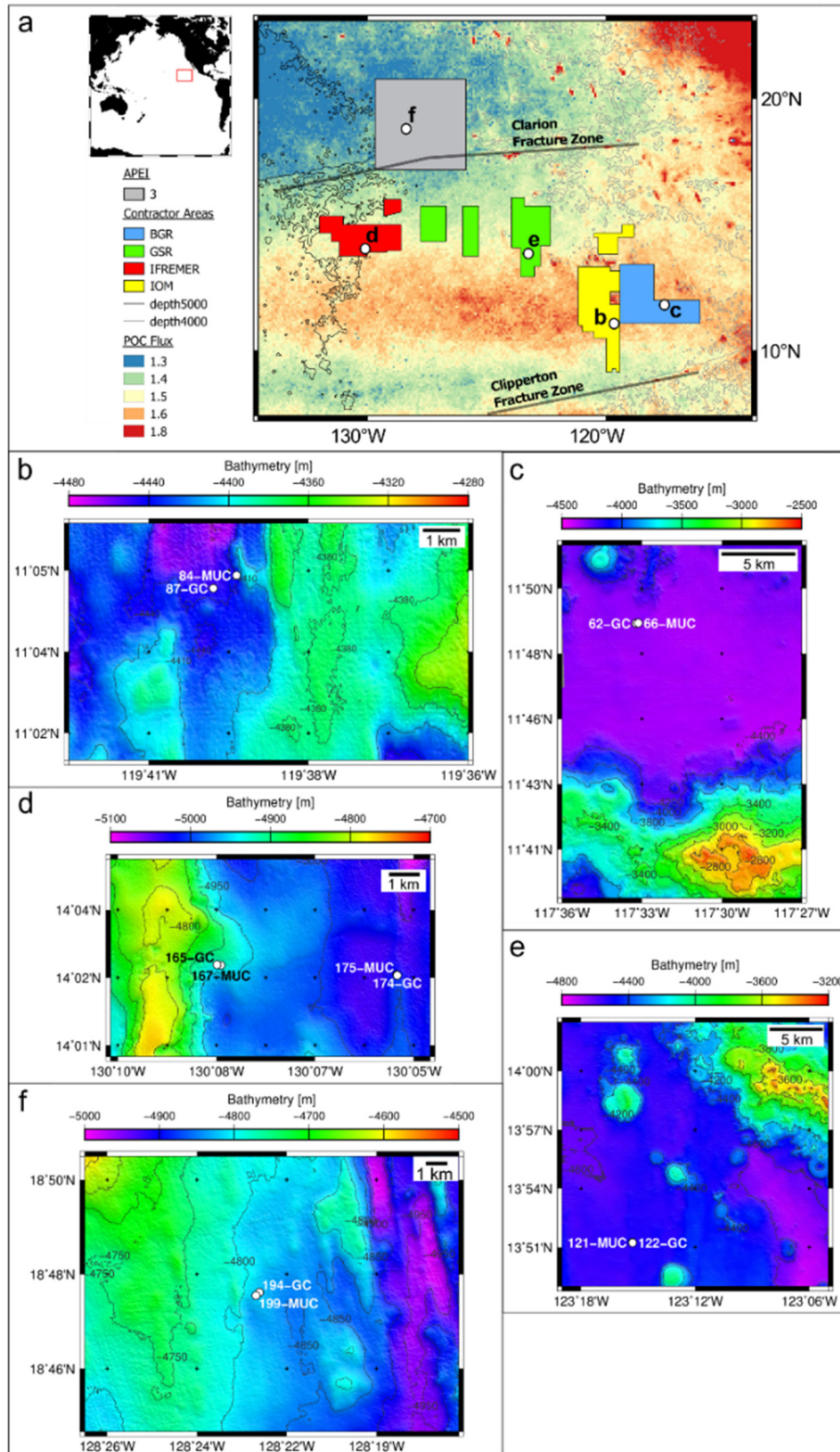
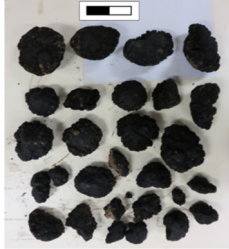


Figure 1: Maps of the study area during RV SONNE cruise SO239 showing (a) the four investigated exploration areas in the CCZ, the APEI3 and the sampling stations (white circles). The background colors indicate the estimated upper limit in POC flux [$\text{mg C}_{\text{org}} \text{m}^{-2} \text{d}^{-1}$] to the seafloor by Lutz et al. (2007) (modified after Vanreusel et al., 2016). Detailed hydroacoustic maps created with the multibeam system EM122 (Martínez Arbizu and Haeckel, 2015; Greinert, 2016) show the locations of the sampling stations with b: IOM; c: BGR; d: IFREMER; e: GSR; f: APEI3. The maps were produced with GMT5 (Wessel et al., 2013).

Table 1: MUC and GC cores investigated in this study including information on geographic position, water depth and core length. Nodule coverage shows the density and size of nodules recovered from the sediment surface at the box corer (BC) station nearest to MUC and GC locations. Nodule sampling area is 0.25 m², the length of scale (■) corresponds to 10 cm.

| Area | Station SO239- | Device | Latitude [N] | Longitude [W] | Water depth [m] | Core length [cm] | Nodule coverage |
|--------|----------------|--------|--------------|---------------|-----------------|------------------|---|
| BGR | 60 | BC | 11°48.46' | 117°33.02' | 4324.5 | |  |
| BGR | 62 | GC | 11°49.12' | 117°33.22' | 4312.2 | 900 | |
| BGR | 66 | MUC | 11°49.13' | 117°33.13' | 4314.8 | 36 | |
| IOM | 84 | MUC | 11°4.73' | 119°39.48' | 4430.8 | 43 |  |
| IOM | 87 | GC | 11°4.54' | 119°39.83' | 4436 | 930 | |
| IOM | 89 | BC | 11°4.55' | 119°39.65' | 4436.5 | | |
| GSR | 121 | MUC | 13°51.25' | 123°15.3' | 4517.7 | 30 |  |
| GSR | 122 | GC | 13°51.23' | 123°15.29' | 4517.7 | 740 | |
| GSR | 128 | BC | 13°51.10' | 123°15.12' | 4510.7 | | |
| IFRE-1 | 165 | GC | 14°2.63' | 130°8.39' | 4922.7 | 927 |  |
| IFRE-1 | 167 | MUC | 14°2.62' | 130°8.32' | 4918.8 | 29 | |
| IFRE-1 | 180 | BC | 14°2.50' | 130°8.18' | 4936.4 | | |
| IFRE-2 | 174 | GC | 14°2.44' | 130°5.1' | 5008 | 734 | no nodules |
| IFRE-2 | 175 | MUC | 14°2.45' | 130°5.11' | 5005.5 | 36 | |
| APEI3 | 194 | GC | 18°47.54' | 128°22.33' | 4815.5 | 576 |  |
| APEI3 | 195 | BC | 18°47.75' | 128°21.73' | 4833.4 | | |
| APEI3 | 199 | MUC | 18°47.46' | 128°22.42' | 4816.6 | 32 | |

3.1 Pore-water and sediment sampling

Immediately after core recovery, sediment cores were transferred into the cold room of the RV SONNE at a temperature of ~ 4 °C. Two MUC cores were separately used for (1) oxygen measurements and subsequent solid-phase sampling and (2) the retrieval of bottom

water and pore water by means of rhizons with an average pore size of 0.1 μm (Seeberg-Elverfeldt et al., 2005). Pore water was sampled at intervals of 1 cm in the upper 10 cm and at 2 cm below. For solid-phase investigations the sample interval for the MUC cores was 1 cm.

The GCs were cut into 1 m segments on deck and stored in the cold room for at least 12 h in order to allow temperature equilibration of the sediments before oxygen measurements were performed. After the oxygen measurements, the segments were split into two halves from which the 'working half' was used for pore-water and sediment sampling while the other half was kept undisturbed and archived. Pore-water and sediment from the GCs were sampled every 20 cm.

During the pore-water sampling by rhizons, the first mL of extracted pore water was discarded in order to avoid any dilution or oxidation. Sample aliquots of typically 2 mL for nitrate (NO_3) were stored in amber vials sealed with a PTFE septum-bearing lid at $-20\text{ }^\circ\text{C}$. For the analyses of further dissolved pore-water constituents, aliquots of the remaining pore-water samples were diluted 1:10 and acidified with 0.145 M sub-boiling distilled HNO_3 and stored at $4\text{ }^\circ\text{C}$ in Zinsser vials. All sediment samples were taken using either cut-off syringes with a volume of about 12 mL or with a plastic spatula and stored at $-20\text{ }^\circ\text{C}$ in plastic vials. Sediment samples from suboxic intervals of the cores were stored in argon-flushed gas-tight glass bottles at $-20\text{ }^\circ\text{C}$ until further analysis.

3.2 *Ex situ* oxygen measurements

Oxygen concentrations in the sediment were determined using amperometric Clark-type oxygen sensors with an internal reference and equipped with a guard cathode (Revsbech, 1989) according to the procedure described by Ziebis et al. (2012) and Mewes et al. (2014). The electrodes (Unisense, Denmark) are made of glass with a 6 cm long tip that was inserted into a hyperdermic needle (diameter 1.1 mm, length 50 mm) and had a response time shorter than 10 s. Signals were amplified and transformed to mV by a picoamperemeter, digitalized by an analogue/digital converter (ADC 216, Unisense, Denmark) and recorded using the software PROFIX (Unisense, Denmark). Measurements were recorded at each sampling point for 2–3 min and mean oxygen saturation values were taken when signals were stable to calculate the depth profiles. For the two-point calibration of the oxygen sensors, Ar-flushed (0% oxygen saturation) and air-purged (100% oxygen saturation) local bottom water was used. High-resolution (1 mm) vertical profiles of oxygen concentrations across the sediment/water interface were accomplished for MUC cores by use of a micromanipulator down to a maximum sediment depth of 5–6 cm. For oxygen measurements in deeper parts of the MUC core as well

as for all GCs, holes were drilled through the walls of the core liners in intervals of 1 cm for MUCs and of 5 cm for GCs for the insertion of the microelectrode.

3.3 Pore-water analyses

In the home laboratory at the Alfred Wegener Institute Helmholtz Centre for Polar and Marine Research in Bremerhaven (AWI), NO_3^- was determined using a QuAatro Continuous Segmented Flow Analyzer (Seal Analytical) with a detection limit of $1.9 \mu\text{M}$. Based on duplicate measurements of NO_3^- , the accuracy of the analysis was determined to be $< 4.9\%$. Dissolved manganese (Mn^{2+}) was determined in the acidified pore-water subsamples by inductively coupled plasma optical emission spectrometry (ICP-OES; IRIS Intrepid ICP-OES Spectrometer, Thermo Elemental) with a detection limit of $0.05 \mu\text{M}$. Based on the triplicate determination of each sample the reproducibility was $< 1.5\%$ for Mn^{2+} .

3.4 Solid-phase analyses

To avoid any interference of the salt matrix in the pore water on the sediment composition, bulk sediment data, total organic carbon and total sulfur contents have been corrected post-analytically according to Kuhn (2013) with the mass percentage of the saline pore water (w') and the mass percentage of H_2O of the wet sediment (w) with the pore water containing 96.5% H_2O (Eq. (1)). With the mass of the salt s [%] (Eq. (2)) the solid-phase composition c' has been calculated using the measured solid-phase composition c (Eq. (3)).

$$w' = w * 100/96.5 \quad (1)$$

$$s = 100 * \frac{w' - w}{100 - w} \quad (2)$$

$$c' = c * \frac{100}{100 - s} \quad (3)$$

3.4.1 Total organic carbon content

The content of total organic carbon (TOC) was analyzed using an Eltra CS2000. About 100 mg of freeze-dried, homogenized sediment were weighed into a ceramic cup. Samples were decalcified with 0.5 mL 10% HCl at 250 °C for 2 h before analysis. As the total carbon (TC) consists mostly of TOC in the analyzed samples, total inorganic carbon (TIC) occurs only in negligible amounts. Based on an in-house reference material precision of the analysis was determined to be $< 3.7\%$ ($n=83$).

3.4.2 Radioisotope analyses of ^{231}Pa and ^{230}Th

For the isotope dilution analysis by Inductively Coupled Plasma-Sector Field-Mass Spectrometry (ICP-SF-MS, Element2, Thermo Scientific) freeze-dried and homogenized sediment samples were spiked with about 9 pg ^{229}Th , 0.7 pg ^{233}Pa and 800 pg ^{236}U as internal standards and weighed out in Teflon vials. Total acid digestions were performed in the microwave system MARS Xpress (CEM) according to the procedure described by Kretschmer et al. (2010) and Nöthen and Kasten (2011). Acids were of sub-boiling distilled (HNO_3 , HCl) or suprapur® (HF) quality. About 50 mg of freeze-dried and homogenized bulk sediment were digested in an acid mixture of 65% HNO_3 (3 mL), 30% HCl (2 mL) and 40% HF (0.5 mL) at ~ 230 °C. The digested solutions were fumed off to dryness with the microwave evaporation accessory (CEM XpressVap) and re-dissolved under pressure in 1 M HNO_3 (5 mL) at ~ 200 °C. The residue was filled up to 50 mL with 1 M HNO_3 . After the total acid digestion, 80% of the total digest volume were co-precipitated with $\text{Fe}(\text{OH})_3$. Separation of Pa, Th and U was performed by ion exchange chromatography with the Anion Exchange Resin AG®1-X8 (Bio-Rad) after the protocols of Anderson and Fleer (1982) and Andersson and Schöberg (2012). Poly-Prep® gravity flow columns filled with AG®1-X8 resin were conditioned with 9 M HCl (3 * 4 mL) before loading the sample and eluting Th with 9 M HCl (3 * 4 mL), Pa with 9 M $\text{HCl}/0.14$ M HF (4 * 3 mL) and U with 0.1 M HCl (4 * 3 mL), successively. All acids were of sub-boiling distilled or suprapur® quality. The Th, Pa and U eluates were collected and evaporated in Teflon beakers. The Th eluates were purified on a second column with 9 M HCl (400 μL and 6 * 2 mL) for Th, 9 M $\text{HCl}/0.14$ M HF (6 * 2 mL) for Pa and 0.1 M HCl (3 * 4 mL) for U. Separated Th, Pa and U fractions were evaporated, redissolved in HNO_3 and diluted to 1 M HNO_3 for the isotope dilution analysis using ICP-SF-MS with the desolvation system Apex Q (ESI). Data correction for the formation of thorium hydride ($^{232}\text{ThH}^+$), ^{232}Th peak tailing and the instrument mass bias were assessed as described by Kretschmer et al. (2011). Based on the reference material Urem-11 (SARM-31) average accuracy and precision were 0.5% and 1.2% for ^{235}U , 2.4% and 1.2% for ^{230}Th and 0.3% and 2.6% for ^{231}Pa , respectively (n=5).

Sedimentation rates were calculated following the algorithm by Faure (1977), where t is the age[yr] of the sediment and $\frac{{}^{230}\text{Th}_{ex}}{{}^{231}\text{Pa}_{ex}}$ is the specific activity ratio at a certain sediment depth x . Here, we used the well constrained value in the bioturbated layer above (Supplementary Fig. 1) as the starting value b , respectively (Eq. 4).

$$t = \frac{1}{82574.86} \ln \left[\frac{\left(\frac{{}^{230}\text{Th}_{ex}}{{}^{231}\text{Pa}_{ex}} \right)_x}{\left(\frac{{}^{230}\text{Th}_{ex}}{{}^{231}\text{Pa}_{ex}} \right)_b} \right] \quad (4)$$

Mass accumulation rates [$\text{g cm}^{-2} \text{ kyr}^{-1}$] were determined by the product of sedimentation rate [cm kyr^{-1}] and dry bulk density (DBD) [g cm^{-3}].

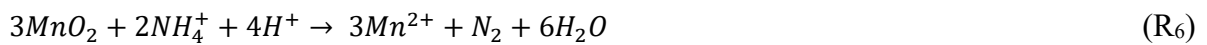
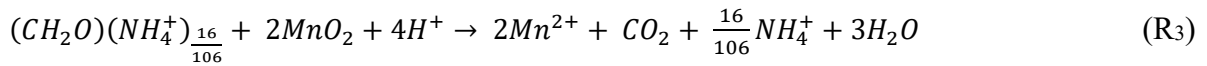
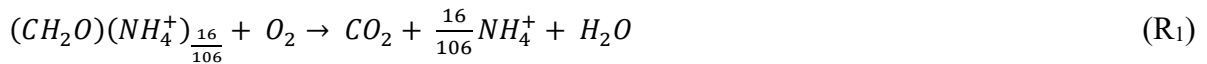
3.5 Geochemical model setup and reaction network

A one-dimensional steady-state reaction transport model (e.g. Boudreau, 1997) that couples reactions through a discretized steady state reaction-transport equation was used to interpret the sedimentary geochemistry at the various CCZ sites (Eq. (5)):

$$0 = \frac{\partial D_{i,j} \vartheta_i \left(\frac{\partial C_{i,j}}{\partial z} \right)}{\partial z} - \frac{\partial \omega_i \vartheta_i C_{i,j}}{\partial z} + \alpha_i \vartheta_i (C_{i,j} - C_{0,j}) + \vartheta_i \sum R_{i,j} \quad (5)$$

where z is sediment depth, and i, j represent subscripts depicting depth and species-dependence, respectively. C is the species concentration (aqueous or solid species, Supplementary material Table 2); D is the diffusive mixing coefficient taking tortuosity (Boudreau, 1997) and bioturbation (Eq. (6)) into account ($D_i = B_i + D_{m,i}$); ϑ is the volume fraction for the aqueous (i.e. the porosity φ) or solid ($1 - \varphi$) phases; ω is the velocity of either the aqueous or the solid phase (v or w respectively); α_i is the bioirrigation coefficient (0 for solid species, Eq. (7)); $\sum R_{i,j}$ is the sum of the reactions affecting the given species j .

The reaction-transport model consists of 8 geochemical species and 6 reactions (Supplementary material Table 1):



The chemical reactions during organic carbon degradation were assumed to follow the Redfield ratio stoichiometry with the organic-bound nitrogen to carbon ratio of 16:106 (Redfield, 1934). Biologically induced mixing profiles were assumed to follow a modified logistic function where the break attenuation depths were assumed to be the same for both bioirrigation and bioturbation:

$$B_i = B_0 \exp\left(\frac{z_{mix}-z}{z_{att}}\right) / \left(1 + \exp\left(\frac{z_{mix}-z}{z_{att}}\right)\right) \quad (6)$$

$$\alpha_i = \alpha_0 \exp\left(\frac{z_{mix}-z}{z_{att}}\right) / \left(1 + \exp\left(\frac{z_{mix}-z}{z_{att}}\right)\right) \quad (7)$$

where α_0 and B_0 are constants representing the maximum bioirrigation and bioturbation coefficients at sediment-water interface, z_{mix} is the depth to where α_0 and B_0 become half their value and z_{att} is the attenuation of the biogenically induced mixing with depth.

Porosity data were fit for each station and showed an exponential decrease with depth typical of compacting sediment (not shown) and were fit with the following equation:

$$\varphi_i = \varphi_\infty (\varphi_0 - \varphi_\infty) \exp(-\beta z) \quad (8)$$

where φ_∞ is the porosity at compaction, φ_0 is the porosity at the sediment water interface, and β is the depth-attenuation coefficient. Sediment thicknesses for the diagenetic model were extracted from NCEI's global ocean sediment thickness grid (Whittaker et al., 2013). For the BGR site, sediment thicknesses were inferred from nearby core locations with similar pore-water Mn profiles (SO240-9KL, SO240-96SL; Kuhn et al., 2017). The model was coded in R (version 3.2.4) using the ReacTran package (Soetaert and Meysman, 2012) to solve Eq. (5) and the marelac package (Soetaert et al., 2010) to solve the molecular diffusion coefficients for the modeled species ($D_{m,i}$). The advective velocities of solid and pore water phases were solved using the compact grid function within the ReacTran package, which takes sedimentary compaction into account.

4. Results

4.1 Core description

All study sites show light brown clay-dominated siliceous ooze with variable surface nodule coverage (Table 1). The sediments in the APEI3 site are dominated by dense and dry, dark brown sediment with a comparably low degree of lithological variation. All other sites are characterized by light brown sediments with irregular dark patches and layers throughout.

4.2 Pore water

Bottom-water oxygen concentrations measured with the CTD (SBE 43 oxygen self-regenerative WetLabs Clark-sensor) are 156 μM in the APEI3 area, 153 μM in the IFREMER area, 150 μM in the GSR area, 147 μM in the IOM area and 144 μM in the BGR area (Fig. 2). In the surface sediments, oxygen concentrations usually decrease rapidly with depth in the upper 30 cm (Fig. 2). However, in contrast to the other sites, the surface sediments of the APEI3 and IFRE-1 sites show only a slight decrease in oxygen. Oxygen concentrations below detection limit are reached at various sediment depths while the sediments at the APEI3 and the GSR sites remain oxic throughout. The oxygen penetration depth (OPD) is 1 m at the BGR site, 3 m at the IOM site, 4.5 m at the IFRE-1 site and 3.8 m at the IFRE-2 site.

Pore-water Mn^{2+} occurs below the OPD within a wide concentration range of 0.2–25 μM (Fig. 2). At the IFRE-1 site, Mn^{2+} concentrations $< 1 \mu\text{M}$ are between 4.5 and 7 m while the IFRE-2 site shows a concave-up profile with higher concentrations of up to 5.5 μM . At the IOM site, Mn^{2+} increases downward to 13 μM and slightly decreases below 8 m. Overall, the highest Mn^{2+} concentrations were measured at the BGR site with up to 25 μM at 3.3 m and a subsequent decrease in concentrations with depth.

NO_3^- concentrations generally increase with depth from bottom water concentrations of 35 μM at the sediment surface to 45 μM in the upper 30 cm (Fig. 2). The APEI3 and GSR sites show NO_3^- concentrations in the surface sediments of up to 53 μM and 70 μM , respectively. A decrease of NO_3^- with depth below 30 cm is detected at the BGR, IOM and IFRE-2 sites to about 35 μM at the bottom of the cores. At the APEI3, IFRE-1 and GSR sites, NO_3^- concentrations remain mostly constant throughout the deep sediment core.

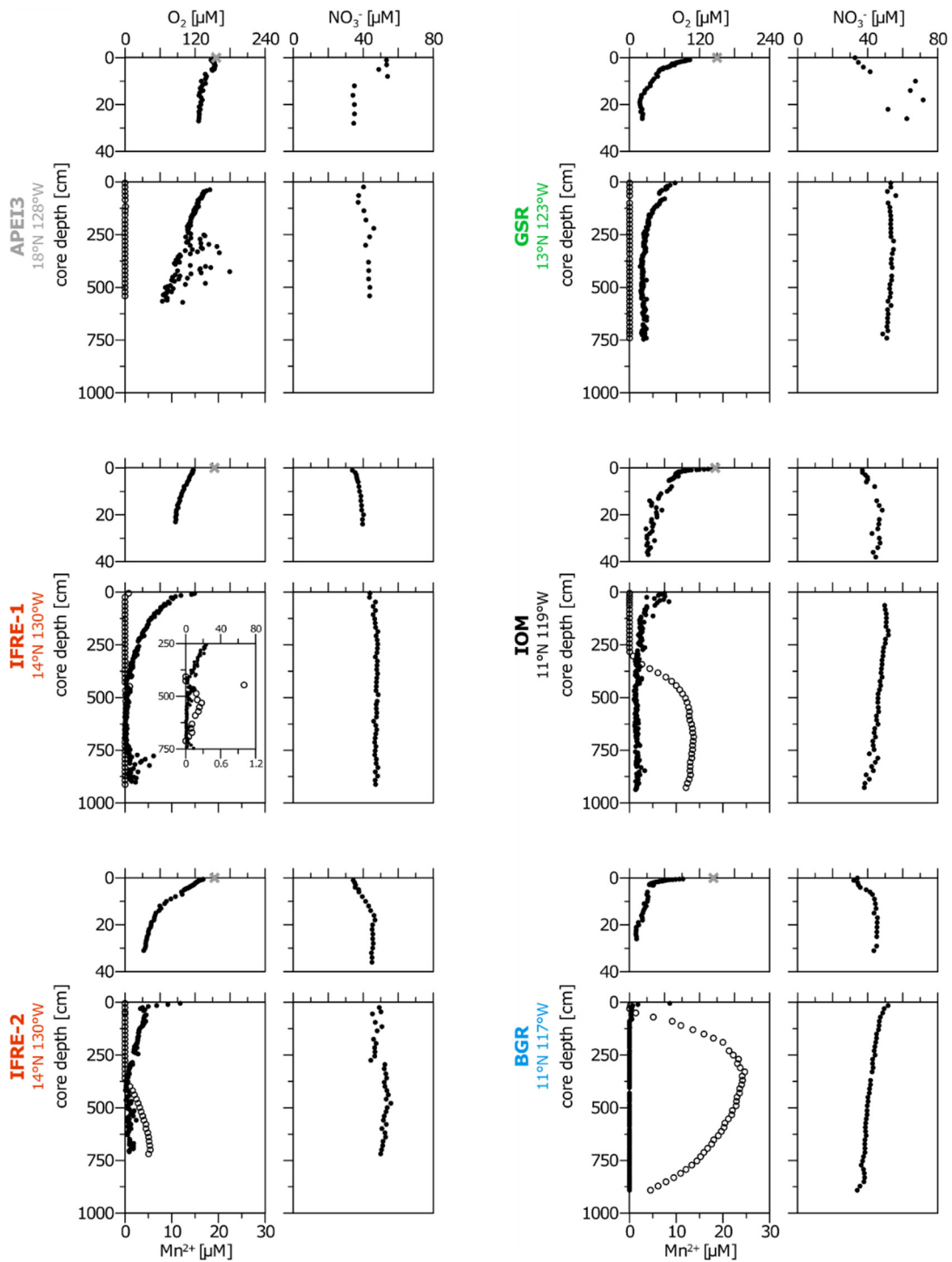


Figure 2: Pore-water profiles of oxygen, dissolved Mn(II) and nitrate of the APEI3, IFREMER, GSR, IOM and BGR sites. The inset plot for the IFRE-1 site show oxygen (black dots) and dissolved Mn(II) concentrations (open circles) on separate axes (upper axis: oxygen; lower axis: Mn(II)) between 2.5 and 7.5 m sediment depth. Bottom-water oxygen concentrations measured by CTD are indicated (grey crosses).

4.3 Solid phase

4.3.1 Total organic carbon

The TOC contents generally decrease with depth in the upper 30 cm (Fig. 3). The lowest surface sediment TOC contents of 0.2 wt% are found in the APEI3. Both, the IFRE-1 and IFRE-2 sites, show 0.3–0.4 wt% of TOC while the GSR site and the IOM site have 0.5 wt% of TOC. The highest contents with 0.6 wt% are found at the BGR site. Below 30 cm, the TOC remains < 0.2 wt% (Fig. 3). A drop to TOC contents of < 0.1 wt% is found at the GSR site below 5 m sediment depth.

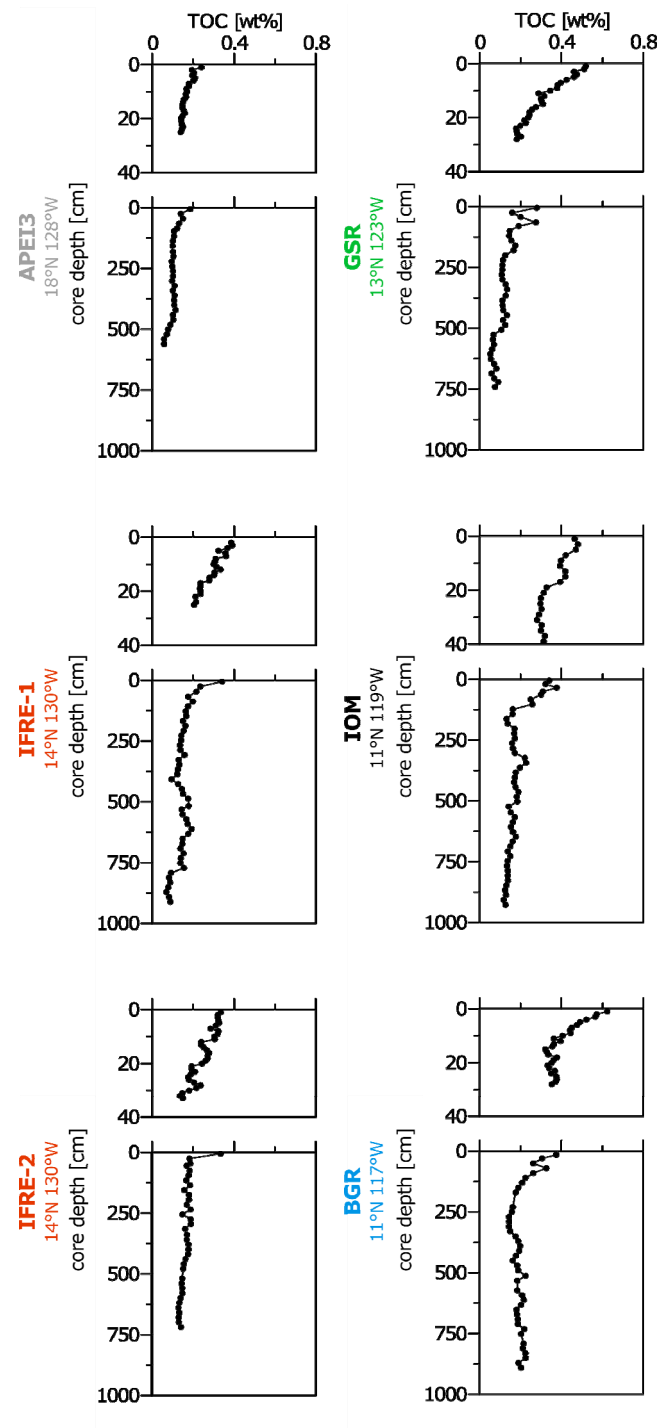


Figure 3: Solid-phase profiles of TOC of the APEI3, IFREMER, GSR, IOM and BGR sites.

4.3.2 Sedimentation rates and bioturbation depth

Sedimentation rates range between 0.2 and 1.15 cm kyr⁻¹ (Fig. 4). The rates at the APEI3 and the GSR sites are at least threefold lower than at the IFRE-1 and IOM sites. Bioturbation is usually limited to the upper 7 cm whereas the bioturbated layer at the IOM site reaches down to 13 cm (Supplementary Fig. 1).

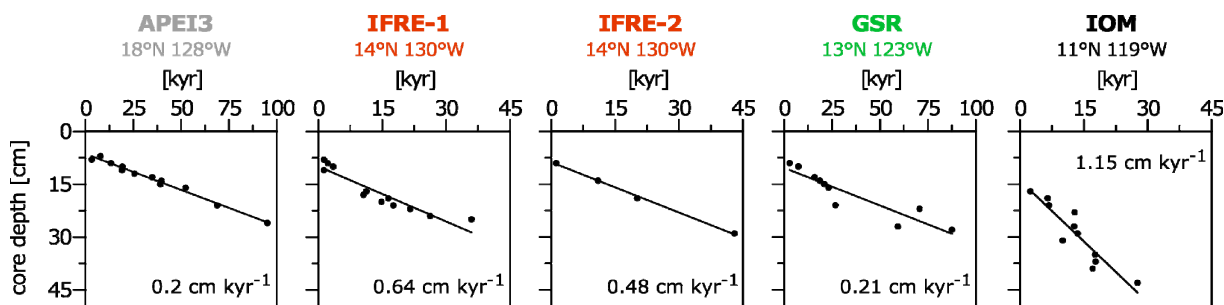


Figure 4: $^{230}\text{Th}/^{231}\text{Pa}$ -derived sedimentation rates for the uppermost 50 cm of the sediments of the APEI3, IFREMER, GSR and IOM sites.

5. Discussion

5.1 POC flux to the seafloor and sedimentation rates

Pelagic deep-sea sediments receive little organic matter (OM) due to generally low surface water productivity and great water depth (Heath et al., 1977; Müller and Suess, 1979; Honjo, 1980). For the prediction of carbon export production at any water depth, Suess (1980) developed an empirical algorithm from sediment trap measurements and primary production (PP) rates in the respective surface waters. Several studies have applied modified algorithms after Suess (1980) (e.g., Dymond et al., 1997; Tyrell, 1999) and Martin et al. (1987) (e.g., Emerson et al., 1997; Fischer et al., 2000) for predicting the vertical POC flux. However, these commonly applied relationships between POC flux and water depth generally overestimate the flux of OM to depth (Buesseler et al., 2007; Buesseler and Boyd, 2009; Henson et al., 2011; Arndt et al., 2013 and references therein). Lutz et al. (2002) developed regional algorithms including region-specific sinking and remineralization rates, i.e. labile and refractory POC fractions in the water column. Using this empirical parameterization of the POC flux to depth, Lutz et al. (2007) combined a time series of remotely sensed net PP in the surface waters, sea surface temperature and sediment trap POC flux data to construct models with global predictions of POC fluxes to the seafloor. According to the model by Lutz et al. (2007), about $1.7 \text{ mg C}_{\text{org}} \text{ m}^{-2} \text{ d}^{-1}$ is delivered to the seafloor at the BGR and IOM sites, $1.5 \text{ mg C}_{\text{org}} \text{ m}^{-2} \text{ d}^{-1}$ reaches the sediments of the GSR and IFREMER sites and $1.3 \text{ mg C}_{\text{org}} \text{ m}^{-2} \text{ d}^{-1}$ settles to the seafloor in the APEI3 area (Fig. 1). These fluxes may be biased due to (1) significant uncertainties in the NPP estimates based on satellite data and (2) several potential errors in the trapping efficiency of sediment traps (Lutz et al., 2007 and references therein). Furthermore, with water depths of 4–5 km, the export production may be laterally drifted during settling, especially by strong bottom currents in the proximity of seamounts (e.g., Mewes et al., 2014). We implemented the POC fluxes given by Lutz et al. (2007), which can be regarded as rough estimates, into our reaction transport model and adjusted these values

in order to fit the measured profiles of TOC and the oxidants. Our diagenetic model reproduces the Lutz et al. (2007) fluxes within 20% (Table 2). Only a slight discrepancy occurs between the POC fluxes derived from both models for the APEI3 and BGR sites. Compared to the other studied contract areas, the water column in the APEI3 area is characterized by a less pronounced OMZ (Martínez Arbizu and Haeckel, 2015). Thus, due to the significantly longer oxygen exposure time of settling POC, which is the key parameter determining the degradation efficiency of POC (e.g. Banse, 1990; Hartnett et al., 1998; Zonneveld et al., 2010; Cavan et al., 2017), the degradation in the water column may be enhanced in this area. The regional differences in the OMZ thickness may limit the empirical algorithm used by Lutz et al. (2007) for calculating the POC flux to the seafloor. Thus, POC fluxes in the APEI3 area could be slightly overestimated. Conversely, the POC flux in the BGR area has likely been underestimated as the water column is characterized by an extensive OMZ (Martínez Arbizu and Haeckel, 2015) aiding the POC preservation in the water column and triggering a higher POC flux to the sediment (Table 2). This is consistent with our 20% lower fluxes at the APEI3 site and 20% higher POC flux at the BGR site in comparison with the Lutz et al. (2007) fluxes.

Table 2: Fluxes of POC and oxygen into the sediment and depth-integrated rates of the predominant biogeochemical processes derived from the diagenetic model.

| Biogeochemical process | Unit | BGR | IOM | GSR | IFRE-1 | IFRE-2 | APEI3 |
|--|--|------------|------------|------------|---------------|---------------|--------------|
| POC flux | [mg C m ⁻² d ⁻¹] | 1.99 | 1.54 | 1.51 | 1.47 | 1.5 | 1.07 |
| O ₂ flux top | [mg O ₂ m ⁻² d ⁻¹] | 5.18 | 4.24 | 3.61 | 4.3 | 4.37 | 2.58 |
| O ₂ reduction | [mg C m ⁻² d ⁻¹] | 1.92 | 1.44 | 1.38 | 1.3 | 1.45 | 0.93 |
| NO ₃ ⁻ reduction | [mg C m ⁻² d ⁻¹] | 1.5E-03 | 1.7E-03 | 3.3E-02 | 5.5E-03 | 5.0E-03 | 8.7E-04 |
| Mn(IV) reduction | [mg C m ⁻² d ⁻¹] | 1.5E-03 | 6.1E-04 | 1.6E-02 | 5.7E-04 | 4.6E-03 | 1.4E-03 |
| Nitrification | [mg N m ⁻² d ⁻¹] | 0.01 | 0.13 | 0.14 | 0.10 | 0.14 | 0.03 |
| Mn ²⁺ oxidation | [mg O ₂ m ⁻² d ⁻¹] | 0.062 | 0.026 | 0.06 | 0.025 | 0.029 | 0.016 |
| Mn-annamox | [mg Mn m ⁻² d ⁻¹] | 0.14 | 0.005 | 0 | 0 | 0 | 0 |

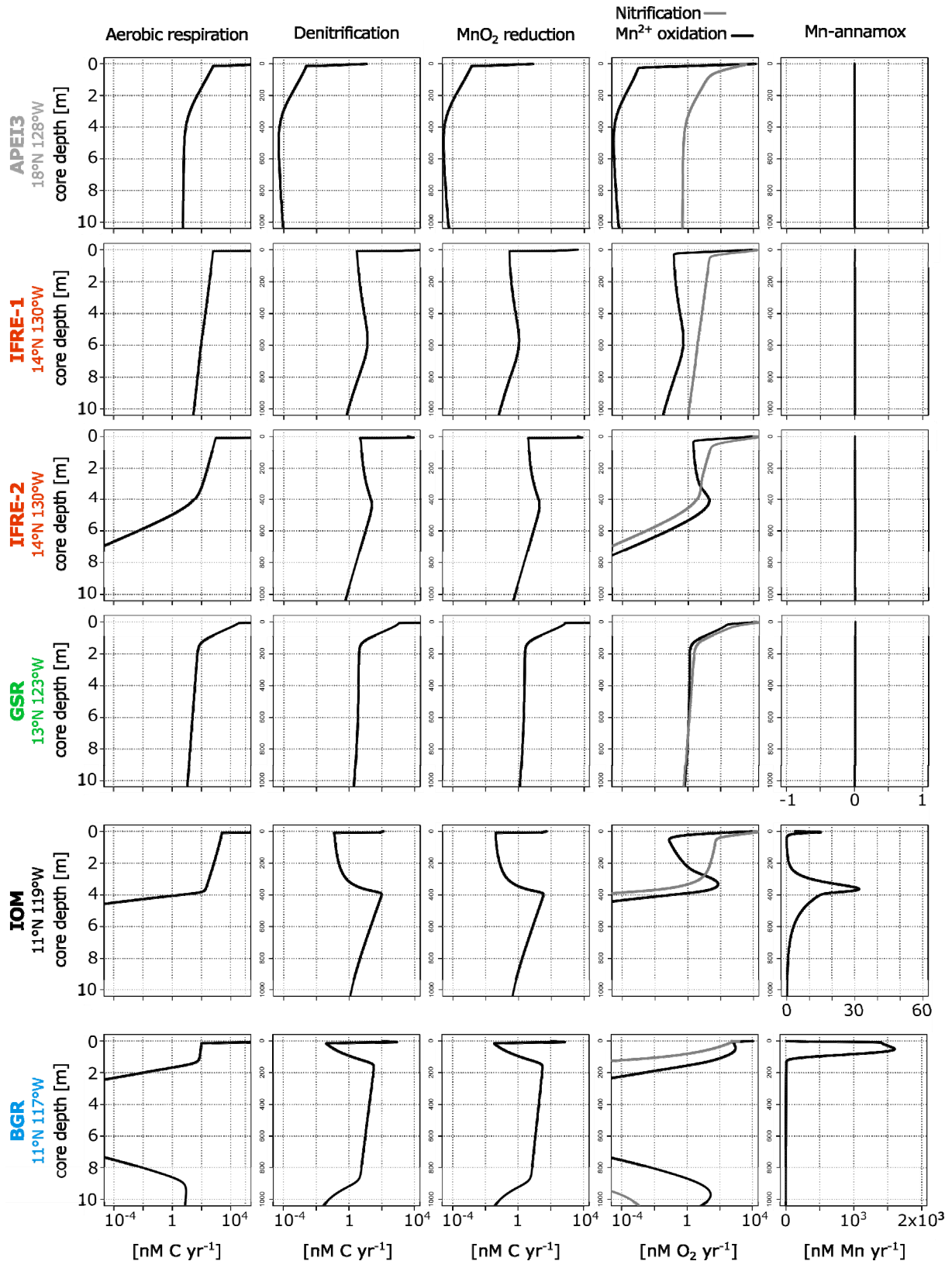


Figure 5: Model results for all sites including the biogeochemical processes of aerobic respiration, Mn(IV) reduction, denitrification, Mn²⁺ oxidation, nitrification and Mn-annamox (R₁–R₆).

Although considerably higher estimated POC fluxes between 1.5 and 11.5 mg C_{org} m⁻² d⁻¹ have been reported from nearby stations (Murray and Kuivila, 1990; Mogollón et al., 2016), the TOC

contents at the sediment surface at all sites are mostly in agreement with published values from the CCZ ranging from 0.1–0.6 wt% (Müller, 1977; Müller and Mangini, 1980; Jahnke et al., 1982; Murray and Kuivila, 1990; Mewes et al., 2014; Mewes et al. 2016). Mewes et al. (2014) have presented geochemical data for sediments from the BGR contract area “East” with two sites close (< 5 km) to a large seamount between the BGR and IOM area (A1-1-MN, A1-2-NN) and two sites far away from seamounts (A5-1-BN, A5-2-SN). While the surface sediment TOC contents are similar at all stations, a comparably rapid decrease in TOC contents with depth occurs at the sites adjacent to the seamount with relatively high POC fluxes of $10 \text{ mg C}_{\text{org}} \text{ m}^{-2} \text{ d}^{-1}$ (Fig. 6; Mogollón et al., 2016). Our BGR site shows up to 20% higher TOC contents in the upper 30 cm than the sites studied by Mewes et al. (2014) and also decrease rapidly with sediment depth (Fig. 6). Khripounoff et al. (2006) reported 25% higher TOC contents in the upper 30 cm at a site in the IFREMER area (Fig. 6). Variations in local estimated POC fluxes, TOC contents and sedimentation rates are potentially a result of strong local heterogeneities of bottom water currents which can be intensified, attenuated and deflected in the vicinity of seamounts and ridges (Hogg, 1973; Gould et al., 1981; Mohn and Beckmann, 2002; Xu and Lavelle, 2017) and cause kilometer-scale differences in the supply and composition of sediments (Turnewitsch et al., 2004; Mewes et al., 2014; Turnewitsch et al., 2015). The relatively high sedimentation rates at the IOM site of 1.15 cm kyr^{-1} may be associated with sediment focusing. Furthermore, sediments of different composition may be delivered from the slopes of nearby seamounts and ridges by gravity-induced processes (e.g., Stanley and Taylor, 1977; Jeong et al., 1994).

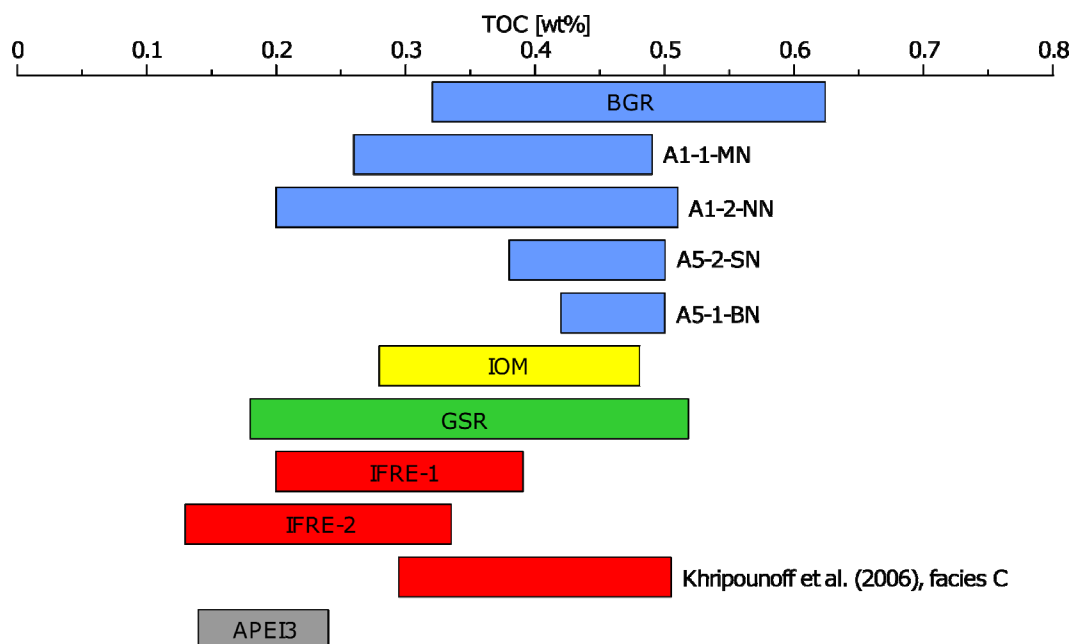


Figure 6: Comparison of the TOC contents of surface sediments (upper 30 cm) within the different contract areas. The data for the BGR sites A1-1-MN, A1-2-NN, A5-2-SN, A5-1-BN from cruise SO205 are taken from Mewes et al. (2014). The range of TOC contents comprises the lowest to highest measured contents throughout MUC cores taken at the individual sites. The highest TOC content at each site was determined at the sediment surface, i.e. in the uppermost centimeter of the sediment.

5.2 Organic matter degradation

Müller et al. (1988) have suggested that aerobic respiration is the dominant biogeochemical process degrading sedimentary OM in the CCZ and previous modeling studies for the BGR contract area “East” (Table 2; Fig. 5; Mewes et al., 2016; Mogollón et al., 2016) have supported this assumption. Our model simulations are in line with these findings and show that aerobic respiration consumes more than 90% of the OM delivered to the seafloor while denitrification and Mn(IV) reduction together consume less than 1%. These numbers agree well with rates derived from the previous modeling studies for the BGR contract area “East” (Table 2; Fig. 5; Mewes et al., 2016; Mogollón et al., 2016). The zone in which manganese and nitrate reduction co-occur will hereafter be referred to as “suboxic zone” in which neither oxygen nor hydrogen sulfide are present (Berner, 1981). Most of the ammonia liberated from OM degradation becomes nitrified in the oxic zone so that the nitrate concentrations increase with depth in the upper 30 cm of sediment (Fig. 2; Fig. 5). Additionally to nitrification, the breakup of nitrate-rich organic compounds may contribute to the relatively high NO_3^- concentrations in the surface sediments at the APEI3 and GSR sites (e.g., Jørgensen and Gallardo, 1999). The bioturbated layer includes the upper 6–13 cm of the oxic sediment which is in good agreement with the average mixing bioturbation depth of 10 cm (Boudreau, 1994).

The determined low sedimentation rates of 0.2 to 1.15 cm kyr⁻¹ in combination with low POC fluxes to the seafloor (< 2 mg m⁻² d⁻¹) lead to low carbon burial rates of less than 0.15 mg m⁻² d⁻¹ (based on depth-integrated rates, cf. Table 2), which are consistent with other organic carbon burial estimates for the CCZ (e.g., Jahnke, 1996). The highly refractory TOC fraction of < 0.2 wt% below 20 cm is insufficient to reduce nitrate (Table 2; Fig. 5; Supplementary Table 2; Mogollón et al., 2016). These observations are in agreement with Müller and Mangini (1980) and Müller et al. (1988) who state that with sedimentation rates of 0.2–0.4 cm kyr⁻¹ OM is almost completely remineralized within the uppermost meter of the sediments. Mewes et al. (2014) determined carbon respiration rates for sediments in the BGR contract area “East” that showed twofold higher respiration rates in the upper oxic sediments compared to the depth-integrated rates of aerobic respiration derived from our diagenetic model (Table 2). This offset may be caused by the alteration of the microbial communities during sediment retrieval, i.e. decompression (e.g., Park and Clark, 2002), and the different approaches of respiration rate determination. Moreover, the discrepancy in the respiration rates may reflect the lateral heterogeneity in the supply of TOC related to the interaction of currents with rough seafloor topography, in particular seamounts. Twofold higher rates of aerobic respiration at the BGR site compared to the APEI3 site are a result of twofold higher POC fluxes to the seafloor at the BGR site than at the APEI3 site in the proximity of the carbon-starved North Pacific gyre. Consequently, the APEI3 site does not represent the (bio)geochemical conditions of the sites in the European contract areas investigated in the framework of this study. This observation is in agreement with Vanreusel et al. (2016) who explained the significantly lower faunal densities in the APEI3 with primary productivity being much lower compared to in the contract areas.

5.3 Redox zonation and oxygen fluxes

The *ex situ* sediment oxygen concentrations are in good agreement with other oxygen data for the equatorial Pacific Ocean (Murray and Grundmanis, 1980; Jahnke et al., 1982; Berelson et al., 1990; Hammond et al., 1996; Khripounoff et al., 2006; Rühlemann et al., 2011; Røy et al., 2012; Mewes et al., 2014; Mewes et al., 2016). In accordance with oxygen measurements by Mewes et al. (2014), bottom water oxygen measurements of the overlying water of the MUC cores using amperometric Clark-type oxygen sensors are systematically 10–20% higher than bottom-water concentrations determined with the CTD 20–30 m above the seafloor (Martínez Arbizu and Haeckel, 2015). This offset is most likely a result of sampling artifacts that occurred during retrieval of the MUC cores or of atmospheric oxygen diffusion into the bottom water of the surface sediments during *ex situ* measurements, which biases the oxygen concentrations down to about 0.4 cm sediment depth. The threshold of 0.4 cm has been

determined in this study by triplicate profiling across the water-sediment interface resulting in systematically higher oxygen concentrations of each consecutively measured profile. Therefore, we excluded oxygen concentrations in the uppermost 0.4 cm from the calculation of oxygen gradients and fluxes and used the CTD oxygen concentrations as bottom water values (Table 2; Table 3). The oxygen data obtained for the IOM site indicate that oxygen is not completely depleted throughout the sediment core (Fig. 2). However, the detection of dissolved Mn^{2+} in pore water below 3 m sediment depth suggests that oxygen is absent in this interval. We attribute this discrepancy to some calibration problems of one of the sensors at the beginning of the cruise which affected the oxygen measurements at the BGR and IOM sites. Additionally, the discrepancy between the GSR oxygen concentrations of the MUC and the GC is attributed to small-scale variations or to miscalibration of the oxygen sensor. Even though the oxygen data shows sampling artifacts and miscalibration, which partly bias the absolute oxygen concentrations, it can be used in combination with the pore-water Mn^{2+} data to delineate the sedimentary redox zonation. As the oxygen data at the bottom water-sediment interface is particularly affected, oxygen fluxes into the sediment are given with an error of $< 5\%$.

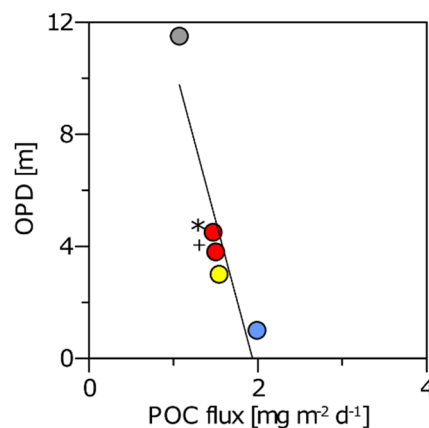


Figure 7: Correlation between the oxygen penetration depth (OPD) and the POC fluxes used as boundary conditions for the diagenetic model. Based on interpolation of the oxygen profile at the APEI3 site, oxygen may be consumed at 11.5 m. The linear regression through the BGR (blue), IOM (yellow), *IFRE-1 (red), +IFRE-2 (red) and APEI3 (grey) sites shows a coefficient of determination of $r^2 = 0.85$.

The OPD inversely correlates with the POC flux ($r^2 = 0.85$; Fig. 7). The OPD of 1 m at the BGR site is shallower than the OPD reported for other sites studied in this region which range between 1.8 and 3 m depth (Mewes et al., 2014). Such small-scale variation is reflected in the oxygen gradients with $2.6\text{--}5.6 \mu\text{M O}_2 \text{ mm}^{-1}$ in the sediments in the BGR area (Table 3). OPDs are generally deeper at sites with medium-sized or big (3–10 cm) nodules at the sediment surface than at sites with small-size (1–8 cm) or without nodules at the surface (Mewes et al., 2014). The two IFREMER sites (IFRE-1 and IFRE-2) are ~ 6 km apart with medium-sized

surface nodules at the IFRE-1 site and no nodules at the IFRE-2 site (Table 1) and in accordance with the findings of Mewes et al. (2014), the OPD at the IFRE-1 site is located 70 cm deeper than at the IFRE-2 site (Fig. 2). However, the depth-integrated rates of Mn(IV) and nitrate reduction are not significantly higher at the IFRE-2 site compared to the IFRE-1 site (Table 2; Fig. 5) which disagrees with the results presented by Mewes et al. (2014). This discrepancy may be connected to almost twofold higher sedimentation rates proposed by the authors for the nodule-free sites compared to the sites with medium-sized/big nodules while in the IFREMER area, sedimentation rate at the IFRE-1 site exceeds the rate at the IFRE-2 site. In accordance with the low respiration rates at the APEI3 site, the oxygen gradient over the upper 0.4–1 cm of sediment is low at $0.2 \mu\text{M O}_2 \text{ mm}^{-1}$ (Table 3). At depth, oxygen concentrations are scattered at the APEI3 site. We interpret this as an analytical artifact because the sediments at the APEI3 site were very dry and consolidated and have therefore very likely impacted the sensor measurements.

Table 3: Oxygen gradients calculated from oxygen profiles for the uppermost 0.4–1 cm of sediment. Negative gradients indicate the oxygen flux into the sediment. The data from SO205 were taken from Mewes et al. (2014). Note that the oxygen gradient at the GSR site is biased due to miscalibration of the sensor.

| Station | Oxygen gradient [$\mu\text{M mm}^{-1}$] |
|-------------|--|
| SO205-05MUC | -3.5 |
| SO205-06MUC | -2.6 |
| SO205-46MUC | -5.6 |
| SO205-48MUC | -9 |
| BGR | -5 |
| IOM | -7 |
| GSR | -8.3 |
| IFRE-1 | -3.5 |
| IFRE-2 | -1.7 |
| APEI3 | -0.2 |

In the suboxic zone, Mn^{2+} concentrations between 0.2–25 μM agree well with reported values in the CCZ (Emerson et al., 1980; Jahnke et al., 1982; Mewes et al., 2014). Mn^{2+} is mainly mobilized by the dissimilatory reduction of Mn(IV) phases below the OPD (Figs. 2 and 5). As proposed by Mogollón et al. (2016) for adjacent sites, the observed concomitant decrease of nitrate in the suboxic zone of the sediment core from the BGR area suggest that the biogeochemical cycles of manganese and nitrogen are coupled. Excess ammonium produced by OC degradation in the oxic zone may escape aerobic nitrification and diffuse downwards

into the suboxic zone where it can act as electron donor during manganese oxide reduction (Mn-annamox, Luther et al., 1997). Mn-annamox may induce the liberation of Mn^{2+} into the pore water of the sediments of the BGR and IOM sites with reaction rates similar to the rates published by Mogollón et al. (2016) (Table 2; Fig. 5). The nitrate concentrations determined within the framework of this study are in correspondence with previously published nitrate pore-water data from the CCZ ranging from 30–70 μM (Jahnke et al., 1982; Jeong et al., 1994; Mewes et al., 2014; Mewes et al., 2016; Mogollón et al., 2016). Nitrate reduction is very weak at these sites due to the low and refractory OM content (Table 2). Iron and manganese oxidation coupled to nitrate reduction is probably also not feasible due to the low Mn^{2+} concentrations and Fe^{2+} levels below detection limit.

5.3.1 Deep Mn^{2+} oxidation

Decreasing-with-depth profiles of Mn^{2+} at the IFRE-1, IOM and BGR sites indicate that Mn^{2+} is consumed by either precipitation of an authigenic carbonate mineral (e.g., Gingele and Kasten, 1994) or by oxidation at depth (Fig. 2). Due to the fact that alkalinity is low in these sediments (data not shown), and thus, precipitation of a Mn carbonate phase is unlikely, we suggest that at depth, Mn^{2+} is most likely oxidized by oxygen diffusing from the underlying basaltic basement. Such upward diffusive supply of oxygen from oxic seawater circulating in the oceanic crust was first shown for the German contract area “East” by Mewes et al. (2016) and has recently been documented to be widespread in the area by Kuhn et al. (2017). At the IFRE-1 site, Mn^{2+} is consumed at 7 m depth. Based on interpolation of the Mn^{2+} profiles, Mn^{2+} is reoxidized at ~ 9.25 m depth at the BGR site while it is consumed at ~ 20 m depth at the IOM site. The low-temperature circulation of seawater through the basaltic crust (e.g., Fisher and Wheat, 2010; Ziebis et al., 2012) underlying the sediments of the CCZ had so far only been shown for the BGR area “East” on the base of increasing-with-depth oxygen and decreasing-with-depth Mn^{2+} profiles (Mewes et al., 2016; Kuhn et al., 2017). Numerous seamounts and faults in the eastern CCZ have been shown to facilitate the recharge and subsequent discharge of oxic seawater into and from oceanic crust and diffusion of oxygen into the overlying sediments. The BGR, IOM, and IFRE-1 sites are located about 5 km, 3 km and 1 km, respectively from the adjacent ridge flanks (Fig. 1). At these sites, the sediment drape thicknesses range between 20 and 83 m (Supplementary Table 2). In comparison, the sites studied by Kuhn et al. (2017) in the BGR area had an average sediment thickness of 48 m. The Mn^{2+} profile at the IFRE-2 site does not indicate Mn^{2+} oxidation at depth while the sediments at the APEI3 and GSR sites are oxic throughout. The extended oxic zones at the APEI3 and GSR sites probably result from low organic carbon supply and respiration (Table 2), which is

insufficient to fully consume the oxygen diffusing into the sediment from both the overlying seawater and the underlying basaltic crustal fluids. However, the retrieved core lengths of up to 7.5 m do not allow the identification of deep oxidative processes at these locations. Based on our pore-water data, widespread deep Mn^{2+} oxidation occurs at three sites of various contract areas within the CCZ.

6. Conclusion

We studied six abyssal sites in the Clarion-Clipperton Zone of five European contract areas for the exploration of polymetallic nodules and one site in an Area of Particular Environmental Interest (APEI3) over a distance of about 1300 km. The sites differ in POC fluxes to the seafloor ($1\text{--}2 \text{ mg m}^{-2} \text{ d}^{-1}$) and sedimentation rates ($0.2\text{--}1.15 \text{ cm kyr}^{-1}$) while the bioturbation depth is mostly limited to the upper 7 cm of the sediment. Solid-phase contents, pore-water profiles and the applied transport reaction model demonstrate significant inter-areal differences in sedimentation rates, the extension of oxic and suboxic zones and rates of organic matter remineralization. We show that the observed variability in redox zonation at the study sites is determined by differences in (1) surface water productivity and associated POC flux to the seafloor, (2) sediment accumulation rate and (3) the oxidation of pore-water Mn^{2+} at depth. Diagenetic modeling indicates that due to the low sedimentation rates, the labile fractions of organic carbon are restricted to the upper 20 cm of the sediment where OC degradation is dominated (90%) by aerobic respiration. Mn(IV) reduction and denitrification each consume less than 1% of the refractory organic matter. The suboxic zone is characterized by a wide range of Mn^{2+} concentrations where the sites with the highest POC fluxes indicate further production of Mn^{2+} by Mn-annamox. Mn^{2+} -mediated denitrification is absent at all sites due to insufficient Mn^{2+} concentrations. Downward decreasing Mn^{2+} concentrations at three sites indicate the widespread oxidation of Mn^{2+} at depth throughout the CCZ. Due to very low POC fluxes of $1 \text{ mg m}^{-2} \text{ d}^{-1}$ to the seafloor in the APEI3 area, respiration rates at this site are about twofold lower than in the investigated European contract areas. Consequently, we infer that the preservation area APEI3 does not represent the depositional conditions and biogeochemical processes that are dominating in the investigated European contract areas. The POC fluxes to the seafloor and the sedimentation rates generally correlate with surface water productivity, however, within a given contract area, small-scale spatial (intra-areal) variations in geochemical conditions and biogeochemical processes are caused by (1) various extents of POC degradation processes in the water column and (2) small-scale interactions of bottom water currents and topography affecting the sedimentation pattern.

This study represents the first biogeochemical baseline study that advances our knowledge about regional variations of natural depositional and geochemical conditions as well as biogeochemical processes in the sediments of the vast deep-sea area of the CCZ. Our findings may deliver important baseline data to be used for the assessment of the impact of potential deep-sea mining activities. They will also serve as an input for the further development of the Environmental Management Plan by the International Seabed Authority (ISA).

Acknowledgements

We thank captain Lutz Mallon, the crew and the scientific party of RV SONNE cruise SO239 for the technical and scientific support. Thanks to Jennifer Ciomber, Benjamin Löffler and Vincent Ozegowski for their participation in onboard sampling and analysis. For analytical support in the home laboratory and during data evaluation we are grateful to Ingrid Stimac, Olaf Kreft, Dennis Köhler, Ingrid Dohrmann and Dr. Gerhard Kuhn (all at AWI). For providing the bathymetric grids we thank Prof. Dr. Jens Greinert (GEOMAR). Special thanks to Dr. Matthias Haeckel (GEOMAR), Prof. Dr. Gerhard Bohrmann (MARUM, University of Bremen), Dr. Timothy G. Ferdelman (MPI Bremen) and Dr. Gerard Versteegh for much appreciated discussions. We thank the four reviewers for their helpful comments that have improved this manuscript. This study is funded by the German Federal Ministry of Education and Research (BMBF) in the framework of the JPI Oceans project MiningImpact (grant no. 03F0707G) as part of the JPI-Oceans pilot action EcoMining-DEU – Ecological Aspects of Deep-Sea Mining. Dr. José M. Mogollón was partially funded by the Netherlands Earth System Science Centre (NESSC). We acknowledge further financial support from the Helmholtz Association (Alfred Wegener Institute Helmholtz Centre for Polar and Marine Research). The data are available via the data management portal OSIS-Kiel and the geological data network PANGAEA.

References

- Anderson, R.F., Fleer, A.P., 1982. Determination of natural actinides and plutonium in marine particulate material. *Anal. Chem.* 54, 1142–1147. doi:10.1021/ac00244a030.
- Andersson, P.S., Schöberg, H., 2012. Determination of ²³²Th and ²³⁰Th in seawater using a chemical separation procedure and thermal ionization mass spectrometry. *Limnol. Oceanogr. Methods* 10, 296–303. doi:10.4319/lom.2012.10.296.
- Arndt, S., Jørgensen, B.B., LaRowe, D.E., Middelburg, J.J., Pancost, R.D., Regnier, P., 2013. Quantifying the degradation of organic matter in marine sediments: a review and synthesis. *Earth-Science Reviews* 123, 53–86. doi:10.1016/j.earscirev.2013.02.008.
- Arrhenius, G., 1952. Sediment cores from the East Pacific. Elanders boktryckeri aktiebolag, Göteborg.
- Banse, K., 1990. New views on the degradation and disposition of organic particles as collected by sediment traps in the open sea. *Deep-Sea Res. Part A: Oceanogr. Res. Pap.* 37(7), 1177–1195.
- Bender, M.L., 1983. The manganese nodule program. *Eos Trans. AGU* 64(5), 42–43. doi:10.1029/EO064i005p00042.
- Berelson, W.M., Hammond, D.E., Cutter, G.A., 1990. In situ measurements of calcium carbonate dissolution rates in deep-sea sediments. *Geochim. Cosmochim. Acta* 54, 3013–3020. doi:10.1016/0016-7037(90)90118-5.
- Berger, W.H., 1974. Deep-sea sedimentation. In: *The Geology of Continental Margins* (eds. Burk, C.A., Drake, C.L.). Springer, New York, 213–241.
- Berner, R.A., 1981. A new geochemical classification of sedimentary environments. *J. Sediment. Res.* 51, 359–365.
- Bischoff, J.L., Piper, D.Z., 1979. Marine Geology and Oceanography of the Pacific Manganese Nodule Province. Springer, New York.
- Boudreau, B.P., 1994. Is burial velocity a master parameter for bioturbation? *Geochim. Cosmochim. Acta* 58, 1243–1249.
- Boetius, A., Haeckel, M., 2018. Mind the seafloor. *Science* 359 (6371), 34–36. <https://doi.org/10.1126/science.aap7301>.
- Boudreau, B.P., 1997. A one-dimensional model for bed-boundary layer particle exchange. *J. Mar. Sys.* 11, 279–303. doi:10.1016/S0924-7963(96)00127-3.
- Buesseler, K.O., Boyd, P.W., 2009. Shedding light on processes that control particle export and flux attenuation in the twilight zone of the open ocean. *Limnol. Oceanogr.* 54, 1210–1232.
- Buesseler, K.O., Antia, A.N., Chen, M., Fowler, S.W., Gardner, W.D., Gustafsson, O., Harada, K., Michaels, A.F., Rutgers van der Loeff, M., Manmohan, S., Steinberg, D.K., Trull, T., 2007. An assessment of the use of sediment traps for estimating upper ocean particle fluxes. *J. Mar. Res.* 65, 345–416.
- Calvert, S.E., Price, N.B., 1977. Geochemical variation in ferromanganese nodules and associated sediments from the Pacific Ocean. *Mar. Chem.* 5, 43–74.
- Cavan, E.L., Trimmer, M., Shelley, F., Sanders, R., 2017. Remineralization of particulate organic carbon in an ocean oxygen minimum zone. *Nat. Commun.* 8, 14847. doi:10.1038/ncomms14847
- Chun, C., 1908. Manganknollen. In: *Wissenschaftliche Ergebnisse der Deutschen Tiefsee-Expedition auf dem Dampfer "Valdivia" 1898–1899* (ed. Chun, C). 111–114.

- Craig, J.D., 1979. The relationship between bathymetry and ferromanganese deposits in the north equatorial Pacific. *Mar. Geol.* 29, 165–186. doi:10.1016/0025-3227(79)90107-5.
- D'Hondt, S., Jørgensen, B.B., Miller, D.J., Batzke, A., Blake, R., Cragg, B.A., Cypionka, H., Dickens, G.R., Ferdelman, T., Hinrichs, K.-U., Holm, N.G., Mitterer, R., Spivack, A., Wang, G., Bekins, B., Engelen, B., Ford, K., Gettemy, G., Rutherford, S.D., Sass, H., Skilbeck, C.G., Aiello, I.W., Guèrin, G., House, C.H., Inagaki, F., Meister, P., Naehr, T., Niitsuma, S., Parkes, R.J., Schippers, A., Smith, D.C., Teske, A., Wiegel, J., Padilla, C.N., Acosta, J.L.S., 2004. Distributions of Microbial Activities in Deep Subseafloor Sediments. *Science* 306, 2216–2221. doi:10.1126/science.1101155.
- Dymond, J., Collier, R., McManus, J., Honjo, S., Manganini, S., 1997. Can the aluminium and titanium contents of ocean sediments be used to determine the paleoproductivity of the oceans? *Paleoceanography* 12, 586–593.
- Emerson, S., Jahnke, R., Bender, M., Froelich, P., Klinkhammer, G., Bowser, C., Setlock, G., 1980. Early diagenesis in sediments from the eastern equatorial Pacific, I. Pore water nutrient and carbonate results. *Earth Planet. Sci. Lett.* 49, 57–80. doi:10.1016/0012-821X(80)90150-8.
- Emerson, S., Quay, P., Karl, D., Winn, C., Tupas, L., Landry, M., 1997. Experimental determination of the organic carbon flux from open-ocean surface waters. *Nature* 389, 951–954.
- Faure, G., 1977. Principles of Isotope Geology, Wiley.
- Fischer, G., Ratmeyer, V., Wefer, G., 2000. Organic carbon fluxes in the Atlantic and the Southern Ocean: relationship to primary production compiled from satellite radiometer data. *Deep-Sea Res. Part II* 47, 1961–1997.
- Fisher, A.T., Wheat, C.G., 2010. Seamounts as Conduits for Massive Fluid, Heat, and Solute Fluxes on Ridge Flanks. *Oceanography* 23, 74–87.
- Gingele, F.X., Kasten, S., 1994. Solid-phase manganese in Southeast Atlantic sediments: Implications for the paleoenvironment. *Mar. Geol.* 121, 317–332.
- Glover, A.G., Smith, C.R., Paterson, G.L.J., Wilson, G.D.F., Hawkins, L., Shearer, M., 2002. Polychaete species diversity in the central Pacific abyss: Local and regional patterns and relationships with productivity. *Mar. Ecology Progress Series* 240, 157–170. doi:10.3354/meps240157.
- Gould, W.J., Hendry, R., Huppert, H.E., 1981. An abyssal topographic experiment. *Deep-Sea Res.* 28A, 409–440.
- Greinert, J., 2016. Swath sonar multibeam EM122 bathymetry during SONNE cruise SO239 with links to raw data files. PANGAEA. doi.pangaea.de/10.1594/PANGAEA.859456.
- Halbach, P., Friedrich, G., von Stackelberg, U. (eds.), 1988. The manganese nodule belt of the Pacific Ocean. Enke, Stuttgart.
- Hammond, D.E., McManus, J., Berelson, W.M., Kilgore, T.E., Pope, R.H., 1996. Early diagenesis of organic material in equatorial Pacific sediments: stoichiometry and kinetics. *Deep-Sea Res. Part II: Top. Stud. Oceanogr.* 43, 1365–1412. doi:10.1016/0967-0645(96)00027-6.
- Hartnett, H.E., Keil, R.G., Hedges, J.I., Devol, A.H., 1998. Influence of oxygen exposure time on organic carbon preservation in continental margin sediments. *Nature* 391, 572–575.

- Heath, G.R., Moore, T.C., Dauphin, J.P., 1977. Organic carbon in deep-sea sediments. In: *The Fate of Fossil Fuel CO₂ in the Oceans* (eds. Anderson, N.R., Malanioff, A.). Plenum Press, New York, 605–625.
- Henson, S.A., Sanders, R., Madsen, E., Morris, P.J., Le Moigne, F., Quartly, G.D., 2011. A reduced estimate of the strength of the ocean's biological carbon pump. *Geophys. Res. Lett.* 38, L04606. doi:10.1029/2011GL046735.
- Hogg, N.G., 1973. On the stratified Taylor column. *J. Fluid Mech.*, 58, 517–537.
- Honjo, S., 1980. Material fluxes and modes of sedimentation in the mesopelagic and bathypelagic zones. *J. Mar. Res.* 38, 53–97.
- International Seabed Authority (ISA), 2010. A Geological Model for Polymetallic Nodule Deposits in the Clarion-Clipperton Fracture Zone. Technical Study 6, Kingston, 211.
- Jahnke, R.A., 1996. The global ocean flux of particulate organic carbon: Areal distribution and magnitude. *Glob. Biogeochem. Cycles* 10, 71–88
- Jahnke, R.A., Emerson, S.R., Murray, J.W., 1982. A model of oxygen reduction, denitrification, and organic matter mineralization in marine sediments¹. *Limnol. Oceanogr.* 27, 610–623. doi:10.4319/lo.1982.27.4.0610.
- Jeong, K.S., Kang, J.K., Chough, S.K., 1994. Sedimentary processes and manganese nodule formation in the Korea Deep Ocean Study (KODOS) area, western part of Clarion-Clipperton fracture zones, northeast equatorial Pacific. *Mar. Geol.* 122, 125–150. doi:10.1016/0025-3227(94)90208-9.
- Johnson, D.A., 1972. Ocean-Floor Erosion in the Equatorial Pacific. *Geol. Soc. of Am. Bulletin* 83, 3121–3144. doi:10.1130/0016-7606(1972)83[3121:OEITEP]2.0.CO;2.
- Jones, D.O.B., Kaiser, S., Sweetman, A.K., Smith, C.R., Menot, L., Vink, A., 2017. Biological responses to disturbance from simulated deep-sea polymetallic nodule mining. *PLoS ONE* 12(2):e0171750. doi:10.1371/journal.pone.0171750.
- Jørgensen, B.B., Gallardo, V.A., 1999. Thioploca spp.: filamentous sulfur bacteria with nitrate vacuoles. *FEMS Microbiol. Ecology* 28, 301–313.
- Juan, C., Van Rooij, D., De Bruycker, W., 2018. An assessment of bottom current controlled sedimentation in Pacific Ocean abyssal environments. *Mar. Geol.* 403, 20–33.
- Kalvelage, T., Lavik, G., Jensen, M.M., Revsbech, N.P., Löscher, C., Schunck, H., Desai, D.K., Hauss, H., Kiko, R., Holtappels, M., LaRoche, J., Schmitz, R.A., Graco, M.I., Kuypers, M.M.M., 2015. Aerobic Microbial Respiration In Oceanic Oxygen Minimum Zones. *PLoS ONE* 10(7):e0133526. doi:10.1371/journal.pone.0133526.
- Khripounoff, A., Caprais, J.-C., Crassous, P., Etoubleau, J., 2006. Geochemical and biological recovery of the disturbed seafloor in polymetallic nodule fields of the Clipperton-Clarion Fracture Zone (CCFZ) at 5,000-m depth. *Limnol. Oceanogr.* 51, 2033–2041. doi:10.4319/lo.2006.51.5.2033.
- Klinkhammer, G.P., 1980. Early diagenesis in sediments from the eastern equatorial Pacific, II. Pore water metal results. *Earth Planet. Sci. Lett.* 49, 81–101. doi:10.1016/0012-821X(80)90151-X.
- Kretschmer, S., Geibert, W., Rutgers van der Loeff, M.M., Schnabel, C., Xu, S., Mollenhauer, G., 2011. Fractionation of ²³⁰Th, ²³¹Pa, and ¹⁰Be induced by particle size and composition within an opal-rich sediment of the Atlantic Southern Ocean. *Geochim. Cosmochim. Acta* 75, 6971–6987. doi:10.1016/j.gca.2011.09.012.

- Kretschmer, S., Geibert, W., Rutgers van der Loeff, M.M., Mollenhauer, G., 2010. Grain size effects on ^{230}Th inventories in opal-rich and carbonate-rich marine sediments. *Earth Planet. Sci. Lett.* 294, 131–142. doi:10.1016/j.epsl.2010.03.021.
- Kuhn, T., Versteegh, G.J.M, Villinger, H., Dohrmann, I., Heller, C., Koschinsky, A., Kaul, N., Ritter, S., Wegorzewski, A.V, Kasten, S., 2017. Widespread seawater circulation in 18–22 Ma oceanic crust: Impact on heat flow and sediment geochemistry. *Geology* 45(9), 799–802. doi: 10.1130/G39091.1.
- Kuhn, G., 2013. Don't forget the salty soup: Calculations for bulk marine geochemistry and radionuclide geochronology. Goldschmidt 2013, Florence, Italy, 25 August 2013 – 30 August 2013. doi:10.1180/minmag.2013.077.5.11.
- Lodge, M., Johnson, D., Le Gurun, G., Wengler, M., Weaver, P., Gunn, V., 2014. Seabed mining: International Seabed Authority environmental management plan for the Clarion-Clipperton Zone. A partnership approach. *Mar. Policy* 49, 66–72. doi:10.1016/j.marpol.2014.04.006.
- Luther, G.W., Sundby, B., Lewis, B.L., Brendel, P.J., Silverberg, N., 1997. Interactions of manganese with the nitrogen cycle: Alternative pathways to dinitrogen. *Geochim. Cosmochim. Acta* 61, 4043–4052. doi:10.1016/S0016-7037(97)00239-1.
- Lutz, M.J., Caldeira, K., Dunbar, R.B., Behrenfeld, M.J., 2007. Seasonal rhythms of net primary production and particulate organic carbon flux to depth describe the efficiency of biological pump in the global ocean. *J. Geophys. Res.* 112, C10011. doi:10.1029/2006JC003706.
- Lutz, M.J., Dunbar, R.B., Caldeira, K., 2002. Regional variability in the vertical flux of particulate organic carbon in the ocean interior. *Glob. Biogeochem. Cycles* 16, 1037–1055.
- Madureira, P., Brekke, H., Cherkashov, G., Rovere, M., 2016. Exploration of polymetallic nodules in the Area: Reporting practices, data management and transparency. *Mar. Policy* 70, 101–107. doi:10.1016/j.marpol.2016.04.051.
- Martin, J.H., Knauer, G.A., Karl, D.M., Broenkow, W.W., 1987. VERTEX: Carbon cycling in the northeast Pacific. *Deep-Sea Res. Part A* 34, 267–285.
- Martínez Arbizu, P., Haeckel, M., 2015. RV SONNE Fahrtbericht / Cruise Report SO239: EcoResponse Assessing the Ecology, Connectivity and Resilience of Polymetallic Nodule Field Systems, Balboa (Panama) – Manzanillo (Mexico,) 11.03.–30.04.2015 (Report No. doi:10.3289/GEOMAR_REP_NS_25_2015). GEOMAR Helmholtz-Zentrum für Ozeanforschung, Kiel, Germany.
- Mero, J. L., 1965. The Mineral Resources of the Sea. Elsevier Oceanography Series 1, 312 pp.
- Mewes, K., Mogollón, J.M., Picard, A., Rühlemann, C., Kuhn, T., Nöthen, K., Kasten, S., 2014. Impact of depositional and biogeochemical processes on small scale variations in nodule abundance in the Clarion-Clipperton Fracture Zone. *Deep-Sea Res. Part I: Oceanogr. Res. Pap.* 91, 125–141. doi:10.1016/j.dsr.2014.06.001.
- Mewes, K., Mogollón, J.M., Picard, A., Rühlemann, C., Eisenhauer, A., Kuhn, T., Ziebis, W., Kasten, S., 2016. Diffusive transfer of oxygen from seamount basaltic crust into overlying sediments: An example from the Clarion–Clipperton Fracture Zone. *Earth Planet. Sci. Lett.* 433, 215–225. doi:10.1016/j.epsl.2015.10.028.
- Miljutin, D.M., Miljutina, M.A., Martínez Arbizu, P., Galeron, J., 2011. Deep-sea nematode assemblage has not recovered 26 years after experimental mining of polymetallic nodules (CCFZ, Pacific). *Deep-Sea Res. Part I: Oceanogr. Res. Pap.* 58, 885–897.

- Mogollón, J.M., Mewes, K., Kasten, S., 2016. Quantifying manganese and nitrogen cycle coupling in manganese-rich, organic carbon-starved marine sediments: Examples from the Clarion-Clipperton fracture zone. *Geophys. Res. Lett.* 43, 2016GL069117. doi:10.1002/2016GL069117
- Mohn, C., Beckmann, A., 2002. The upper ocean circulation at Great Meteor Seamount. *Ocean Dynamics* 52, 179–193. doi:10.1007/s10236-002-0017-4.
- Müller, P.J., 1977. CN ratios in Pacific deep-sea sediments: Effect of inorganic ammonium and organic nitrogen compounds sorbed by clays. *Geochim. Cosmochim. Acta* 41, 765–776. doi:10.1016/0016-7037(77)90047-3.
- Müller, P.J., Mangini, A., 1980. Organic carbon decomposition rates in sediments of the Pacific manganese nodule belt dated by ²³⁰Th and ²³¹Pa. *Earth Planet. Sci. Lett.* 51, 94–114. doi:10.1016/0012-821X(80)90259-9.
- Müller, P.J., Suess, E., 1979. Productivity, sedimentation rate, and sedimentary organic matter in the oceans – I. Organic carbon preservation. *Deep-Sea Res. Part A. Oceanogr. Res. Pap.* 26, 1347–1362. doi:10.1016/0198-0149(79)90003-7.
- Müller, P.J., Hartmann, M., Suess, E., 1988. The chemical environment of pelagic sediments. In: *The Manganese Nodule Belt of the Pacific Ocean: Geological Environment, Nodule Formation, and Mining Aspects* (eds. Halbach, P., Friedrich, G., von Stackelberg, U.). Enke, Stuttgart, 70–90.
- Murray, J., Renard, A.F., 1891. Deep-sea deposits (based on the specimens collected during the voyage of HMS Challenger in the years 1872 to 1876). Report on the scientific results of the voyage of H.M.S. Challenger during the years 1873–76; John Menzies and Co., Edinburgh, United Kingdom.
- Murray, J.W., Grundmanis, V., 1980. Oxygen Consumption in Pelagic Marine Sediments. *Science* 209, 1527–1530. doi:10.1126/science.209.4464.1527.
- Murray, J.W., Kuivila, K.M., 1990. Organic matter diagenesis in the northeast Pacific: transition from aerobic red clay to suboxic hemipelagic sediments. *Deep-Sea Res. Part A. Oceanogr. Res. Pap.* 37, 59–80. doi:10.1016/0198-0149(90)90029-U.
- Nöthen, K., Kasten, S., 2011. Reconstructing changes in seep activity by means of pore water and solid phase Sr/Ca and Mg/Ca ratios in pockmark sediments of the Northern Congo Fan. *Mar. Geol.* 287, 1–13. doi:10.1016/j.margeo.2011.06.008.
- Park, C.B., Clark, D.S., 2002. Rupture of the Cell Envelope by Decompression of the Deep-Sea Methanogen *Methanococcus jannaschii*. *Appl. Environ. Microbiol.* 68, 1458–1463.
- Redfield, A.C., 1934. On the proportions of organic derivations in sea water and their relation to the composition of plankton. In: *James Johnstone Memorial Volume* (ed. Daniel, R.J.). University Press of Liverpool, 176–192.
- Revsbech, N.P., 1989. An oxygen microsensor with a guard cathode. *Limnol. Oceanogr.* 34, 474–478. doi:10.4319/lo.1989.34.2.0474.
- Røy, H., Kallmeyer, J., Adhikari, R.R., Pockalny, R., Jørgensen, B.B., D'Hondt, S., 2012. Aerobic Microbial Respiration in 86-Million-Year-Old Deep-Sea Red Clay. *Science* 336, 922–925. doi:10.1126/science.1219424.
- Rühlemann, C., Kuhn, T., Wiedicke, M., Kasten, S., Mewes, K., Picard, A., 2011. Current status of manganese nodule exploration in the German license area. Proc. of the 9th ISOPE Conference, Maui, 168–173.

- Seeberg-Elverfeldt, J., Schlüter, M., Feseker, T., Kölling, M., 2005. Rhizon sampling of porewaters near the sediment-water interface of aquatic systems. *Limnol. Oceanogr. Methods* 3, 361–371. doi:10.4319/lom.2005.3.361.
- Smith, C.R., De Leo, F.C., Bernardino, A.F., Sweetman, A.K., Arbizu, P.M., 2008. Abyssal food limitation, ecosystem structure and climate change. *Trends in Ecology & Evolution* 23(9), 518–528.
- Soetaert, K., Meysman, F., 2012. Reactive transport in aquatic ecosystems: Rapid model prototyping in the open source software R. *Environmental Modelling & Software* 32, 49–60. doi:10.1016/j.envsoft.2011.08.011.
- Soetaert, K., Petzoldt, T., & Setzer, R. W., 2010. Solving differential equations in R: package deSolve. *J. Statistical Software* 33(9), 1–25.
- von Stackelberg, U., Beiersdorf, H., 1987. Manganese nodules and sediments in the equatorial North Pacific Ocean. *Geol. Jahrb. D* 87.
- von Stackelberg, U., Beiersdorf, H., 1991. The formation of manganese nodules between the Clarion and Clipperton fracture zones southeast of Hawaii. *Mar. Geol.* 98, 411–423. doi:10.1016/0025-3227(91)90113-I.
- Stanley, D.J., Taylor, P.T., 1977. Sediment transport down a seamount flank by a combined current and gravity process. *Mar. Geol.* 23, 77–88.
- Suess, E., 1980. Particulate organic carbon flux in the oceans – surface productivity and oxygen utilization. *Nature* 288, 260–263. doi:10.1038/288260a0.
- Theyer, F., Mayer, L. A., Scotia, N., Barron, J. A., 1985. 33. THE EQUATORIAL PACIFIC HIGH-PRODUCTIVITY BELL ELEMENTS FOR A SYNTHESIS OF DEEP SEA DRILLING PROJECT LEG 85 RESULTS1.
- Turnewitsch, R., Reyss, J.-L., Chapman, D.C., Thomson, J., Lampitt, R.S., 2004. Evidence for a sedimentary fingerprint of an asymmetric flow field surrounding a short seamount. *Earth Planet. Sci. Lett.* 222, 1023–1036. doi:10.1016/j.epsl.2004.03.042.
- Turnewitsch, R., Lahajnar, N., Haeckel, M., Christiansen, B., 2015. An abyssal hill fractionates organic and inorganic matter in deep-sea surface sediments. *Geophys. Res. Lett.* 42, 7663–7672. doi:10.1002/2015GL065658.
- Tyrell, T., 1999. The relative influences of nitrogen and phosphorus on oceanic primary production. *Nature* 400, 525–531.
- Vanreusel, A., Hilario, A., Ribeiro, P.A., Menot, L., Arbizu, P.M., 2016. Threatened by mining, polymetallic nodules are required to preserve abyssal epifauna. *Sci. Rep.* 6, 26808. doi:10.1038/srep26808.
- Wegorzewski, A.V., Kuhn, T., 2014. The influence of suboxic diagenesis on the formation of manganese nodules in the Clarion Clipperton nodule belt of the Pacific Ocean. *Mar. Geol.* 357, 123–138. doi:10.1016/j.margeo.2014.07.004.
- Wessel, P., W. H. F. Smith, R. Scharroo, J. Luis, and F. Wobbe, 2013. Generic Mapping Tools: Improved Version Released, *EOS Trans. AGU* 94(45), 409–410. doi:10.1002/2013EO450001.
- Whittaker, J., Goncharov, A., Williams, S., Müller, R. D., Leitchenkoy, G., 2013. Global sediment thickness dataset updated for the Australian-Antarctic Southern Ocean, *Geochem. Geophys. Geosyst.* doi:10.1002/ggge.20181.

- Wishner, K.F., Ashjian, C.J., Gelfman, C., Gowing, M.M., Kann, L., Levin, L.A., Mullineaux, L.S., Saltzman, J., 1995. Pelagic and benthic ecology of the lower interface of the Eastern Tropical Pacific oxygen minimum zone. *Deep-Sea Res. Part I: Oceanogr. Res. Pap.* 42, 93–115. doi:10.1016/0967-0637(94)00021-J.
- Xu, G., Lavelle, J.W., 2017. Circulation, hydrography, and transport over the summit of Axial Seamount, a deep volcano in the Northeast Pacific. *J. Geophys. Res. Oceans* 122, 5404–5422. doi:10.1002/2016JC012464.
- Ziebis, W., McManus, J., Ferdelman, T., Schmidt-Schierhorn, F., Bach, W., Muratli, J., Edwards, K.J., Villinger, H., 2012. Interstitial fluid chemistry of sediments underlying the North Atlantic gyre and the influence of subsurface fluid flow. *Earth Planet. Sci. Lett.* 323–324, 79–91. doi:10.1016/j.epsl.2012.01.018
- Zonneveld, K.A.F., Versteegh, G.J.M., Kasten, S., Eglinton, T.I., Emeis, K.C., Huguet, C., Koch, B.P., de Lange, G.J., Middelburg, J.J., Mollenhauer, G., Prahl, F.G., Rethemeyer, J., Wakeham, S.G., 2010. Selective preservation of organic matter in marine environments; processes and impact on the sedimentary records. *Biogeosciences* 7, 483–511.

CHAPTER III:

Calcium phosphate control of REY patterns of siliceous-ooze-rich deep-sea sediments from the central equatorial Pacific

Sophie A. L. Paul^{a,*}, Jessica B. Volz^b, Michael Bau^a, Male Köster^b, Sabine Kasten^{b,c}, Andrea Koschinsky^a

^a Jacobs University Bremen, Department of Physics and Earth Sciences, Bremen, Germany
(corresponding author: s.paul@jacobs-university.de, Tel.: +49 421 200 3228)

^b Alfred Wegener Institute Helmholtz Centre for Polar and Marine Research, Bremerhaven, Germany

^c University of Bremen, Faculty of Geosciences, Klagenfurter Strasse, Bremen, Germany

Manuscript published in *Geochimica et Cosmochimica Acta* 251 (2019) 56–72;
doi:10.1016/j.gca.2019.02.019

Abstract

Rare earth elements and yttrium (REY) are often used as proxies for (paleo)environmental conditions and for the reconstruction of element sources and transport pathways. Many geological systems are well described with respect to the behavior of REY but deep-sea sediments with their manifold processes impacting the sediment during early diagenesis leave some questions about the origin and development of the shale-normalized REY (REY_{SN}) patterns unanswered. Here we report REY data for sediment solid phase and pore water from the upper 10 m of deep-sea sediments from the Clarion-Clipperton Zone (CCZ) in the central equatorial Pacific. The solid-phase REY profiles show highest concentrations at depth below 5–8 m. The REY_{SN} patterns show an enrichment in middle REY (MREY) (La_{SN}/Gd_{SN} between 0.35 and 0.60; Gd_{SN}/Yb_{SN} between 1.19 and 1.47) and either no or negative Ce_{SN} and Y_{SN} anomalies (i.e. chondritic to sub-chondritic Y/Ho ratios between 24.7 and 28.7). Based on correlation analyses of bulk sediment element concentrations and sequential extractions, we suggest that a Ca phosphate phase controls the distribution and the patterns of REY in these silty clay pelagic sediments rich in siliceous ooze. The MREY enrichment develops at the sediment-water interface and intensifies systematically with depth. The negative Ce_{SN} anomaly intensifies with depth possibly because Ce is mostly bound to Mn and Fe (oxyhydr)oxides. Therefore, Ce concentrations remain relatively constant throughout the sediment core, while its trivalent REY neighbors are mostly hosted by the Ca phosphate phase that continuously incorporates REY from ambient pore waters. The non-redox-sensitive trivalent REY concentrations increase with depth, producing or enhancing a negative Ce_{SN} anomaly through coupled substitution of REY^{3+} and Na^+ for Ca^{2+} . The solid-phase REY_{SN} pattern is therefore determined by the pore-water REY_{SN} pattern and not suitable for paleoceanographic interpretation. The similarity of the pore-water and solid-phase REY_{SN} patterns suggests, however, that only minor fractionation occurs during REY incorporation into the Ca phosphate crystal structure.

1. Introduction

Rare earth elements (REE) encompass the lanthanide series from La to Lu in the periodic table, 15 elements with atomic numbers 57–71. They are useful proxies for environmental conditions and processes because of their similar physico-chemical properties and geochemical behavior (e.g., Elderfield and Greaves, 1982; Cantrell and Byrne, 1987; Toyoda et al., 1990). The REE are exclusively trivalent in the natural environment, with the exception of Ce and Eu which also occur in the tetra- and divalent state, respectively. Yttrium, which is exclusively trivalent and of almost the same ionic size as its geochemical twin Ho, is often combined with the REE as the REY. The trivalent REE's ionic radii decrease with increasing atomic number which is referred to as the “lanthanide contraction” (Seitz et al., 2007 and references therein). These minimal changes in ionic radii are sufficient to lead to fractionation of the REY during incorporation into crystal lattices or during chemical complexation. Depending on the ionic radii, either the light REY (LREY; La–Nd), middle REY (MREY; Sm–Dy) or heavy REY (HREY; Ho–Lu) may be preferentially scavenged or mobilized, which then leads to fractionation and, therefore, distinct signatures in shale-normalized (SN) REY patterns (e.g., Cantrell and Byrne, 1987; Elderfield, 1988). From these patterns, past and present environmental conditions, such as ancient seawater composition, the influence of hydrothermal activities on sediments, and sediment provenance can be inferred (German et al., 1990; Bau and Dulski, 1999; Bright et al., 2009; Viehmann et al., 2015; Kashiwabara et al., 2018). Several studies have targeted the distribution of REY in Pacific pelagic sediments (e.g., Elderfield et al., 1981; Glasby et al., 1987; Toyoda et al., 1990; Toyoda and Tokonami, 1990; Toyoda and Masuda, 1991; Kon et al., 2014); mostly focusing on surface sediments and interactions of surface sediments with manganese nodules. To our knowledge, less attention has been paid so far to the impact of early diagenesis in deeper subsurface sediments on REY (e.g., Soyol-Erdene and Huh, 2013; Zhang et al., 2016). Understanding the behavior of REY during early diagenesis is important, however, when aiming to use them as proxies for paleoenvironmental reconstructions (Bright et al., 2009; Trotter et al., 2016).

In modern seawater, dissolved HREY show an enrichment in the REY_{SN} patterns (Fig. 1) because the LREY are preferentially scavenged by particles in the water column (e.g., Elderfield, 1988; Chen et al., 2015). Except for Ce, REY concentrations increase with water depth (e.g., Alibo and Nozaki, 1999; Chen et al., 2015), because the REY are bound to particulate matter in surface waters and released at greater depth when particles dissolve or are microbially degraded. In contrast, dissolved Ce concentrations decrease with depth (e.g., Chen et al., 2015) because of Ce³⁺ oxidation and Ce⁴⁺ fixation at sinking particles in oxic

seawater. Once Ce^{3+} is oxidized to Ce^{4+} , it is usually less mobile and will participate less in exchange reactions (Goldberg et al., 1963; Piper, 1974b; de Baar et al., 1985; Sholkovitz et al., 1993; Bau and Dulski, 1996; Bau and Koschinsky, 2009) unless the solution is rich in complexing agents such as CO_3^{2-} or siderophores (e.g., Möller and Bau, 1993; Bau et al., 2013; Kraemer et al., 2015). This may lead to the development of a negative Ce_{SN} anomaly in the REY_{SN} pattern of the solution (e.g., seawater) and a positive Ce_{SN} anomaly in the solid material (e.g., marine hydrogenetic Fe-Mn crusts and nodules; Fig. 1) (Piper, 1974b; Elderfield and Greaves, 1982; Kasten et al., 1998). If, however, sinking Mn and/or Fe (oxyhydr)oxide particles with positive Ce_{SN} anomaly cross a redox-cline and enter anoxic seawater, these particles re-dissolved and produce anoxic seawater with a positive Ce_{SN} anomaly (de Baar et al., 1988; Bau et al., 1997). Note however, that formation of the negative Ce_{SN} anomaly of oxic seawater is not confined to the marine environment, but already develops during terrestrial weathering and characterizes the truly dissolved REY_{SN} patterns of river waters (Merschel et al., 2017; Pourret and Tuduri, 2017). Besides Ce, Eu can also show pronounced positive or negative anomalies in REY_{SN} patterns, as observed, for example, in high-temperature hydrothermal environments (Michard, 1989). In low-temperature systems such as pelagic sediments, however, Eu is present in the trivalent oxidation state (Bau, 1991). After particle deposition, diagenesis can impact the distribution of the REY in the sediment and pore water leading to deviations from the seawater REY_{SN} pattern (Haley et al., 2004; Bright et al., 2009; Abbott et al., 2016; Trotter et al., 2016). The alteration of the pore-water REY pool during early diagenesis is also suggested by the distinct Nd isotopic composition of pore waters, which differs from that of bottom water (Abbott et al., 2016; Du et al., 2016). The dominant biogeochemical process during early diagenesis in the upper 10 m of Clarion-Clipperton Zone (CCZ) sediment was shown to be aerobic respiration followed by denitrification and Mn oxide reduction (Mogollón et al., 2016; Volz et al., 2018). For the sediments of the CCZ typical oxygen penetration depths of 1–4.5 m have been reported (Rühlemann et al., 2011; Mewes et al., 2014; Mogollón et al., 2016; Volz et al., 2018). Recent studies have also shown that in some areas within the CCZ the sediments overlying the oceanic crust are fully oxic. This phenomenon was explained by sediment alteration by upward diffusing oxygen from the basaltic crust in which low-temperature circulation of seawater occurs, especially in areas close to seamounts and faults (Mewes et al., 2016; Kuhn et al., 2017). This shows that deep oxygen penetration depths on meter scales prevail in the study area. Previous studies of REY in sediments from the central Pacific concluded that biogenic Ca phosphates such as apatite, are the main hosts of REY in Pacific deep-sea sediments and that the biogenic phosphate is largely composed of fish

debris, i.e. bones and teeth (e.g., Elderfield et al., 1981; Toyoda et al., 1990; Toyoda and Tokonami, 1990; Toyoda and Masuda, 1991; Kon et al., 2014). Unaltered conodonts, defined by a low color index (Epstein et al., 1977; Bertram et al., 1992), fish debris and marine phosphorites show REY_{SN} patterns similar to those of seawater, i.e. La_{SN}/Yb_{SN} << 1, a negative Ce_{SN} anomaly and positive anomalies of La_{SN}, Gd_{SN}, and Y_{SN}, i.e. superchondritic Y/Ho ratios (marine phosphorite, Fig. 1). Altered conodonts, defined by a high color index (Epstein et al., 1977; Bertram et al., 1992), and fish debris show higher REY concentrations and MREY enrichment, deviating from the seawater REY_{SN} pattern (Fig. 1). Several authors suggested coupled substitution as the process for REY uptake into apatite as Ca²⁺ in Ca phosphates is easily replaced through coupled substitution by a REE³⁺ together with a monovalent element of similar size (e.g., Na⁺) (Elderfield et al., 1981; Rønsbo, 1989; Jarvis et al., 1994).

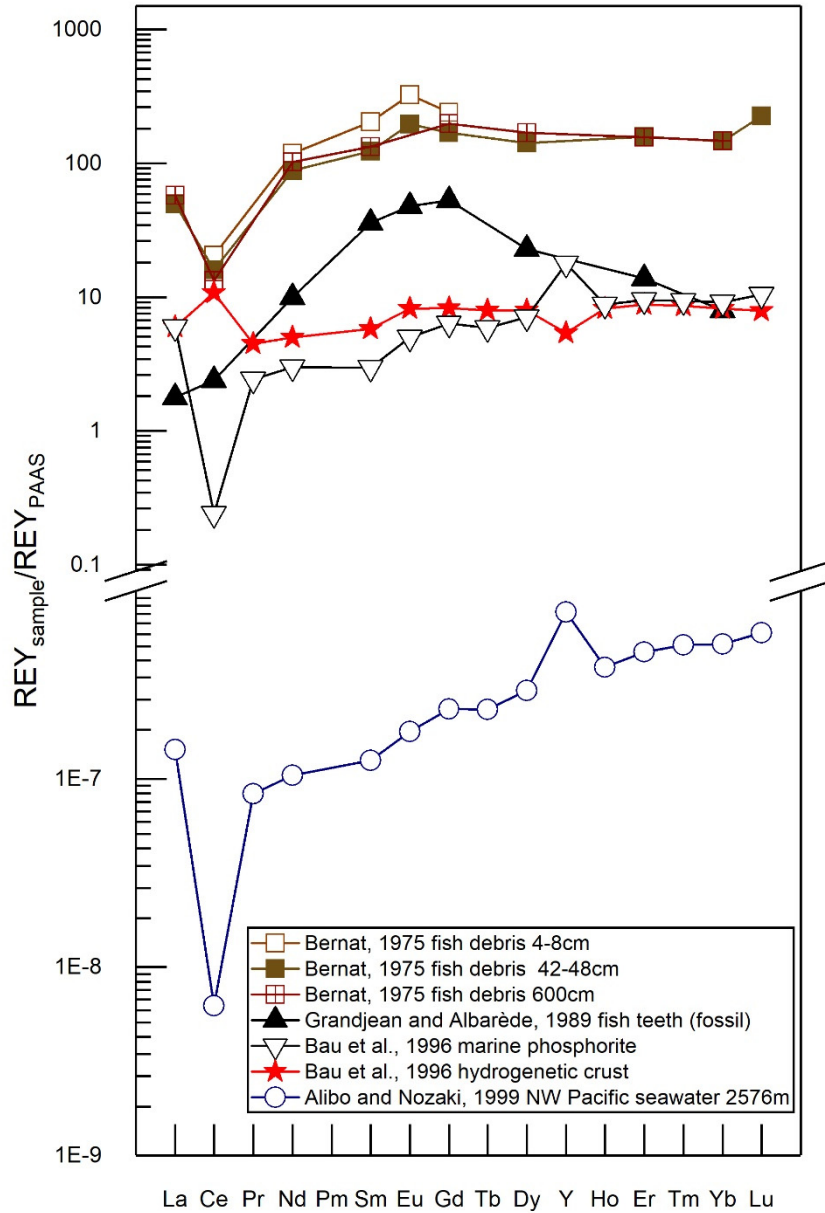


Figure 1: REY_{SN} patterns of fish debris, fossil fish teeth, marine phosphorite, hydrogenetic Fe-Mn crust, and seawater (PAAS from Taylor and McLennan, 1985, except Dy from McLennan, 1989). (See above-mentioned references for further information.)

In this contribution we aimed at elucidating the controls on the REY distribution in CCZ sediments as well as the processes that might have caused the alteration of primary REY_{SN} patterns during oxic and suboxic early diagenesis.

2. Samples and Methods

2.1 Geological setting of the study site

The CCZ is located in the central equatorial Pacific and bracketed by the Clarion Fracture Zone to the North and the Clipperton Fracture Zone to the South. Both faults extend west-southwest from the East Pacific Rise (EPR), where the Pacific crust forms and moves west from the spreading center. The oceanic crust in the CCZ dates from the Late Cretaceous (~ 100 Ma) to the Miocene (~ 5 Ma) (Eittreim et al., 1992; Barckhausen et al., 2013). Surface sediments are dominated by siliceous ooze (mostly radiolarians and diatoms) and silty mud (Berger, 1974; Müller et al., 1988; International Seabed Authority, 2010; Mewes et al., 2014; Kuhn, 2015; Volz et al., 2018). The preservation of calcareous material in marine sediments depends on the carbonate compensation depth (CCD) below which calcite dissolves. Today, the seafloor is mostly below the CCD located at approx. 4500 m water depth (e.g., Berger, 1970; Lyle, 2003) and the surface sediments show carbonate concentrations < 1 wt% (Sharma, 2017). The particulate organic carbon (POC) flux is low and varies from 1 mg C_{org} m⁻² d⁻¹ in the northern part of the study area and 1.5 mg C_{org} m⁻² d⁻¹ in the central to western part to 2 mg C_{org} m⁻² d⁻¹ in the south-eastern part (Lutz et al., 2007; Vanreusel et al., 2016; Volz et al., 2018). Total organic carbon (TOC) contents in the surface sediments range from 0.2–0.45 wt% and under approx. 1 m depth, the TOC contents are below 0.2 wt% (Volz et al., 2018). Sedimentation rates are between 0.2 and 1.15 cm kyr⁻¹ for the uppermost 50 cm of the sediment (Mewes et al., 2014; Mogollón et al., 2016; Volz et al., 2018).

Based on extrapolation of the sedimentation rate in the surface sediment (Volz et al., 2018), the cores represent approx. 2.5–3 million years of depositional history. For core 194GC, we assume relatively constant sedimentation rates of 0.2 cm kyr⁻¹ (Volz et al., 2018) and no hiatus is visible. Therefore, the age at the core bottom at ca. 580 cm could be around 2.9 Ma. The high sedimentation rate of 1.15 cm kyr⁻¹ for core 87GC might be due to sediment focusing or the delivery of material from nearby seamounts (Volz et al., 2018). An extrapolation of the sedimentation rate for the entire core length is therefore not appropriate. Beryllium isotope dating for cores from the nearby BGR contractor area show that sedimentation rates were about 0.3 cm kyr⁻¹ until 2 Ma and significantly lower before (0.04 cm kyr⁻¹) (Mewes et al., 2014). The core bottom age could be between 2.6 and 3.6 Ma. Since core 165GC shows a hiatus at 790 cm, dating is even more complicated. Based on the sedimentation rate determined for surface sediments (0.64 cm kyr⁻¹, Volz et al., 2018) the sediment at 790 cm depth could be 1.2 Ma. Below the hiatus, lower TOC and higher Mn contents suggest the deposition of different

material, that was associated with the closure of the Panama Isthmus 2.5 Ma for sediment with a similar composition below a hiatus at 420 cm in the BGR contractor area (Mewes et al., 2014).

2.2 Sampling

The sediment samples were taken during RV SONNE cruise SO239 in 2015 in the CCZ as part of the BMBF-EU Joint Programming Initiative Healthy and Productive Seas and Oceans (JPI Oceans) pilot action “Ecological Aspects of Deep-Sea Mining (EcoMining/MiningImpact)” (Fig. 2; Martinez Arbizu and Haeckel, 2015). A gravity corer (GC) was used for the retrieval of sediment cores of up to 10 m length. A total of six GCs were selected for REY analyses of which three cores with extensive carbonate or metalliferous (Fe, Mn) layers were excluded for this study. The sediment cores 87GC and 165GC were retrieved in two European contract areas for the exploration of manganese nodules, namely the area of the eastern European consortium IOM (InterOceanMetal) and the French IFREMER area (Institut Français de Recherche pour l'Exploitation de la Mer), respectively (Table 1). Furthermore, core 194GC originates from the third of the nine Areas of Particular Environmental Interest (APEIs) located around the contractor areas, which is excluded from any mining activities (Table 1). The solid phase was sampled in 20–100 cm intervals for REY analyses, taking approx. 2 cm layers for one subsample. An upward diffusion of oxygen from the basaltic crust as explained in the introduction is expected to occur at sites 87GC and 165GC, indicated by decreasing dissolved Mn^{2+} concentrations in the pore water in both cores at depth, suggesting oxidation of Mn^{2+} at ~ 20 m and 7 m, respectively (Volz et al., 2018).

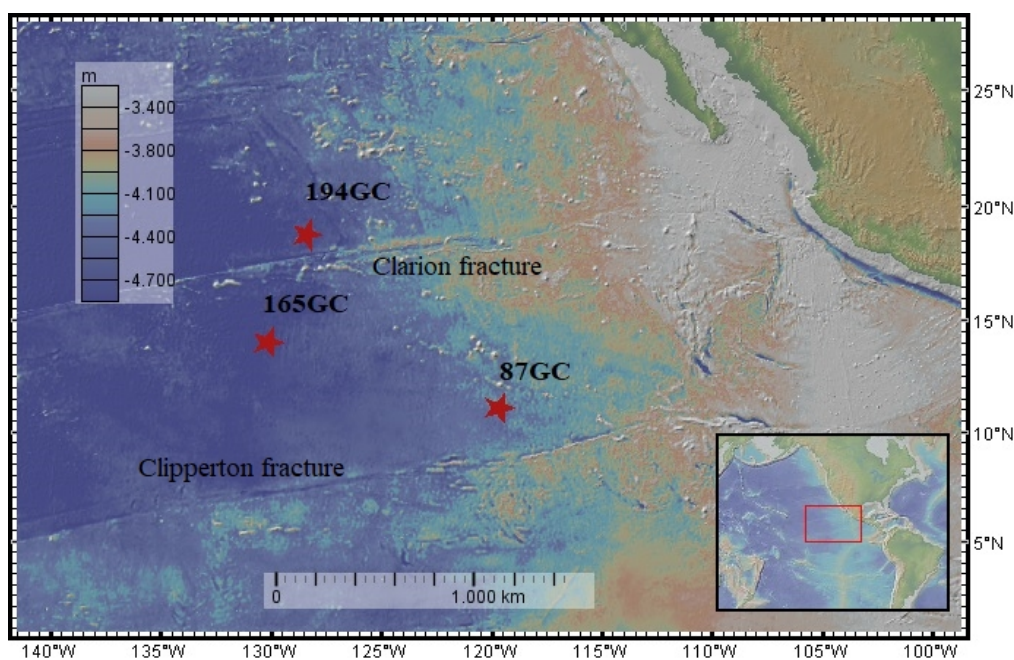


Figure 2: Core sampling locations of 87GC and 165GC in the CCZ and of 194GC north of the Clarion Fracture Zone. The map was created using GeoMapApp.

Pore-water samples were obtained by filling sediment into acid pre-cleaned 50 mL centrifuge vials and centrifuging at 2800 rpm for 40 min. Afterwards, the supernatant was filtered through 0.1 M suprapure hydrochloric acid (HCl) and deionized water pre-cleaned 0.2 μm cellulose acetate syringe filters. The filter size was chosen because it is a common physical size limit for the dissolved fraction. Samples were immediately acidified with 1 μL suprapure HCl (30%) per 1 mL sample.

Table 1: Overview of GC sampling sites.

| Sample ID | Location | Core length (cm) | Contractor area | Water depth (m) |
|-----------|----------------------------|------------------|-----------------|-----------------|
| 87GC | 11° 04.54' N 119° 39.83' W | 942 | IOM | 4436 |
| 165GC | 14° 02.63' N 130° 08.39' W | 927 | IFREMER | 4922.7 |
| 194GC | 18° 47.54' N 128° 22.33' W | 576 | APEI 3 | 4815.5 |

In addition to REY analyses of bulk acid digestions described in Section 2.3, REY were analyzed in six sequential extraction solutions corresponding to an upper and lower part in each core and scanning electron microscope (SEM) analyses are presented for two samples of core 165GC. Pore-water REY data could only reliably be reported for three samples of the lower part of 194GC.

2.3 Analytical methods

Total acid digestions were performed at the Alfred Wegener Institute Helmholtz Centre for Polar and Marine Research (AWI), Marine Geochemistry laboratory in Bremerhaven, Germany. 50 mg of freeze-dried and homogenized sediments were digested in the MARS Xpress (CEM) microwave system at 230 °C after the procedure by Nöthen and Kasten (2011) and Volz et al. (2018). A mixture of 3 mL sub-boiling distilled 65% nitric acid (HNO_3), 2 mL sub-boiling distilled 30% HCl, and 0.5 mL suprapur® 40% hydrofluoric acid (HF) was used for the treatment. The digested solutions were evaporated and the solid residue subsequently re-dissolved in 5 mL 1 M HNO_3 at 200 °C. After full digestion, the residue was filled up to 50 mL with 1 M HNO_3 .

Major element concentrations (Al, Ca, Fe, K, Mn, Na, P, S, Ti) were determined at AWI, Bremerhaven, using an IRIS Intrepid ICP-OES, Thermo Elemental. The NIST-2702 was used as certified reference material (CRM). Analytical accuracy was within 7% for all elements ($n=12$) and the relative standard deviation (RSD) within 3% except for Na (9%) (for details see Table EA1). For the REY and Ba, ICP-MS measurements were carried out at Jacobs University

Bremen (JUB), using a Perkin Elmer Nexion 350x, for pore-water analyses coupled to an Apex Q (ESI) for improved background and sensitivity. A multi-element standard containing 2 ppb of all measured elements was used for external calibration and the linearity was checked with a 4 ppb multi-element standard. A mixture of the elements Ru, Re, and Bi was used as an internal standard to correct for sample matrix effects and machine drift. Blanks were four to five orders of magnitude below REY sediment concentrations for LREY and two to three orders of magnitude lower for HREY. Due to low REY concentrations in some pore waters relative to blank concentrations (e.g., in several samples from shallow depths), it was not possible to determine REY data for all porewater samples. Interferences from Ba and some LREE oxides and hydroxides were corrected for by experimentally determined oxide and hydroxide yields of molecular ions. NIST-2702 from the AWI digestions (n=10) and BHVO-2 from a different acid digestion performed at JUB (n=1) were used to check machine performance. Accuracy was within 4% for both CRMs except for Y (6%) in BHVO-2 and Sm (6%) and Nd (9%) in NIST-2702. The RSD was within 7% for NIST-2707 and 5% for BHVO-2 (see Supplementary Tables EA2 and EA3 for details; for more information see, for example, Bau et al. (2018)). To the best of our knowledge no CRM REY data exist for pore waters. Results for bulk sediments were corrected for the porewater salt matrix according to Kuhn (2013) and Volz et al. (2018) to adjust for impairment of pore-water constituents on the sediment composition. These correction factors range between 3 and 13% but the correction does not affect the REY_{SN} patterns.

2.4 Reporting

The C_{eSN} anomaly was calculated after Bau and Dulski (1996):

$$\frac{C_e}{C_{e^*}} = \frac{C_e(SN)}{(0.5 \cdot La(SN) + 0.5 \cdot Pr(SN))} \quad (1)$$

REY concentrations in mg/kg were used for anomaly calculations of dry bulk sediment, leachates, and pore water. For convenience, we refer to a negative C_{eSN} anomaly if C_{eSN}/C_{eSN}^{*} is < 0.9, to no anomaly if it is between 0.9 and 1.1, and to a positive anomaly if it is > 1.1.

2.5 Sequential extraction

In order to differentiate between sedimentary Mn and Fe (oxyhydr)oxides as well as different solid-phase Fe binding forms, an extraction protocol was developed combining the methods presented by Koschinsky and Halbach (1995), Koschinsky et al. (2001), and Poulton and Canfield (2005) (Table 2; Köster, 2017). The sequential extractions were performed at room temperature (ca. 22 °C) at AWI, Bremerhaven. Fresh sediment portions equivalent to

100 mg dry sediment were treated with 10 mL of the respective extraction reagent for specific reaction times (Table 2). After centrifugation (4000 rpm, 5 min), the supernatant leaching solution was filtered through a 0.2 μm polyethersulfone membrane for analysis while the residue was subsequently treated with the next extraction reagent (Table 2). Solution carry-over was minimized as much as possible during filtration but to avoid loss of sediment it could not be prevented in all samples. The sediment was not washed with deionized water between leaching steps. Comparison of bulk sediment data with the results of the combined leaching steps resulted in up to 25% higher concentrations of major elements and REY for the added sequential extraction steps, which might be due to error propagation of sequential extraction measurements or due to contamination. Results above 100%, however, only occurred for one sample (87GC-827 cm). Iron, Mn, and P were measured at AWI, Bremerhaven and REY at JUB as described in the analytical methods section above.

Table 2: Leaching scheme for the sequential extraction of Mn and Fe (oxyhydr)oxides (adapted from Köster, 2017).

| Step | Associated mineral phase | Extraction reagent | Extraction time [h] | pH | Method after |
|------|---|--|---------------------|-----|--------------|
| I | Pore-water and sorbed Fe, Mn Carbonate-associated Fe, Mn | 1 M Na-acetate | 24 | 4.5 | 1 |
| II | Easily reducible Mn oxides | 0.1 M hydroxylamine-HCl | 2 | 2 | 2,3 |
| III | Easily reducible Fe oxides | 1 M hydroxylamine-HCl | 48 | | 1 |
| IV | Reducible Fe oxides | Na-dithionite (50 g/L)/0.2M Na-citrate solution | 2 | 4.8 | 1 |
| V | Magnetite | 0.2 M NH_4 -oxalate/0.17 M oxalic acid | 6 | | 1 |

1: Poulton and Canfield, 2005

2: Koschinsky and Halbach, 1995

3: Koschinsky et al., 2001

2.6 Scanning electron microscopy

Untreated, fresh, carbon-coated sediment samples were analyzed by scanning electron microscopy (SEM) combined with a QUANTAX energy-dispersive X-ray spectrometer (EDS, Bruker) at AWI, Bremerhaven. The spectral imaging tool ESPRIT HyperMap was used to create quantitative element maps (scan time: 25 min) including Ba, Ca, Fe, Mn, P, S, Sr, As, Cr, Ni, Zn, Mo.

3. Results

3.1 Bulk solid-phase major elements

The major elements show a mostly conservative profile in the upper meters of all sediment cores (Fig. 3). The detrital elements such as Al, K, and Ti decrease at depth, while Fe, Mn, Ba, S, Ca, and P, concentrations increase: in 87GC below ca. 730 cm depth, in 165GC below ca. 790 cm depth and in 194GC below ca. 500 cm depth (Fig. 3). At these depths, the sediments also display a color change from tan to dark brown (Fig. 3). The northernmost core, 194GC, shows overall higher concentrations of Al, K, Fe, and Ti but lower Ba and S concentrations than the cores 87GC and 165GC. Except for Ce, REY concentrations also increase with depth (Fig. 3).

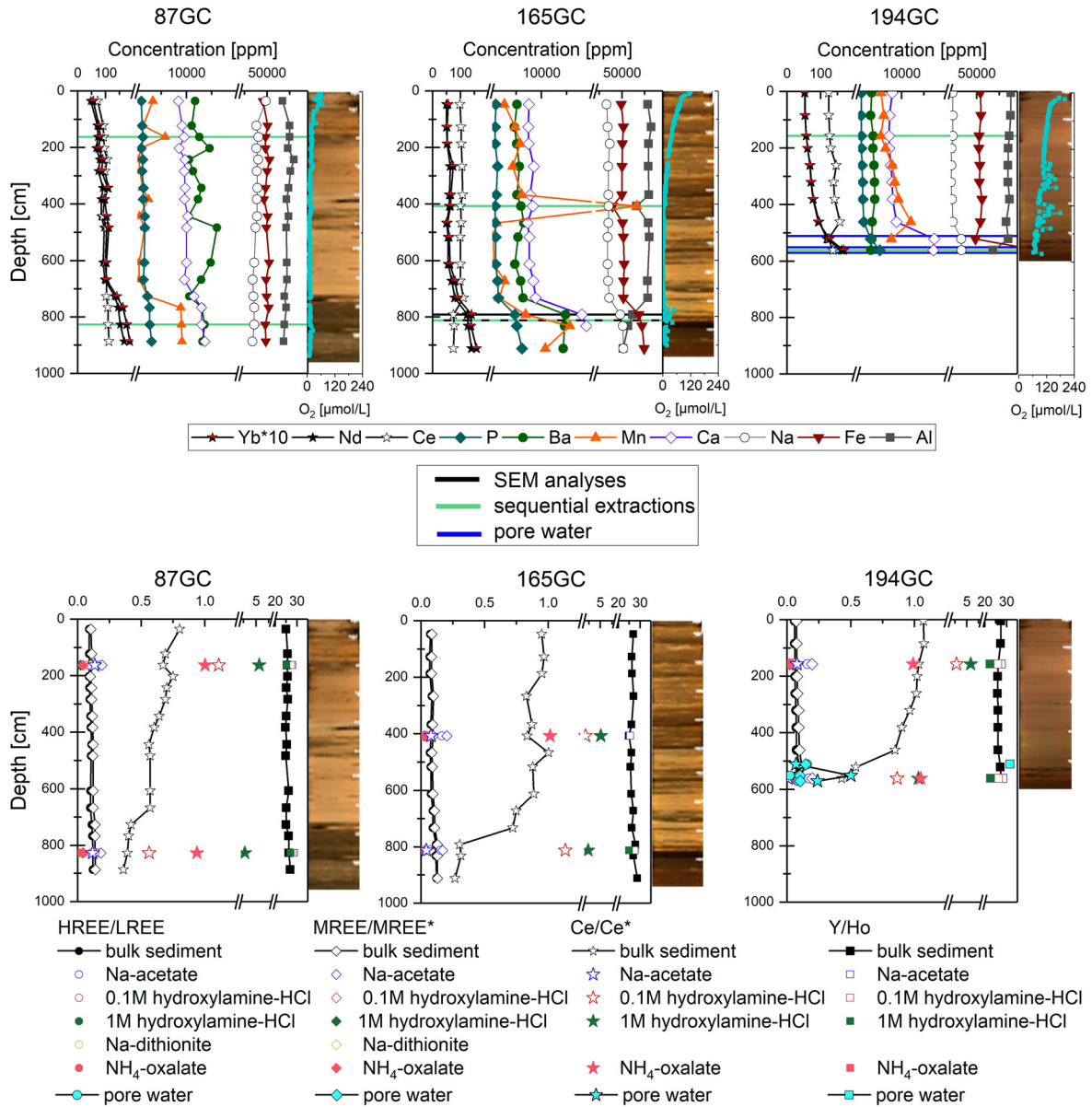


Figure 3: Top: Depth profiles of selected major elements and three representative REY (Ce, Nd, Yb). Yb concentrations were multiplied by 10 to fit the scale of the figure. Core pictures depict that the sediment gets darker with depth in all cores and has thin dark layers throughout. Oxygen data from Volz et al. (2018). Bottom: Depth profiles of REY parameters HREE/LREE, MREE/MREE*, Ce/Ce*, and Y/Ho for bulk sediment, the sequential extraction solutions (Na-dithionite only for HREE/LREE and MREE/MREE* for 194GC-561 cm), and pore water (Y/Ho only for 194GC-511 cm).

$$\text{HREE/LREE} = (\text{Ho} + \text{Er} + \text{Tm} + \text{Yb} + \text{Lu}) / (\text{La} + \text{Ce} + \text{Pr} + \text{Nd}).$$

$$\text{MREE/MREE}^* = (\text{Sm} + \text{Eu} + \text{Gd} + \text{Tb} + \text{Dy}) / ((\text{La} + \text{Ce} + \text{Pr} + \text{Nd} + \text{Ho} + \text{Er} + \text{Tm} + \text{Yb} + \text{Lu}) * 2).$$

3.2 REY concentrations and shale-normalized patterns of bulk solid phase

Total REY concentrations (Σ REY) in the CCZ vary between ca. 270 ppm and 850 ppm. REY concentrations increase two- to threefold at depth in all cores: in 87GC at 700 cm, in 165GC at 790 cm and in 194GC at 460 cm. The depth of this REY concentration increase appears to coincide with the sediment color change to dark brown at the lower core end.

The REY_{SN} patterns (Fig. 4) show an enrichment of MREY and HREY over the LREY and a slight MREY enrichment: La_{SN}/Gd_{SN} ratios range between 0.35 and 0.60 and Gd_{SN}/Yb_{SN} ratios between 1.19 and 1.47. There is a trend of increasing Gd/Yb ratio and decreasing La/Gd ratio with depth, i.e. the enrichment of MREY over LREY and HREY increases. Most layers show a negative Ce_{SN} anomaly with Ce_{SN}/Ce_{SN}* ratio from 0.27 to 0.89 and significant variation between cores and with depth. The negative Ce_{SN} anomaly develops (165GC and 194GC) or becomes increasingly negative with depth (87GC) (Fig. 5). It also increases in size with increasing P concentration (Fig. 5). Pore-water REY_{SN} patterns show slight MREY enrichment and a negative Ce_{SN} anomaly, similar to the sediments (Fig. 6).

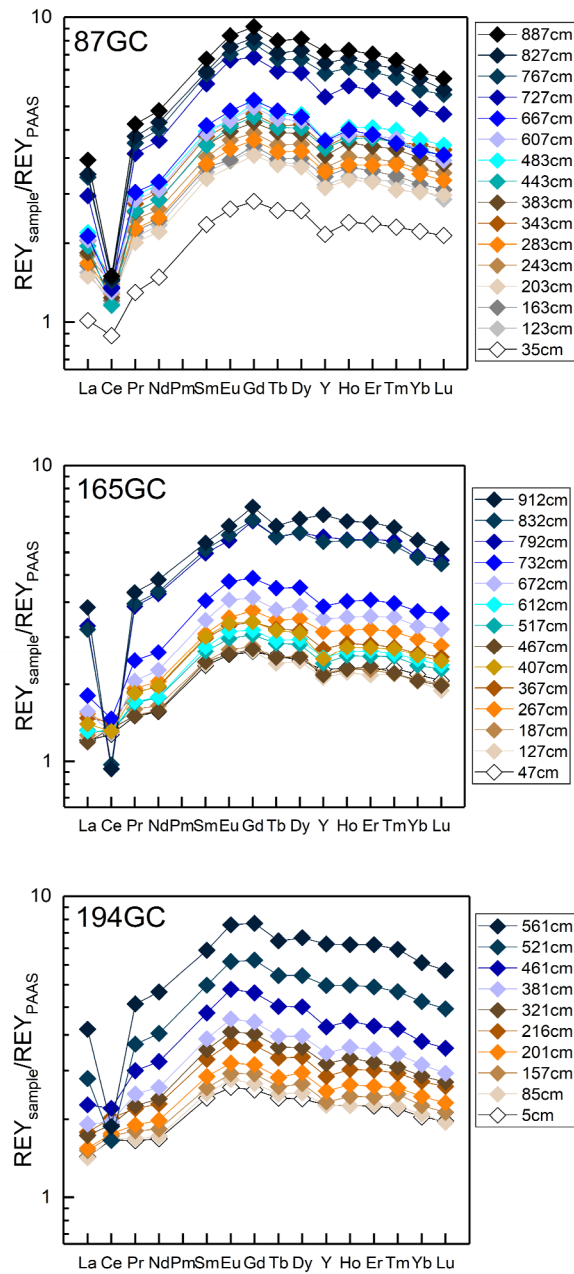


Figure 4: REY_{SN} patterns of selected sediment layers of the three cores investigated in this study (PAAS from Taylor and McLennan, 1985, except for Dy from McLennan, 1989). All cores and layers show a slight enrichment of MREY and HREY and most layers display a negative Ce_{SN} anomaly.

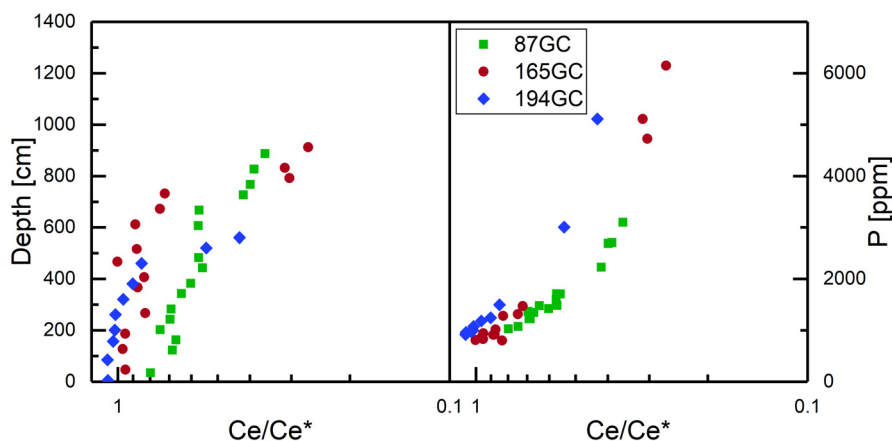


Figure 5: Increase of negative Ce_{SN} anomaly with depth and with increasing P concentration. See equation (1) in chapter 2.4 for the calculation of the Ce_{SN} anomaly.

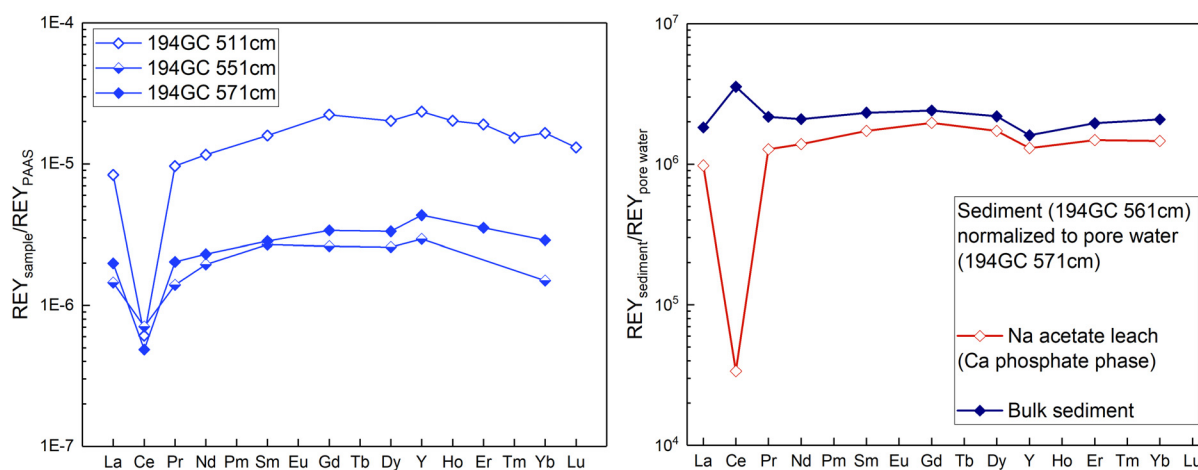


Figure 6: Left: REY_{SN} patterns of pore waters from 194GC (PAAS from Taylor and McLennan, 1985, except Dy from McLennan, 1989). All patterns show an enrichment of the MREY and a pronounced negative Ce_{SN} anomaly. Right: Bulk sediment and Ca phosphate phase normalized to pore water.

3.3 Sequential extraction

Selected samples were leached according to the extraction protocol by Köster (2017; Table 2). All REY except Ce are predominantly leached in the first step with Na-acetate (Fig. 7, Supplementary data 3). Cerium is partially leached in the Na-acetate (1–31% compared to bulk sediment), and 0.1 M hydroxylamine-HCl (4–22% compared to bulk sediment) steps but mostly in the 1 M hydroxylamine step (35–59% compared to bulk sediment). Small portions of REY are leached in the Na-dithionite and NH_4 -oxalate steps. Similar to the REY except Ce, P is predominantly dissolved in the Na-acetate step, while Mn is mostly leached in the 0.1 M hydroxylamine-HCl step and Fe in the Na-dithionite step (Fig. 7; for details see Supplementary data 3).

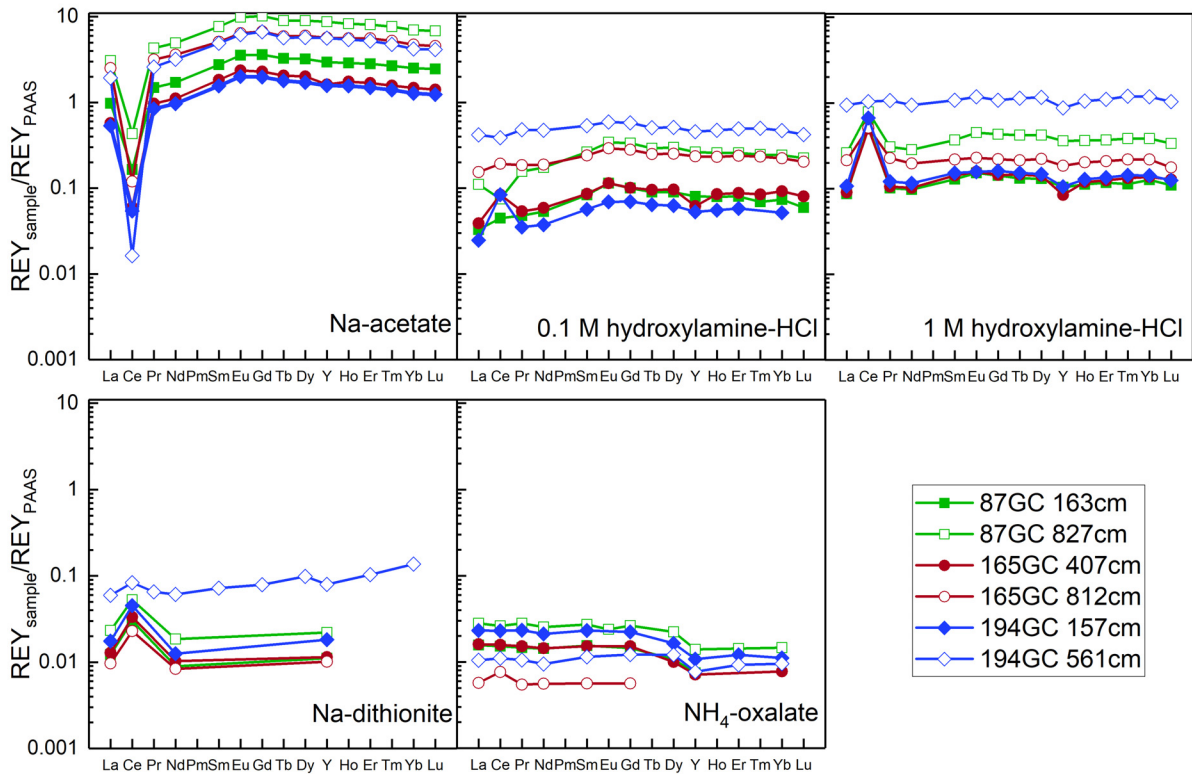


Figure 7: REY_{SN} patterns of sequential leaching solutions of selected sediment layers from the three cores (PAAS from Taylor and McLennan, 1985, except Dy from McLennan, 1989). From each core one sample from an upper and lower part of the core was selected. Some data points are missing for the Na-dithionite and NH_4 -oxalate patterns due to concentrations below the LOQ.

The Na-acetate REY_{SN} patterns show a marked negative Ce_{SN} anomaly (0.01–0.13) in all layers and a slight MREY enrichment (Fig. 7). The 0.1 M hydroxylamine-HCl REY_{SN} patterns display positive Ce_{SN} anomalies (1.1–2.8) in the upper parts of the cores and slightly negative Ce_{SN} anomalies in the lower parts of cores 87GC and 194GC (0.56 and 0.86) or a slightly positive Ce_{SN} anomaly (1.13) in core 165GC. For the 1 M hydroxylamine-HCl REY_{SN} pattern, we can discern pronounced positive Ce_{SN} anomalies (2.33–5.83) – except for 194GC-561 cm (1.03) – and sub-chondritic Y/Ho ratios, i.e. negative Y_{SN} anomalies, in all layers (19.3–27.0; Fig. 7). Positive Ce_{SN} anomalies are also found in the Na-dithionite extracts (Fig. 7). In the REY_{SN} patterns of the NH_4 -oxalate leach, only 165GC-812 cm has a positive Ce_{SN} anomaly (1.38), the other layers show no anomaly.

3.4 Scanning electron microscopy

Scanning electron microscopy (SEM) images show that P and Ca are associated and occur in the same particles (Fig. 8). Particles are of ca. 20-100 μm size.

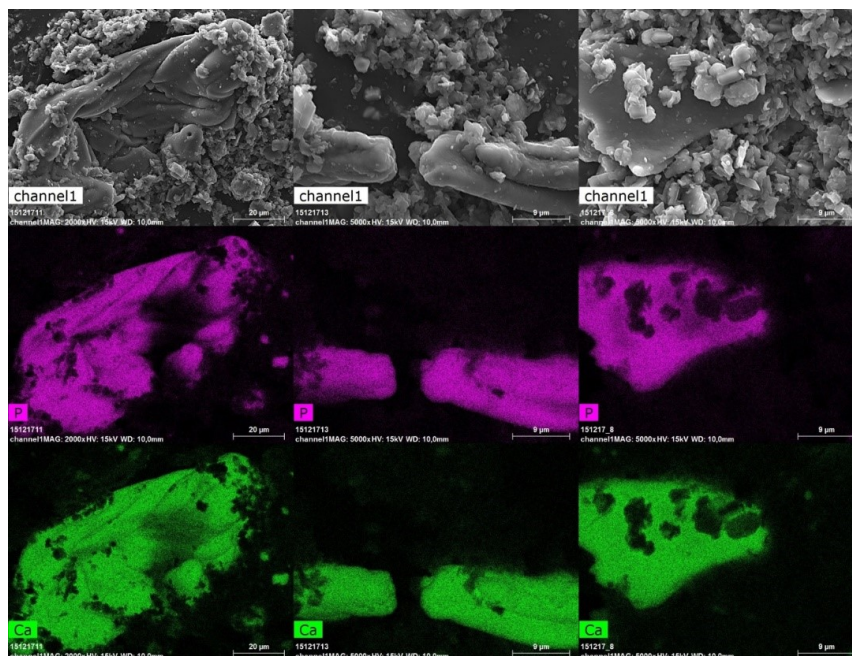


Figure 8: Scanning electron microscopy (SEM) images of particles rich in phosphorus and calcium; examples from layers 165GC-792 cm (left and middle) and 165GC-812 cm (right).

4. Discussion

4.1 Control on REY composition of bulk sediment

All cores show a positive correlation of P and Ca (Fig. 9), suggesting the presence of calcium phosphates (“apatite”: $\text{Ca}_5[(\text{F}, \text{Cl}, \text{OH})](\text{PO}_4)_3$) in the sediment. Overall concentrations of “apatite”, however, are low. Phosphorous and Nd, the latter representing the REY, correlate positively in all cores (Fig. 9); correlations of REY with P are better than with Ca, because Ca is also associated with other minerals, e.g., Ca carbonates. Exceptions can be seen for cores 165GC (792–912 cm) and 194GC (521–561 cm) where P concentrations are higher while REY concentrations remain in the same range as in the other samples (Fig. 9). Even if the outliers are included in the linear regression, the correlation of REY with P within each core is still positive and better than for REY with other elements (Table 3), suggesting that Ca phosphates may also be the dominating REY-controlling phase at depth in these cores.

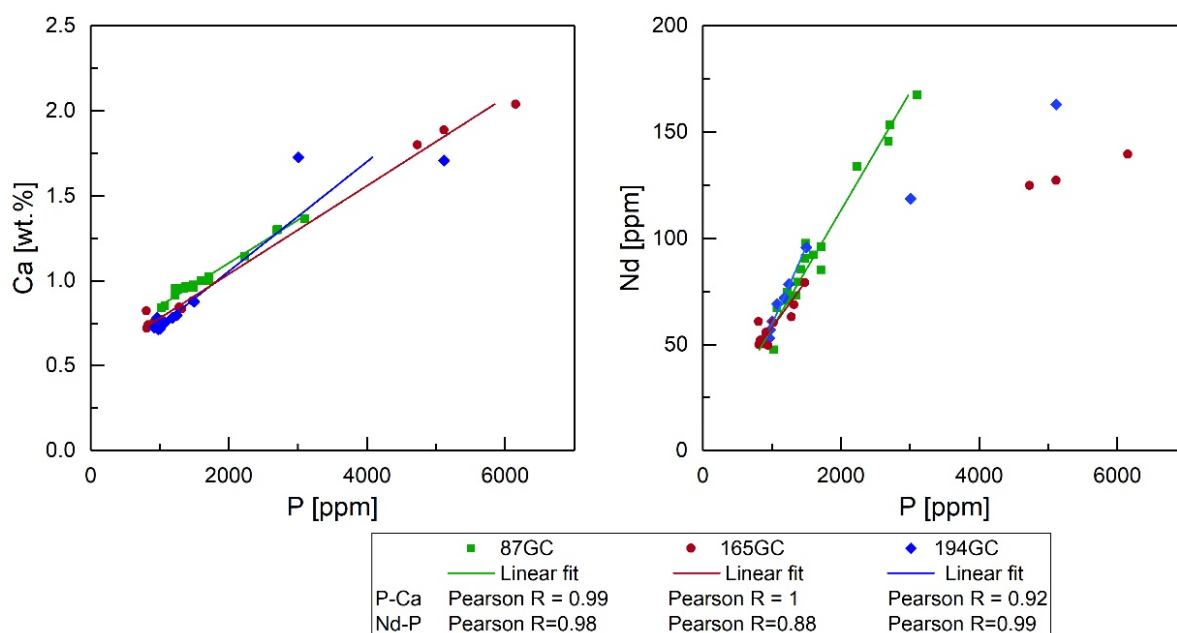


Figure 9: Left: P vs. Ca plot. Right: P vs. Nd plot. Nd represents the REY. Linear regression lines for the cores in both graphs and Pearson R correlation coefficients in the legend. All cores show positive correlations of P and Ca and P and Nd. The deepest layers in 165GC (792–912 cm) and 194GC (521–561 cm) deviate from the linear regression due to a lower Nd/P ratio (for further discussion see text).

As all cores show either no or even negative correlations between the REY and the detritus indicators Al, K, and Ti (Table 3), detrital minerals are unlikely to host a significant fraction of the total REY budget of the sediments. There are positive correlations of the REY with Fe and Mn (Table 3) but if the REY were controlled by hydrogenous Fe or Mn (oxyhydr)oxides, they should show positive Ce_{SN} (Toyoda et al., 1990) and negative Y_{SN} anomalies (Bau and Koschinsky, 2009), which our REY_{SN} patterns do not (compare Figs. 1 and 4). Additionally, an impact of the redox zonation on the REY_{SN} patterns could be expected if the REY were bound to Mn oxides, because Mn oxides dissolve in the suboxic layer. Yet, there is no change in REY_{SN} patterns between oxic and suboxic sections of the sediments (see Figs. 3 and 4) and the REY_{SN} patterns are similar in the three cores regardless of the redox zonation. For core 165GC, there is a strong positive correlation of Nd with Ba and S (Table 3), which could be an indicator that barite ($BaSO_4$) is a REY-controlling phase. Due to size constraints, however, the REY fit better into the crystal structure of Ca phosphate than Ba sulfate (Guichard et al., 1979). The same holds true for other biogenic minerals, such as calcite and opal (Piper, 1974a; Elderfield et al., 1981; Grandjean and Albarède, 1989, and references therein).

Table 3: Pearson R correlation coefficients of Nd, representing the REY, with various major elements of the bulk sediment digestions. Data correlated for the completely analyzed core sections.

| Core | Ca | P | Al | Ti | K | Fe | Mn | Ba | S |
|-------|------|------|-------|-------|-------|------|------|-------|-------|
| 87GC | 0.97 | 0.98 | -0.46 | -0.35 | -0.71 | 0.16 | 0.73 | 0.18 | -0.18 |
| 165GC | 0.99 | 0.98 | -0.91 | -0.97 | -0.85 | 0.92 | 0.07 | 0.97 | 0.97 |
| 194GC | 0.91 | 0.97 | -0.87 | -0.93 | -0.88 | 0.78 | 0.89 | -0.34 | 0.86 |

Besides the positive correlation of REY and P, the Nd/P ratio (Fig. 10) remains similar with depth, further supporting the association of REY with phosphates. Exceptions are the deep layers in cores 165GC and 194GC (Fig. 10), which also deviated from the linear regression line (Fig. 9). Phosphorus and Ca concentrations are extremely high at the bottom of those two cores, potentially due to increased deposition of apatite material because of increased surface water productivity (Toyoda et al., 1990). The REY, however, did not become enriched to the same degree as P and Ca and are present in similar concentrations as in core 87GC at the bottom. This suggests that REY uptake into the apatite was limited by REY availability in the pore water.

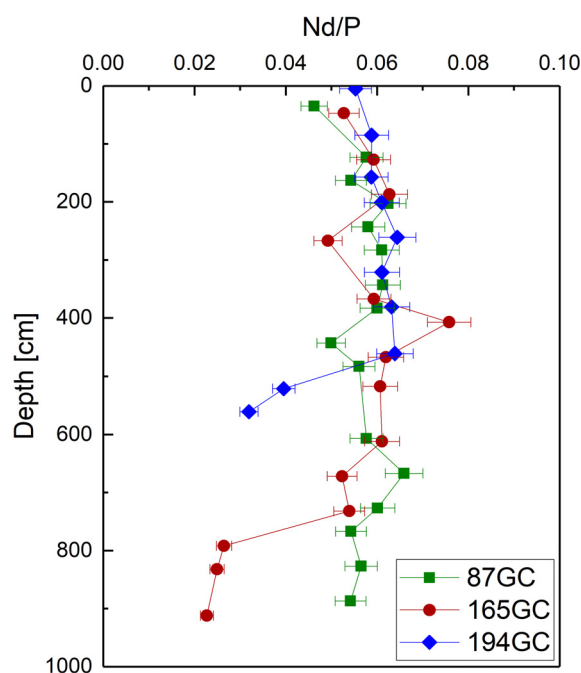


Figure 10: Nd/P ratio of bulk sediment at different depths for cores 87GC, 165GC and 194GC. Nd represents the REY. Similar values with depth suggest that the ratio of REY to P stays the same except in the deep layers (165GC 792–912 cm and 194GC 521–561 cm) where lower Nd/P values suggest that P is more enriched than the REY. The relative uncertainty of Nd/P based on NIST-2702 digestions ($n = 12$ for P and $n = 10$ for Nd) and measurements is 6.27%.

The SEM results validated the association of Ca and P (Fig. 8), and together with the REY-P correlations (Fig. 9) as well as the constant Nd/P ratio with depth (Fig. 10), suggest that Ca phosphates are the overall dominating REY host phase in these sediments over ca. 1000 km and irrespective of redox conditions, corroborating the conclusions of other studies (e.g., Elderfield et al., 1981; Toyoda et al., 1990; Toyoda and Tokonami, 1990; Toyoda and Masuda, 1991; Ziegler et al., 2007; Kon et al., 2014).

4.2 Sequential extraction: REY in phosphate phases

Sequential extraction protocols specifically designed for phosphorous leaching (Ruttenberg, 1992; Filippelli and Delaney, 1996; Schenau and De Lange, 2000) show comparable steps to the sequential extraction used in this study. The 1 M Na-acetate solution (step 1 in Table 2) has been frequently used to extract biogenic and authigenic phosphate (step 3 in Ruttenberg, 1992; Filippelli and Delaney, 1996; Schenau and De Lange, 2000). Fish debris (apatite present as $\text{Ca}_5\text{OH}(\text{PO}_4)_3$) can be converted to authigenic carbonate fluorapatite (CFA; $\text{Ca}_5\text{F}(\text{PO}_4)_3$) during diagenesis through substitution of fluoride for hydroxyl ions, which makes the apatite more stable and difficult to dissolve (Schenau and De Lange, 2000, and references therein). Reducible Fe-oxides such as goethite and hematite were leached in the Na-dithionite extraction (Poulton and Canfield, 2005), step 4 in this study. Sodium-dithionite was also used to extract Fe-bound P by Ruttenberg (1992), Filippelli and Delaney (1996), and Schenau and De Lange (2000) as step 2 of their sequential extraction protocols. Hydrogenous Mn and Fe oxides except for goethite were leached using 0.1 M hydroxylamine-HCl in acetic acid by Toyoda and Masuda (1991) for REE leaching, which is comparable to steps 2 and 3 of the leaching protocol by Köster (2017; Table 2).

Approximately 40–100% of REY except Ce and ca. 80–100% of P occur in the Na-acetate extraction fraction compared to the bulk sediment. Exceptions are 194GC-157 cm and -561 cm with 59% and 54% P, respectively, and 87GC-827 cm, with basically all P and REY in the Na-acetate fraction. Differences in Na-acetate extraction can be seen for the different REY groups: LREY ca. 40–100%, MREY ca. 70–100%, and HREY ca. 60–100%. In the remaining steps, ca. 2–20% are leached in the 0.1 M and 1 M hydroxylamine-HCl steps each, and ca. 0–1% in each the Na-dithionite and NH_4 -oxalate steps. For further details see Supplementary data 3. This suggests that P is predominantly present in the phosphate phase and that the REY are associated with this P phase. Only Ce is associated with oxidic Mn and Fe phases (0.1 and 1 M hydroxylamine-HCl extract, 4–22% and 35–59% Ce, respectively). The REY in the phosphate fraction (Fig. 7 Na-acetate) control the overall REY_{SN} patterns in our

samples (Fig. 4), revealing that both the pronounced negative Ce_{SN} anomaly and the MREY enrichment can be attributed to this phase.

4.3 Alteration of biogenic Ca phosphates during early diagenesis

The impact of diagenetic processes on REY patterns in apatite has been extensively discussed for fossil apatite and the applicability of its REY patterns for paleoceanographic reconstructions (Grandjean and Albarède, 1989; Reynard et al., 1999; Bright et al., 2009; Chen et al., 2015; Trotter et al., 2016). Various researchers (Wright et al., 1984; Grandjean and Albarède, 1989; Reynard et al., 1999) proposed that the seawater REY pattern could be recorded in biogenic apatite without fractionation, which would lead to a preservation of the seawater pattern (in modern seawater: negative Ce_{SN} anomaly, HREY enrichment). This is, however, not what we see in the samples in this study. The REY_{SN} patterns presented here are rather similar to altered fish debris (compare Figs. 1 and 4), a main component of which is biogenic Ca phosphate (Elderfield et al., 1981; Toyoda et al., 1990; Kon et al., 2014). Unaltered Ca phosphates, i.e. fish teeth and marine phosphorites (Fig. 1), show a seawater-derived pattern. Once they get altered after deposition, (i) the positive Y_{SN} anomaly disappears, (ii) the REY concentrations increase, and (iii) the MREY enrichment develops.

The missing positive Y_{SN} anomaly clearly shows that the Ca phosphates did not get their REY_{SN} pattern from seawater, which typically has super-chondritic Y/Ho weight-ratios (e.g., Y/Ho ca. 47–77, Bau and Dulski, 1994; 54–56, Alibo and Nozaki, 1999) in contrast to slightly sub-chondritic to chondritic Y/Ho ratios of 24.7–28.7 from the Ca phosphates in this study.

Apatite in living organisms has REY concentrations that are too low to explain the enrichment in sedimentary Ca phosphate. Moreover, the deviation from the seawater REY_{SN} pattern points to a post-mortem modification during diagenesis (Wright et al., 1984; Elderfield and Pagett, 1986; Reynard et al., 1999; Bright et al., 2009; Auer et al., 2017). In addition, Toyoda and Tokonami (1990) showed that REE accumulation in apatite is too slow to reach the high concentrations found in sedimentary apatite before burial and that the REY must have been scavenged from ambient pore waters. Pore-water REY concentrations are one to two orders of magnitude higher than seawater concentrations (Alibo and Nozaki, 1999; Soyol-Erdene and Huh, 2013), contributing to the observed enrichment of REY in diagenetic Ca phosphates. Therefore, transport to the seafloor by settling particles carrying REY, such as organic particles or Mn- and Fe-(oxyhydr)oxides, and release to the pore water during organic matter degradation or desorption from Mn and Fe (oxyhydr)oxides under oxic conditions is more likely (Elderfield et al., 1981; Kashiwabara et al., 2018). At the seafloor, REY get incorporated into Ca

phosphates (Elderfield et al., 1981; Grandjean and Albarède, 1989; Haley et al., 2004; Chen et al., 2015) through $\text{Ca}^{2+} \leftrightarrow \text{REY}^{3+}$ ion exchange (Elderfield et al., 1981; Auer et al., 2017). The fact that Na concentrations in the bulk sediment increase at the same depth as REY concentrations (Fig. 3) corroborates the suggestion that coupled substitution of Ca^{2+} by REY^{3+} and Na^+ is the uptake mechanism of REY into apatite. As there is only minor fractionation of the REY during their incorporation into Ca minerals, such as Ca carbonates and phosphates by coupled substitution (Webb and Kamber, 2000; Nothdurft et al., 2004), this suggests that ambient pore water is the source of REY in the Ca phosphates. The matching pore-water REY_{SN} patterns for core 194GC and the bulk sediments (compare Figs. 4 and 6) as well as the smooth line when normalizing the Ca phosphate phase from the Na-acetate leaching step to pore water (Fig. 6), confirms that the trivalent REY are incorporated without major fractionation. The MREY enrichment of the Ca phosphates is therefore also taken over from the pore water. The Ca phosphate signature, hence, develops at the sediment-water interface during aerobic early diagenesis. Because of the low sedimentation rate in pelagic sediments, the settled particles stay at the seafloor surface for centuries to millennia and undergo degradation and dissolution during early diagenesis (Elderfield et al., 1981; Reynard et al., 1999). The MREY enriched pattern is already developed at shallow depth (194GC-5 cm), which shows that the shift away from the seawater pattern happens at the sediment-water interface and the pattern intensifies with depth because of slightly better fitting ionic radii of the MREY than the LREY and HREY into the Ca phosphate crystal structure when substituting REY for Ca (Wright, 1990). The increase of the MREY enrichment with depth is a sign of further diagenetic overprint. The MREY enrichment in recent sediments is much less pronounced than in fossil apatites (e.g., Grandjean and Albarède, 1989; compare Figs. 1 and 4). All three observed shifts away from the seawater REY_{SN} pattern, i.e. sub-chondritic Y/Ho, high $\sum \text{REY}$ concentrations, and MREY enrichment, prove that Ca phosphates are not a suitable archive for paleoceanographic reconstructions for e.g., seawater chemistry. Our results corroborate previous findings that fossil apatite REY patterns resemble modern pore-water patterns (Trotter et al., 2016).

4.4 Pore-water REY pool

As we described in Section 4.3 that the MREY enrichment in the bulk sediment and Ca phosphate phase is pore water derived, it remains to discern how the MREY enrichment in the pore water develops as well as what the REY source to the pore water is. A variety of solid-phase fractions could be potential sources of REY to the pore water: Ca carbonates and phosphates, POC, Mn and Fe (oxyhydr)oxides. REY in the pore water cannot originate from Ca carbonate or Ca phosphate phases because those show a primary seawater REY_{SN} pattern

(HREY enrichment) (Webb and Kamber, 2000; Nothdurft et al., 2004; Bau and Alexander, 2006) when they get deposited and would release that seawater pattern to the pore water, which we do not see for the 194GC pore-water REY_{SN} patterns (Fig. 6). The MREY enriched pore-water pattern could result from the release of REY from decaying POC at the sediment-water interface that are subsequently stabilized by dissolved organic carbon (DOC) and lead to a MREY enriched pattern in the dissolved pore-water pool (Tang and Johannesson, 2010; Soyol-Erdene and Huh, 2013). There is, however, too little TOC (< 0.2-0.45 wt% Volz et al., 2018) to explain the extent of REY increase. In addition, the highest REY concentrations in the pore water and the bulk solid phase should then be visible in the upper 1 m of the cores where highest TOC concentrations prevail. The aging of Mn and Fe (oxyhydr)oxides may release REY to the pore water, also under oxic conditions (Kashiwabara et al., 2018). Fe-Mn crusts, for example, show a decrease in REY concentrations from the outside to the inside (Bau et al., 1996), i.e. with increasing age the concentration decreases, pointing to a release of REY from the solid phase. This might be due to progressive crystallization of the amorphous precipitates and exclusion of REY from the crystal lattices, similar to dehydration (e.g., Koschinsky and Halbach, 1995). These REY are then redistributed to phosphate phases via pore water. The REY source also has to have insoluble Ce(IV) compounds, because Ce is not released to the Ce-depleted pore water (Fig. 6). This is typical for Mn and Fe (oxyhydr)oxides, at the surface of which Ce³⁺ can be oxidized to Ce⁴⁺ (Takahashi et al., 2007; Bau and Koschinsky, 2009; Kashiwabara et al., 2018). The Mn and Fe phases of the sequential extraction (0.1 and 1 M hydroxylamine-HCl) also show slight MREY enrichment (Fig. 7), suggesting Mn and Fe phases as the REY source to the pore water. The released REY can then reach other layers by diffusion (e.g., Elderfield and Sholkovitz, 1987) so that the REY redistribution should not only be restricted to the layer where the REY originate from. A REY source might be located at even greater depth from which the REY diffuse upwards.

4.5 Increase of negative Ce_{SN} anomaly with depth

Our Ce_{SN} anomaly values fit well with data from other studies conducted in the Pacific (0.48–0.79: Toyoda and Masuda, 1991). Besides the development of the MREY enrichment and the concentration increase at depth, a decrease of Ce_{SN}/Ce_{SN}* values with depth is observed (Fig. 5).

One aspect that impacts the distribution of Ce_{SN} anomalies is bioproductivity: Negative Ce_{SN} anomalies are found in sediments with higher surface water productivity but not in sediments

underlying less productive surface waters (Toyoda et al., 1990). A fish debris sample from a low bioproductivity area even showed a positive Ce_{SN} anomaly (Toyoda and Masuda, 1991). The primary productivity in the equatorial Pacific Ocean decreases from east to west and coincides with the occurrence of negative Ce_{SN} anomalies in the upper 100 cm of sediment (Toyoda et al., 1990). Following this pattern, low latitudes in the Pacific Ocean display negative Ce_{SN} anomalies and high latitudes show positive Ce_{SN} anomalies, and a shift of negative Ce_{SN} anomalies to no Ce_{SN} anomalies from east to west in surface sediments can be observed (Toyoda et al., 1990). In the eastern core 87GC from this study, Ce_{SN} anomalies in the surface sediments are around 0.8. Farther west and north, away from the equator, cores 165GC and 194GC show no Ce_{SN} anomalies in surface sediments (Fig. 11). At depth, however, both cores (165GC and 194GC) have negative Ce_{SN} anomalies (0.27 and 0.43) similar to core 87GC from the eastern CCZ.

Decreasing Ce/Ce^* values with depth have been found in a 70 m long ODP core from the Central Pacific (26°N, 147.5°W), where they were largely explained by different mineralogy (red clay vs nannofossil ooze) (Ziegler and Murray, 2007). In this study, however, we see a smooth decrease of Ce_{SN}/Ce_{SN}^* values in the upper meters of the cores, but this decrease intensifies with depth (Fig. 11). Layers with similar Ce_{SN}/Ce_{SN}^* values can be seen in the three cores, but they occur at different depths. In core 165GC, the layer with Ce_{SN}/Ce_{SN}^* values of 0.7–0.36 (Fig. 11) is missing which might be due to a hiatus located at 790 cm, which is common in the Late Miocene and Paleo-Pleistocene sections in the CCZ (Johnson, 1972; von Stackelberg and Beiersdorf, 1991; International Seabed Authority, 2010). The transition from lighter to darker sediment at this depth is distinct. There must have been a drastic change in sedimentation rate, non-deposition, or erosion of previously deposited material that lead to the abrupt change visible in the sediment record (Craig, 1979; von Stackelberg and Beiersdorf, 1991; Mewes et al., 2014; Volz et al., 2018). Deposition similar to the other areas studied here must have commenced again afterwards as the major element and REY profiles are in the same range as in cores 87GC and 194GC. The change is visible for other parameters as well: change in sediment color, jump in Ca vs P concentration as well as concentration increases for the other major elements, as well as a change in the MREY pattern (small Gd_{SN} anomaly appears) while it stays the same for all layers in the upper part of core 165GC. The transition at the bottom of core 194GC is much smoother and there is no hiatus in this core. The age at the bottom of the core might still be similar to that at the bottom of core 165GC below the hiatus, but in core 194GC it is due to the low sedimentation rate (0.2 cm kyr⁻¹ compared to 0.64 cm kyr⁻¹ in core 165GC, Volz et al., 2018).

| 87GC | | 165GC | | 194GC | | Color legend |
|------|--------------------------------------|-------|--------------------------------------|-------|--------------------------------------|--------------|
| (cm) | Ce _{SN} /Ce _{SN} * | (cm) | Ce _{SN} /Ce _{SN} * | (cm) | Ce _{SN} /Ce _{SN} * | |
| | | | | 5 | *1.07 | 1.07 |
| | | | | 85 | *1.07 | 1.03 |
| | | | | 157 | *1.03 | 1.02 |
| | | | | 201 | *1.02 | 1 |
| | | | | 261 | *1.02 | 0.97 |
| | | 47 | *0.95 | 321 | *0.96 | 0.96 |
| | | 127 | *0.97 | 381 | *0.9 | 0.95 |
| | | 187 | *0.95 | | | 0.9 |
| | | 267 | 0.83 | | | 0.89 |
| | | 367 | 0.88 | | | 0.88 |
| | | 407 | 0.83 | | | 0.87 |
| | | 467 | *1 | | | 0.85 |
| 35 | 0.8 | 517 | 0.87 | 461 | 0.85 | 0.83 |
| 123 | 0.69 | 612 | 0.89 | | | 0.8 |
| 163 | 0.67 | 672 | 0.75 | | | 0.75 |
| 203 | 0.75 | 732 | 0.72 | | | 0.72 |
| 243 | 0.7 | | | | | 0.7 |
| 283 | 0.69 | | | | | 0.69 |
| 343 | 0.64 | | | | | 0.67 |
| 383 | 0.6 | | | | | 0.64 |
| 443 | 0.56 | | | | | 0.6 |
| 483 | 0.57 | | | | | 0.57 |
| 607 | 0.57 | | | | | 0.56 |
| 667 | 0.57 | | | | | 0.54 |
| | | | | 521 | 0.54 | 0.43 |
| 727 | 0.42 | | | 561 | 0.43 | 0.42 |
| 767 | 0.4 | | | | | 0.4 |
| 827 | 0.39 | | | | | 0.39 |
| 887 | 0.36 | | | | | 0.36 |
| | | 792 | 0.3 | | | 0.31 |
| | | 832 | 0.31 | | | 0.3 |
| | | 912 | 0.27 | | | 0.27 |

Figure 11: Ce/Ce* values for each layer. Ce/Ce* was calculated according to equation (1) in the text. Yellow star symbols denote no Ce_{SN} anomaly. Values decrease with depth in all three cores, starting with different Ce/Ce* values at the top of the sediment cores.

In contrast to all other REY which are sequentially extracted with phosphate in the Na-acetate leaching step, Ce is mostly leached with Mn and Fe phases. Other studies also found REY (except for Ce) in the easily leachable fraction (0.5 mol/L HCl or 0.2 mol/L H₂SO₄) of Pacific sediments (e.g., Kato et al., 2011) and studies of Fe-Mn crusts proved that the trivalent REY are associated with phosphate and/or Fe phases while Ce is linked to Mn phases (De Carlo, 1991) or as found here, with both, the Mn and Fe (oxyhydr)oxide phase (Bau and Koschinsky, 2009). This association of Ce with a different phase than the other REY also indicates that the Ce_{SN} anomaly is also sensitive to concentration variations of the trivalent REY and not only to changes in Ce concentration (De Carlo, 1991). In our samples, the Ce

concentration shows only little change, but the trivalent REY concentrations increase significantly and systematically with depth. The Ce_{SN} anomaly is, therefore, mostly a result of increasing concentrations of trivalent REY, corroborating results of Elderfield et al. (1981) who also found that there is no significant diagenetic remobilization of Ce compared to the other REY.

An explanation for the increase of the Ce_{SN} anomaly with depth is that Ce^{3+} adsorbs to Mn and Fe (oxyhydr)oxides (as we see from the sequential extractions; see also Bau and Koschinsky, 2009) and only then is oxidized at the surface of the metal (oxyhydr)oxides. These Ce^{4+} compounds, however, cannot be released to pore water in the oxic part of the sediment column close to the surface, in contrast to the REY^{3+} . The trivalent REY in the Ce-depleted pore water are later incorporated into the Ca phosphate component, producing negative Ce_{SN} anomalies. Chen et al. (2015) expected the Ce_{SN} anomaly to become smaller with depth as Mn oxides are reduced in the suboxic zone and release Ce. This change, however, cannot be observed in our sample set in which the solid-phase Ce concentration does not increase when conditions become suboxic, i.e. where hydrogen sulfide and oxygen are absent and Mn (IV) and nitrate reduction take place (450 cm 165GC ($O_2 < 10 \mu\text{mol/L}$) and 300 cm 87GC ($O_2 < 20 \mu\text{mol/L}$); and 300 cm 87GC; Volz et al., 2018). This could be explained by the fact that Ce may mostly be bound to clusters of discrete Ce (IV) oxide phases of low solubility or Fe-oxyhydroxides (as indicated by sequential extraction), which were shown to be preserved and not subject to reductive dissolution in the suboxic zone of the CCZ sediments at depths down to ca. 10 m (Volz et al., 2018; Heller et al., 2018).

5. Conclusions

We suggest Ca phosphates as the host phase for REY in siliceous-ooze-rich silty clay sediments in the abyssal Pacific Ocean. The phosphates become overprinted during early diagenesis: a MREY enrichment over the LREY and HREY develops at the sediment-water interface by uptake of REY from pore water, the positive Y_{SN} anomaly disappears, and a negative Ce_{SN} anomaly becomes increasingly negative with depth or develops where no negative Ce_{SN} anomaly is present at the sediment surface. The bulk sediment solid-phase Ce concentrations remain relatively constant, while trivalent REY concentrations increase with depth due to continuous incorporation of REY from the pore water by coupled substitution, creating a larger negative Ce_{SN} anomaly. This is because Ce is mostly bound to Mn and Fe (oxyhydr)oxides as Ce(IV) while the other trivalent REY are bound to Ca phosphates.

The matching pore water, Na-acetate sequential extraction, and bulk solid-phase REY_{SN} patterns show that the apatite takes over the pore-water REY_{SN} pattern with only minor fractionation. Our findings are hence also relevant for paleoceanographic work because biogenic apatites in fossil records are frequently used to reconstruct ancient seawater chemistry. Our results, however – like those of some other studies (Elderfield and Pagett, 1986; Sholkovitz et al., 1989; Toyoda and Tokonami, 1990; Reynard et al., 1999; Bright et al., 2009; Chen et al., 2015) – advise caution when using REY patterns for paleoceanographic reconstructions since the pattern seems to be strongly diagenetically influenced and determined by the pore-water REY pool. Additionally, the negative Ce_{SN} anomaly often interpreted as a sign of oxic seawater in paleoenvironmental reconstructions was produced during early diagenesis in our samples and does not reflect the negative Ce_{SN} anomaly of modern seawater.

Even though we found similar REY patterns and apatite as the REY host phase over large geographic distances of ca. 1000 km, it has to be considered that sediment composition in the study area can be highly variable on different spatial scales. More research is necessary to describe REY behavior during early diagenesis in CCZ sediments with different mineralogy, e.g., extensive carbonate or metalliferous layers.

There is still little knowledge about REY cycling in pore waters and the exchange between pore waters and different sediment fractions. Analyses of the Nd isotopic composition might hence be beneficial to constrain REY sources to deep-sea pore waters.

Acknowledgements

This work was made possible by the captain and crew of RV SONNE and the chief scientist Pedro Martínez Arbizu on cruise SO239 and their help during the sampling campaign. Our appreciation goes to Annika Moje and Inken Preuss from Jacobs University Bremen (the latter now at GEOMAR Kiel) and Ingrid Dohrmann and Ingrid Stimac from the Alfred Wegener Institute Helmholtz Centre for Polar and Marine Research for help during sampling onboard RV SONNE and in the home laboratories. We thank Susann Henkel for help with developing the sequential extraction protocol and Gerhard Kuhn and Ruth Cordelair for providing and helping with the SEM analyses. This work was funded by the German Federal Ministry of Education and Research in the framework of the JPI Oceans project MiningImpact (grant numbers 03F0707F+G). We thank the three reviewers and associate editor Tina van de Flierdt for their helpful comments and suggestions to improve this manuscript.

References

- Abbott, A.N., Haley, B.A., McManus, J., 2016. The impact of sedimentary coatings on the diagenetic Nd flux. *Earth Planet. Sci. Lett.* 449, 217–227. <https://doi.org/10.1016/j.epsl.2016.06.001>.
- Alibo, D.S., Nozaki, Y., 1999. Rare earth elements in seawater: particle association, shale-normalization, and Ce oxidation. *Geochim. Cosmochim. Acta* 63, 363–372.
- Auer, G., Reuter, M., Hauzenberger, C.A., Piller, W.E., 2017. The impact of transport processes on rare earth element patterns in marine authigenic and biogenic phosphates. *Geochim. Cosmochim. Acta* 203, 140–156. <https://doi.org/10.1016/j.gca.2017.01.001>.
- de Baar, H.J.W., Bacon, M.P., Brewer, P.G., Bruland, K.W., 1985. Rare earth elements in the Pacific and Atlantic Oceans. *Geochim. Cosmochim. Acta* 49, 1943–1959.
- de Baar, H.J.W., German, C.R., Elderfield, H., van Gaans, P., 1988. Rare earth element distributions in anoxic waters of the Cariaco Trench. *Geochim. Cosmochim. Acta* 52, 1203–1219.
- Barckhausen, U., Bagge, M., Wilson, D.S., 2013. Seafloor spreading anomalies and crustal ages of the Clarion-Clipperton Zone. *Mar. Geophys. Res.* 34, 79–88.
- Bau, M., 1991. Rare-Earth Element Mobility During Hydrothermal and Metamorphic Fluid Rock Interaction and the Significance of the Oxidation-State of Europium. *Chem. Geol.* 93, 219–230.
- Bau, M., Alexander, B., 2006. Preservation of primary REE patterns without Ce anomaly during dolomitization of Mid-Paleoproterozoic limestone and the potential re-establishment of marine anoxia immediately after the “Great Oxidation Event.” *South African J. Geol.* 109, 81–86.
- Bau, M., Dulski, P., 1999. Comparing yttrium and rare earths in hydrothermal fluids from the Mid-Atlantic Ridge : implications for Y and REE behaviour during near-vent mixing and for the Y/Ho ratio of Proterozoic seawater. *Chem. Geol.* 155, 70–90.
- Bau, M., Dulski, P., 1996. Distribution of yttrium and rare-earth elements in the Penge and Kuruman iron-formations, Transvaal Supergroup, South Africa. *Precambrian Res.* 79, 37–55.
- Bau, M., Dulski, P., 1994. Evolution of the Yttrium-Holmium Systematics of Seawater Through Time. *Mineral. Mag.* 58A, 61–62.
- Bau, M., Koschinsky, A., 2009. Oxidative scavenging of cerium on hydrous Fe oxide: Evidence from the distribution of rare earth elements and yttrium between Fe oxides and Mn oxides in hydrogenetic ferromanganese crusts. *Geochem. J.* 43, 37–47.
- Bau, M., Koschinsky, A., Dulski, P., Hein, J.R., 1996. Comparison of the partitioning behaviours of yttrium, rare earth elements, and titanium between hydrogenic marine ferromanganese crust and seawater. *Geochim. Cosmochim. Acta* 60, 1709–1725.
- Bau, M., Möller, P., Dulski, P., 1997. Yttrium and lanthanides in eastern Mediterranean seawater and their fractionation during redox-cycling. *Mar. Chem.* 56, 123–131.
- Bau, M., Schmidt, K., Pack, A., Bendel, V., Kraemer, D., 2018. The European Shale: An improved data set for normalisation of rare earth element and yttrium concentrations in environmental and biological samples from Europe. *Appl. Geochemistry* 90, 142–149.

- Bau, M., Tepe, N., Mohwinkel, D., 2013. Siderophore-promoted transfer of rare earth elements and iron from volcanic ash into glacial meltwater, river and ocean water. *Earth Planet. Sci. Lett.* 364, 30–36. <https://doi.org/10.1016/j.epsl.2013.01.002>.
- Berger, W.H., 1974. Deep-sea sedimentation. In: *The Geology of Continental Margins* (eds. Burk, C.A., Drake, C.L.). Springer, New York, 213–241.
- Berger, W.H., 1970. Planktonic Foraminifera: Selective solution and the lysocline. *Mar. Geol.* 8, 111–138.
- Bernat, M., 1975. Les isotopes de l'uranium et du thorium et les terres rares dans l'environnement marin. *Cah. ORSTOM Ser. Geol* 7, 65–83.
- Bertram, C.J., Elderfield, H., Aldridge, R.J., Conway Morris, S., 1992. $^{87}\text{Sr}/^{86}\text{Sr}$, $^{143}\text{Nd}/^{144}\text{Nd}$ and REEs in Silurian phosphatic fossils. *Earth Planet. Sci. Lett.* 113, 239–249.
- Bright, C.A., Cruse, A.M., Lyons, T.W., MacLeod, K.G., Glascock, M.D., Ethington, R.L., 2009. Seawater rare-earth element patterns preserved in apatite of Pennsylvanian conodonts? *Geochim. Cosmochim. Acta* 73, 1609–1624. <https://doi.org/10.1016/j.gca.2008.12.014>.
- Cantrell, K.J., Byrne, R.H., 1987. Rare earth element complexation by carbonate and oxalate ions. *Geochim. Cosmochim. Acta* 51, 597–605.
- de Carlo, E.H., 1991. Paleoceanographic implications of rare earth element variability within a Fe-Mn crust from the central Pacific Ocean. *Mar. Geol.* 98, 449–467.
- Chen, J., Algeo, T.J., Zhao, L., Chen, Z.Q., Cao, L., Zhang, L., Li, Y., 2015. Diagenetic uptake of rare earth elements by bioapatite, with an example from Lower Triassic conodonts of South China. *Earth-Science Rev.* 149, 181–202. <https://doi.org/10.1016/j.earscirev.2015.01.013>.
- Craig, J.D., 1979. The relationship between bathymetry and ferromanganese deposits in the north equatorial Pacific. *Mar. Geol.* 29, 165–186.
- Du, J., Haley, B.A., Mix, A.C., 2016. Neodymium isotopes in authigenic phases, bottom waters and detrital sediments in the Gulf of Alaska and their implications for paleo-circulation reconstruction. *Geochim. Cosmochim. Acta* 193, 14–35. <https://doi.org/10.1016/j.gca.2016.08.005>.
- Eittreim, S.L., Ragozin, N., Gnibidenko, H.S., Helsley, C.E., 1992. Crustal age between the Clipperton and Clarion Fracture Zones. *Geophys. Res. Lett.* 12, 2365–2368.
- Elderfield, H., 1988. The Oceanic Chemistry of the Rare-Earth Elements. *Philos. Trans. R. Soc. A Math. Phys. Eng. Sci.* 325, 105–126.
- Elderfield, H., Greaves, M.J., 1982. The rare earth elements in seawater. *Nature* 296, 214–219.
- Elderfield, H., Hawkesworth, C.J., Greaves, M.J., Calvert, S.E., 1981. Rare earth element geochemistry of oceanic ferromanganese nodules and associated sediments. *Geochim. Cosmochim. Acta* 45, 513–528.
- Elderfield, H., Pagett, R., 1986. Rare earth elements in ichthyoliths: variations with redox conditions and depositional environment. *Sci. Total Environ.* 49, 175–197.
- Elderfield, H., Sholkovitz, E.R., 1987. Rare earth elements in the pore waters of reducing nearshore sediments. *Earth Planet. Sci. Lett.* 82, 280–288.
- Epstein, A.G., Epstein, J.B., Harris, L.D., 1977. Conodont color alteration – an index to organic metamorphism. *USGS Prof. Pap.* 995, 27 pp.
- Filippelli, G.M., Delaney, M.L., 1996. Phosphorus geochemistry of equatorial Pacific sediments. *Geochim. Cosmochim. Acta* 60, 1479–1495.

- German, C.R., Klinkhammer, G.P., Edmond, J.M., Mitra, A., Elderfield, H., 1990. Hydrothermal scavenging of rare-earth elements in the ocean. *Nature* 345, 516–518.
- Glasby, G.P., Gwozdz, R., Kunzendorf, H., Friedrich, G., Thijssen, T., 1987. The distribution of rare earth and minor elements in manganese nodules and sediments from the equatorial and S.W. Pacific. *Lithos* 20, 97–113.
- Goldberg, E.D., Koide, M., Schmitt, R.A., Smith, R.H., 1963. Rare-Earth distributions in the marine environment. *J. Geophys. Res.* 68, 4209–4217.
- Grandjean, P., Albarède, F., 1989. Ion probe measurement of rare earth element in biogenic phosphates. *Geochim. Cosmochim. Acta* 53, 3179–3183.
- Guichard, F., Church, T.M., Treuil, M., Jaffrezic, H., 1979. Rare earths in barites: distribution and effects on aqueous partitioning. *Geochim. Cosmochim. Acta* 43, 983–997.
- Haley, B.A., Klinkhammer, G.P., McManus, J., 2004. Rare earth elements in pore waters of marine sediments. *Geochim. Cosmochim. Acta* 68, 1265–1279.
- Heller, C., Kuhn, T., Versteegh, G.J.M., Wegorzewski, A.V., Kasten, S., 2018. The geochemical behavior of metals during early diagenetic alteration of buried manganese nodules. *Deep. Res. Part I Oceanogr. Res. Pap.* 142, 16–33. <https://doi.org/10.1016/j.dsr.2018.09.008>.
- International Seabed Authority (ISA), 2010. A Geological Model of Polymetallic Nodule Deposits in the Clarion Clipperton Fracture Zone, Kingston, Jamaica.
- Jarvis, I., Burnett, W.C., Nathan, Y., Almbaydin, F.S.M., Attia, A.K.M., Castro, L.N., Flicoteaux, R., Hilmy, M.E., Husain, V., Qutawnah, A.A., Serjani, A., Zanin, Y.N., 1994. Phosphorite geochemistry: State-of-the-art and environmental concerns. *Eclogae Geol. Helv.* 87, 643–700.
- Johnson, D.A., 1972. Ocean-Floor Erosion in the Equatorial Pacific. *Geol. Soc. of Am. Bulletin* 83, 3121–3144. doi:10.1130/0016-7606(1972)83[3121:OEITEP]2.0.CO;2.
- Kashiwabara, T., Toda, R., Nakamura, K., Yasukawa, K., Fujinaga, K., Kubo, S., Nozaki, T., Takahashi, Y., Suzuki, K., Kato, Y., 2018. Synchrotron X-ray spectroscopic perspective on the formation mechanism of REY-rich muds in the Pacific Ocean. *Geochim. Cosmochim. Acta* 240, 274–292. <https://doi.org/10.1016/j.gca.2018.08.013>.
- Kasten, S., Glasby, G.P., Schulz, H.D., Friedrich, G., Andreev, S.I., 1998. Rare earth elements in manganese nodules from the South Atlantic Ocean as indicators of oceanic bottom water flow. *Mar. Geol.* 146, 33–52.
- Kato, Y., Fujinaga, K., Nakamura, K., Takaya, Y., Kitamura, K., Ohta, J., Toda, R., Nakashima, T., Iwamori, H., 2011. Deep-sea mud in the Pacific Ocean as a potential resource for rare-earth elements. *Nat. Geosci.* 4, 535–539. <https://doi.org/10.1038/ngeo1185>.
- Kon, Y., Hoshino, M., Sanematsu, K., Morita, S., Tsunematsu, M., Okamoto, N., Yano, N., Tanaka, M., Takagi, T., 2014. Geochemical characteristics of apatite in heavy REE-rich Deep-Sea Mud from Minami-Torishima Area, Southeastern Japan. *Resour. Geol.* 64, 47–57.
- Koschinsky, A., Fritsche, U., Winkler, A., 2001. Sequential leaching of Peru Basin surface sediment for the assessment of aged and fresh heavy metal associations and mobility. *Deep-Sea Res. Part II* 48, 3683–3699.
- Koschinsky, A., Halbach, P., 1995. Sequential leaching of marine ferromanganese precipitates: Genetic implications. *Geochim. Cosmochim. Acta* 59, 5113–5132.
- Köster, M., 2017. Reactivity and spatial variation of Mn and Fe mineral phases in sediments of the eastern Clarion-Clipperton Zone, Pacific Ocean. Universität Bremen.

- Kraemer, D., Kopf, S., Bau, M., 2015. Oxidative mobilization of cerium and uranium and enhanced release of “immobile” high field strength elements from igneous rocks in the presence of the biogenic siderophore desferrioxamine B. *Geochim. Cosmochim. Acta* 165, 263–279. <https://doi.org/10.1016/j.gca.2015.05.046>.
- Kuhn, G., 2013. Don't forget the salty soup: Calculations for bulk marine geochemistry and radionuclide geochronology. Goldschmidt 2013, Florence, Italy, 25 August 2013 – 30 August 2013. doi:10.1180/minmag.2013.077.5.11.
- Kuhn, T., 2015. RV SONNE SO240, Cruise Report / Fahrtbericht, Manzanillo (Mexico): May 3rd, 2015, Manzanillo (Mexico): June 16th, 2015, 185. https://doi.org/10.2312/cr_so240.
- Kuhn, T., Versteegh, G.J.M., Villinger, H., Dohrmann, I., Heller, C., Koschinsky, A., Kaul, N., Ritter, S., Wegorzewski, A.V., Kasten, S., 2017. Widespread seawater circulation in 18–22 Ma oceanic crust: Impact on heat flow and sediment geochemistry. *Geology* 45, 799–802.
- Lutz, M.J., Caldeira, K., Dunbar, R.B., Behrenfeld, M.J., 2007. Seasonal rhythms of net primary production and particulate organic carbon flux to depth describe the efficiency of biological pump in the global ocean. *J. Geophys. Res. Ocean.* 112.
- Lyle, M., 2003. Neogene carbonate burial in the Pacific Ocean. *Paleoceanography* 18. <http://doi.wiley.com/10.1029/2002PA000777>.
- Martínez Arbizu, P., Haeckel, M., 2015. RV SONNE Fahrtbericht / Cruise Report SO239: EcoResponse Assessing the Ecology, Connectivity and Resilience of Polymetallic Nodule Field Systems, Balboa (Panama) – Manzanillo (Mexico,) 11.03.–30.04.2015 (Report No. doi:10.3289/GEOMAR_REP_NS_25_2015), GEOMAR Helmholtz-Zentrum für Ozeanforschung, Kiel, Germany.
- McLennan, S.M., 1989. Rare Earth Elements in Sedimentary Rocks: Influence of Provenance and Sedimentary Process. In: *Geochemistry and Mineralogy of Rare Earth Elements, MSA Reviews in Mineralogy* (eds. Lipin, B.R., McKay, G.A.). 169–200.
- Merschel, G., Bau, M., Schmidt, K., Münker, C., Dantas, E.L., 2017. Hafnium and neodymium isotopes and REY distribution in the truly dissolved, nanoparticulate/colloidal and suspended loads of rivers in the Amazon Basin, Brazil. *Geochim. Cosmochim. Acta* 213, 383–399.
- Mewes, K., Mogollón, J.M., Picard, A., Rühlemann, C., Kuhn, T., Nöthen, K., Kasten, S., 2014. Impact of depositional and biogeochemical processes on small scale variations in nodule abundance in the Clarion-Clipperton Fracture Zone. *Deep. Res. Part I Oceanogr. Res. Pap.* 91, 125–141. <https://doi.org/10.1016/j.dsr.2014.06.001>.
- Mewes, K., Mogollón, J.M., Picard, A., Rühlemann, C., Eisenhauer, A., Kuhn, T., Ziebis, W., Kasten, S., 2016. Diffusive transfer of oxygen from seamount basaltic crust into overlying sediments : An example from the Clarion – Clipperton Fracture Zone. *Earth Planet. Sci. Lett.* 433, 215–225. <https://doi.org/10.1016/j.epsl.2015.10.028>.
- Michard, A., 1989. Rare earth element systematics in hydrothermal fluids. *Geochim. Cosmochim. Acta* 53, 745–750.
- Mogollón, J.M., Mewes, K., Kasten, S., 2016. Quantifying manganese and nitrogen cycle coupling in manganese-rich, organic carbon-starved marine sediments: Examples from the Clarion-Clipperton fracture zone. *Geophys. Res. Lett.* 43, 7114–7123.
- Möller, P., Bau, M., 1993. Rare-earth patterns with positive cerium anomaly in alkaline waters from Lake Van, Turkey. *Earth Planet. Sci. Lett.* 117, 671–676.

- Müller, P.J., Hartmann, M., Suess, E., 1988. The chemical environment of pelagic sediments. In: *The Manganese Nodule Belt of the Pacific Ocean: Geological Environment, Nodule Formation, and Mining Aspects* (eds. Halbach, P., Friedrich, G., von Stackelberg, U.). Enke, Stuttgart, 70–90.
- Nothdurft, L.D., Webb, G.E., Kamber, B.S., 2004. Rare earth element geochemistry of Late Devonian reefal carbonates, Canning Basin, Western Australia: Confirmation of a seawater REE proxy in ancient limestones. *Geochim. Cosmochim. Acta* 68, 263–283.
- Nöthen, K., Kasten, S., 2011. Reconstructing changes in seep activity by means of pore water and solid phase Sr / Ca and Mg / Ca ratios in pockmark sediments of the Northern Congo Fan. *Mar. Geol.* 287, 1–13. <https://doi.org/10.1016/j.margeo.2011.06.008>.
- Piper, D.Z., 1974a. Rare earth elements in ferromanganese nodules and other marine phases. *Geochem. Cosmochim. Acta* 38, 1007–1022.
- Piper, D.Z., 1974b. Rare earth elements in the sedimentary cycle: A summary. *Chem. Geol.* 14, 285–304.
- Poulton, S.W., Canfield, D.E., 2005. Development of a sequential extraction procedure for iron: Implications for iron partitioning in continentally derived particulates. *Chem. Geol.*
- Pourret, O., Tuduri, J., 2017. Continental shelves as potential resource of rare earth elements. *Sci. Rep.* 7, 1–6. <https://doi.org/10.1038/s41598-017-06380-z>.
- Reynard, B., Lécuyer, C., Grandjean, P., 1999. Crystal-chemical controls on rare-earth element concentrations in fossil biogenic apatites and implications for paleoenvironmental reconstructions. *Chem. Geol.* 155, 233–241.
- Rønsbo, J.G., 1989. Coupled substitutions involving REEs and Na and Si in apatites in alkaline rocks from Ilímaussaq intrusion, South Greenland, and the petrological implications. *Am. Mineral.* 74, 896–901.
- Rühlemann, C., Kuhn, T., Wiedicke, M., Kasten, S., Mewes, K., Picard, A., 2011. Current status of manganese nodule exploration in the German license area. *Proc. of the 9th ISOPE Conference*, Maui, 168–173.
- Ruttenberg, K.C., 1992. Development of a sequential extraction method for different forms of phosphorus in marine sediments. *Limnol. Oceanogr.* 37, 1460–1482.
- Schenau, S.J., De Lange, G.J., 2000. A novel chemical method to quantify fish debris in marine sediments. *Limnol. Ocean.* 45, 963–971.
- Seitz, M., Oliver, A.G., Raymond, K.N., 2007. The lanthanide contraction revisited. *J. Am. Chem. Soc.* 129, 11153–11160.
- Sharma, R., 2017. Deep-sea mining: Resource potential, technical and environmental considerations.
- Sholkovitz, E.R., Church, T.M., Arimoto, R., 1993. Rare Earth element composition of precipitation, precipitation particles, and aerosols. *J. Geophys. Res.* 98, 20587.
- Sholkovitz, E.R., Piepgras, D.J., Jacobsen, S.B., 1989. The pore water chemistry of rare earth elements in Buzzards Bay sediments. *Geochim. Cosmochim. Acta* 53, 2847–2856.
- Soyol-Erdene, T.O., Huh, Y., 2013. Rare earth element cycling in the pore waters of the Bering Sea Slope (IODP Exp. 323). *Chem. Geol.* 358, 75–89. <https://doi.org/10.1016/j.chemgeo.2013.08.047>.
- von Stackelberg, U., Beiersdorf, H., 1991. The formation of manganese nodules between the Clarion and Clipperton fracture zones southeast of Hawaii. *Mar. Geol.* 98, 411–423.

- Takahashi, Y., Manceau, A., Geoffroy, N., Marcus, M.A., Usui, A., 2007. Chemical and structural control of the partitioning of Co, Ce, and Pb in marine ferromanganese oxides. *Geochemica Cosmochim. Acta* 71, 984–1008.
- Tang, J., Johannesson, K.H., 2010. Ligand extraction of rare earth elements from aquifer sediments: Implications for rare earth element complexation with organic matter in natural waters. *Geochim. Cosmochim. Acta* 74, 6690–6705. <https://doi.org/10.1016/j.gca.2010.08.028>.
- Taylor, S.R., McLennan, S.M., 1985. The Continental Crust: Its Composition and Evolution. An Examination of the Geochemical Record Preserved in Sedimentary Rocks.
- Toyoda, K., Masuda, A., 1991. Chemical leaching of pelagic sediments: Identification of the carrier of Ce anomaly. *Geochem. J.* 25, 95–119.
- Toyoda, K., Nakamura, Y., Masuda, A., 1990. Rare earth elements of Pacific pelagic sediments. *Geochim. Cosmochim. Acta* 54, 1093–1103.
- Toyoda, K., Tokonami, M., 1990. Diffusion of rare-earth elements in fish teeth from deep sea sediments. *Nature* 345, 183–187.
- Trotter, J.A., Barnes, C.R., McCracken, A.D., 2016. Rare earth elements in conodont apatite: Seawater or pore-water signatures? *Palaeogeogr. Palaeoclimatol. Palaeoecol.* 462, 92–100. <https://doi.org/10.1016/j.palaeo.2016.09.007>.
- Vanreusel, A., Hilario, A., Ribeiro, P.A., Menot, L., Martínez Arbizu, P., 2016. Threatened by mining, polymetallic nodules are required to preserve abyssal epifauna. *Sci. Rep.* 6, 1–6. <https://doi.org/10.1038/srep26808>.
- Viehmann, S., Bau, M., Hoffmann, J.E., Münker, C., 2015. Geochemistry of the Krivoy Rog Banded Iron Formation, Ukraine, and the impact of peak episodes of increased global magmatic activity on the trace element composition of Precambrian seawater. *Precambrian Res.* 270, 165–180.
- Volz, J.B., Mogollón, J.M., Geibert, W., Martínez Arbizu, P., Koschinsky, A., Kasten, S., 2018. Natural spatial variability of depositional conditions, biogeochemical processes and element fluxes in sediments of the eastern Clarion-Clipperton Zone, Pacific Ocean. *Deep. Res. Part I Oceanogr. Res. Pap.* 140, 159–172. <https://doi.org/10.1016/j.dsr.2018.08.006>.
- Webb, G.E., Kamber, B.S., 2000. Rare earth elements in Holocene reefal microbialites: A new shallow seawater proxy. *Geochim. Cosmochim. Acta* 64, 1557–1565.
- Wright, J., 1990. Conodont Apatite: Structure and Geochemistry. In *Skeletal Biomineralization: Patterns, Processes and Evolutionary Trends (Volume 1)* (ed. Carter, J.G.). Van Nostrand Reinhold, New York. 445–459. <http://doi.wiley.com/10.1029/SC005p0149>.
- Wright, J., Seymour, R.S., Shaw, H.F., 1984. REE and Nd isotopes in conodont apatite: Variations with geological age and depositional environment. *Geol. Soc. Am. Special Pa.* 325–340.
- Zhang, L., Algeo, T.J., Cao, L., Zhao, L., Chen, Z.Q., Li, Z., 2016. Diagenetic uptake of rare earth elements by conodont apatite. *Palaeogeogr. Palaeoclimatol. Palaeoecol.* 458, 176–197. <https://doi.org/10.1016/j.palaeo.2015.10.049>.
- Ziegler, C.L., Murray, R.W., 2007. Geochemical evolution of the central Pacific Ocean over the past 56 Myr. *Paleoceanography* 22.

CHAPTER IV:

Post-depositional manganese mobilization during the last glacial period in sediments of the eastern Clarion-Clipperton Fracture Zone, Pacific Ocean

Jessica B. Volz^{a,*}, Bo Liu^a, Male Köster^a, Susann Henkel^a, Andrea Koschinsky^b, Sabine Kasten^{a,c}

^a Alfred Wegener Institute Helmholtz Centre for Polar and Marine Research, Bremerhaven, Germany (corresponding author: jessica.volz@awi.de, Tel.: +49 471 4831 1842)

^b Jacobs University Bremen, Department of Physics and Earth Sciences, Bremen, Germany

^c University of Bremen, Faculty of Geosciences, Klagenfurter Strasse, Bremen, Germany

Revised manuscript submitted to *Earth and Planetary Science Letters*.

Abstract

Numerous studies have provided compelling evidence that the Pacific Ocean has experienced substantial glacial/interglacial changes in bottom-water oxygenation associated with enhanced carbon dioxide storage in the glacial deep ocean. Under postulated low glacial bottom-water oxygen concentrations (O_2^{bw}), redox zonation, biogeochemical processes and element fluxes in the sediments must have been distinctively different during the last glacial period (LGP) compared to current well-oxygenated conditions.

In this study, we have investigated six sites situated in various European contract areas for the exploration of polymetallic nodules within the Clarion-Clipperton Zone (CCZ) in the NE Pacific and one site located in a protected Area of Particular Environmental Interest (APEI3) north of the CCZ. We found bulk sediment Mn maxima of up to 1 wt% in the upper oxic 10 cm of the sediments at all sites except for the APEI3 site. The application of a combined leaching protocol for the extraction of sedimentary Mn and Fe minerals revealed that mobilizable Mn(IV) represents the dominant Mn (oxyhydr)oxide phase with more than 70% of bulk solid-phase Mn. Steady state transport-reaction modelling showed that at postulated glacial O_2^{bw} of 35 μM , the oxic zone in the sediments was much more compressed than today where upward diffusing pore-water Mn^{2+} was oxidized and precipitated as authigenic Mn(IV) at the oxic-suboxic redox boundary in the upper 5 cm of the sediments. Transient transport-reaction modelling demonstrated that with increasing O_2^{bw} during the last glacial termination to current levels of $\sim 150 \mu\text{M}$, (1) the oxic-suboxic redox boundary migrated deeper into the sediments and (2) the authigenic Mn(IV) peak was continuously mixed into subsequently deposited sediments by bioturbation causing the observed mobilizable Mn(IV) enrichment in the surface sediments. Such a distinct mobilizable Mn(IV) maximum was not found in the surface sediments of the APEI3 site, which indicates that the oxic zone was not as condensed during the LGP at this site due to two- to threefold lower organic carbon burial rates. Leaching data for sedimentary Fe minerals suggest that Fe(III) has not been diagenetically redistributed during the LGP at any of the investigated sites. Our results demonstrate that the basin-wide deoxygenation in the NE Pacific during the LGP was associated with (1) a much more compressed oxic zone at sites with carbon burial fluxes higher than $1.5 \text{ mg C}_{\text{org}} \text{ m}^{-2} \text{ d}^{-1}$, (2) the authigenic formation of a sub-surface mobilizable Mn(IV) maximum in the upper 5 cm of the sediments and (3) a possibly intensified suboxic-diagenetic growth of polymetallic nodules. As our study provides evidence that authigenic Mn(IV) precipitated in the surface sediments under postulated low glacial O_2^{bw} , it contributes to resolving a long-standing controversy concerning the origin of widely observed Mn-rich layers in glacial/deglacial deep-sea sediments.

1. Introduction

Some of the most extensive deposits of polymetallic nodules have been found in the Pacific Ocean, notably in the Clarion-Clipperton Zone (CCZ) in the NE Pacific (e.g., Halbach et al., 1988). Polymetallic nodules are generally made up of irregular, concentrically banded micro-layers of Mn and Fe (oxyhydr)oxides forming around a nucleus (e.g., Halbach et al., 1988). They precipitate either (1) hydrogenetically with dissolved or colloidal metals from seawater or (2) diagenetically by the supply of metals via the oxic-diagenetic (i.e. precipitation under oxic conditions) or suboxic-diagenetic (i.e. precipitation from suboxic pore water) growth pathways (e.g., Halbach et al., 1988). Hydrogenetic nodules are generally small (~ 1–5 cm) due to slow growth rates of about 1 to 10 mm Myr⁻¹, while diagenetic nodules are bigger (5 cm to more than 10 cm) as they are growing at rates of several hundred millimeters per million years (e.g., Halbach et al., 1988). Most nodules of the CCZ show alternating Mn growth layers of hydrogenetic and diagenetic origin (e.g., Halbach et al., 1988; Wegorzewski and Kuhn, 2014; Heller et al., 2018). As the sediments of the CCZ are currently characterized by a broad upper oxic zone expanding over > 0.5 m, nodule growth is presently dominated by hydrogenetic and oxic-diagenetic accretion (e.g., Halbach et al., 1988; Mewes et al., 2014; 2016; Wegorzewski and Kuhn, 2014; Kuhn et al., 2017; Volz et al., 2018; Heller et al., 2018). The occurrence of older suboxic-diagenetic Mn growth layers indicates that suboxic surface sediment redox conditions may have occurred in the CCZ in the past (e.g., Wegorzewski and Kuhn, 2014; Heller et al., 2018). Further studies have shown that the upper 10–15 cm of the sediments of the eastern CCZ are characterized by solid-phase Mn enrichments (Mewes et al., 2014). Core-top solid-phase Mn peaks as well as solid-phase Mn enrichments buried deeper in the sediments have also been observed in early studies from the eastern equatorial Pacific (Lynn and Bonatti, 1965; Berger et al., 1983; Piper, 1988), in the Atlantic Ocean (e.g., Froelich et al., 1979; Gingele and Kasten, 1994; Mangini et al., 2001) and more recently in the Southern Ocean (Presti et al., 2011; Jaccard et al., 2016; Wu et al., 2018). The formation of such sedimentary Mn maxima is controlled by primary input and diagenetic redistribution associated with the reductive dissolution of Mn (oxyhydr)oxides, during which released Mn²⁺ diffuses upwards and re-precipitates as authigenic Mn(IV) during oxidation (e.g., Froelich et al., 1979; Burdige and Gieskes, 1983; Gingele and Kasten, 1994). However, the current redox zonation in the sediments of the eastern Pacific (Mewes et al., 2014; Volz et al., 2018) as well as in the Southern Ocean (e.g., Presti et al., 2011) does not allow for the authigenic formation of the observed MnO₂ enrichments at shallow sediment depth. Sediment leaching experiments for the extraction of the mobilizable Mn(IV) phase after Koschinsky et al. (2001) from Mn-rich CCZ

surface sediments have revealed that the enrichment is dominated by mobilizable Mn(IV), which is reductively dissolved under slightly reducing conditions (Koschinsky et al., 2001; Mewes et al., 2014). Considering $^{10}\text{Be}/^9\text{Be}$ -based sedimentation rates of less than 0.6 cm kyr^{-1} (Mewes et al., 2014), this mobilizable Mn(IV) enrichment is associated with sediments deposited up to 30 kyr before present (BP). This includes sediment deposits of the last glacial maximum (LGM; $\sim 21 \text{ kyr BP}$), which are currently located at $\sim 10 \text{ cm}$ depth. Thus, a more compressed oxic zone than currently observed may have allowed for Mn^{2+} to diffuse upwards and precipitate as an authigenic Mn(IV) phase close to the sediment surface during the last glacial period (LGP; $\sim 15\text{--}28 \text{ kyr BP}$) and may also have facilitated the suboxic-diagenetic accretion of polymetallic nodules (e.g., Wegorzewski and Kuhn, 2014).

Several studies have suggested that the widely observed solid-phase Mn maxima in deep-sea sediments throughout the global ocean are relics of the onset of ocean ventilation at glacial/interglacial transitions since middle Pleistocene ages when the bottom water was oxygenated (e.g., Mangini et al., 1990; 2001; Jaccard et al., 2009; 2016; Wu et al., 2018). More precisely, the authors proposed that less oxygenated bottom water during glacial periods may have facilitated pore-water Mn^{2+} diffusion from deeper sediments into surface sediments (e.g., Jaccard et al., 2009; 2016; Wu et al., 2018), or even, into the suboxic bottom water (e.g., Mangini et al., 1990). At the last glacial termination (LGT) and, presumably, at each preceding glacial/interglacial transition, the onset of ocean ventilation oxygenated the bottom water and might have caused the oxidation of Mn^{2+} and subsequent burial of authigenic Mn (oxyhydr)oxides (e.g., Mangini et al., 1990; Wu et al., 2018). However, recent studies have provided compelling evidence that while bottom-water oxygen concentrations (O_2^{bw}) during the LGP were significantly lower throughout the eastern Pacific Ocean than today, they did not reach suboxic levels (Bradtmiller et al., 2010; Jacobel et al., 2017; Hoogakker et al., 2018; Anderson et al., 2019).

Other redox-sensitive elements such as U also indicate that the oxic-suboxic redox boundary was located at shallow sediment depths during the LGP as authigenic U(IV) enrichments are found in glacial deposits at various locations in the eastern Pacific (e.g., Bradtmiller et al., 2010; Jacobel et al., 2017). Authigenic U(IV) precipitates under similar reducing sediment redox conditions at which pore-water nitrate is consumed and the dissimilatory Fe(III) reduction commences (e.g., Froelich et al., 1979; Jacobel et al., 2017). Based on paleomagnetic data for sediments of the abyssal NW Pacific, Korff et al. (2016) have identified magnetite-depleted glacial sediments, which were attributed to low O_2^{bw} causing the reductive dissolution of magnetite.

Past changes in sediment redox conditions can be reconstructed based on the assemblage and reactivity of sedimentary Mn and Fe minerals, which can be determined by using sequential chemical leaching protocols (e.g., Koschinsky et al., 2001; Poulton and Canfield, 2005). Here, we apply a combined leaching scheme based on the protocols by Koschinsky et al. (2001) and Poulton and Canfield (2005) for the organic-carbon-lean and mostly oxic sediments of the CCZ in order to determine different sedimentary Mn and Fe pools, including (1) carbonate-associated Fe and Mn, (2) easily reducible Mn (oxyhydr)oxides, (3) easily reducible Fe oxides (4) reducible Fe oxides and (5) magnetite. We have studied surface sediments from six sites located in European contract areas for the exploration of polymetallic nodules within the CCZ, and one site situated in an Area of Particular Environmental Interest (APEI3) north of the CCZ. We hypothesize that lower O_2^{bw} during the LGP allowed upward diffusing Mn^{2+} to precipitate as authigenic Mn(IV) close to the sediment-water interface. Furthermore, we propose that the authigenic Mn(IV) peak was continuously mixed into subsequently deposited sediments due to bioturbation, which caused the observed Mn(IV) enrichments in the upper 10–15 cm of the sediments of the CCZ. We applied one-dimensional transport-reaction modelling to assess whether significantly lower glacial O_2^{bw} could have created a much more compressed oxic zone than currently observed in the sediments of the CCZ.

2. Material and methods

As part of the BMBF-EU JPI Oceans pilot action “Ecological Aspects of Deep-Sea Mining (MiningImpact)”, multicorer (MUC) and 10-m-long gravity corer (GC) cores were collected during RV SONNE cruise SO239 in 2015 (Martínez Arbizu and Haeckel, 2015). The MUC sediment cores were retrieved from four European contract areas for the exploration of polymetallic nodules and from one of the Areas of Particular Environmental Interest (APEI3) (Fig. 1; Table 1). The investigated contract areas include the German BGR (Bundesanstalt für Geowissenschaften und Rohstoffe) area, the Belgian GSR (Global Sea Mineral Resources NV) area, the French IFREMER (Institut Français de Recherche pour l'Exploitation de la Mer) area and the Eastern European IOM (InterOceanMetal) area, while the APEI3 is excluded from any potential mining activities. Two sites are located in the BGR area, namely in the “reference area” (BGR-RA) and in the “prospective area” (BGR-PA) for potential future polymetallic nodule exploitation. For the development of the combined leaching procedure, we used sediment samples of MUC core SO205-65 retrieved from the BGR area during RV SONNE cruise SO205 in 2010 in the framework of the MANGAN project (Fig. 1; Table 1; Rühlemann et al., 2010; Mewes et al., 2016).

The surface sediments throughout the investigated contract areas are characterized by clay-dominated siliceous oozes with variable nodule sizes (1–10 cm) and distributions at the seafloor (Table 1; Mewes et al., 2014; Volz et al., 2018). All MUC sediment cores investigated in the framework of this study are oxic throughout (Volz et al., 2018). In order to characterize the investigated sites, key parameters, including sedimentation rate, depositional flux of particulate organic carbon (POC), bioturbation depth and oxygen penetration depth (OPD) are summarized in Table 1, which were originally presented elsewhere and are based on studies of 10 to 14-m-long GC and piston cores (Mewes et al., 2014; Mewes et al., 2016; Mogollón et al., 2016; Volz et al., 2018). At most of the investigated sites, suboxic conditions are found at different depth below the OPD, where the reduction of Mn(IV) and nitrate coexist in the absence of oxygen and sulfide. Dissolved Fe^{2+} was not detected at any of the investigated sites (Mogollón et al., 2016; Volz et al., 2018).

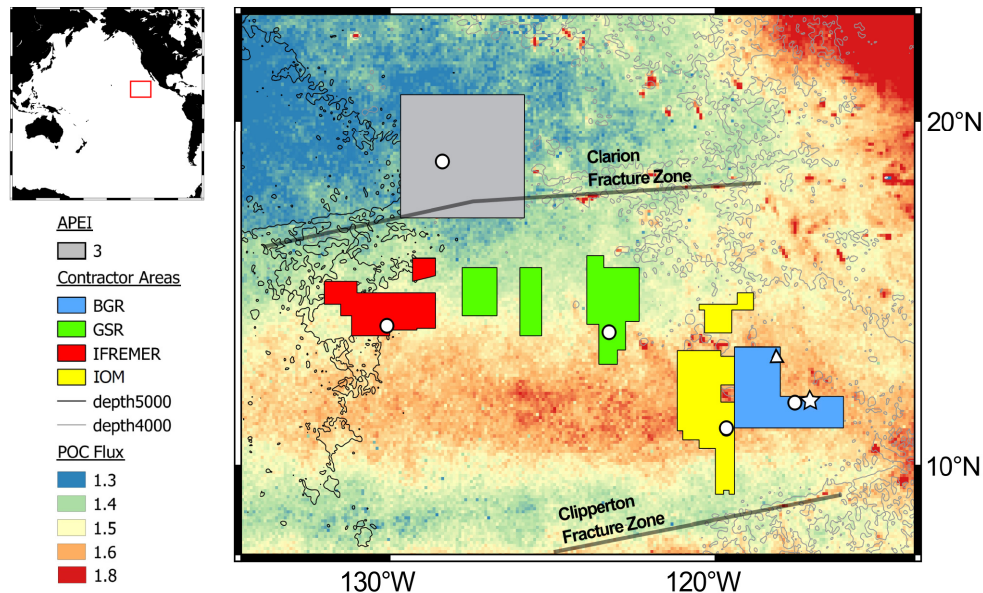


Figure 1: Map of the investigated sampling sites (open circles, star and triangle) in the different European contract areas for the exploration of polymetallic nodules and in the APEI3. The IFRE-1 and IFRE-2 sites are both located in the IFREMER area (open circle). The BGR area includes the BGR-RA (open circle), BGR-PA (open star) and SO205-65 (open triangle; Rühlemann et al., 2010; Mewes et al., 2016) sites. Background colors indicate the maximum POC flux [$\text{mg C}_{\text{org}} \text{m}^{-2} \text{d}^{-1}$] to the seafloor estimated by Lutz et al. (2007). Map is modified after Volz et al. (2018).

Table 1: Investigated MUC sampling sites with geographic position and water depth. If not indicated otherwise, sampling station characteristics, such as sedimentation rate (Sed. rate), flux of particulate organic carbon (POC) to the seafloor, bioturbation depth (Bioturb. depth), oxygen penetration depth (OPD) and nodule size are taken from Volz et al. (2018). Information for site SO205-65 is taken from Rühlemann et al. (2010) and Mewes et al. (2016). For the BGR-PA site, information is taken from an adjacent site (A5-2-SN; 11°57.22'N, 117°0.42'W) studied by Mewes et al. (2014) and Mogollón et al. (2016).

| Site | Latitude [N] | Longitude [W] | Water depth [m] | Sed. rate [cm kyr ⁻¹] | POC flux [mg m ⁻² d ⁻¹] | Bioturb. depth [cm] | OPD [m] | Nodule size |
|----------|--------------|---------------|-----------------|-----------------------------------|--|---------------------|-------------------|------------------------------|
| SO205-65 | 13°10.50' | 118°06.30' | 4283.0 | 0.38 ¹ | 1.2 ¹ | 5 ¹ | oxic ¹ | small to medium ² |
| BGR-PA | 11°50.64' | 117°03.44' | 4132.0 | ~0.53 ³ | ~6.9 ³ | ~5 ³ | ~2 ^{3,4} | medium ⁵ |
| BGR-RA | 11°49.13' | 117°33.13' | 4314.8 | 0.65 | 1.99 | 7 | 0.5 | medium |
| IOM | 11°04.73' | 119°39.48' | 4430.8 | 1.15 | 1.54 | 13 | 3 | medium |
| GSR | 13°51.25' | 123°15.30' | 4517.7 | 0.21 | 1.51 | 8 | >7.4 | big |
| IFRE-1 | 14°02.62' | 130°08.32' | 4918.8 | 0.64 | 1.47 | 7 | 4.5 | medium |
| IFRE-2 | 14°02.45' | 130°05.11' | 5005.5 | 0.48 | 1.5 | 8 | 3.8 | no nodules |
| APEI3 | 18°47.46' | 128°22.42' | 4816.6 | 0.2 | 1.07 | 6 | >5.7 | small |

¹Mewes et al. (2016)

²Rühlemann et al. (2010)

³Mogollón et al. (2016)

⁴Mewes et al. (2014)

⁵Martínez Arbizu and Haeckel (2015)

2.1 Sediment sampling

Immediately after core recovery, all MUC sediment cores retrieved during cruise SO239 were transferred into the cold room at a temperature of ~4 °C. Sediment sampling was performed in 1 cm resolution and every 2 cm at the IOM site. All sediment samples were taken with a plastic spatula and stored in plastic vials at -20 °C until further analysis.

2.2 Total acid digestion

Total acid digestions were performed in a microwave system MARS Xpress (CEM) with the evaporation accessory CEM XpressVap. About 50 mg of freeze-dried, homogenized bulk sediment were digested in an acid mixture of 65% sub-boiling distilled HNO₃ (3 mL), 30% sub-boiling distilled HCl (2 mL) and 40% suprapur® HF (0.5 mL) at ~230 °C. Bulk Mn, Fe and Al contents were determined using inductively coupled plasma optical emission spectrometry (IRIS Intrepid ICP-OES Spectrometer, Thermo Elemental). Based on the standard reference material NIST 2702 accuracy and precision of the analysis was 5.9% and 3.7% for Al, 7.1% and 4.6% for Fe and 3.7% and 3.5% for Mn, respectively (n=67). Bulk sediment data have been corrected post-analytically for the interference of the pore-water salt matrix on the

sediment composition (Volz et al., 2018). Bulk element contents of Mn and Fe were normalized to Al in order to calculate the excess fractions relative to the pelagic background sedimentation.

2.3 Sequential extraction of Mn and Fe (oxyhydr)oxides

A specific extraction protocol for the separation of Mn (oxyhydr)oxides and Fe (oxyhydr)oxides from Pacific sediments and Mn nodules has been presented by Koschinsky et al. (2001). Poulton and Canfield (2005) have developed a sequential leaching procedure, which targets different sedimentary Fe pools. In order to determine the availability and reactivity of both Mn and Fe mineral phases, and to reconstruct the potential past redox cycling of Mn and Fe, we have combined these two procedures.

Combined leaching protocol: method testing

The protocols by Koschinsky et al. (2001) and Poulton and Canfield (2005) have first been separately applied on sediments of core SO205-65 (Table 1) to test their selectivity for Mn (oxyhydr)oxides and various Fe minerals (Fig. 2). About 100 mg of freeze-dried homogenized sediment were sequentially treated with 10 mL of the respective extraction reagents for given reaction times (Koschinsky et al., 2001; Poulton and Canfield, 2005) and centrifuged afterwards (4000 rpm, 5 min). The supernatant extraction solutions were filtered through a 0.2 μm polyethersulfone membrane before Mn and Fe concentrations were determined upon dilution using ICP-OES (IRIS Intrepid ICP-OES Spectrometer, Thermo Elemental). Calibration standards were produced in 0.3 M HNO_3 or in Milli-Q® (Na-dithionite; see Table 2) and adjusted to the different reagent matrices in order to prevent matrix effects during analysis.

The first two leaching steps primarily mobilize adsorbed and pore-water cations as well as carbonate-associated Fe and Mn, respectively (Koschinsky et al., 2001; Poulton and Canfield, 2005). As the concentrations of Fe and Mn were below detection limit during the method test with SO205-65 sediment samples (Fig. 2), the first two steps were merged in the combined extraction protocol (Table 2, step I). The major difference between the both extraction protocols is the concentration, pH value and reaction time of the extraction reagent hydroxylamine-HCl. As Koschinsky et al. (2001) have intended to only extract the easily mobilizable fraction of Mn, the 0.1 M hydroxylamine-HCl solution is adjusted to pH 2, while Poulton and Canfield (2005) have used a 1 M hydroxylamine-HCl in 25% v/v acetic acid solution for the extraction of easily reducible Fe oxides at $\text{pH} < 2$. On average, 74% of bulk sediment Mn (Mn_{total}) is extracted with 0.1 M hydroxylamine-HCl (Mn_{mobil}) (Fig. 2A). In order to separate mobilizable Mn

(oxyhydr)oxides (Mn_{mobil}) from easily reducible Fe (oxyhydr)oxides (Fe_{ox1}) in the combined extraction protocol, the sediment samples are sequentially treated with 0.1 M hydroxylamine-HCl and 1 M hydroxylamine-HCl (Table 2, step II and III, respectively). Only 2% of bulk sediment Fe (Fe_{total}) are mobilized with 0.1 M hydroxylamine-HCl (Fe_{mobil}) representing easily reducible Fe (oxyhydr)oxides (Fig. 2A). The remaining fraction of easily reducible Fe (oxyhydr)oxides is extracted with 1 M hydroxylamine-HCl (Table 2). Using the protocol after Poulton and Canfield (2005), an average of 20% of Fe_{total} is extracted by Na-dithionite (Fe_{ox2}) and 5% by ammonium oxalate (Fe_{mag} ; Fig. 2B). Therefore, we have implemented these extraction steps into the combined leaching protocol (Table 2, step IV and V, respectively).

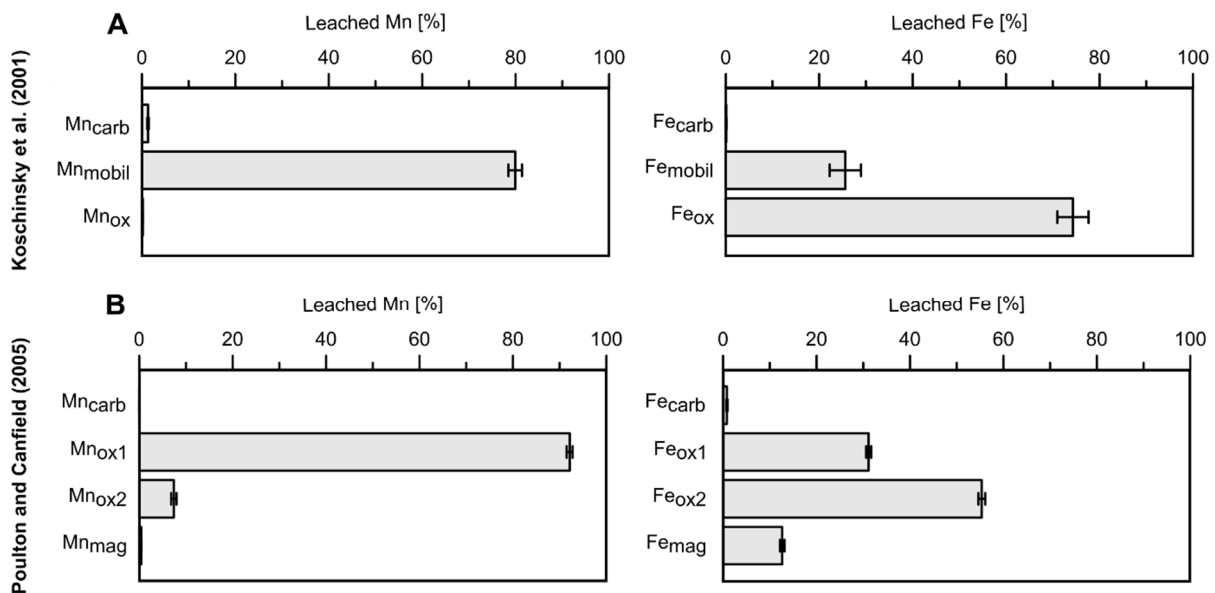


Figure 2: Method test of the leaching protocols after (A) Koschinsky et al. (2001) and (B) Poulton and Canfield (2005) separately applied on sediment samples from MUC core SO205-65 (Fig. 1; Table 1). Sequentially leached percentages of Mn and Fe oxides after the protocol by Koschinsky et al. (2001) (Mn_{carb} , Fe_{carb} ; Mn_{mobil} , Fe_{mobil} ; Mn_{ox} , Fe_{ox}) and Poulton and Canfield (2005) (Mn_{carb} , Fe_{carb} ; Mn_{ox1} , Fe_{ox1} ; Mn_{ox2} , Fe_{ox2} ; Mn_{mag} , Fe_{mag}) are shown with respect to bulk sediment contents of Mn and Fe (Mn_{total} ; Fe_{total}).

Application of the combined leaching protocol

For the sequential extraction of Mn and Fe (oxyhydr)oxides of sediment samples from RV SONNE cruise SO239 investigated in this study, the combined leaching procedure was performed on samples taken every 3 cm using acid-cleaned vials (Table 2). Since the process of freeze-drying might increase the crystallinity of Mn and Fe (oxyhydr)oxides (e.g., Rapin et al., 1986), fresh sediment samples equivalent to ~ 100 mg of dry sediment were used. Dry sediment masses were calculated using the mass of the interstitial water (Volz et al., 2018). In

order to monitor the recovery of the sequential extractions, the sediment residues were completely dissolved after the last extraction step (see section 2.1.). The recovery is defined as the sum of leachable contents (step I–V, Table 2) and residual contents divided by bulk contents. It was determined for three sediment cores with systematically high values for Fe (104–124%) and Mn (96–143%). These elevated recoveries are most likely caused by the slight sediment inhomogeneity of fresh sediment samples used for the combined leaching protocol, while bulk contents were determined on freeze-dried, homogenized samples. Furthermore, as we have not washed the sediment samples in between the extraction steps, higher recovery values for the leached sediments could also be associated with a successive carry-over of Mn and Fe due to the incomplete removal of the extraction reagent after the respective leaching step. The %RSD was determined based on triplicate measurement of each sample and was < 2% for Mn and < 2.8% for Fe. Based on in-house reference material, the analytical precision was < 6% for Fe and Mn (n=12).

Table 2: Protocol for the combined leaching scheme combining the methods after Koschinsky et al. (2001) and Poulton and Canfield (2005).

| Step | Associated mineral phase | Terminology | Extraction reagent* | Extraction time | pH |
|------|--|--|---|-----------------|-----|
| I | Carbonate-associated Fe and Mn | Mn _{carb} Fe _{carb} | 1 M Na-acetate | 24 h | 4.5 |
| II | Mobilizable Mn and associated Fe | Mn _{mobil} Fe _{mobil} | 0.1 M hydroxylamine-HCl | 2 h | 2 |
| III | Easily reducible Fe oxides and associated Mn | Fe _{ox1} Mn _{ox1} | 1 M hydroxylamine-HCl | 48 h | |
| IV | Reducible Fe oxides | Fe _{ox2} | Na-dithionite (50 g L ⁻¹)/0.2 M Na-citrate solution | 2 h | 4.8 |
| V | Magnetite | Fe _{mag} | 0.2 M ammonium oxalate/0.17 M oxalic acid | 6 h | |

*All extraction steps performed at ~ 20 °C

2.4 Geochemical model setup and reaction network

A one-dimensional steady state transport-reaction model, which couples biogeochemical reactions through a discretized steady state transport-reaction equation (e.g., Boudreau, 1997a) was used to assess whether postulated glacial O₂^{bw} of 35 μM (Hoogakker et al., 2018; Anderson et al., 2019) could have caused a near-surface oxic-suboxic redox boundary. We have applied the model for the BGR-RA, IFRE-2 and APEI3 sites in order to cover a large area in the CCZ over a distance of about 1300 km (Fig. 1). The simulations were performed for the upper 2 m at the BGR-RA site, 7.5 m at the IFRE-2 site and 6 m at the APEI3 site using pore-water data from 10-m-long GC cores published in Volz et al. (2018)

(Supplementary Table S1). A transient transport-reaction model (Eq. S1; S2) was applied on all sites in order to simulate the depth distribution of mobilized Mn(IV) contents for the last 21 kyr. For this simulation, we have assumed that O_2^{bw} of 35 μM have prevailed between 15–21 kyr BP (Hoogakker et al., 2018; Anderson et al., 2019). Between 14–15 kyr BP, O_2^{bw} is assumed to have increased linearly to current concentrations of 120 μM , 150 μM and 160 μM , respectively (Volz et al., 2018; Hoogakker et al., 2018). A detailed description of the model setup, parameterization and sensitivity tests is presented in the Supplementary material S1. All species, parameters, boundary conditions and reaction terms are listed in the Supplementary Tables S1 and S2.

3. Results

Bulk sediment

Total solid-phase Mn contents (Mn_{total}) in the upper 25 cm of the sediments are within 0.1 and 1 wt% at all sites (Fig. 3A) with decreasing contents with depth at both BGR sites, the GSR and the IFRE-2 sites. At the IFRE-1 site, Mn_{total} does not decrease with depth but shows a subsurface peak of 0.8 wt% at 20 cm depth. In contrast to overall decreasing solid-phase Mn contents over depth at most sites, Mn_{total} contents remain relatively constant in the sediments at the APEI3 site at 0.6 wt% throughout the sediment core. The profiles of bulk sediment Mn/Al mimic the Mn_{total} profiles at all sites and range between 0.01 and 0.17 (Fig. 3A).

Total Fe contents (Fe_{total}) vary between 4 and 5 wt% at all sites except for the APEI3 site, where Fe_{total} is between 5 and 6 wt% (Fig. 3B). Bulk sediment Fe/Al profiles resemble the Fe_{total} profiles at all sites within the range of 0.6 and 0.7 (Fig. 3B).

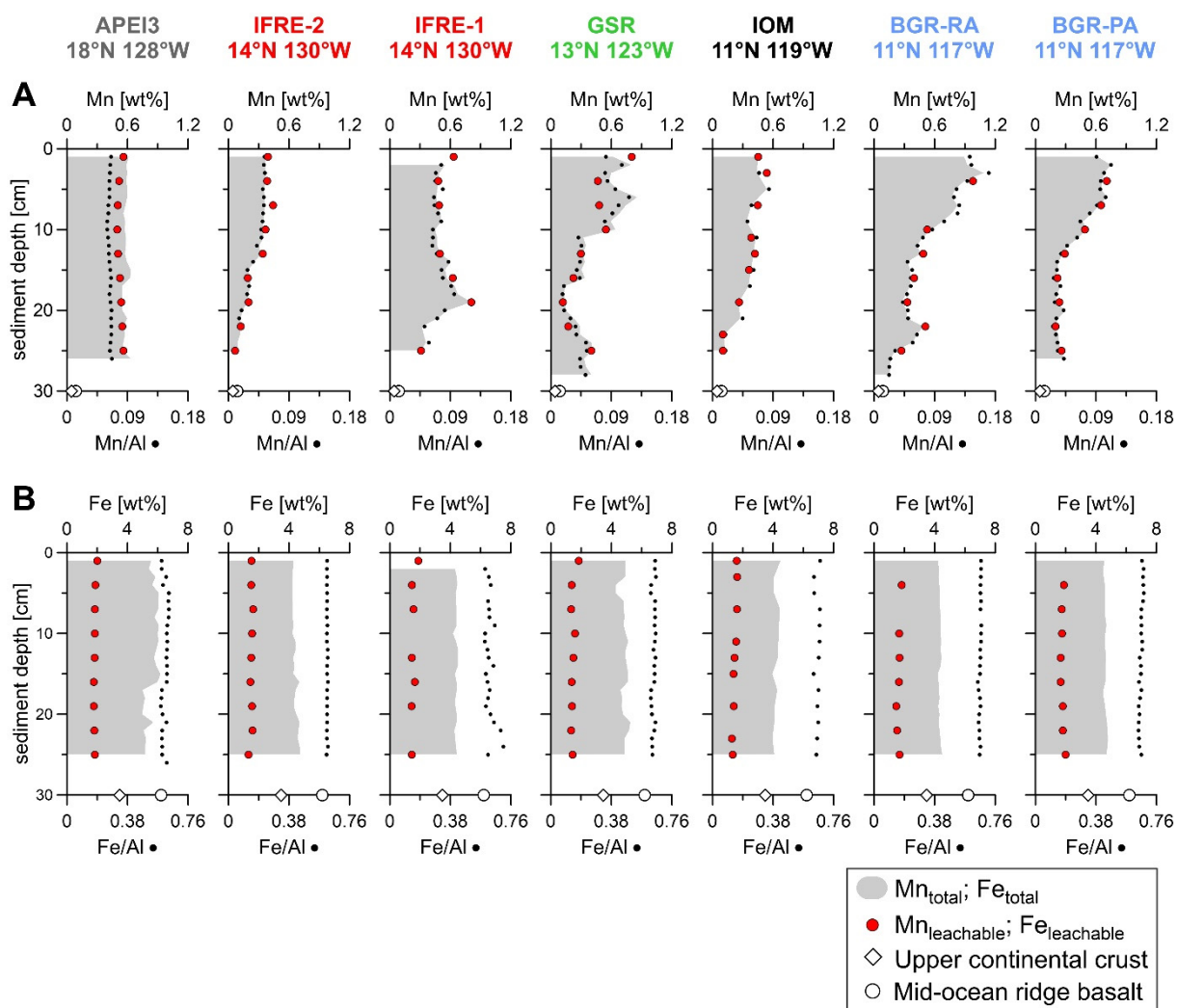


Figure 3: Bulk sediment contents of Mn and Fe (Mn_{total} ; Fe_{total}), total leachable contents of Mn and Fe ($Mn_{leachable}$; $Fe_{leachable}$) using the combined leaching protocol (Table 2) and Mn_{total}/Al_{total} and Fe_{total}/Al_{total} ratios (black dots) for all investigated sites. Average values for the upper continental crust (diamond) and mid-ocean ridge basalts (circle) are taken from Rudnick and Gao (2004) and Klein (2004), respectively.

Leachable Mn and Fe (oxyhydr)oxides

In total, more than 85% of Mn_{total} is extracted ($Mn_{leachable}$) during the combined sequential leaching procedure (Fig. 3A). Only 30–40% of Fe_{total} is leached with the combined extraction scheme ($Fe_{leachable}$; Fig. 3B). The depth profiles of $Mn_{leachable}$ and $Fe_{leachable}$ mimic the bulk contents Mn_{total} and Fe_{total} , respectively, at all sites.

Between 94 and 99% of $Mn_{leachable}$ is leached in the Mn_{mobil} and Mn_{ox1} fractions at all sites (Table 2; Fig. 4A). Mn_{mobil} contents fluctuate between 0.1 and 0.8 wt%, while Mn_{ox1} contents are below 0.2 wt% (Fig. 4A). Between 92 and 96% of $Fe_{leachable}$ is leached in the Fe_{ox1} (including Fe_{mobil}), Fe_{ox2} and Fe_{mag} fractions with contents of 0.25–0.65 wt%, 0.75–1 wt% and 0.22–0.32 wt%, respectively (Table 2; Fig. 4B).

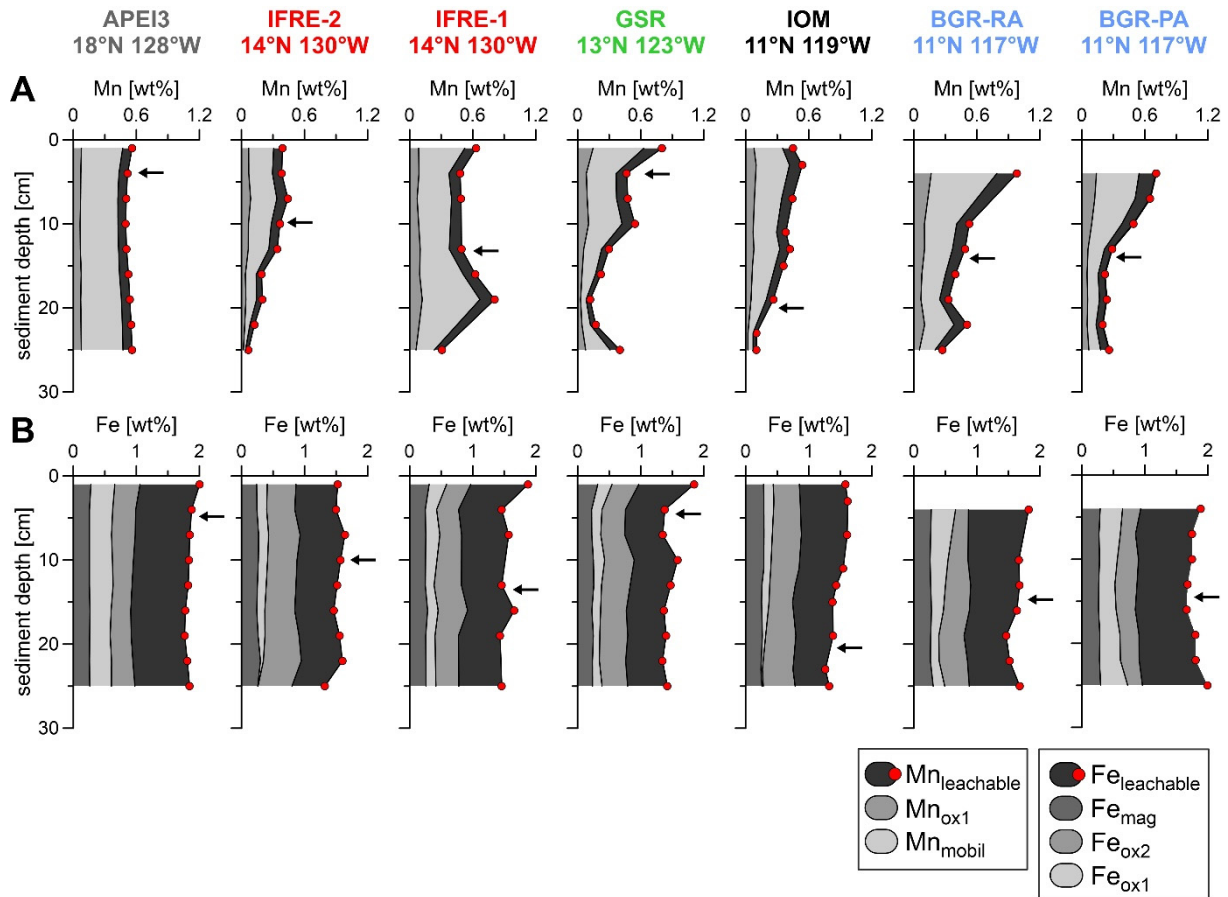


Figure 4: Total leachable contents of Mn and Fe ($Mn_{leachable}$; $Fe_{leachable}$) and contents of sequentially leached Mn oxides (Mn_{mobil} , Mn_{ox1}) and Fe oxides (Fe_{ox1} (including Fe_{mobil}); Fe_{ox2} ; Fe_{mag}) using the combined leaching protocol (Table 2) for all investigated sites. Black arrows indicate the location of the LGM sediment surface based on $^{230}Th/^{231}Pa$ -derived sedimentation rates (Table 1).

Transport-reaction modelling

Transport-reaction simulations were performed for the BGR-RA, IFRE-2 and APEI3 sites (Fig. 5). At current O_2^{bw} of 120 μM at the BGR-RA site, 150 μM at the IFRE-2 site, authigenic Mn(IV) (Mn_{mobil}) precipitates at the current oxic-suboxic redox boundary at 0.5 m and 3.8 m depth, respectively (Table 1; Volz et al., 2018). At current O_2^{bw} of 160 μM at the APEI3 site, oxygen penetrates at least 5.7 m into the sediments, and thus, authigenic Mn_{mobil} is currently not forming in the recovered sediments (Table 1; Volz et al., 2018). At postulated glacial O_2^{bw} of 35 μM , the oxic-suboxic redox boundary is located at 5 cm depth at the BGR-RA and IFRE-2 sites. Consequently, high Mn_{mobil} contents of 0.95 wt% and 0.55 wt% form in the upper 5 cm of the sediments at the BGR-RA and IFRE-2 sites, respectively (Fig. 5A and 5B). Below, Mn_{mobil} contents decrease sharply with depth with a residual Mn_{mobil} fraction below the oxic-suboxic redox boundary at the BGR-RA site. At the APEI3 site, postulated glacial O_2^{bw} of 35 μM induce overall lower oxygen concentrations in the sediments but suboxic conditions are

not reached (Fig. 5C). Therefore, the Mn_{mobil} fraction shows constant contents of 0.45 wt% over depth at the APEI3 site as a result of the initial depositional flux of Mn (see Supplementary Tables S1). The transient transport-reaction model reveals that after the increase of O_2^{bw} from 35 μM to current oxygen levels between 14–15 kyr BP, Mn_{mobil} contents are mostly steady throughout the upper 7 cm of the sediments with Mn_{mobil} contents of almost 0.6 wt% and 0.4 wt% at the BGR-RA and IFRE-2 sites, respectively (Fig. 5). At present, Mn_{mobil} contents are 0.5 wt% and 0.3 wt% at the BGR-RA and IFRE-2 sites, respectively. Below a subsurface Mn_{mobil} peak at 15 cm depth, Mn_{mobil} contents decrease sharply with depth at the BGR-RA and IFRE-2 sites. The transient transport-reaction model for the APEI3 site shows that the depth distribution of Mn_{mobil} remains constant over time (Fig. 5C).

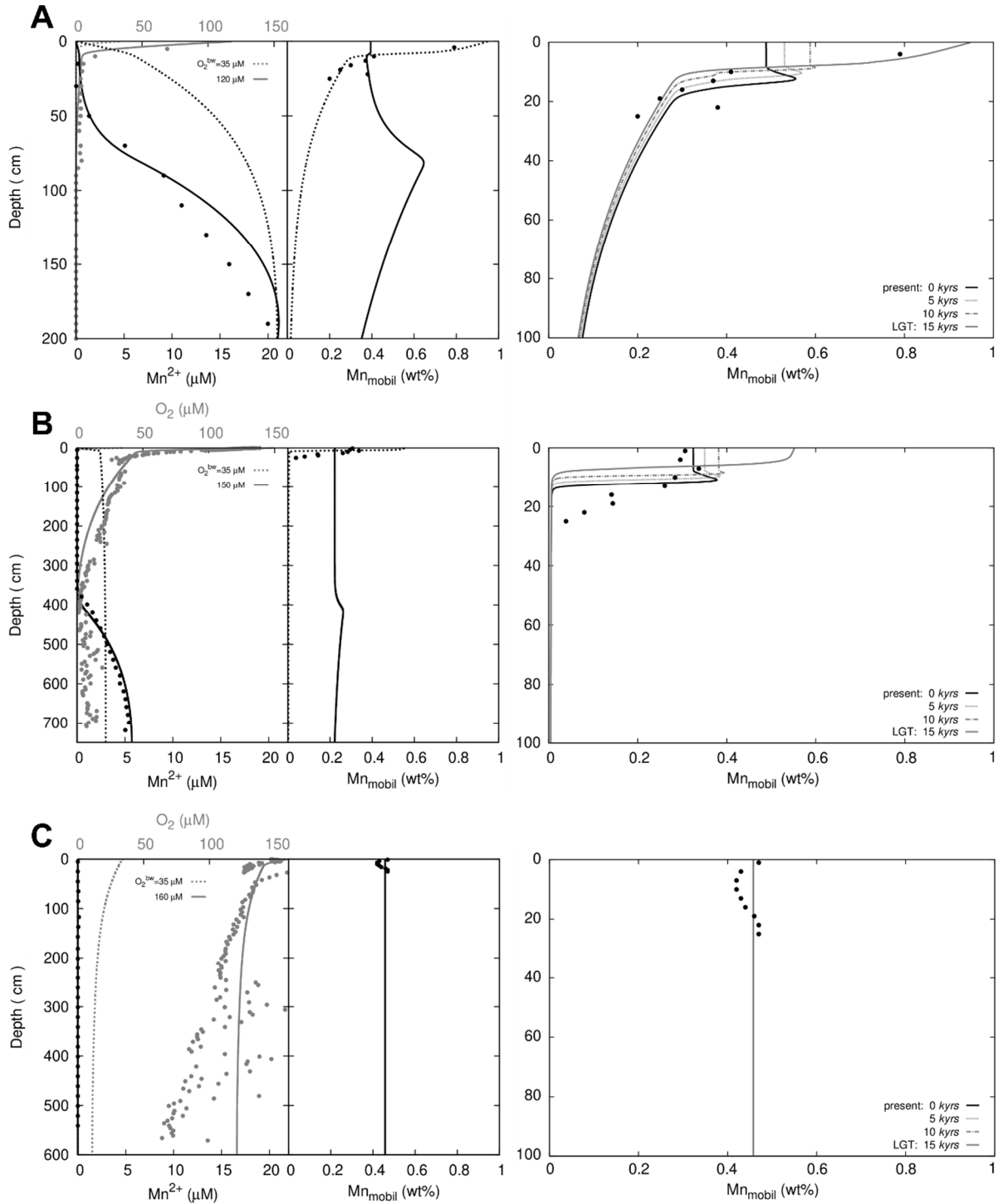


Figure 5: Model results for the BGR-RA site (A), the IFRE-2 site (B) and the APEI3 site (C) including the steady state transport-reaction simulations (left) and the transient transport-reaction simulations (right). Concentrations of oxygen (grey dots) and Mn^{2+} (black dots) for 10-m-long GC cores were taken from Volz et al. (2018). Left: Simulations were performed for bottom-water oxygen concentrations (O_2^{bw}) of 120 μM for the BGR-RA site (solid line), 150 μM for the IFRE-2 site (solid line), 160 μM for the APEI3 site (solid line) and glacial O_2^{bw} of 35 μM (dashed line). Right: Simulations for the depth distribution of Mn_{mobil} after linearly increasing O_2^{bw} from 35 μM to 120 μM (BGR-RA), 150 μM (IFRE-2) and 160 μM (APEI3) between 14–15 kyr. Measured contents of mobilizable Mn(IV) (Mn_{mobil}) are indicated (black dots).

4. Discussion

Past redox changes in sediments of the CCZ

Highest bulk Mn contents (Mn_{total}) of up to 1 wt% occur in the upper 10 cm of the oxic sediments at most of the investigated sites with bulk Mn/Al values well above the average ratios of the upper continental crust and mid-ocean ridge basalts (Fig. 3A; Rudnick and Gao, 2004; Klein, 2004). Similar bulk Mn distribution patterns have been reported for other sites within the CCZ (e.g., Piper, 1988; Mewes et al., 2014; Heller et al., 2018). The modern geochemical zonation in the sediments of the CCZ does not allow for upward diffusing Mn^{2+} to precipitate as authigenic Mn(IV) at a depth shallower than the current OPD below 0.5 m depth (Table 1; Fig. 5; Mewes et al., 2014; 2016; Kuhn et al., 2017; Volz et al., 2018). Therefore, we suggest that the near-surface Mn_{total} maxima (Fig. 3A) has formed under conditions, when the oxic-suboxic redox boundary was located at a shallower depth in the past. This assumption is supported by the applied combined leaching procedure to determine the mobilizable content of Mn (Mn_{mobil}), which represents > 70% of Mn_{total} (Fig. 4A). The Mn_{mobil} fraction has most likely been diagenetically redistributed in the past under suboxic conditions and precipitated as authigenic Mn_{mobil} phase at a shallow oxic-suboxic boundary (e.g., Koschinsky et al, 2001; Mewes et al., 2014). Further indication for past near-surface suboxic conditions in CCZ sediments is provided by surface nodules and buried nodules, which consist of alternating Mn layers of hydrogenetic and suboxic-diagenetic origin (e.g., Halbach et al., 1988; Wegorzewski and Kuhn, 2014; Heller et al., 2018). While hydrogenetic and oxic-diagenetic accretion currently dominates nodule growth, older suboxic-diagenetic Mn growth layers found in nodules of the BGR area provide evidence for a more condensed oxic zone in the past (e.g., Wegorzewski and Kuhn, 2014). In addition, partially dissolved Mn growth layers found in buried nodules in oxic sediments strongly suggest that the OPD must have been located at shallower sediment depth in the past (Heller et al., 2018). The $^{230}Th/^{231}Pa$ -based sedimentation rates at the investigated sites determined by Volz et al. (2018) range between 0.2–1.2 cm kyr⁻¹ (Table 1). Based on these accumulation rates, the sediments containing the authigenic Mn_{mobil} enrichment were usually deposited within the last 20–30 kyr, including sediment deposits from the LGM (Fig. 4A).

Several factors have been reported to potentially cause a more condensed oxic zone than currently observed in the sediments of the CCZ: (1) higher burial fluxes of particulate organic carbon (POC) to the seafloor due to higher surface water productivity, (2) lower O_2^{bw} inducing better preservation of organic matter or 3) a combination of both factors (e.g., Mewes et

al., 2014; Wegorzewski and Kuhn, 2014; Heller et al., 2018). Compared to the CCZ, sediments of the manganese nodule field in the Peru Basin (PB) are currently characterized by much shallower OPDs of 5–15 cm depth (e.g., Haeckel et al., 2001). About twofold higher POC fluxes to the seafloor in the PB compared to the CCZ cause this condensed oxic zone, which allows suboxic-diagenetic accretion to contribute to nodule growth in the PB (e.g., Haeckel et al., 2001; Koschinsky et al., 2001). Thus, in order to have exceeded the flux of oxygen into the sediments and consequently compress the oxic zone in the sediments of the CCZ during the LGP, the POC flux to the seafloor must have been at least twofold higher than today (e.g., Wegorzewski and Kuhn, 2014). Studies have proposed that surface water productivity and POC burial in the eastern Pacific might have been increased during the LGP due to intensified trade winds and therefore enhanced nutrient upwelling and aeolian dust input (e.g., Thomas et al., 2000), which could have affected the sediments of the CCZ. However, a variety of complementary approaches has indicated that ocean dynamics, i.e. upwelling and stratification, impose a strong regulative effect on surface water productivity and the POC export to the deep ocean (e.g., Perks et al., 2002; Winckler et al., 2016; Costa et al., 2017). Studies using biogenic opal, Ba_{xs} and dust fluxes in the equatorial Pacific as well as selectively preserved organic matter compounds in the sediments have shown that higher POC fluxes have occurred after the LGP, namely during the last deglaciation (e.g., Bradtmiller et al., 2006; Anderson et al., 2019). Additionally, there is strong indication that lower O_2^{bw} have prevailed in the eastern Pacific during the LGP due to changes in ocean circulation rather than enhanced POC burial (e.g., Perks et al., 2002; Winckler et al., 2016; Costa et al., 2017). Throughout the eastern Pacific Ocean, independent proxies have provided evidence for lower O_2^{bw} during the LGP, including (1) sub-surface solid-phase Mn enrichments (Mangini et al., 1990), (2) the enrichment of authigenic U(IV) in LGP deposits (e.g., Jaccard et al., 2009; Bradtmiller et al., 2010; Jacobel et al., 2017), (3) the carbon isotope composition and I/Ca ratios in planktonic foraminifera (e.g., Hoogakker et al., 2018) and (4) geochemical proxies for the differences in POC rain rate and the preservation of organic compounds (Anderson et al., 2019). Although the glacial bottom water was not suboxic, which has been suggested by Mangini et al. (1990), oxygen was probably mostly consumed in the sediments as a result of significantly lower O_2^{bw} than today (Jaccard et al., 2009; Hoogakker et al., 2018; Anderson et al., 2019).

Diagenetic Mn mobilization during the last glacial period

In order to assess whether lower glacial O_2^{bw} may have facilitated the development of a shallow oxic-suboxic redox boundary, we have performed steady state transport-reaction modelling for the BGR-RA, IFRE-2 and APEI3 sites (Fig. 5). Furthermore, we used a transient

model to simulate the authigenic Mn_{mobil} depth distribution during the downward migration of the oxic-suboxic boundary at the last glacial termination ~ 15 kyr ago (LGT; Fig. 5; e.g., Hoogakker et al., 2018). Hoogakker et al. (2018) and Anderson et al. (2019) have reconstructed low O_2^{bw} for the LGM in the eastern equatorial Pacific within the range of 35–55 μM , which we have applied for the glacial scenario in the transport-reaction model (Supplementary Table S1). For the transient approach, we assumed that O_2^{bw} increased between 14–15 kyr from 35 μM to current oxygen levels of 120 μM at the BGR-RA site, 150 μM at the IFRE-2 site, and 160 μM at the APEI3 site (Volz et al., 2018; Hoogakker et al., 2018). The initial depositional flux of Mn (oxyhydr)oxides was assumed to be independent of O_2^{bw} and has been estimated based on the terrigenous-free bulk Mn accumulation rate at the APEI3 site, where Mn(IV) most probably has not been diagenetically redistributed after deposition as indicated by the lack of a surface Mn enrichment (Figs. 3A and 4A; further discussed in the next section). In a study on the effects of progressive O_2^{bw} depletion on biogeochemical processes and element fluxes in estuarine sediments, Katsev et al. (2007) have considered that a fraction of upward diffusing Mn^{2+} , which is released into the bottom water re-precipitates as hydrogenetic Mn(IV) phases. Our steady state transport-reaction model for the glacial scenario indicates that due to relatively slow reaction kinetics during the oxidation of Mn^{2+} at the oxic-suboxic boundary in the uppermost 5 cm of the sediments, a fraction of Mn^{2+} might diffuse into the bottom water (Fig. 5; Table 3). Therefore, we have adapted the recycling coefficient introduced by Katsev et al. (2007) assuming that 60% of Mn^{2+} , which diffuses into the bottom water is oxidized and re-precipitates hydrogenetically as Mn_{mobil} . The remaining 40% of upward diffusing Mn^{2+} may accumulate onto nodules at the sediment-water interface (SWI), contributing to the nodule growth via suboxic-diagenetic accretion (e.g., Wegorzewski and Kuhn, 2014). At the BGR-RA site, comparably high Mn_{mobil} contents of 0.8 wt% at ~ 4 cm depth are probably dominated by hydrogenetically precipitated Mn_{mobil} (Fig. 4A). The content of Mn_{mobil} may be underestimated as we have not considered the pool of Mn_{mobil} in nodules at the sediment surface and in buried nodules in the transport-reaction model. For the precipitation of authigenic Mn_{mobil} at the oxic-suboxic boundary in the upper few centimeters of the LGP sediments, the choice of the bioturbation coefficient becomes crucial (see Supplementary Fig. S1). Based on the transport-reaction model presented in Volz et al. (2018), we have assumed bioturbation coefficients of $0.5 \text{ cm}^2 \text{ yr}^{-1}$ for all simulated sites with logarithmically declining bioturbation coefficients below O_2^{bw} of $62.5 \mu\text{M}$ as suggested by Katsev et al. (2007).

Table 3: Model-derived downward O₂ fluxes and upward Mn²⁺ fluxes [$\mu\text{mol cm}^{-2} \text{yr}^{-1}$] at the sediment-water interface for glacial bottom-water oxygen concentrations (O₂^{bw}) of 35 μM (e.g., Hoogakker et al., 2018; Anderson et al., 2019) and current O₂^{bw} of 120 μM at the BGR-RA site, 150 μM at the IFRE-2 site and 160 μM at the APEI3 site (Volz et al., 2018).

| Site | O ₂ ^{bw} | O ₂ flux | Mn ²⁺ flux |
|---------------|------------------------------|---------------------|-----------------------|
| BGR-RA | 35 μM | 5.976 | -0.052 |
| BGR-RA | 120 μM | 6.009 | -0.003 |
| IFRE-2 | 35 μM | 4.215 | -0.037 |
| IFRE-2 | 150 μM | 4.537 | -6E-5 |
| APEI3 | 35 μM | 0.327 | -6E-6 |
| APEI3 | 160 μM | 0.324 | -1E-7 |

Due to current Mn²⁺ upward fluxes of less than 0.04 ng cm⁻² yr⁻¹, low amounts of authigenic Mn_{mobil} precipitate at ~ 80 cm and at 400 cm depth at the BGR-RA and IFRE-2 sites, respectively, while authigenic Mn_{mobil} is presently not precipitating at the APEI3 site due to an entirely oxic sediment column (Fig. 5; Mogollón et al., 2016; Volz et al., 2018). At lower O₂^{bw} of ~ 100 μM , the redox boundary reaches the lowermost bioturbated layer at ~ 7 cm depth at the BGR-RA and IFRE-2 sites with diffusive upward fluxes of Mn²⁺ at the SWI (Fig. 5; Table 3). Assuming that 40% of upward diffusing Mn²⁺ at the SWI accrete onto nodules (Katsev et al., 2007), the suboxic-diagenetic Mn²⁺ flux into the nodules is about 1.2 $\mu\text{g cm}^{-2} \text{yr}^{-1}$. This Mn²⁺ flux is in the same range as the suboxic-diagenetic nodule accumulation rates for surface nodules adjacent to the BGR-RA site, which was estimated as 2 $\mu\text{g cm}^{-2} \text{yr}^{-1}$ (Wegorzewski and Kuhn, 2014). Once O₂^{bw} drop below 62.5 μM , the bioturbated layer reaches oxygen levels at which bioturbation decreases (e.g., Diaz and Rosenberg, 1995; Katsev et al., 2007). Consequently, authigenic Mn_{mobil} is efficiently precipitated at the oxic-suboxic boundary in the upper few centimeters of the sediments at the BGR-RA and IFRE-2 sites (see Supplementary Fig. S1). At glacial O₂^{bw} of 35 μM , the oxic-suboxic boundary was located in the upper 5 cm of the sediments where authigenic Mn_{mobil} precipitated (Fig. 5). As expected, all Mn_{mobil} is reductively dissolved and mobilized under suboxic conditions at the IFRE-2 site, while a fraction of Mn_{mobil} remains in the sediment below the oxic-suboxic boundary at the BGR-RA site (Fig. 5). Depending on the degradability of the labile TOC fraction, it can be entirely consumed during aerobic respiration or may be further degraded during the dissimilatory reduction of Mn (oxyhydr)oxides (e.g., Froelich et al., 1979; Arndt et al., 2013). Associated with the lateral gradient of POC fluxes to the seafloor (Fig. 1; Table 1; Volz et al., 2018), the degradation coefficient for the labile TOC fraction may be higher at the BGR-RA site than at the IFRE-2 site (see Supplementary Table S1). Thus, the labile TOC fraction is completely degraded during aerobic respiration at the BGR-RA site, while Mn_{mobil} is reductively dissolved

in the suboxic zone at the IFRE-2 site as a result of incomplete consumption of the labile TOC fraction during aerobic respiration (Fig. 5).

The LGM sediment surface was buried with sedimentation rates of 0.65 and 0.48 cm kyr⁻¹ at the BGR-RA and IFRE-2 sites, respectively (Table 1; Fig. 6; Volz et al., 2018). During the enhancement of ocean ventilation during the last deglaciation (e.g., Hoogakker et al., 2018), the LGM sediment surface was located at about 3 cm depth at the BGR-RA and IFRE-2 sites (Fig. 6). As diagenetic conditions were at steady state with O₂^{bw} of 35 μM between 21–15 kyr, the Mn_{mobil} depth distribution remained the same during this time (Figs. 5 and 6). Increasing O₂^{bw} at the LGT caused the downward migration of the oxic-suboxic boundary, where only small amounts of authigenic Mn_{mobil} precipitated (Figs. 5 and 6). After the re-establishment of bioturbation during increasing oxygen concentrations in the sediments, the Mn_{mobil} maximum was probably mixed within the bioturbated upper 7 cm of the sediments over time (Figs. 5 and 6).

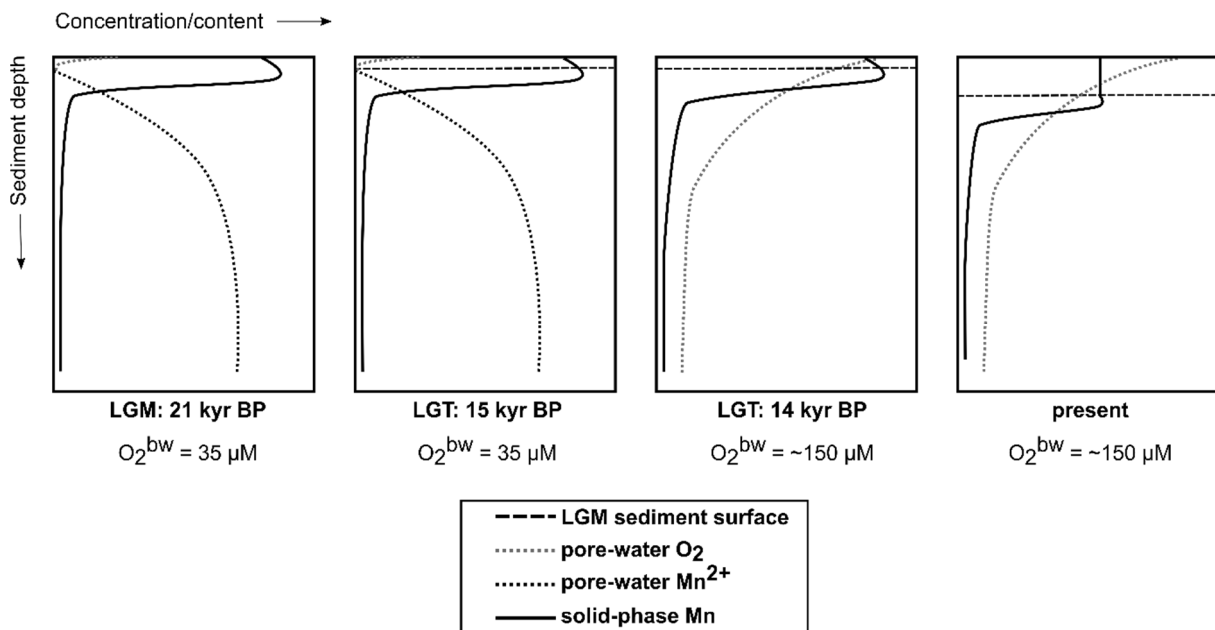


Figure 6: Conceptual model for the depth distribution of authigenic Mn(IV) (Mn_{mobil}) since the last glacial maximum (LGM) 21 kyr before present (BP) and under current geochemical conditions in the sediments of the CCZ. During the last glacial termination (LGT) between 14–15 kyr BP, bottom-water oxygen concentrations O₂^{bw} increase from 35 μM to ~ 150 μM within 1000 years.

Spatial variation in sediment redox conditions during the LGP

The observed Mn_{mobil} enrichments in the uppermost 10 cm of the sediments at most of the investigated sites in the CCZ indicates that diagenetic redistribution of Mn has occurred widespread throughout the NE Pacific (Figs. 3 and 4; Mewes et al., 2014). In contrast, Mn_{mobil}

contents are constant throughout the upper 25 cm at the APEI3 site, suggesting that Mn(IV) has not been diagenetically mobilized at this site in the past (Figs. 3 and 4). The depth position of the oxic-suboxic boundary in the sediments is controlled by the burial flux of POC, O_2^{bw} , availability of Mn (oxyhydr)oxides and sedimentation rate (e.g., Froelich et al., 1979; Burdige and Gieskes, 1983; Gingele and Kasten, 1994). Compared to the other investigated sites within the CCZ, the POC flux to the seafloor at the APEI3 site is almost twofold lower (e.g., Lutz et al., 2007; Volz et al., 2018). Therefore, the sediments at the APEI3 site are currently dominated by an extensive oxic zone, which penetrates more than 5.7 m into the sediment (Table 1). At this location, low POC fluxes to the seafloor of $1 \text{ mg } C_{org} \text{ m}^{-2} \text{ d}^{-1}$ in combination with low sedimentation rates of 0.2 cm kyr^{-1} result in TOC burial rates that are two- to threefold lower than at the BGR-RA and IFRE-2 sites (Table 1; Volz et al., 2018). Due to these significantly lower carbon burial rates, the sediments at the APEI3 site have most likely not reached suboxic conditions at glacial O_2^{bw} of $35 \text{ } \mu\text{M}$, and thus, did not experience significant suboxic-diagenetic Mn mobilization (Figs. 3A and 5C). This assumption is consistent with nodules at the sediment surface of the APEI3 site, which are significantly smaller than at the sites within the exploration areas (Table 1). These small nodules most likely have been formed exclusively by hydrogenetic and oxic-diagenetic accretion and not via an alternation of hydrogenetic and suboxic-diagenetic accumulation as observed at the other study sites in the CCZ (Halbach et al., 1988; Wegorzewski and Kuhn, 2014; Heller et al., 2018). These findings are in agreement with a study on nodules and surface sediments from the adjacent APEI6 area, where the nodules have formed exclusively by hydrogenetic and oxic-diagenetic growth (Menendez et al., 2018). Almost constant Mn_{mobil} contents in the uppermost 15 cm of the sediments in the APEI6 area further indicate that Mn has not been subject to suboxic mobilization (Menendez et al., 2018).

The enrichment of authigenic U(IV) in glacial deposits at several locations throughout the Pacific further indicates that the oxic-suboxic redox boundary was located at shallow depth during glacial periods (e.g., Jaccard et al., 2009; Bradtmiller et al., 2010; Jacobel et al., 2017), and thus, reductive Fe(III) dissolution may have occurred during the LGP in sediments of some areas in the deep Pacific Ocean (e.g., Korff et al., 2016). Thus, postulated glacial O_2^{bw} of $35 \text{ } \mu\text{M}$ may have caused redox conditions in the sediments of the CCZ allowing for the reductive dissolution of Fe(III). Bulk Fe contents (Fe_{total}) at the investigated sites are in good agreement with other studies, which have reported 4–7 wt% Fe for surface sediments of the CCZ (e.g., Piper, 1988). Only 30–40% of Fe_{total} are extracted during the entire combined leaching process ($Fe_{leachable}$; Fig. 3B; Table 2), while the remaining 60–70% of Fe_{total} are most likely bound to clay minerals (e.g., Rateev et al., 1969). The contents of the Fe(oxyhydr)oxide phases

do not vary significantly over depth at all investigated sites with mostly constant proportions of Fe_{ox1} , Fe_{ox2} and Fe_{mag} (Fig. 4B). Thus, even with significantly lower glacial O_2^{bw} , sediment redox conditions did not go beyond Mn reduction and post-depositional Fe redistribution did most likely not occur within the surface sediments of the CCZ. These findings are in line with the study of Heller et al. (2018) on buried nodules of the CCZ, which shows that Mn layers are partly dissolved while reductive mobilization of Fe upon burial did not occur.

5. Conclusion

We have studied surface sediments from six sites located in European contract areas for the exploration of polymetallic nodules within the eastern Clarion-Clipperton Zone in the NE Pacific Ocean and one site north of the CCZ in an Area of Particular Environmental Interest (APEI3). Except for the APEI3 site, all sites show bulk solid-phase Mn maxima of up to 1 wt% in the uppermost 10 cm of the sediments. Through the application of a combined leaching protocol for the sequential extraction of both mobilizable Mn (oxyhydr)oxides and various Fe (oxyhydr)oxide pools, we show that the surface sediment bulk Mn maxima are dominated (> 70%) by easily mobilizable Mn(IV). Due to oxygen penetration depths of > 0.5 m, the determined mobilizable Mn(IV) enrichments cannot have formed diagenetically under modern redox conditions. Thus, the mobilizable Mn(IV) fraction may have been formed by diagenetic relocation induced by more reducing redox conditions in the past. Lower bottom-water oxygen concentrations (O_2^{bw}) have been suggested to have prevailed basin-wide in the Pacific Ocean during the last glacial period (LGP). As a consequence, the oxic zone in the sediments was probably more condensed. Using a steady-state transport-reaction model, we demonstrate that at proposed glacial O_2^{bw} of 35 μ M, the oxic-suboxic redox boundary is located at a much shallower sediment depth than at present. Under these conditions, authigenic Mn(IV) precipitated in the upper 5 cm of the sediments, while a fraction of upward diffusing Mn^{2+} possibly contributes to the suboxic-diagenetic nodule growth. Transient transport-reaction modelling reveals that with the onset of ocean ventilation at the glacial termination 15 kyr ago, (1) the oxic-suboxic boundary shifted downward to current sediment depths, while (2) the authigenic Mn(IV) peak was mixed into subsequently depositing Holocene sediments by bioturbation. The absence of a mobilizable Mn(IV) maximum in the surface sediments of the APEI3 site indicates that the oxic zone was not as compressed during the LGP at this site due to two- to threefold lower carbon burial rates than at the sites located within the contract areas. As the APEI3 site differs significantly with respect to geochemical conditions as well as nodule size and coverage, it is not representative for the sites located in the European contract areas. Although evidence has been provided that reducing sediment redox conditions have allowed

for dissimilatory Fe(III) reduction to occur at several locations in the Pacific during the LGP, our data on sequentially extracted Fe (oxyhydr)oxides indicate that Fe was not diagenetically redistributed in the sediments of our study sites.

This study represents the first baseline study on the redox cycling of Mn and Fe in deep-sea sediments of the CCZ and advances our knowledge about past changes in the oxygenation state of deep-waters of the Pacific Ocean. Our findings provide important aspects, which may improve the interpretation of Pacific sedimentary archives, and, more precisely, contribute to the long-standing discussion about the origin of Mn-rich layers widely observed in glacial deep-sea sediments.

Acknowledgements

We thank captain Lutz Mallon, the crew and the scientific party of RV SONNE cruise SO239 for the technical and scientific support. Thanks to Jennifer Ciomber, Benjamin Löffler and Vincent Ozegowski for their participation in sampling and analysis onboard. For analytical support in the home laboratory and during data evaluation we are grateful to Ingrid Stimac, Olaf Kreft, Dennis Köhler, Ingrid Dohrmann (all at AWI). Special thanks to Dr. Matthias Haeckel (GEOMAR), Prof. Dr. Gerhard Bohrmann (MARUM, University of Bremen), Dr. Timothy G. Ferdelman (MPI Bremen), Dr. Walter Geibert (AWI) and Dr. Gerard Versteegh for much appreciated discussions.

This study is funded by the Bundesministerium für Bildung und Forschung (BMBF Grant 03F0707G) as part of the JPI-Oceans pilot action “Ecological Aspects of Deep-Sea Mining (MiningImpact)”. We acknowledge further financial support from the Helmholtz Association (Alfred Wegener Institute Helmholtz Centre for Polar and Marine Research). The data are available via the data management portal OSIS-Kiel and the geological data network PANGAEA.

References

- Anderson, R.F., Sachs, J.P., Fleisher, M.Q., Allen, K.A., Yu, J., Koutavas, A., Jaccard, S.L., 2019. Deep-sea oxygen depletion and ocean carbon sequestration during the last ice age. *Global Biogeochem. Cycles* 33, 301–317. doi:10.1029/2018GB006049.
- Arndt, S., Jørgensen B.B., LaRowe D.E., Middelburg, J.J., Pancost R.D., Regnier P., 2003. Quantifying the degradation of organic matter in marine sediments: A review and synthesis, *Earth Sci. Rev.* 123, 53–86. doi.org/10.1016/j.earscirev.2013.02.008.
- Berger, W.H., Finkel, R.C., Killingley, J.S., Marching, V., 1983. Glacial-Holocene transition in deep sea sediments: Manganese spike in the east-equatorial Pacific. *Nature* 303, 231–233.
- Boudreau, B.P., 1996. The diffusive tortuosity of fine-grained unlithified sediments, *Geochim. Cosmochim. Acta* 60, 3139–3142. doi: 10.1016/0016-7037(96)00158-5.
- Boudreau, B.P., 1997a. A one-dimensional model for bed-boundary layer particle exchange. *J. Mar. Syst.* 11, 279–303. doi:10.1016/S0924-7963(96)00127-3.
- Boudreau, B. P., 1997b. Diagenetic models and their implementation: Modelling transport and reactions in aquatic sediments. Springer, Berlin, Heidelberg, New York.
- Bradtmiller, L.I., Anderson, R.F., Sachs, J.P., Fleisher, M.Q., 2010. A deeper respired carbon pool in the glacial equatorial Pacific Ocean. *Earth Planet. Sci. Lett.* 299, 417–425.
- Bradtmiller, L.I., Anderson, R.F., Fleisher, M.Q., Burckle, L.H., 2006. Diatom productivity in the equatorial Pacific Ocean from the last glacial period to the present: A test of the silicic acid leakage hypothesis. *Paleoceanography* 21, PA4201. doi:10.1029/2006PA001282.
- Burdige, D.J., Gieskes, J.M., 1983. A pore water/solid phase diagenetic model for manganese in marine sediments. *Am. J. Sci.* 283, 29–47.
- Costa, K.M., Jacobel, A.W., McManus, J.F., Anderson, R.F., Winckler, G., Thiagarajan, N., 2017. Productivity patterns in the equatorial Pacific over the last 30,000 years. *Global Biogeochem. Cycles* 31(5), 850–865. <https://doi.org/10.1002/2016GB005579>.
- Diaz, R., Rosenberg, R., 1995. Marine benthic hypoxia: A review of its ecological effects and the behavioural response of benthic macrofauna. *Oceanogr. Mar. Biol. Annu. Rev.* 33, 245–303.
- Finney, B.P., Lyle, M.W., 1988. Sedimentation at MANOP Site H (eastern equatorial Pacific) over the past 400,000 years: climatically induced redox variations and their effects on transition metal cycling. *Paleoceanography* 3, 169–189.
- Froelich, P.N., Klinkhammer, G.P., Bender, M.L., Luedke, L.A., Heath, G.R., Cullen, C., Dauphin, P., Hammond, D., Hartmann, B., Maynard, V., 1979. Early oxidation of organic matter in pelagic sediments of the Eastern Equatorial Pacific, suboxic diagenesis. *Geochim. Cosmochim. Acta* 43, 1075–1090.
- Gingele, F.X., Kasten, S., 1994. Solid-phase manganese in Southeast Atlantic sediments: Implications for the paleoenvironment. *Mar. Geol.* 121, 317–332.
- Haeckel, M., König, I., Riech, V., Weber, M.E., and Suess, E., 2001. Pore water profiles and numerical modelling of biogeochemical processes in Peru Basin deep-sea sediments. *Deep. Res. Part II Top. Stud. Oceanogr.* 48, 3713–3736. doi:10.1016/S0967-0645(01)00064-9.
- Halbach, P., Friedrich, G., von Stackelberg, U. (eds.), 1988. The manganese nodule belt of the Pacific Ocean. Enke, Stuttgart.

- Heller, C., Kuhn, T., Versteegh, G.J., Wegorzewski, A.V., Kasten, S., 2018. The geochemical behavior of metals during early diagenetic alteration of buried manganese nodules. *Deep-Sea Res. Part I* 142, 16–33.
- Hoogakker, B.A.A., Lu, Z., Umling, N., Jones, L., Zhou, X., Rickaby, R.E.M., Thunell, R., Cartapanis, O., Galbraith, E., 2018. Glacial expansion of oxygen-depleted seawater in the eastern tropical Pacific. *Nature* 562(7727), 410–413. 10.1038/s41586-018-0589-x.
- Jaccard, S.L., Galbraith, E.D., Martínez-García, A., Anderson, R.F., 2016. Covariation of deep Southern Ocean oxygenation and atmospheric CO₂ through the last ice age. *Nature* 530, 207–210.
- Jaccard, S.L., Galbraith, E.D., Sigman, D.M., Haug, G.H., Francois, R., Pedersen, T.F., Dulski, P., Thierstein, H.R., 2009. Subarctic Pacific evidence for a glacial deepening of the oceanic respired carbon pool. *Earth Planet. Sci. Lett.* 277, 156–165. doi:10.1016/j.epsl.2008.10.017.
- Jacobel, A.W., McManus, J.F., Anderson, R.F., Winckler, G., 2017. Repeated storage of respired carbon in the equatorial Pacific Ocean over the last three glacial cycles. *Nat. Commun.* 8. doi:10.1038/s41467-017-01938-x.
- Katsev, S., Chaillou, G., Sundby, B., Mucci, A., 2007. Effects of progressive oxygen depletion on sediment diagenesis and fluxes: A model for the lower St. Lawrence River Estuary. *Limnol. Oceanogr.* 52. doi:10.4319/lo.2007.52.6.2555.
- Klein, E.M., 2004. Geochemistry of the Igneous Oceanic Crust. In: *Treatise on Geochemistry* (eds. Holland, H.D., Turekian, K.K.). Elsevier, Amsterdam, 3. 433–463.
- Korff, L., von Dobeneck, T., Frederichs, T., Kasten, S., Kuhn, G., Gersonde, R., Diekmann, B., 2016. Cyclinic magnetite dissolution in Pleistocene sediments of the abyssal northwest Pacific Ocean: Evidence for glacial oxygen depletion and carbon trapping. *Paleoceanography* 31, 600–624. doi:10.1002/2015PA002882.
- Koschinsky, A., Fritsche, U., Winkler, A., 2001. Sequential leaching of Peru Basin surface sediment for the assessment of aged and fresh heavy metal associations and mobility. *Deep-Sea Res. Part II* 48, 3683–3699.
- Kuhn, T., Versteegh, G.J.M., Villinger, H., Dohrmann, I., Heller, C., Koschinsky, A., Kaul, N., Ritter, S., Wegorzewski, A.V., Kasten, S., 2017. Widespread seawater circulation in 18–22 Ma oceanic crust: Impact on heat flow and sediment geochemistry. *Geology* 45, 799–802. doi: 10.1130/G39091.1.
- Lutz, M.J., Caldeira, K., Dunbar, R.B., Behrenfeld, M.J., 2007. Seasonal rhythms of net primary production and particulate organic carbon flux to depth describe the efficiency of biological pump in the global ocean. *J. Geophys. Res.* 112, C10011. doi:10.1029/2006JC003706.
- Lynn, D.C., Bonatti, E., 1965. Mobility of manganese in diagenesis of deep-sea sediments. *Mar. Geol.* 3, 457–474.
- Mangini, A., Jung, M., Laukenmann, S., 2001. What do we learn from peaks of uranium and of manganese in deep sea sediments? *Mar. Geol.* 177(1–2), 63–78. 10.1016/s0025-3227(01)00124-4
- Mangini, A., Eisenhauer, A., Walter, P., 1990. Response of manganese in the ocean to the climatic cycles in the Quaternary. *Paleoceanography*, 5(5), 811–821.

- Martínez Arbizu, P., Haeckel, M., 2015. RV SONNE Fahrtbericht / Cruise Report SO239: EcoResponse Assessing the Ecology, Connectivity and Resilience of Polymetallic Nodule Field Systems, Balboa (Panama) – Manzanillo (Mexico) 11.03.–30.04.2015 (Report No. doi:10.3289/GEOMAR_REP_NS_25_2015). GEOMAR Helmholtz-Zentrum für Ozeanforschung, Kiel, Germany.
- Menendez, A., James, R.H., Lichtschlag, A., Connelly, D., Peel, K., 2018. Controls on the chemical composition on ferromanganese nodules in the Clarion-Clipperton Fracture Zone, eastern equatorial Pacific. *Mar. Geol.* 409, 1–14.
- Mewes, K., Mogollón, J.M., Picard, A., Rühlemann, C., Eisenhauer, A., Kuhn, T., Ziebis, W., Kasten, S., 2016. Diffusive transfer of oxygen from seamount basaltic crust into overlying sediments: An example from the Clarion-Clipperton Fracture Zone. *Earth Planet. Sci. Lett.* 433, 215–225. doi:10.1016/j.epsl.2015.10.028.
- Mewes, K., Mogollón, J.M., Picard, A., Rühlemann, C., Kuhn, T., Nöthen, K., Kasten, S., 2014. Impact of depositional and biogeochemical processes on small scale variations in nodule abundance in the Clarion-Clipperton Fracture Zone. *Deep-Sea Res. Part I: Oceanogr. Res. Pap.* 91, 125–141. doi:10.1016/j.dsr.2014.06.001.
- Mogollón, J.M., Mewes, K., Kasten, S., 2016. Quantifying manganese and nitrogen cycle coupling in manganese-rich, organic carbon-starved marine sediments: Examples from the Clarion-Clipperton fracture zone. *Geophys. Res. Lett.* 43, 2016GL069117. doi:10.1002/2016GL069117.
- Perks, H.M., Charles, C.D., Keeling, R.F., 2002. Precessionally forced productivity variations across the equatorial Pacific. *Paleoceanography* 17, 1037. doi:10.1029/2000PA000603.
- Piper, D.Z., 1988. The metal oxide fraction of pelagic sediment in the equatorial North Pacific Ocean: A source of metals in ferromanganese nodules. *Geochim. Cosmochim. Acta* 52, 2127–2145.
- Poulton, S.W., Canfield, D.E., 2005. Development of a sequential extraction procedure for iron: implications for iron partitioning in continentally derived particulates. *Chem. Geol.* 214, 209–221.
- Presti, M., Barbara, L., Denis, D., Schmidt, S., De Santis, L., Crosta, X., 2011. Sediment delivery and depositional patterns off Adélie Land (East Antarctica) in relation to late Quaternary climatic cycles. *Mar. Geol.* 284(1–4), 96–113. doi:10.1016/j.margeo.2011.03.012.
- Rapin, F., Tessier, A., Campbell, P.G., Carigan, R., 1986. Potential artifacts in the determination of metal partitioning in sediments by a sequential extraction procedure. *Environ. Sci. Tech.* 20, 836–840.
- Rateev, M.A., Gorbunova, Z.N., Lisitzyn, A.P., Nosov, G.L., 1969. The distribution of clay minerals in the Oceans. *Sedimentology* 13.
- Rudnick, R.L., Gao, S. 2004. Composition of the continental crust. In: *Treatise on Geochemistry* (eds. Holland, H.D., Turekian, K.K.). Elsevier, Amsterdam, 3. 1–65.
- Rühlemann, C., Baumann, L., Blöthe, M., Bruns, A., Eisenhauer, A., Georgens, R., Hansen, J.W., Heuer, L., Kasten, S., Kuhn, T., Martinez-Arbizu, P., Milyutina, M., Mewes, K., Picard, A., Rutkowski, J., Schott, T., Schückel, S., Schückel, U., Schwarz-Schampera, U., Tiltack, A., Utecht, C., Wohrl, C., Zoch, D., 2010. Cruise report SO-205 MANGAN, Microbiology, Paleoceanography and Biodiversity in the Manganese Nodule Belt of the equatorial Pacific, p. 248.

- Soetaert, K., Meysman, F., 2012. Reactive transport in aquatic ecosystems: Rapid model prototyping in the open source software R. *Environ. Model. Softw.* 32, 49–60. doi:10.1016/j.envsoft.2011.08.011.
- Soetaert, K., Petzoldt, T., & Setzer, R. W., 2010. Solving differential equations in R: package deSolve. *J. Stat. Softw.* 33, 1–25.
- Thomas, E., Turekian, K.K., Wei, K.-Y., 2000. Productivity control of fine particle transport to equatorial Pacific sediment. *Global Biogeochem. Cycles* 14, 945–955.
- Volz, J., Mogollón, J.M., Geibert, W., Martínez Arbizu, P., Koschinsky, A., Kasten, S., 2018. Natural spatial variability of depositional conditions, biogeochemical processes and element fluxes in sediments of the eastern Clarion-Clipperton Zone, Pacific Ocean. *Deep-Sea Res. Part I* 140, 159–172.
- Wegorzewski, A.V., Kuhn, T., 2014. The influence of suboxic diagenesis on the formation of manganese nodules in the Clarion Clipperton nodule belt of the Pacific Ocean. *Mar. Geol.* 357, 123–138. doi:10.1016/j.margeo.2014.07.004.
- Winckler, G., Anderson, R.F., Jaccard, S.L., Marcantonio, F., 2016. Ocean dynamics, not dust, have controlled equatorial Pacific productivity over the past 500,000 years. *PNAS* 113, 6119–6124. doi:10.1073/pnas.1600616113.
- Wu, L., Wang, R., Xiao, W., Krijgsman, W., Li, Q., Ge, S., Ma, T., 2018. Late Quaternary Deep Stratification-Climate Coupling in the Southern Ocean: Implications for Changes in Abyssal Carbon Storage. *Geochemistry, Geophysics, Geosystems* 19(2), 379–395. 10.1002/2017GC007250.

CHAPTER V:

Impact of small-scale disturbances on geochemical conditions, biogeochemical processes and element fluxes in sediments of the eastern Clarion-Clipperton Zone, Pacific Ocean

Jessica B. Volz^a, Laura Haffert^b, Matthias Haeckel^b, Andrea Koschinsky^c, Sabine Kasten^{a,d}

^a Alfred Wegener Institute Helmholtz Centre for Polar and Marine Research, Bremerhaven, Germany (corresponding author: jessica.volz@awi.de, Tel: +49 471 4831 1842)

^b GEOMAR Helmholtz Centre for Ocean Research Kiel, Kiel, Germany

^c Jacobs University Bremen, Department of Physics and Earth Sciences, Bremen, Germany

^d University of Bremen, Faculty of Geosciences, Klagenfurter Strasse, Bremen, Germany

Manuscript under review at *Biogeosciences*.

Abstract

The thriving interest in harvesting deep-sea mineral resources, such as polymetallic nodules, calls for environmental impact studies, and ultimately, for regulations for environmental protection. Industrial-scale deep-sea mining of polymetallic nodules most likely has severe consequences for the natural environment. However, the effects of mining activities on deep-sea ecosystems, sediment geochemistry and element fluxes are still poorly conceived. Predicting the environmental impact is challenging due to the scarcity of environmental baseline studies as well as the lack of mining trials with industrial mining equipment in the deep sea. Thus, currently we have to rely on small-scale disturbances simulating deep-sea mining activities as a first-order approximation to study the expected impacts on the abyssal environment.

Here, we investigate surface sediments in disturbance tracks of seven small-scale benthic impact experiments, which have been performed in four European contract areas for the exploration of polymetallic nodules in the Clarion-Clipperton Zone (CCZ). These small-scale disturbance experiments were performed 1 day to 37 years prior to our sampling program in the German, Polish, Belgian and French contract areas using different disturbance devices. We show that the depth distribution of solid-phase Mn in the upper 20 cm of the sediments in the CCZ provides a reliable tool for the determination of the disturbance depth, which has been proposed in a previous study (Paul et al., 2018). We found that the upper 5–15 cm of the sediments were removed during various small-scale disturbance experiments in the different exploration contract areas. Transient transport-reaction modelling for the Polish and German contract areas reveals that the removal of the surface sediments is associated with the loss of reactive labile organic carbon. As a result, oxygen consumption rates decrease significantly after the removal of the surface sediments, and consequently, oxygen penetrates up to tenfold deeper into the sediments inhibiting denitrification and Mn(IV) reduction. Our model results show that the post-disturbance geochemical re-equilibration is controlled by diffusion until the reactive labile TOC fraction in the surface sediments is partly re-established and the biogeochemical processes commence. While the re-establishment of bioturbation is essential, the geochemical re-equilibration of the sediments is ultimately controlled by the burial rates of organic matter. Hence, under current depositional conditions, the new geochemical equilibrium in the sediments of the CCZ is reached only on a millennia scale even for these small-scale disturbances simulating deep-sea mining activities.

1. Introduction

The accelerating global demand for metals and rare-earth elements are driving the economic interest in deep-sea mining (e.g., Glasby, 2000; Hoagland et al., 2010; Wedding et al., 2015). Seafloor minerals of interest include (1) polymetallic nodules (e.g., Mero, 1965), (2) massive sulfide deposits (e.g., Scott, 1987) and (3) cobalt-rich crusts (e.g., Halkyard, 1985). As the seafloor within the Clarion-Clipperton Zone (CCZ) in the NE Pacific holds one of the most extensive deposits of polymetallic nodules with considerable base metal quantities, commercial exploitation of seafloor mineral deposits may focus on the CCZ (e.g., Mero, 1965; Halbach et al., 1988; Rühlemann et al., 2011; Hein et al., 2013; Kuhn et al., 2017a). The exploration, and ultimately, industrial exploitation of polymetallic nodules demands for international regulations for the protection of the environment (e.g., Halfar and Fujita, 2002; Glover and Smith, 2003; Davies et al., 2007; van Dover, 2011; Ramirez-Llodra et al., 2011; Boetius and Haeckel, 2018). The International Seabed Authority (ISA) is responsible for regulating the exploration and exploitation of marine mineral resources as well as for protecting and conserving the marine environment beyond the exclusive economic zones of littoral states from harmful effects (ISA, 2010). The ISA has granted temporal contracts for the exploration of polymetallic nodules in the CCZ, engaging all contract holders to explore resources, test mining equipment and assess the environmental impacts of deep-sea mining activities (ISA 2010; Lodge et al., 2014; Madureira et al., 2016).

Although a considerable number of environmental impact studies have been conducted in different nodule fields, the prediction of environmental consequences of potential future deep-sea mining is still difficult (e.g., Ramirez-Llodra et al., 2011; Jones et al., 2017; Gollner et al., 2017; Cuvelier et al., 2018). In case of the CCZ, the evaluation of the environmental impact of deep-sea mining activities is challenging due to the fact that baseline data on the natural spatial heterogeneity and temporal variability of depositional conditions, benthic communities and the biogeochemical processes in the sediments are scarce (e.g., Mewes et al., 2014; 2016; Vanreusel et al., 2016; Mogollón et al., 2016; Juan et al., 2018; Volz et al., 2018; Menendez et al., 2018; Hauquier et al., 2019). In addition, there is no clear consensus on the most appropriate mining techniques for the commercial exploitation of nodules, and technical challenges due to the inaccessibility of nodules at great water depths between 4000–5000 m have limited the deployment of deep-sea mining systems until today (e.g., Chung, 2010; Jones et al., 2017).

The physical removal of nodules as hard-substrate habitats has severe consequences for the nodule-associated sessile fauna as well as the mobile fauna (Bluhm, 2001; Smith et al., 2008; Purser et al., 2016; Vanreusel et al., 2016). With slow nodule growth rates of a few millimeters per million years (e.g., Halbach et al., 1988; Kuhn et al., 2017a), the deep-sea fauna may not recover for millions of years (Vanreusel et al., 2016; Jones et al., 2017; Gollner et al., 2017; Stratmann et al., 2018). In addition to the removal of deep-sea fauna as well as seafloor habitats, the exploitation of nodules is associated with (1) the removal, mixing and re-suspension of the upper 4 cm to more than several tens of centimeters of the sediments, (2) the re-deposition of material from the suspended sediment plume, and (3) potentially also the compaction of the surface sediments due to weight of the nodule collector (Thiel, 2001; Oebius et al., 2001; König et al., 2001; Grupe et al., 2001; Radziejewska, 2002; Khripounoff et al., 2006; Cronan et al., 2010; Paul et al., 2018; Gillard et al., 2019). The wide range of estimations for the disturbance depth may be associated with (1) various devices used for the deep-sea disturbance experiments (Brockett and Richards, 1994; Oebius et al., 2001; Jones et al., 2017), (2) distinct sediment properties in different nodule fields of the Pacific Ocean (e.g., Cronan et al., 2010; Hauquier et al., 2019) as well as (3) different approaches for the determination of the disturbance depth (e.g., Oebius et al., 2001; Grupe et al., 2001; Khripounoff et al., 2006). Based on the observation that bulk solid-phase Mn contents decrease over depth in the surface sediments of the DISCOL area, Paul et al. (2018) have suggested that the depth distribution of solid-phase Mn and associated metals (e.g., Mo, Ni, Co, Cu) could be used to trace the sediment removal by disturbances. In addition, other solid-phase properties such as organic carbon contents (TOC), porosity and radioisotopes may be suitable for the determination of the disturbance depth.

The most reactive TOC compounds, found in the bioturbated uppermost sediment layer, are the main drivers for early diagenetic processes (e.g., Froelich et al., 1979; Berner, 1981) and are expected to be removed during mining activities (König et al., 2001). Thus, strong biogeochemical implications can be expected in the sediments after deep-sea mining activities. König et al. (2001) have applied numerical modelling to study the consequences of the removal of the upper 10 cm of the sediments in the DISCOL area in the Peru Basin. They showed that the degradation of TOC during aerobic respiration, denitrification and Mn(IV) reduction may be decreased for centuries strongly influencing the oxygen penetration depth (OPD).

Here, we investigate the impact of various small-scale disturbances on geochemical conditions, biogeochemical processes and element fluxes in surface sediments of the CCZ. These small-scale disturbance tracks were created up to 37 years ago in four different European

contract areas for the exploration of polymetallic nodules, including the German BGR (Bundesanstalt für Geowissenschaften und Rohstoffe) area, the Belgian GSR (Global Sea Mineral Resources NV) area, the French IFREMER (Institut Français de Recherche pour l'Exploitation de la Mer) area and the Polish IOM (InterOceanMetal) area. In order to determine the disturbance depths of the different small-scale disturbances in the different European contract areas, we correlate the depth distributions of solid-phase Mn and total organic carbon (TOC) between disturbed sites and undisturbed reference sites using the Pearson product-moment correlation coefficient. On this basis, we (1) assess the short- and long-term consequences of small-scale disturbances on redox zonation and element fluxes and (2) determine how much time is needed for the re-establishment of a geochemical equilibrium in the sediments after the disturbances. Our work includes pore-water and solid-phase analyses as well as the application of a transient one-dimensional transport-reaction model.

2. Material and methods

As part of the European JPI Oceans pilot action “Ecological Aspects of Deep-Sea Mining (MiningImpact)”, multiple corer (MUC) and gravity corer (GC) sediment cores were taken during RV SONNE cruise SO239 in March/April 2015 from undisturbed sites in various European contract areas for the exploration of polymetallic nodules (Fig. 1; Table 1; Martínez Arbizu and Haeckel, 2015). These undisturbed reference sites were chosen in close proximity (< 5 km) to small-scale disturbance experiments for the simulation of deep-sea mining, which were created up to 37 yr ago and re-visited during cruise SO239 (Table 1; see Sect. 2.1.1.; Martínez Arbizu and Haeckel, 2015). The sampling of sediments in the disturbance tracks of these experiments were conducted by video-guided push-coring (PC) between 1 day and 37 yr after the initial disturbances using the ROV Kiel 6000 (Table 1; Fig. 2; Martínez Arbizu and Haeckel, 2015).

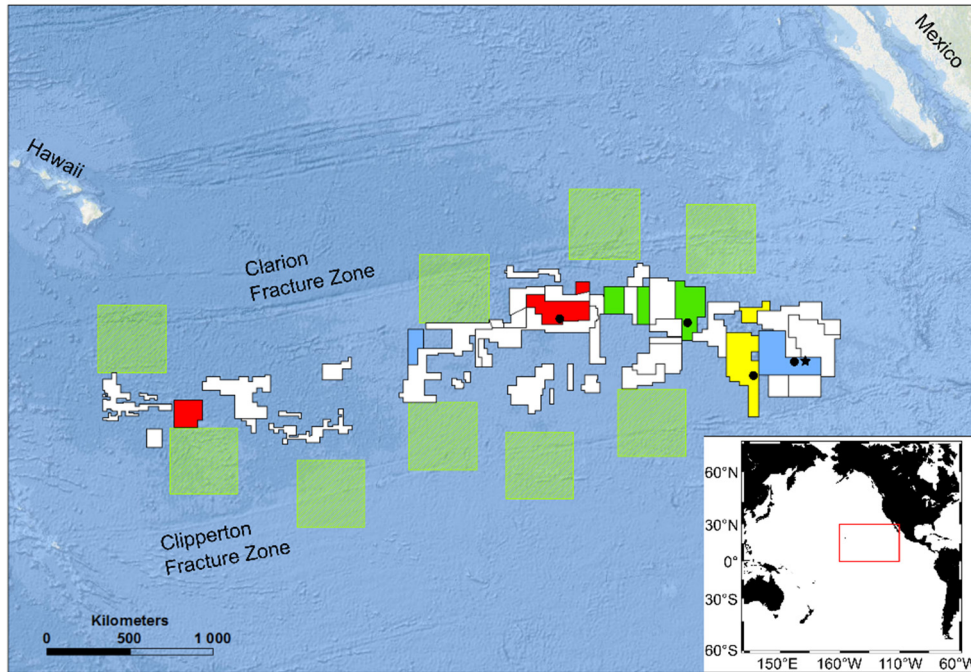


Figure 1: Sampling sites (black circles, black star) in various European contract areas for the exploration of manganese nodules within the Clarion-Clipperton Fracture Zone (CCZ). Investigated stations are located in the German BGR area (blue), eastern European IOM area (yellow), Belgian GSR area (green) and French IFREMER area (red). The two stations within the German BGR area are located in the “prospective area” (BGR-PA, black star) and in the “reference area” (BGR-RA, black circle). The contract areas granted by the International Seabed Authority (ISA) are surrounded by nine Areas of Particular Environmental Interest (APEI), which are excluded from any mining activities (green shaded squares). Geographical data provided by the ISA.

Table 1: MUC and PC cores investigated in this study including information on geographic position, water depth, type and age of the disturbances (years: yr; months: mth; days: d).

| Area | Site | Coring device | Disturbance device/type | Disturbance age | Latitude [N] | Longitude [W] | Water depth [m] |
|----------------|------|---------------|-------------------------|-----------------|--------------|---------------|-----------------|
| BGR-PA | 39 | MUC | - | - | 11°50.64' | 117°03.44' | 4132.0 |
| BGR-PA | 41 | PC | EBS ¹ | 3 yr | 11°50.92' | 117°03.77' | 4099.2 |
| BGR-RA | 62 | GC | - | - | 11°49.12' | 117°33.22' | 4312.2 |
| BGR-RA | 64 | PC | EBS ² | 1 d | 11°48.27' | 117°30.18' | 4332 |
| BGR-RA | 66 | MUC | - | - | 11°49.13' | 117°33.13' | 4314.8 |
| IOM | 84 | MUC | - | - | 11°04.73' | 119°39.48' | 4430.8 |
| IOM | 87 | GC | - | - | 11°04.54' | 119°39.83' | 4436 |
| IOM | 101 | PC | IOM-BIE ³ | 20 yr | 11°04.38' | 119°39.38' | 4387.4 |
| GSR | 121 | MUC | - | - | 13°51.25' | 123°15.3' | 4517.7 |
| GSR | 131 | PC | EBS ² | 1 d | 13°52.38' | 123°15.1' | 4477.6 |
| GSR | 141 | PC | dredge ⁴ | 8 mth | 13°51.95' | 123°15.33' | 4477 |
| IFREMER | 157 | PC | dredge ⁵ | 37 yr | 14°02.06' | 130°07.23' | 4944.5 |
| IFREMER | 161 | PC | EBS ¹ | 3 yr | 14°02.20' | 130°05.87' | 4999.1 |
| IFREMER | 175 | MUC | - | - | 14°02.45' | 130°05.11' | 5005.5 |

¹Epibenthic sledge (EBS) during BIONOD cruises in 2012 onboard L'Atalante (Brenke, 2005; Rühlemann and Menot, 2012; Menot and Rühlemann, 2013)

²Epibenthic sledge (EBS) during RV SONNE cruise SO239 in 2015 (Brenke, 2005; Martínez Arbizu and Haeckel, 2015)

³Benthic impact experiment (BIE); disturbance created with the Deep-Sea Sediment Re-suspension System (DSSRS; e.g., Brockett and Richards, 1994; Kotlinski et al., 1998)

⁴Towed dredge sampling during GSR cruise in 2014 onboard M.V. Mt Mitchell (Jones et al., 2017)

⁵Towed dredge sampling by the Ocean Minerals Company (OMCO) in 1978 onboard Hughes Glomar Explorer (Morgan et al., 1993; Spickermann, 2012)

The different investigated European contract areas within the CCZ include the BGR, IOM, GSR and IFREMER areas. Comprehensive pore-water and solid-phase analyses on the MUC and GC sediment cores from undisturbed sites have been conducted in previous baseline studies and are presented elsewhere (Volz et al., 2018; Volz et al., under review). These analyses include the determination of pore-water oxygen, NO_3^- , Mn^{2+} and NH_4^+ concentrations and contents of total organic carbon (TOC) for MUC and GC sediment cores (Volz et al., 2018) as well as solid-phase bulk Mn contents for the MUC sediment cores (Volz et al., under review). In the framework of this study, we have used these previously published pore-water and solid-phase data as undisturbed reference data for geochemical conditions and sediment composition (Table 1). On this basis, here, we investigate seven small-scale disturbances for the simulation of deep-sea mining (Table 1; see Sect. 2.1.1.; Martínez Arbizu and Haeckel, 2015).

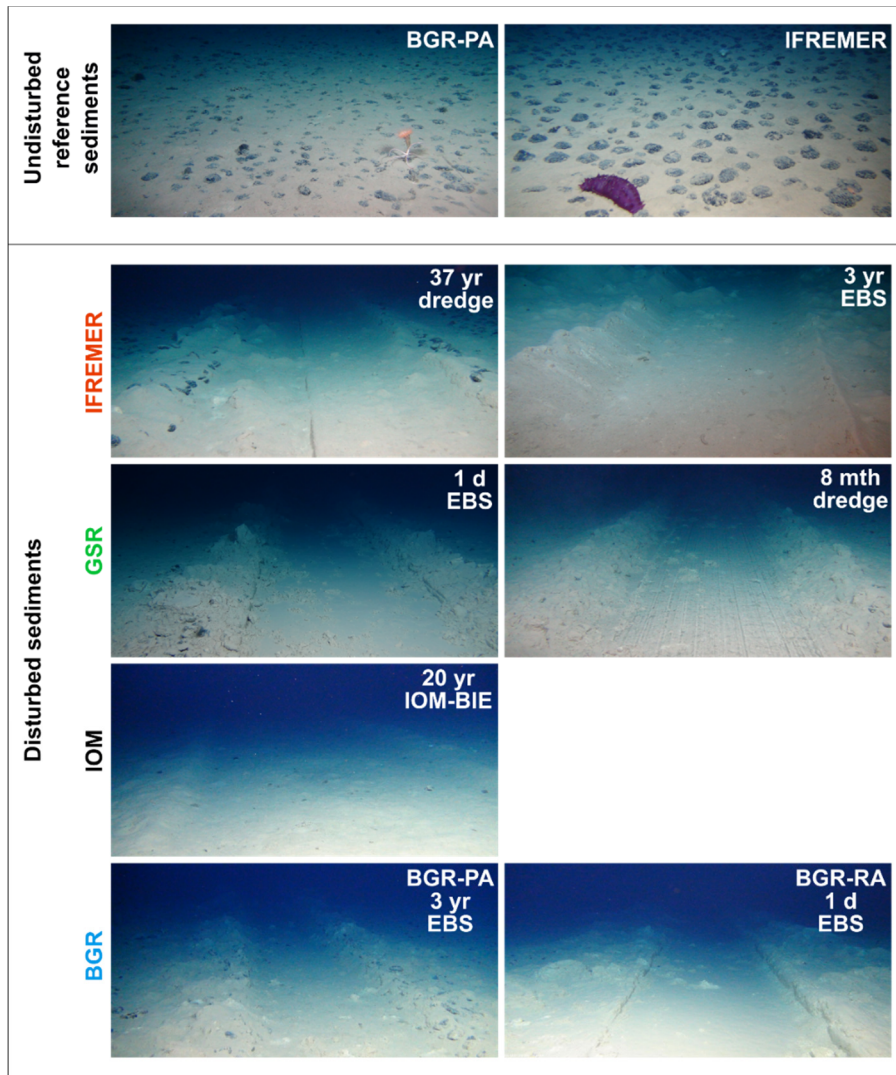


Figure 2: Examples of undisturbed reference sediments in the German BGR-PA area and the French IFREMER area and pictures of small-scale disturbances for the simulation of deep-sea mining within the CCZ, which are investigated in the framework of this study (years: yr; months: mth; days: d). Copyright: ROV KIEL 6000 Team, GEOMAR Helmholtz Centre for Ocean Research Kiel, Germany.

2.1 Site Description

The CCZ is defined by two transform faults, the Clarion Fracture Zone in the north and the Clipperton Fracture Zone in the south and covers an area of about 6 million km² (Fig. 1; e.g., Halbach et al., 1988). The sediments at the investigated sites (Table 1) are dominated by clayey siliceous oozes with various Mn nodule sizes (1–10 cm) and spatial densities (0–30 kg m⁻²) at the sediment surface (Berger, 1974; Kuhn et al., 2012; Mewes et al., 2014; Volz et al., 2018). In order to characterize the investigated sediments with respect to redox zonation, sedimentation rates, fluxes of particulate organic carbon (POC) to the seafloor and bioturbation depths, we have summarized these key parameters, which are originally presented elsewhere, in Table 2 (Volz et al., 2018). Steady state transport-reaction models have shown that aerobic

respiration is the dominant biogeochemical process at all investigated sites, consuming more than 90% of the organic matter delivered to the seafloor (Mogollón et al., 2016; Volz et al., 2018). Below the OPD at more than 0.5 m depth, Mn(IV) and nitrate reduction succeeds in the suboxic zone, where oxygen and sulfide are absent (e.g., Mewes et al., 2014; Mogollón et al., 2016; Kuhn et al., 2017b; Volz et al., 2018). At several sites investigated in this study, including the BGR “reference area” (BGR-RA) and IOM sites, decreasing Mn²⁺ concentrations at depth are probably associated with the oxidation of Mn²⁺ by upward diffusing oxygen circulating through the underlying basaltic crust (Mewes et al., 2016; Kuhn et al., 2017b; Volz et al., 2018).

Table 2: Information of sedimentation rate (Sed. rate), flux of particulate organic carbon (POC) to the seafloor, bioturbation depth (Bioturb. depth), oxygen penetration depth (OPD) based on GC cores from the investigated sites and determined in the study by Volz et al. (2018). Information for the BGR-PA area is taken from an adjacent site (A5-2-SN; 11°57.22’N, 117°0.42’W) studied by Mewes et al. (2014) and Mogollón et al. (2016).

| Area | Sed. rate [cm kyr ⁻¹] | POC flux [mg m ⁻² d ⁻¹] | Bioturb. depth [cm] | OPD [m] |
|---------------|--------------------------------------|---|------------------------|-------------------|
| BGR-PA | ~0.53 ^a | ~6.9 ^a | ~5 ^a | ~2 ^{a,b} |
| BGR-RA | 0.65 | 1.99 | 7 | 0.5 |
| IOM | 1.15 | 1.54 | 13 | 3 |
| GSR | 0.21 | 1.51 | 8 | >7.4 |
| IFRE-1 | 0.64 | 1.47 | 7 | 4.5 |
| IFRE-2 | 0.48 | 1.5 | 8 | 3.8 |
| APEI3 | 0.2 | 1.07 | 6 | >5.7 |

^aMogollón et al. (2016)

^bMewes et al. (2014)

2.1.1 Small-scale disturbances

Since the 1970s, several comprehensive environmental impact studies of deep-sea mining simulations have been carried out in the CCZ, including the Benthic Impact Experiment (BIE; e.g., Trueblood and Ozturgut, 1997; Radziejewska, 2002) and the Japan Deep Sea Impact Experiment (JET; Fukushima, 1995). In addition, numerous small-scale seafloor disturbances have been carried out in the CCZ in the past 40 yr using various tools such as epibenthic sleds (EBS) and dredges (e.g., Vanreusel et al., 2016; Jones et al., 2017). The EBS is towed along the seabed for the collection of benthic organisms (and nodules) thereby also removing the upper few centimeters of the sediments (e.g., Brenke, 2005). In 2015, some of these disturbances were re-visited as part of the BMBF-EU JPI Oceans pilot action “Ecological Aspects of Deep-Sea Mining (MiningImpact)” project in order to evaluate the long-term consequences of such small-scale disturbances on the abyssal benthic ecosystem (Martínez Arbizu and

Haeckel, 2015). For comparison, the Disturbance and Recolonization Experiment (DISCOL), which was conducted in a nodule field in the Peru Basin (PB) in 1989 was re-visited as part of MiningImpact (Boetius, 2015; Greinert, 2015). In the framework of DISCOL, a seafloor area of $\sim 11 \text{ km}^2$ was disturbed with a plough harrow. The impact of the DISCOL experiment was studied 0.5, 3 and 7 yr after the disturbance had been set (e.g., Thiel, 2001).

Comparably small-scale, up to 37 yr old simulations of deep-sea mining in various European contract areas within the CCZ were re-visited in 2015 during the RV SONNE cruise SO239 (Table 1; Fig. 2; Martínez Arbizu and Haeckel, 2015). New small-scale disturbance tracks were created during SO239 in the BGR-RA and in the GSR area “B6” using an EBS in order to add also initial temporal datasets (Table 1; Fig. 2; Martínez Arbizu and Haeckel, 2015). The EBS weighed about 400 kg under normal atmospheric pressure and created a disturbance track of about 1.5 m width (Brenke, 2005). The fresh EBS disturbance tracks in the BGR-RA and GSR areas were re-visited 1 day after their creation. Eight months prior to the cruise SO239, towed dredge sampling was performed in the GSR area by the Belgian contractor (Martínez Arbizu and Haeckel, 2015; Jones et al., 2017). During the BIONOD cruises onboard RV L’Atalante in 2012, the same EBS setup as used during cruise SO239 was deployed in the BGR “prospective area” (BGR-PA) and in the IFREMER area (Table 1; Rühlemann and Menot, 2012; Menot and Rühlemann, 2013; Martínez Arbizu and Haeckel, 2015). In 1995, the Deep-Sea Sediment Re-suspension System (DSSRS) was used during the IOM-BIE (Benthic Impact Experiment) disturbance in the IOM area (Table 1; e.g., Kotlinski and Stoyanova, 1998). The DSSRS weighed 3.2 tons under normal atmospheric pressure and was designed to dredge the seafloor while producing a re-suspended particle plume about 5 m above the seafloor (Brockett and Richards, 1994; Sharma, 2001). Based on the dimensions of the DSSRS device, the disturbance track created during the IOM-BIE disturbance experiment is about 2.5 m wide (Fig. 2; Brockett and Richards, 1994). In 1978, the Ocean Mineral Company (OMCO) created disturbance tracks in the French IFREMER area by towed dredge sampling (Table 1; e.g., Spickermann, 2012).

2.2 Sediment sampling and solid-phase analyses

ROV-operated push cores were sampled at intervals of 1 cm for solid-phase analyses. Bulk sediment data and TOC contents have been corrected after Kuhn (2013) for the interference of the pore-water salt matrix with the sediment composition (Volz et al., 2018). The salt-free volume fraction of the pore water, i.e. the porosity, was determined gravimetrically before and after freeze drying of the wet sediment samples. The salt-corrected

sediment composition c' was calculated from the measured solid-phase composition c using the mass percentage of H_2O of the wet sediment (w), which contains 96.5% H_2O (Eq. (1)).

$$c' = c * \frac{100}{100 - (100 * \frac{(w * \frac{100}{96.5}) - w}{100 - w})} \quad (1)$$

2.2.1 Total acid digestions

Total acid digestions were performed in the microwave system MARS Xpress (CEM) after the protocols by Kretschmer et al. (2010) and Nöthen and Kasten (2011). Approximately 50 mg of freeze-dried, homogenized bulk sediment were digested in an acid mixture of 65% sub-boiling distilled HNO_3 (3 mL), 30% sub-boiling distilled HCl (2 mL) and 40% suprapur® HF (0.5 mL) at ~ 230 °C. Digested solutions were fumed off to dryness, the residue was re-dissolved under pressure in 1 M HNO_3 (5 mL) at ~ 200 °C and then filled up to 50 mL with 1 M HNO_3 . Total bulk Mn and Al contents were determined using inductively coupled plasma optical emission spectrometry (ICP-OES; IRIS Intrepid ICP-OES Spectrometer, Thermo Elemental). Based on the standard reference material NIST 2702 accuracy and precision of the analysis was 3.7% and 3.5% for Mn, respectively (n=67).

2.2.2 Total organic carbon

Total organic carbon (TOC) contents were determined using an Eltra CS2000 element analyzer. Approximately 100 mg of freeze-dried, homogenized sediment were transferred into a ceramic cup and decalcified with 0.5 mL of 10% HCl at 250 °C for 2 h before analysis. Based on an in-house reference material, precision of the analysis was better than 3.7% (n=83).

2.3 Pearson correlation coefficient

In order to determine the disturbance depths, solid-phase bulk Mn contents were correlated between disturbed sediments and undisturbed reference sediments using the Pearson product-moment correlation coefficient r (Eq. (2); Table 1; Pearson, 1895). The Pearson correlation coefficient is a statistical measure of the linear relationship between two arrays of variables with:

$$r = \frac{\sum_{i=1}^n (x - \bar{x})(y - \bar{y})}{\sqrt{\sum_{i=1}^n (x - \bar{x})^2 \sum_{i=1}^n (y - \bar{y})^2}} \quad (2)$$

where n is the sample size, x and y are individual sample points and \bar{x} and \bar{y} are the sample means $\bar{x} = \frac{1}{n} \sum_{i=1}^n x$ and $\bar{y} = \frac{1}{n} \sum_{i=1}^n y$.

While the solid-phase bulk Mn contents of the disturbed sediments were determined in the framework of this study, solid-phase bulk Mn contents from undisturbed reference sediments were taken from Volz et al. (under review). The highest positive linear correlations of solid-phase Mn contents ($r_{\text{Mn}} \sim 1$) between the disturbed sites and the respective undisturbed reference sites (Table 1) were used to determine the depths of the disturbances. In a second step, the same correlation was applied to the TOC contents (r_{TOC}) in order to verify the depth of disturbance. While the TOC contents in the disturbed sediments were determined in the framework of this study, TOC contents from undisturbed reference sediments were taken from Volz et al. (2018).

2.4 Geochemical model setup and reaction network

A transient one-dimensional transport-reaction model (Eq. (3); e.g., Boudreau, 1997; Haeckel et al., 2001) was used (1) to assess the impact of small-scale disturbances on biogeochemical processes, geochemical conditions and element fluxes in sediments of the CCZ and (2) to estimate the time required to establish a new geochemical equilibrium after a small-scale disturbance. We have applied the transient transport-reaction model for the sites in the BGR-RA and IOM areas (Table 1). These sites were chosen due to distinctively different sedimentation rates and OPD (Table 2). We have adapted the steady state transport-reaction model, which was originally presented by Volz et al. (2018) and used pore-water oxygen, NO_3^- , Mn^{2+} and NH_4^+ data as well as TOC contents of GC sediment cores from the same study as undisturbed reference data (Table 1; Table 2). The transient transport-reaction model consists of four aqueous (O_2 , NO_3^- , Mn^{2+} , NH_4^+), four solid species (TOC_{1-3} , MnO_2) and six reactions ($\text{R}_1\text{--R}_6$; Supplementary Table 1) with:

$$\frac{\partial(\vartheta_i C_{i,j})}{\partial t} = \frac{\partial D_{i,j} \vartheta_i \left(\frac{\partial C_{i,j}}{\partial z} \right)}{\partial z} - \frac{\partial \omega_i \vartheta_i C_{i,j}}{\partial z} + \alpha_i \vartheta_i (C_{i,j} - C_{0,j}) + \vartheta_i \sum R_{i,j} \quad (3)$$

where z is sediment depth, and subscripts i, j represent depth and species-dependence, respectively; aqueous or solid species concentration are denoted by C (Supplementary Table 2); D is in case of solutes the effective diffusive mixing coefficient, which has been corrected for tortuosity ($D_{m,i,j}$; Boudreau, 1997). In the case of solids, D represents the bioturbation coefficient (B_i ; Eq. (4)); ϑ is the volume fraction representing the porosity φ for the aqueous phase and $1 - \varphi$ for the solid phase; the velocity of either the aqueous (v) or the solid phase (w) is denoted by the symbol ω ; α_i is the bioirrigation coefficient (0 for solid species; Eq. (5)); and $\sum R_{i,j}$ is the sum of the reactions affecting the given species.

The bioturbation and bioirrigation profiles, i.e. biologically induced mixing of sediment and pore water, respectively, are represented by a modified logistic function:

$$B_i = B_0 \exp\left(\frac{z_{mix}-z_i}{z_{att}}\right) / \left(1 + \exp\left(\frac{z_{mix}-z_i}{z_{att}}\right)\right) \quad (4)$$

$$\alpha_i = \alpha_0 \exp\left(\frac{z_{mix}-z_i}{z_{att}}\right) / \left(1 + \exp\left(\frac{z_{mix}-z_i}{z_{att}}\right)\right) \quad (5)$$

where α_0 and B_0 are constants indicating the maximum bioirrigation and bioturbation intensity at the sediment-water interface; the depth where the bioturbation and bioirrigation intensity is halved is denoted by z_{mix} ; and the attenuation of the biogenically induced mixing with depth is controlled by z_{att} .

Assuming steady-state compaction, the model applies an exponential function that is parameterized according to the available porosity data at each station (e.g., Berner, 1980; Supplementary Fig. 1):

$$\varphi_i = \varphi_\infty (\varphi_0 - \varphi_\infty) \exp(-\beta z) \quad (6)$$

where φ_∞ is the porosity at the ‘infinite depth’, at which point compaction is completed; φ_0 is the porosity at the sediment water interface ($z = 0$); and β is the porosity-attenuation coefficient.

Organic matter was treated in three reactive fractions (3G-model) with first order kinetics. The rate expressions for the reactions (R₁–R₆) include inhibition terms, which are listed together with the rate constants (Supplementary Table 3).

Based on the Pearson correlation coefficient r_{Mn} , we have removed the upper 7 cm of sediments in the transport-reaction model for the IOM-BIE site and the upper 10 cm of sediments in the transport-reaction model for the BGR-RA site. Due to the lack of data on the re-establishment of bioturbation, i.e. the recovery of the bioturbation ‘pump’ after small-scale disturbance experiments, we have tested the effect of different bioturbation scenarios in the transport-reaction model. For the different post-disturbance bioturbation scenarios, we have assumed that bioturbation is inhibited immediately after the disturbance with a linear increase to undisturbed reference bioturbation coefficients (Volz et al., 2018). Based on the work by Miljutin et al. (2011) and Vanreusel et al. (2016), we have assumed that bioturbation should be fully re-established after 100, 200, and 500 yr. As the modelling results for the different time spans were almost identical, we only present here the model that assumes bioturbation is at pre-disturbance intensity 100 yr after the impact (Volz et al., 2018; Supplementary Table 2).

We have applied the transient transport-reaction model under the assumption that the sedimentation rates as well as the POC fluxes to the seafloor remain constant over time (Table 2). The model was coded in MATLAB with a discretization and reaction set-up closely following the steady state model (Volz et al., 2018).

3. Results

3.1 Characterization of disturbed sites

Most of the small-scale disturbances investigated in the framework of this study were created with an EBS (Table 1; Fig. 2). Based on the visual impact inspection of the EBS disturbance tracks in the CCZ, the sediments were mostly pushed aside by the EBS and piled up next to the left and right of the tracks (Fig. 2). In particular, the freshly created 1-day old EBS tracks in the BGR-RA and GSR areas indicate that the sediments were mostly scraped off and accumulated next to the freshly exposed sediment surfaces (Fig. 2). Small sediment lumps occur on top of the exposed sediment surfaces on the EBS tracks, which indicates that some sediment has slid off from the adjacent flanks of the sediment accumulation after the disturbances (Fig. 2). However, the mostly smooth sediment surfaces of the EBS tracks suggest that sediment mixing during the EBS disturbance experiments may be mostly negligible (Fig. 2; Table 1). In the 8-months old dredge track in the GSR area, small furrows occur at the disturbed sediment surface most likely caused by the shape of the dredge (Fig. 2).

3.2 Sediment porosity and solid-phase composition

The sediment porosity shows little lateral variability and ranges between 0.65 and 0.8 throughout the upper 25 cm of the sediments at all investigated disturbed sites (Fig. 3). At the disturbed IOM-BIE site, sediment porosity is about 5% higher in the upper 4 cm of the sediments than below. Total bulk Mn contents in the upper 25 cm of the sediments at the disturbed sites are between 0.1 and 0.9 wt% (Fig. 3). Solid-phase Mn contents decrease with depth at all investigated sites. Total organic carbon (TOC) contents in the upper 25 cm of the sediments at the disturbed sites are within 0.2 and 0.5 wt% (Fig. 3). The TOC contents slightly decrease with depth at all investigated sites.

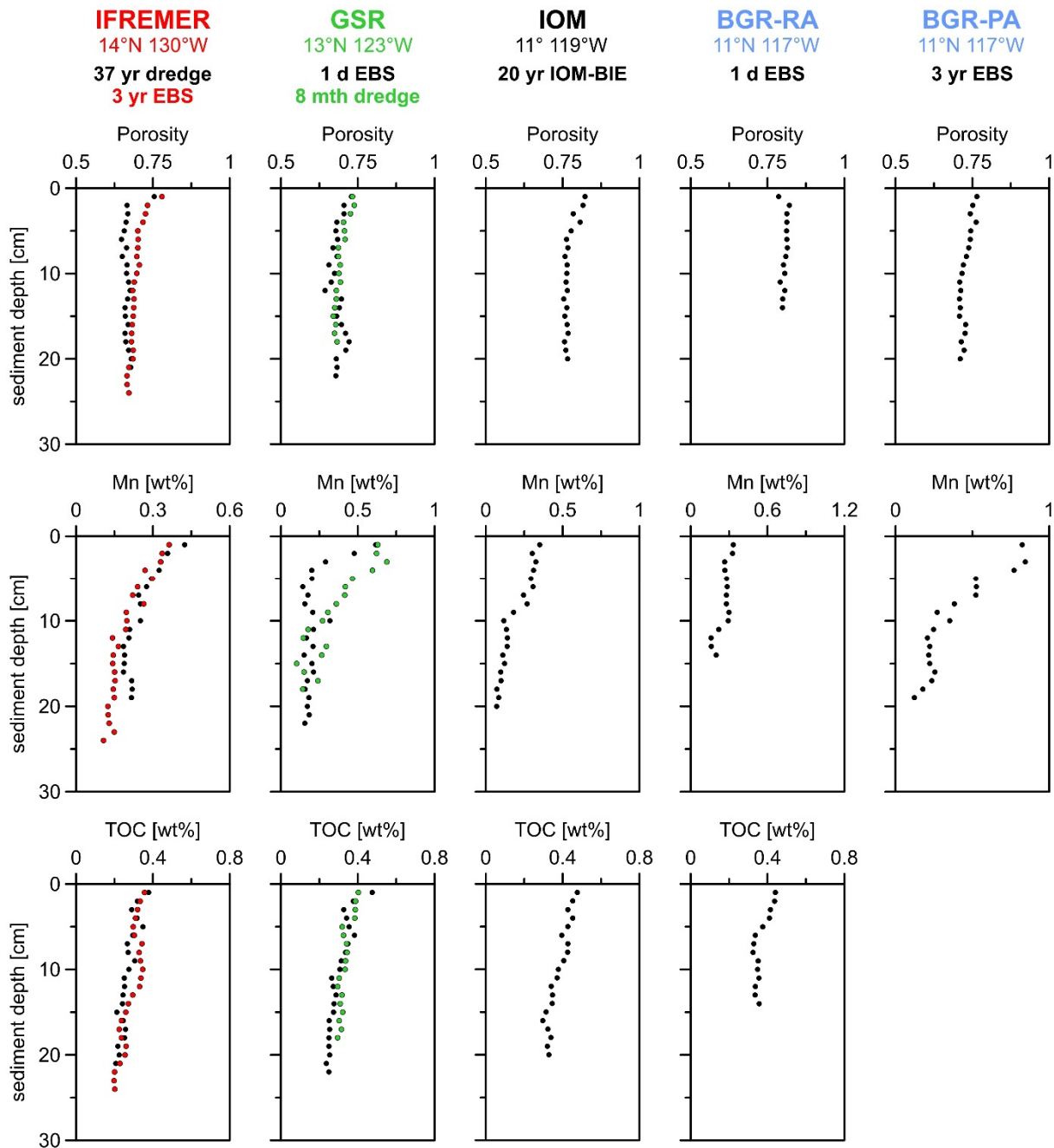


Figure 3: Solid-phase Mn and TOC contents for all disturbed sites investigated in the framework of this study.

3.3 Pearson correlation coefficient and disturbance depths

The Pearson correlation coefficient r_{Mn} for the correlation of solid-phase Mn contents between the disturbed sites and the respective reference sites ranges between 0.72 and 0.97 (Table 3). Based on r_{Mn} , 5–15 cm of sediment has been removed by various disturbance experiments in the different contract areas (Fig. 4). Applying these r_{Mn} -derived disturbance depths for the correlation of the TOC depth distributions between disturbed sites and respective adjacent reference sites gives Pearson correlation coefficients r_{TOC} within 0.73 and 0.91 (Table 3; Fig. 4), which may support the estimates for the disturbance depth based on r_{Mn} . At

the BGR-RA site, the correlation of TOC contents between the disturbed site and the reference site shows negative values. As the sediment porosity in the disturbed sediments correlates well with the porosity in the respective undisturbed reference sediments (Fig. 4), sediment compaction due to the weight of the disturbance device may be negligible during the small-scale disturbances investigated in the framework of this study.

Table 3: Calculated Pearson correlation coefficients r_{Mn} and r_{TOC} for the determination of the disturbance depth of various small-scale disturbances investigated in the framework of this study (compare Table 1).

| Exploration area | Disturbance device/type | Disturbed Site | Reference Site | r_{Mn} | Disturbance depth [cm] | r_{TOC} |
|------------------|-------------------------|----------------|----------------|----------|------------------------|-----------|
| BGR-PA | EBS | 41 | 39 | 0.86 | 5 | - |
| BGR-RA | EBS | 64 | 66 | 0.82 | 15 | -0.4 |
| IOM | IOM-BIE | 101 | 87 | 0.97 | 7 | 0.77 |
| GSR | EBS | 131 | 121 | 0.72 | 6 | 0.88 |
| GSR | dredge | 141 | 121 | 0.88 | 6 | 0.91 |
| IFREMER | dredge | 157 | 175 | 0.74 | 10 | 0.73 |
| IFREMER | EBS | 161 | 175 | 0.93 | 7 | 0.74 |

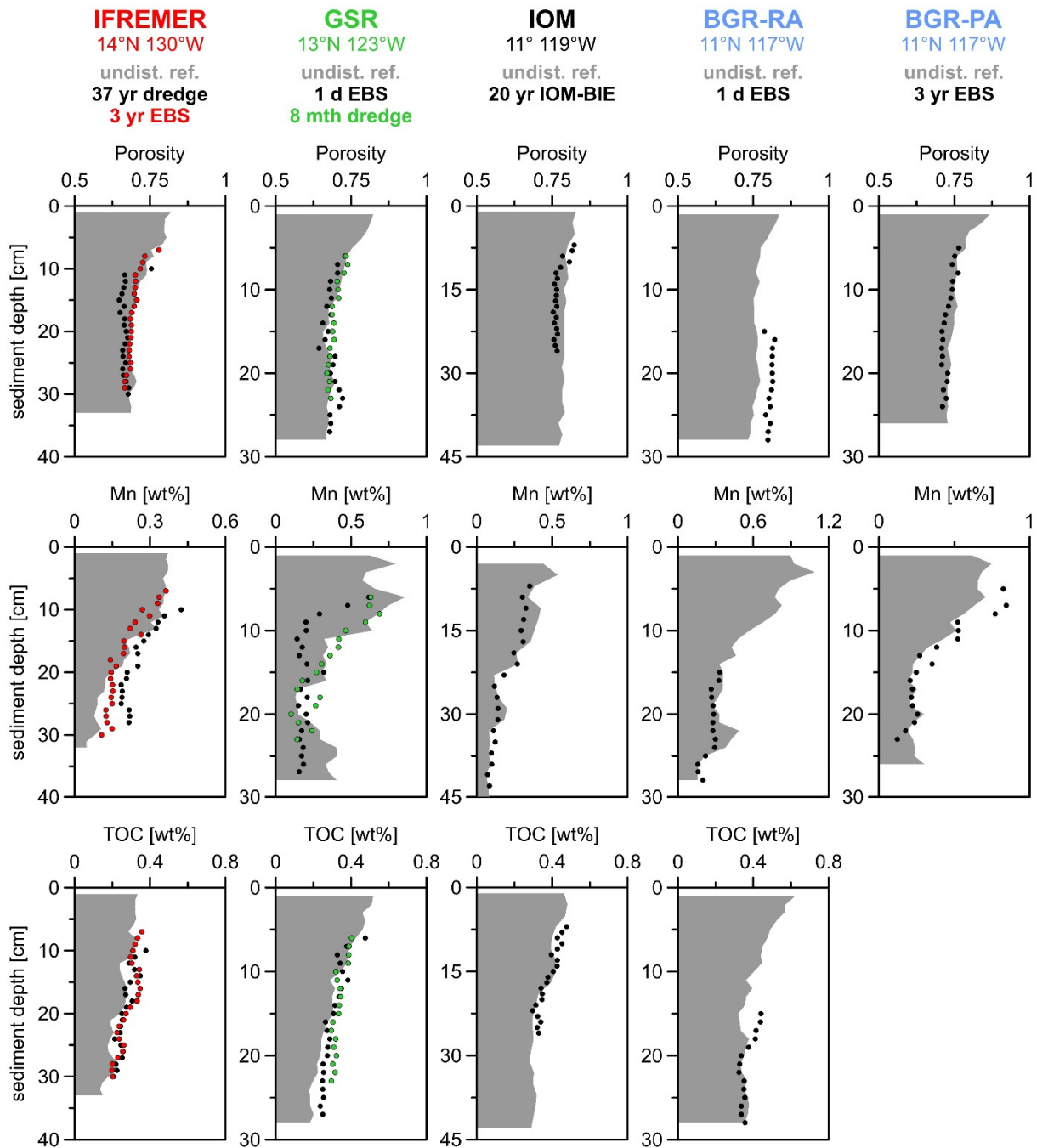


Figure 4: Correlation of solid-phase Mn and TOC contents between the disturbed sites and the respective undisturbed reference sediments (grey shaded profiles) using the disturbance depths determined with the Pearson correlation coefficient (compare Table 3). For the undisturbed reference sediments, solid-phase Mn contents are taken from Volz et al. (under review) and TOC contents are taken from Volz et al. (2018).

3.4 Transport-reaction modelling

The removal of the surface sediments in the transient transport-reaction model for the BGR-RA and IOM-BIE sites is associated with the loss of the reactive labile organic matter (Fig. 5 and 6). About 10 kyr after the removal of the upper 10 cm of the sediments in the model for the BGR-RA site, oxygen penetrates about tenfold deeper into the disturbed sediments than in undisturbed sediments (Table 2; Fig. 5; Volz et al., 2018). At the IOM-BIE site, oxygen reaches the maximum OPD at about 100 yr after the removal of the upper 7 cm of the sediments. At this site, the oxygen front migrates only ~ 1 m deeper than the corresponding OPD in undisturbed sediments (Table 2; Fig. 5; Volz et al., 2018). As a consequence of deeper OPDs at both sites, the oxic-suboxic redox boundary is located at greater depth, with a significant consumption of pore-water Mn^{2+} in the path of the oxygen front. The NH_4^+ concentrations are also being diminished, reaching minima within 100–1000 yr and 1–10 yr after the disturbance experiments in the BGR-RA and IOM areas, respectively. The trend for the NO_3^- is more complicated with lower concentrations during the downward migration of the OPD and augmented concentrations once oxygen concentrations reach their maximum (Figs. 5 and 6).

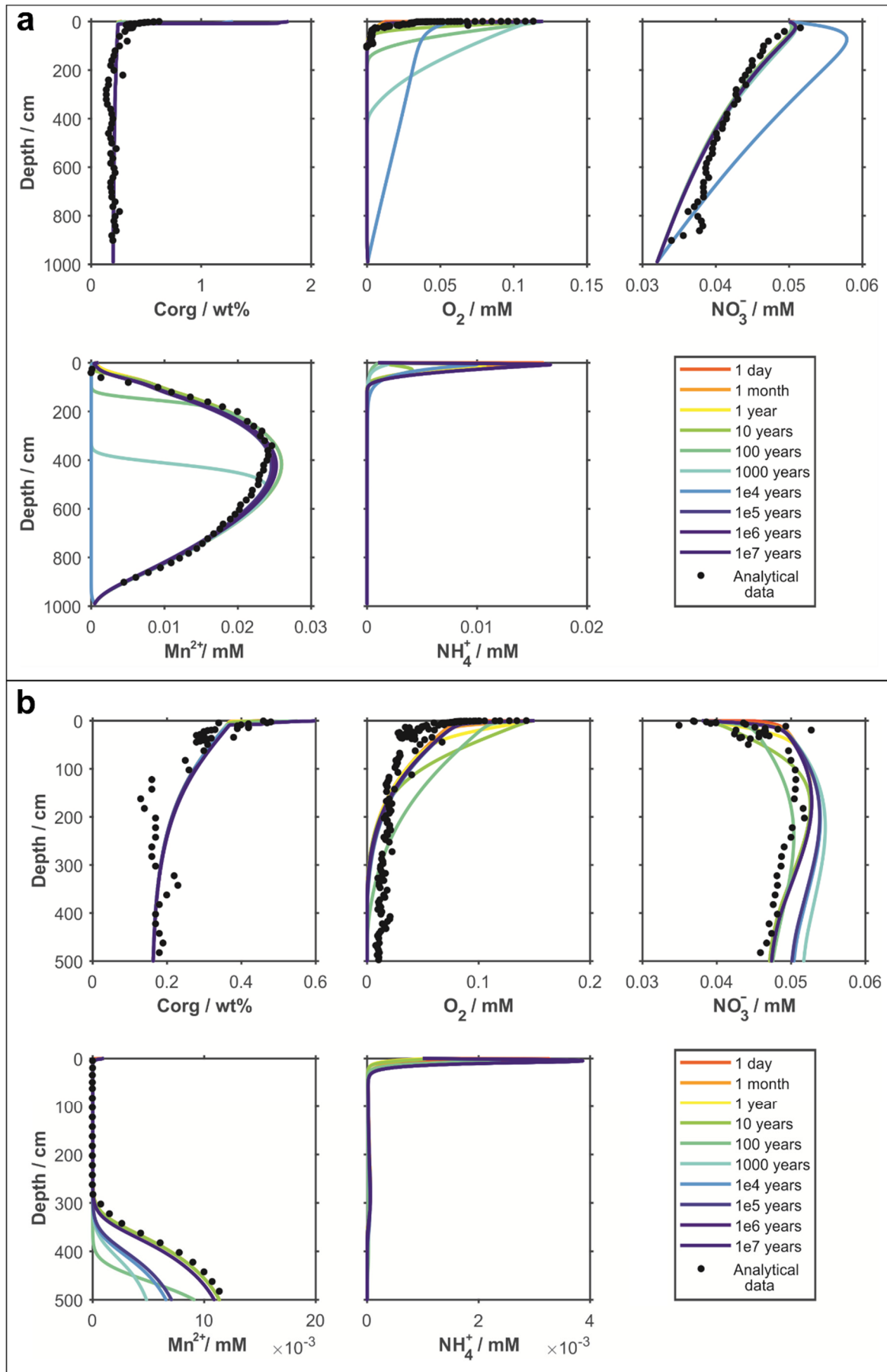


Figure 5: Model results of the transient transport-reaction model for (a) EBS disturbance in the German BGR-RA area and (b) the IOM-BIE disturbance in the eastern European IOM area.

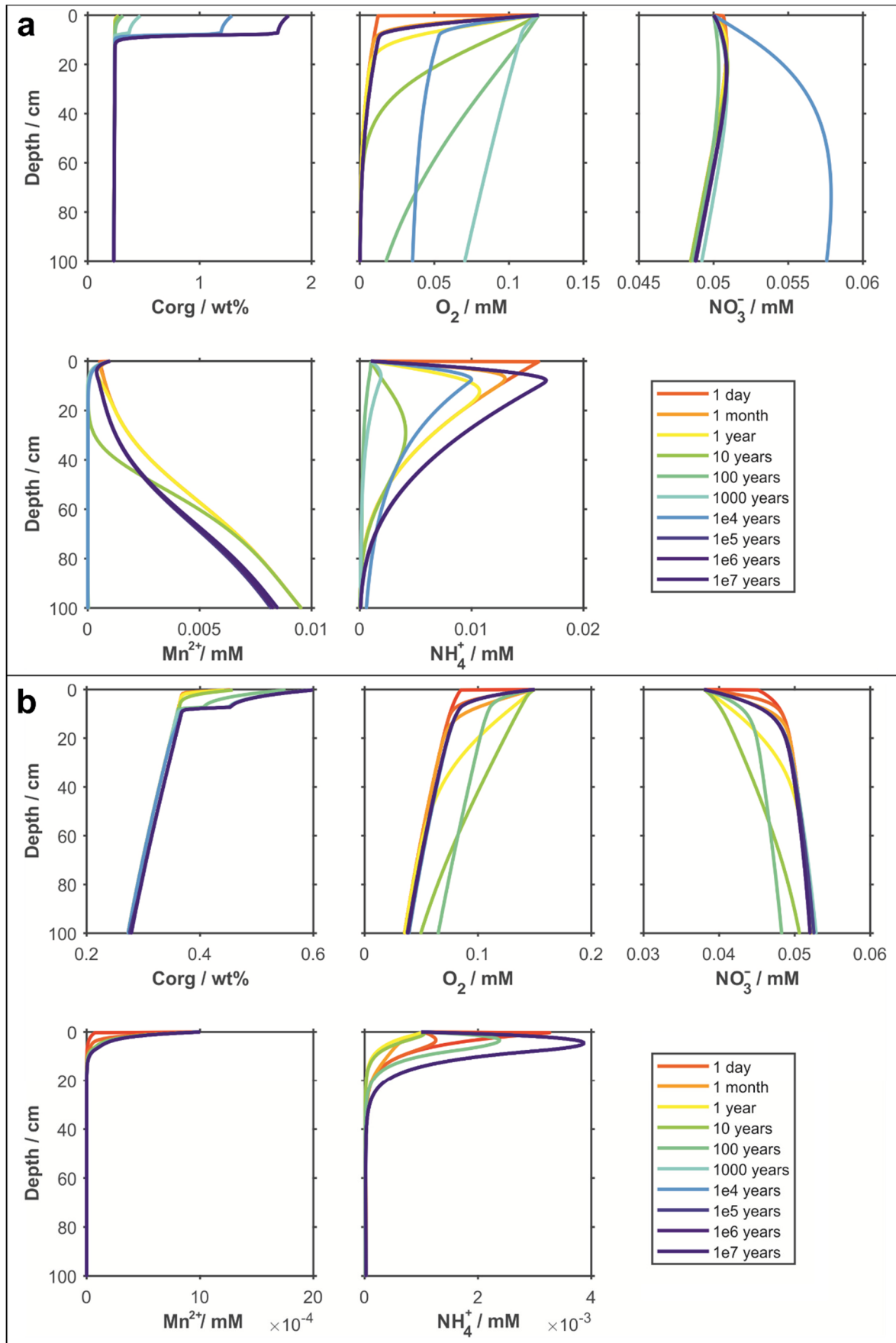


Figure 6: Detailed model results of the transient transport-reaction model for the upper 1 m of the sediments for (a) EBS disturbance in the German BGR-RA area and (b) the IOM-BIE disturbance in the eastern European IOM area.

Naturally, the solute fluxes across the sediment-water interface (SWI) are strongly affected after the surface sediment removal (Fig. 7). The transient transport-reaction model suggests that the oxygen fluxes into the sediments are lowered by a factor of three to six after 10–100 yr at the IOM-BIE and BGR-RA sites, respectively. This trend is mirrored by the decreased release of NH_4^+ and NO_3^- into the bottom water.

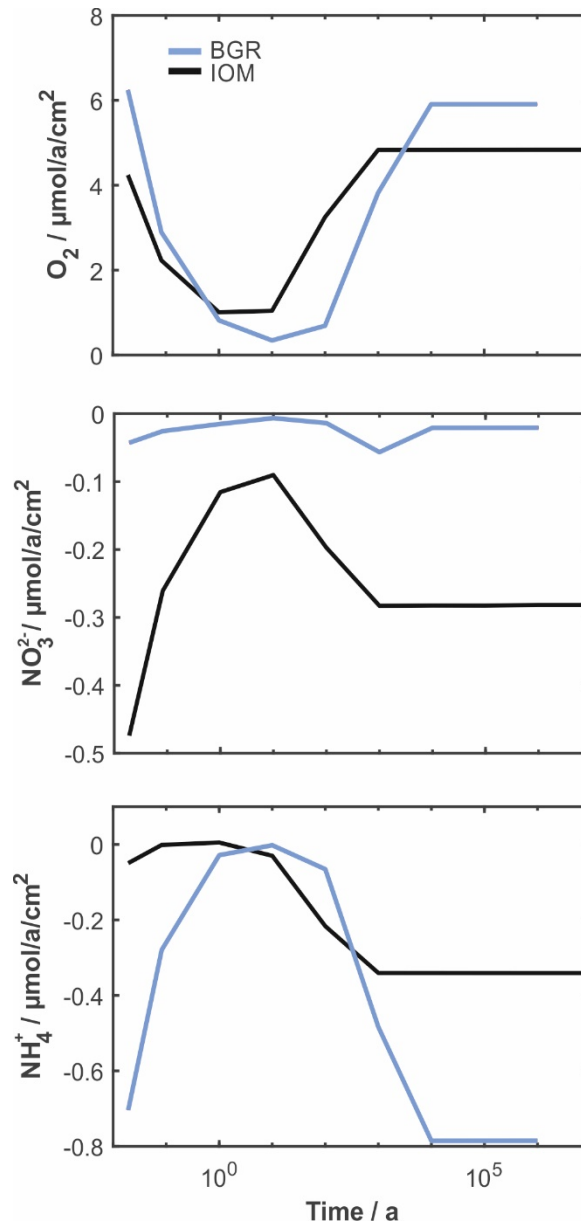


Figure 7: Pore-water fluxes of oxygen (O_2), nitrate (NO_3^{2-}) and ammonia (NH_4^+) at the sediment-water interface obtained by the application of the transient transport-reaction model. Oxygen fluxes into the sediment and fluxes of nitrate and ammonia towards the sediment surface are shown as a function of time after the EBS and IOM-BIE disturbances in the German BGR-RA area (blue) and in the eastern European IOM area (black), respectively.

4. Discussion

4.1 Depths of small-scale disturbance experiments

Our work demonstrates that the depth distribution of solid-phase Mn provides a reliable tool for the determination of the disturbance depths in the sediments of the CCZ (Fig. 4; Table 3). The success of the correlation of solid-phase Mn contents between disturbed and undisturbed reference sediments benefits from several factors:

(1) Sediment mixing during the small-scale disturbance experiments is negligible: The visual impact assessment of the investigated disturbance tracks in the CCZ suggests that sediment mixing during the small-scale disturbance experiments was insignificant (Fig. 2). This observation is in agreement with a recent EBS disturbance experiment, which has been conducted in the DISCOL area in 2015 (Greinert, 2015). The freshly created EBS track in the DISCOL area was re-visited 5 weeks after the disturbance experiment, where the surface sediment was mostly removed and deeper sediment layers were exposed without visible sediment mixing (Boetius, 2015; Paul et al., 2018). In a study on the geochemical regeneration in disturbed sediments of the DISCOL area in the Peru Basin, Paul et al. (2018) have shown that the bulk Mn-rich top sediment layer, which has been observed in undisturbed sediments, is removed in the 5-week old EBS disturbance track. Thus, an important pre-requisite for this method is met and the authors have proposed that the depth distribution of solid-phase Mn may be suitable for the evaluation of the impact as well as for the monitoring of the recovery of small-scale disturbance experiments.

(2) The fact that the solid-phase Mn maxima in the surface sediments of the CCZ appear to be a regional phenomenon (Volz et al., under review): The investigated disturbed sediments as well as the undisturbed reference sediments in the CCZ show decreasing solid-phase Mn contents with depth in the upper 20–30 cm of the sediments (Fig. 3; Fig. 4; Volz et al., under review). In the undisturbed reference sediments, solid-phase Mn contents show maxima of up to 1 wt% in the upper 10 cm of the sediments with distinctly decreasing contents below (Fig. 4; Volz et al., under review). Similar bulk solid-phase Mn distribution patterns have been reported for other sites within the CCZ (e.g., Khripounoff et al., 2006; Mewes et al., 2014; Widmann et al., 2014). Volz et al. (under review) have suggested that the widely observed solid-phase Mn enrichments in the surface sediments of the CCZ formed in association with a more compressed redox zonation, which may have prevailed during the last glacial period as a result of lower bottom-water oxygen concentrations than today. As a consequence of this condensed redox zonation, upward diffusing pore-water Mn^{2+} may have precipitated as authigenic Mn(IV) at a

shallow oxic-suboxic redox boundary in the upper few centimeters of the sediments. After the last glacial period, the authigenic Mn(IV) peak was continuously mixed into subsequently deposited sediments by bioturbation causing the observed broad solid-phase Mn(IV) enrichment in the surface sediments (Fig. 4; Volz et al., under review).

(3) Lastly, the OPD at all sites is located at sediment depths greater than 0.5 m, and thus, diagenetic precipitation of Mn(IV) in the surface sediments (e.g. Gingele and Kasten, 1994) since the last glacial period can be ruled out (Table 2; Mewes et al., 2014; Volz et al., under review).

Based on the depth distribution of solid-phase Mn, our work suggests that between 5 and 15 cm of the surface sediments were removed by the different small-scale disturbance experiments in the CCZ (Table 3; Fig. 4). This range of disturbance depths is in good agreement with other estimates for small-scale disturbances by similar gear in the CCZ and in the DISCOL area, which suggest that the upper 4–20 cm of the sediments were removed (e.g., Thiel, 2001; Oebius et al., 2001; König et al., 2001; Grupe et al., 2001; Radziejewska, 2002; Khripounoff et al., 2006; Paul et al., 2018). However, as the disturbed sites investigated in this study and the respective undisturbed reference sites are located up to 5 km apart from each other, the correlation of solid-phase Mn may be influenced by some spatial heterogeneities in solid-phase Mn contents (Table 1; Mewes et al., 2014). Furthermore, it should be noted, that for the correlation of solid-phase Mn contents between the disturbed and undisturbed reference sites, we have not considered that (1) particles may have re-settled on the freshly exposed sediment surfaces from re-suspended particle plumes (e.g., Jankowski and Zielke, 2001; Thiel, 2001; Radziejewska, 2002; Gillard et al., 2019), (2) sediment has slid off from adjacent flanks of the sediment accumulation after the disturbances (Fig. 2) and (3) sediments have been deposited after the small-scale disturbances at sedimentation rates between 0.2 and 1.2 cm kyr⁻¹ (Table 2; Volz et al., 2018). However, only in the case of the IOM-BIE disturbance, the visual impact assessment suggested that the disturbance surface was concealed, here by re-settling sediments (Fig. 2). The development of a re-suspended particle plume during the disturbance experiments highly depends on various factors, such as sediment properties, seafloor topography, bottom-water currents and the disturbance device (e.g., Gillard et al., 2019). Although local and regional variations in these factors have been reported for the CCZ, they are not well constrained (e.g., Mewes et al., 2014; Aleynik et al., 2017; Volz et al., 2018; Gillard et al., 2019; Hauquier et al., 2019). As the disturbance tracks investigated in the framework of this study are relatively small with a maximum width of 2.5 m (Fig. 2; Brockett and Richards, 1994; Brenke 2005), re-suspended particles may (1) only partly deposit on the disturbance track and (2)

mostly be transported laterally by currents and deposit on top of undisturbed sediments in the proximity of the disturbance tracks (e.g., Fukushima, 1995; Aleynik et al., 2017; Gillard et al., 2019). This is in accordance with the close correlation of the sediment porosity between the disturbed and undisturbed reference sites, which indicates that the deposition of re-settling particles with higher porosity at the sediment surface in the disturbance tracks is insignificant at all sites, except for the IOM-BIE site (Fig. 4). The porosity data further shows that sediment compaction, potentially caused by the weight of the disturbance device (Cuvelier et al., 2018; Hauquier et al., 2019) is insignificant at all disturbed sites.

4.2 Impact of small-scale disturbances on the geochemical system

The geochemical conditions found at the study sites in the CCZ are the result of a balanced interplay of key factors, such as the input of fresh, labile TOC, sedimentation rate and bioturbation intensity (e.g., Froelich et al., 1979; Berner, 1981; Zonneveld et al., 2010; Mogollón et al., 2016; Volz et al., 2018). Together they characterize the upper reactive layer, which in turn plays a crucial role for the location of the OPD in the sediments of the CCZ (e.g., Mewes et al., 2014; Mogollón et al., 2016; Volz et al., 2018). Oxygen is consumed via aerobic respiration during the degradation of organic matter while bioturbation transports fresh, labile TOC into deeper sediments (e.g., Haeckel et al., 2001; König et al., 2001). The presence of labile TOC throughout the bioturbated zone significantly enhances the consumption of oxygen with depth, where oxygen is not as easily replenished by seawater oxygen. Thus, the availability of labile TOC in the bioturbated layer controls the amount of oxygen that passes through the reactive layer into deeper sediments (e.g., König et al., 2001). Below the highly reactive layer, refractory organic matter degradation and secondary redox reactions – such as oxidation of Mn^{2+} – control the consumption of oxygen (Supplementary Table 1; Mogollón et al., 2016; Volz et al., 2018). The oxygen profile, more precisely the position of the OPD, in turn, strongly influences the distribution of other solutes. Below the OPD, denitrification and Mn(IV) reduction commence, albeit at much lower rates, consuming pore-water NO_3^- and releasing Mn^{2+} (Mogollón et al., 2016; Volz et al., 2018). The study sites in the CCZ provide an excellent example for how slight differences in key environmental factors can profoundly change the overall solute profiles with OPDs ranging between 0.5 m (BGR-RA) and > 7.4 m (GSR) as outlined by Volz et al. (2018).

Mining-related removal of the upper 5–15 cm of the sediment results, on one hand, in an almost complete loss of the labile TOC fraction (Fig. 4) as this fraction is restricted to the upper 20 cm of the sediment in the CCZ (e.g., Müller and Mangini, 1980; Emerson, 1985; Müller et

al., 1988; Mewes et al., 2014; Mogollón et al., 2016; Volz et al., 2018). On the other hand, studies on faunal diversity and density in small-scale disturbances in the sediments of the CCZ and in the DISCOL area show that most of the biota is lost immediately after the disturbance experiment (Borowski et al., 1998; 2001; Bluhm et al., 2001; Thiel et al., 2001; Vanreusel et al., 2016; Jones et al., 2017; Gollner et al., 2017). Thus, a drastic decline or stand-still of bioturbation can be expected in the surface sediments.

Based on the results of the transient transport-reaction model, geochemical recovery after small-scale sediment disturbances can be divided into two main phases (Fig. 8):

(1) Since the labile TOC fraction and bioturbating fauna is mostly removed, downward diffusion of oxygen is the main driver shaping solute profiles towards a new geochemical equilibrium in the absence of the reactive layer (Figs. 5 and 6). This entails the downward migration of the OPD, as oxygen is no longer effectively consumed in the upper sediment layer. The presence of oxygen outcompetes denitrification and Mn(IV) reduction and induces NH_4^+ and Mn^{2+} oxidation instead, thus, minimizing pore-water NH_4^+ and Mn^{2+} concentrations (Figs. 5 and 6). At the same time, NO_3^- , as a by-product of aerobic-respiration (e.g., Froelich et al., 1979; Berner, 1981; Haeckel et al., 2001; Mogollón et al., 2016; Volz et al., 2018), is accordingly reduced during denitrification and NO_3^- concentrations are lowered during this first phase.

(2) The second phase is characterized by the increasing influence of reactive fluxes across the seafloor. It takes approximately 1000 yr before any significant build-up of an upper labile TOC layer is re-established (Fig. 6), at which point solute profiles slowly shift towards their pre-disturbance shape (Fig. 7). Interestingly, during the transition time when oxygen is still present at depth but aerobic respiration in the upper sediments has already begun to pick up, NO_3^- concentrations are strongly elevated in the BGR sediments (Figs. 5 and 6). This is due to the fact that NO_3^- is not consumed during denitrification or the Mn-annamox reaction in the presence of oxygen (Mogollón et al., 2016; Volz et al., 2018).

With the importance of bioturbation and the mining-related removal of associated fauna in mind, solute and in particular nutrient fluxes across the seafloor should also be considered. The release of nutrients complements the close link between sediment geochemistry and the food web structure (e.g., Smith et al., 1979; Dunlop et al., 2016; Stratmann et al., 2018) and further emphasizes their interdependencies. Figure 7 depicts fluxes of oxygen, NO_3^- and NH_4^+ across the seafloor. As expected, with the reactive layer being mostly absent, fluxes across the seafloor are severely reduced, which particularly affects the oxygen uptake of the sediments as well as

the release of NO_3^- and NH_4^+ into the bottom water. At about 100 to 1000 yr after the disturbance, concurrent with the build-up of an upper sediment layer containing significant amounts of labile organic matter, fluxes begin to increase again, albeit much slower than the rate of the decrease in fluxes subsequently after the disturbances (Fig. 7, note the logarithmic scale).

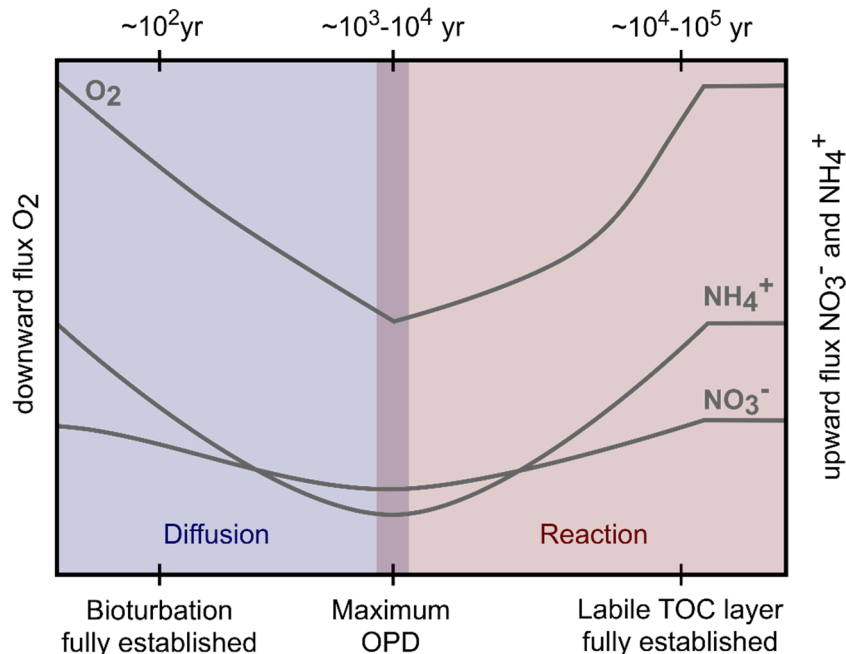


Figure 8: Conceptual model for time-dependent pore-water fluxes of oxygen (O_2), nitrate (NO_3^-) and ammonia (NH_4^+) at the sediment-water interface after the removal of the upper 7–10 cm of the sediments. The re-establishment of bioturbation, the maximum oxygen penetration depth (OPD) as well as the re-establishment of the surface sediment layer dominated by the reactive labile organic matter fraction are indicated as a function of time after the sediment removal.

It should be noted that while bioturbation has a pivotal influence on the undisturbed steady-state profile, it only plays a secondary role in re-establishing the geochemical equilibrium at the disturbed sites in the CCZ. Studies suggest that faunal abundances fully recover within centuries after the disturbance even though the benthic community may be different than prior to the disturbance (e.g., Miljutin et al., 2011; Vanreusel et al., 2016). Due to the extremely slow build-up of the reactive layer with labile TOC, the bioturbation ‘pump’ is active again before any significant amount of labile TOC is present about 1–100 kyr after the disturbance. Thus, full recovery is mainly controlled by the re-establishment of the upper reactive layer, i.e. the accumulation rate of labile TOC on the seafloor.

The transport-reaction model reveals that under current depositional conditions, the re-equilibrated geochemical system is established after 1–10 kyr at the IOM-BIE site, while the

re-establishment of the geochemical equilibrium at the BGR-RA site takes 10–100 kyr (Figs. 5 and 6). Shorter recovery times at the IOM site compared to the BGR-RA site are related to higher sedimentation rates (1.15 instead of 0.65 cm kyr⁻¹) and shallower impact on the sediment (7 cm instead of 10 cm sediment removal). Accordingly, the maximum OPD is reached after 100 yr and 10 kyr at the IOM and BGR-RA site, respectively (Figs. 5 and 6) while the reactive layer is clearly established sooner at the IOM site compared to the BGR-RA site (Fig. 7). Thus, the disturbance depth clearly has a strong influence on the recovery process of the geochemical system of the sediments, highlighting the importance of low-impact mining equipment. Considering that in the CCZ areas of about 8500 km² could be commercially mined in 20 yr per individual mining operation (Madureira et al., 2016), this impact assessment of small-scale disturbance experiments may only represent a first approach for the prediction of the environmental impact of large-scale deep-sea mining activities.

5. Conclusion

We have studied surface sediments from seven small-scale disturbance experiments for the simulation of deep-sea mining, which were performed between 1 day and 37 years prior to our sampling in the NE Pacific Ocean. These small-scale disturbance tracks were created using various disturbance devices in different European contract areas for the exploration of polymetallic nodules within the eastern part of the Clarion-Clipperton Zone (CCZ). Through correlation of solid-phase Mn contents of disturbed and undisturbed reference sediments, we (1) propose that the depth distribution of solid-phase Mn in the sediments of the CCZ provides a reliable tool for the estimation of the disturbance depth and (2) show that 5–15 cm of the sediments were removed during the small-scale disturbance experiments investigated in this study. As the small-scale disturbances are associated with the removal of the surface sediments characterized by reactive labile organic matter, the disturbance depth ultimately determines the impact on the geochemical system in the sediments. The application of a transient transport-reaction model reveals that the removal of the upper 7–10 cm of the surface sediments is associated with a meter-scale downward extension of the oxic zone and the shutdown of denitrification and Mn(IV) reduction. As a consequence of lower respiration rates after the disturbance experiments, the geochemical system in the sediments is controlled by downward oxygen diffusion. While the re-establishment of bioturbation within centuries after the disturbance is important for the geochemical re-equilibration in the disturbed sediments, the rate at which the new geochemical system re-equilibrates ultimately depends on the burial rate of organic matter. Assuming the accumulation of labile organic matter to proceed at current Holocene sedimentation rates in the disturbed sediments, biogeochemical reactions resume in

the reactive surface sediment layer, and thus, the new geochemical equilibrium in the disturbed sediments in the CCZ is reached on a millennial time scale after the disturbance of the surface sediments.

Our study represents the first study on the impact of small-scale disturbance experiments on the sedimentary geochemical system in the prospective areas for polymetallic nodule mining in the CCZ. Our findings on the evaluation of the disturbance depths using solid-phase Mn contents as well as the quantification of the geochemical re-equilibration in the sediments advances our knowledge about the potential long-term consequences of deep-sea mining activities. We propose that mining techniques potentially used for the potential commercial exploitation of nodules in the CCZ may remove less than 10 cm of the surface sediments in order to minimize the impact on the geochemical system in the sediments. Furthermore, the depth distribution of solid-phase Mn may be used for environmental monitoring purposes during future mining activities in the CCZ. This study also provides valuable data for further investigations on the environmental impact of deep-sea mining, such as during the launched JPI Oceans follow-up project MiningImpact 2.

Data availability

The data are available via the data management portal OSIS-Kiel and the WDC database PANGAEA, including the solid-phase bulk sediment Mn and TOC contents (<https://doi.org/10.1594/PANGAEA.904560>) as well as the porosity data (<https://doi.org/10.1594/PANGAEA.904578>).

Author contribution

The study was conceived by all co-authors. JBV carried out the sampling and analyses on board during RV SONNE cruise SO239 and the analytical work in the laboratories at AWI in Bremerhaven. LH and MH modified the numerical transport-reaction model presented in Volz et al. (2018) and provided model results for the long-term effects of small-scale disturbances on geochemical conditions and biogeochemical processes. JBV prepared the manuscript with substantial contributions from all co-authors.

Competing interest

The authors declare that they have no conflict of interest.

Acknowledgements

We thank captain Lutz Mallon, the crew and the scientific party of RV SONNE cruise SO239 for the technical and scientific support. Thanks to Jennifer Ciomber, Benjamin Löffler and Vincent Ozegowski for their participation in sampling and analysis onboard. For analytical support in the home laboratory and during data evaluation we are grateful to Ingrid Stimac, Olaf Kreft, Dennis Köhler, Ingrid Dohrmann (all at AWI). Special thanks to Prof. Dr. Gerhard Bohrmann (MARUM, University of Bremen), Dr. Timothy G. Ferdelman (MPI Bremen) and Dr. Ellen Pape (University of Ghent) for much appreciated discussions.

This study is funded by the Bundesministerium für Bildung und Forschung (BMBF Grant 03F0707A+G) as part of the JPI-Oceans pilot action “Ecological Aspects of Deep-Sea Mining (MiningImpact)”. We acknowledge further financial support from the Helmholtz Association (Alfred Wegener Institute Helmholtz Centre for Polar and Marine Research).

References

- Aleynik, D., Inall, M.E., Dale, A., Vink, A., 2017. Impact of remotely generated eddies on plume dispersion at abyssal mining sites in the Pacific. *Sci. Rep.* 7, 1–14. doi:10.1038/s41598-017-16912-2.
- Berger, W.H., 1974. Deep-sea sedimentation. In: *The Geology of Continental Margins* (eds. Burk, C.A., Drake, C.L.). Springer, New York, 213–241.
- Berner, R.A., 1981. A new geochemical classification of sedimentary environments. *J. Sediment. Petrol.* 51, 359–365.
- Berner, R.A., 1980. *Early Diagenesis: A Theoretical Approach*. Princeton University Press, Princeton, 1–24.
- Bluhm, H., 2001. Re-establishment of an abyssal megabenthic community after experimental physical disturbance of the seafloor. *Deep-Sea Res. Part II Top. Stud. Oceanogr.* 48, 3841–3868.
- Boetius, A., Haeckel, M., 2018. Mind the seafloor. *Science* 359, 34–36. doi:10.1126/science.aap7301.
- Boetius, A., 2015. RV Sonne Fahrtbericht / Cruise Report SO242-2: JPI OCEANS Ecological Aspects of Deep-Sea Mining, DISCOL Revisited, Guayaquil-Guayaquil (Ecuador), 28.08.–01.10.2015, Kiel: Helmholtz-Zentrum für Ozeanforschung.
- Borowski, C., 2001. Physically disturbed deep-sea macrofaunal impacts of a large-scale physical disturbance experiment in the Southeast Pacific. *Deep-Sea Res. Part II Top. Stud. Oceanogr.* 48, 3809–3839.
- Borowski, C., Thiel, H., 1998. Deep-Sea macrofaunal impacts of a large-scale physical disturbance experiment in the Southeast Pacific. *Deep-Sea Res. Part II Top. Stud. Oceanogr.* 45, 55–81.
- Boudreau, B.P., 1997. A one-dimensional model for bed-boundary layer particle exchange. *J. Mar. Syst.* 11, 279–303. doi:10.1016/S0924-7963(96)00127-3.
- Brenke, N., 2005. An Epibenthic sledge for operations on marine soft bottom and bedrock. *J. Mar. Tech. Soc.* 39, 10–19.
- Brockett, T., Richards, C.Z., 1994. Deep-sea mining simulator for environmental impact studies. *Sea Technol.* 35, 77–82.
- Chung, J.S., 2010. Full-Scale, Coupled Ship and Pipe Motions Measured in North Pacific Ocean: The Hughes Glomar Explorer with a 5,000-m-Long Heavy-Lift Pipe Deployed. *Proc. of the 19th ISOPE* 20, 1–6.
- Cronan, D.S., Rothwell, G., Croudace, I., 2010. An ITRAX geochemical study of ferromanganiferous sediments from the Penrhyn basin, South Pacific Ocean. *Mar. Georesour. Geotechnol.* 28, 207–221. doi:10.1080/1064119X.2010.483001.
- Cuvelier, D., Gollner, S., Jones, D.O.B., Kaiser, S., Arbizu, P.M., Menzel, L., Mestre, N.C., Morato, T., Pham, C., Pradillon, F., Purser, A., Raschka, U., Sarrazin, J., Simon-Lledó, E., Stewart, I.M., Stuckas, H., Sweetman, A.K., Colaço, A., 2018. Potential Mitigation and Restoration Actions in Ecosystems Impacted by Seabed Mining. *Front. Mar. Sci.* 5. doi:10.3389/fmars.2018.00467.
- Davies, A.J., Roberts, J.M., Hall-Spencer, J., 2007. Preserving deep-sea natural heritage: emerging issues in offshore conservation and management. *Biol. Conserv.* 138, 299–312. doi:10.1016/j.biocon.2007.05.011.

- Dunlop, K.M., van Oevelen, D., Ruhl, H.A., Huffard, C.L., Kuhnz, L.A., Smith, K.L., 2016. Carbon cycling in the deep eastern North Pacific benthic food web: Investigating the effect of organic carbon input. *Limnol. Oceanogr.* 61, 1956–1968. <https://doi.org/10.1002/lno.10345>, 2016.
- Emerson, S., Fischer, K., Reimers, C., Heggie, D., 1985. Organic carbon dynamics and preservation in deep-sea sediments. *Deep-Sea Res.* 32, 1–21.
- Froelich, P.N., Klinkhammer, G.P., Bender, M.L., Luedke, L.A., Heath, G.R., Cullen, C., Dauphin, P., Hammond, D., Hartmann, B., Maynard, V., 1979. Early oxidation of organic matter in pelagic sediments of the Eastern Equatorial Pacific, suboxic diagenesis. *Geochim. Cosmochim. Acta* 43, 1075–1090.
- Fukushima, T., 1995. Overview "Japan Deep-Sea Impact Experiment = JET", ISOPE-M-95-008, ISOPE.
- Gillard, B., Purkiani, K., Chatzievangelou, D., Vink, A., Iversen, M.H., Thomsen, L., 2019. Physical and hydrodynamic properties of deep sea mining-generated, abyssal sediment plumes in the Clarion Clipperton Fracture Zone (eastern-central Pacific). *Elem. Sci. Anth.* 7.
- Gingele, F.X., Kasten, S., 1994. Solid-phase manganese in Southeast Atlantic sediments: implications for the paleoenvironment. *Mar. Geol.* 121, 317–332.
- Glasby, G.P., 2000. Lessons Learned from Deep-Sea Mining. *Science* 289, 551–553. doi:10.1126/science.289.5479.551.
- Glover, A.G., Smith, C.R., 2003. The deep-sea floor ecosystem: current status and prospects of anthropogenic change by the year 2025. *Environ. Conserv.* 30, 219–241.
- Gollner, S., Kaiser, S., Menzel, L., Jones, D.O.B., Brown, A., Mestre, N.C., van Oevelen, D., Menot, L., Colaço, A., Canals, M., Cuvelier, D., Durden, J.M., Gebruk, A., Egho, G.A., Haeckel, M., Marcon, Y., Mevenkamp, L., Morato, T., Pham, C.K., Purser, A., Sanchez-Vidal, A., Vanreusel, A., Vink, A., Arbizu, P.M., 2017. Resilience of benthic deep-sea fauna to mining activities. *Mar. Environ. Res.* 129, 76–101. doi:10.1016/j.marenvres.2017.04.010.
- Greinert, J., 2015. RV Sonne Fahrtbericht / Cruise Report SO242-1: JPI OCEANS Ecological Aspects of Deep-Sea Mining, DISCOL Revisited, Guayaquil-Guayaquil (Equador), 28.07.–25.08.2015, Kiel: Helmholtz-Zentrum für Ozeanforschung.
- Grupe, B., Becker, H.J., Oebius, H.U., 2001. Geotechnical and sedimentological investigations of deep-sea sediments from a manganese nodule field of the Peru Basin. *Deep. Res. Part II Top. Stud. Oceanogr.* 48, 3593–3608.
- Haeckel, M., König, I., Riech, V., Weber, M.E., Suess, E., 2001. Pore water profiles and numerical modelling of biogeochemical processes in Peru Basin deep-sea sediments. *Deep. Res. Part II Top. Stud. Oceanogr.* 48, 3713–3736. doi:10.1016/S0967-0645(01)00064-9.
- Hauquier, F., Macheriotou, L., Bezerra, T.N., Egho, G., Martínez Arbizu, P., Vanreusel, A., 2019. Geographic distribution of free-living marine nematodes in the Clarion-Clipperton Zone: implications for future deep-sea mining scenarios. *Biogeosciences* 16, 3475–3489.
- Halfar, J., Fujita, R.M., 2002. Precautionary management of deep-sea mining. *Mar. Pol.* 26, 103–106.
- Halkyard, J.E., 1985. Technology for Mining Cobalt Rich Manganese Crusts from Seamounts. *Proc. OCEANS '85.* 352–274.
- Halbach, P., Friedrich, G., von Stackelberg, U. (eds.), 1988. The manganese nodule belt of the Pacific Ocean. Enke, Stuttgart.

- Hein, J.R., Mizell, K., Koschinsky, A., Conrad, T.A., 2013. Deep-ocean mineral deposits as a source of critical metals for high- and green-technology applications: comparison with land-based resources. *Ore Geol. Rev.* 51, 1–14.
- Hoagland, P., Beaulieu, S., Tivey, M.A., Eggert, R.G., German, C., Glowka, L., Lin, J., 2010. Deep-sea mining of seafloor massive sulfides. *Mar. Pol.* 34, 728–732. doi:10.1016/j.marpol.2009.12.001.
- International Seabed Authority (ISA), 2010. A Geological Model for Polymetallic Nodule Deposits in the Clarion-Clipperton Fracture Zone, Technical Study 6, Kingston, 211.
- Jankowski, J.A., Zielke, W., 2001. The mesoscale sediment transport due to technical activities in the deep sea. *Deep. Res. Part II Top. Stud. Oceanogr.* 48, 3487–3521.
- Jones, D.O.B., Kaiser, S., Sweetman, A.K., Smith, C.R., Menot, L., Vink, A., Trueblood, D., Greinert, J., Billett, D.S.M., Martínez Arbizu, P., Radziejewska, T., Singh, R., Ingole, B., Stratmann, T., Simon-Lledó, E., Durden, J.M., Clark, M.R., 2017. Biological responses to disturbance from simulated deep-sea polymetallic nodule mining. *PLoS One* 12, e0171750. <https://doi.org/10.1371/journal.pone.0171750>.
- Juan, C., Van Rooij, D., De Bruycker, W., 2018. An assessment of bottom current controlled sedimentation in Pacific Ocean abyssal environments. *Mar. Geol.* 403, 20–33.
- Khripounoff, A., Caprais, J.-C., Crassous, P., Etoubleau, J., 2006. Geochemical and biological recovery of the disturbed seafloor in polymetallic nodule fields of the Clipperton-Clarion Fracture Zone (CCFZ) at 5,000-m depth. *Limnol. Oceanogr.* 51, 2033–2041. doi:10.4319/lo.2006.51.5.2033.
- König, I., Haeckel, M., Lougear, A., Suess, E., Trautwein, A.X., 2001. A geochemical model of the Peru Basin deep-sea floor - and the response of the system to technical impacts. *Deep. Res. Part II Top. Stud. Oceanogr.* 48, 3737–3756. doi:10.1016/S0967-0645(01)00065-0.
- Kotlinski R., Stoyanova V., 1998. Physical, Chemical, and Geological changes of Marine Environment Caused by the Benthic Impact Experiment at the IOM BIE Site. *Proc. of the 8th ISOPE 2*, 277–281. Montreal, Canada.
- Kretschmer, S., Geibert, W., Rutgers van der Loeff, M.M., and Mollenhauer, G., 2010. Grain size effects on 230Thxs inventories in opal-rich and carbonate-rich marine sediments. *Earth Planet. Sci. Lett.* 294, 131–142. doi:10.1016/j.epsl.2010.03.021, 2010.
- Kuhn, G., 2013. Don't forget the salty soup: Calculations for bulk marine geochemistry and radionuclide geochronology. Goldschmidt 2013, Florence, Italy, 25 August 2013 – 30 August 2013. doi:10.1180/minmag.2013.077.5.11.
- Kuhn, T., Wegorzewski, A., Rühlemann, C., Vink, A., 2017a. Composition, Formation, and Occurrence of Polymetallic Nodules. In: *Deep Sea Mining* (ed. Sharma, R.). Springer, Cham.
- Kuhn, T., Versteegh, G.J.M, Villinger, H., Dohrmann, I., Heller, C., Koschinsky, A., Kaul, N., Ritter, S., Wegorzewski, A.V., Kasten, S., 2017b. Widespread seawater circulation in 18-22 Ma oceanic crust: Impact on heat flow and sediment geochemistry. *Geology* 45, 799–802. doi:10.1130/G39091.1.
- Kuhn, T., Rühlemann, C., Wiedicke-Hombach, M., 2012. Developing a strategy for the exploration of vast seafloor areas for prospective manganese nodule fields. In: *Marine Minerals: Finding the Right Balance of Sustainable Development and Environmental Protection* (eds. Zhou, H, Morgan, C.L.). The Underwater Mining Institute, Gelendzhik, Russia (K 1–12).

- Lodge, M., Johnson, D., Le Gurun, G., Wengler, M., Weaver, P., Gunn, V., 2014. Seabed mining: International Seabed Authority environmental management plan for the Clarion-Clipperton Zone. A partnership approach. *Mar. Pol.* 49, 66–72. doi:10.1016/j.marpol.2014.04.006.
- Madureira, P., Brekke, H., Cherkashov, G., Rovere, M., 2016. Exploration of polymetallic nodules in the Area: Reporting practices, data management and transparency. *Mar. Pol.* 70, 101–107. doi:10.1016/j.marpol.2016.04.051, 2016.
- Martínez Arbizu, P., Haeckel, M., 2015. RV SONNE Fahrtbericht / Cruise Report SO239: EcoResponse Assessing the Ecology, Connectivity and Resilience of Polymetallic Nodule Field Systems, Balboa (Panama) – Manzanillo (Mexico,) 11.03.–30.04.2015 (Report No. doi:10.3289/GEOMAR_REP_NS_25_2015), GEOMAR Helmholtz-Zentrum für Ozeanforschung, Kiel, Germany.
- Menendez, A., James, R.H., Lichtschlag, A., Connelly, D., Peel, K., 2018. Controls on the chemical composition on ferromanganese nodules in the Clarion-Clipperton Fracture Zone, eastern equatorial Pacific. *Mar. Geol.* 409, 1–14.
- Menot, L., Rühlemann, C., and BIONOD Shipboard party, 2013. BIONOD Cruise Science Report, Vol. 2 French Licence Area. Ifremer, REM/EEP/LEP13.06, 57.
- Mero, J.L., 1965. The Mineral Resources of the Sea. Elsevier, Amsterdam.
- Mewes, K., Mogollón, J.M., Picard, A., Rühlemann, C., Eisenhauer, A., Kuhn, T., Ziebis, W., Kasten, S., 2016. Diffusive transfer of oxygen from seamount basaltic crust into overlying sediments: An example from the Clarion-Clipperton Fracture Zone. *Earth Planet. Sci. Lett.* 433, 215–225. doi:10.1016/j.epsl.2015.10.028.
- Mewes, K., Mogollón, J.M., Picard, A., Rühlemann, C., Kuhn, T., Nöthen, K., Kasten, S., 2014. Impact of depositional and biogeochemical processes on small scale variations in nodule abundance in the Clarion-Clipperton Fracture Zone. *Deep-Sea Res. Part I: Oceanogr. Res. Pap.* 91, 125–141. doi:10.1016/j.dsr.2014.06.001.
- Miljutin, D.M., Miljutina, M.A., Martínez Arbizu, P., Galeron, J., 2011. Deep-sea nematode assemblage has not recovered 26 years after experimental mining of polymetallic nodules (CCFZ, Pacific). *Deep-Sea Res. Part I: Oceanogr. Res. Pap.* 58, 885–897.
- Mogollón, J.M., Mewes, K., Kasten, S., 2016. Quantifying manganese and nitrogen cycle coupling in manganese-rich, organic carbon-starved marine sediments: Examples from the Clarion-Clipperton fracture zone. *Geophys. Res. Lett.* 43, 2016GL069117. doi:10.1002/2016GL069117.
- Morgan, C.L., Nichols, J.A., Selk, B.W., Toth, J.R., Wallin, C., 1993. Preliminary analysis of exploration data from Pacific deposits of manganese nodules. *Mar. Georesour. Geotechnol.* 11, 1–25.
- Müller, P.J., Hartmann, M., Suess, E., 1988. The chemical environment of pelagic sediments. In: *The Manganese Nodule Belt of the Pacific Ocean: Geological Environment, Nodule Formation, and Mining Aspects* (eds. Halbach, P., Friedrich, G., von Stackelberg, U.). Enke, Stuttgart, 70–90.
- Müller, P.J., Mangini, A., 1980. Organic carbon decomposition rates in sediments of the Pacific manganese nodule belt dated by ^{230}Th and ^{231}Pa . *Earth Planet. Sci. Lett.* 51, 94–114.
- Nöthen, K., Kasten, S., 2011. Reconstructing changes in seep activity by means of pore water and solid phase Sr/Ca and Mg/Ca ratios in pockmark sediments of the Northern Congo Fan. *Mar. Geol.* 287, 1–13. doi:10.1016/j.margeo.2011.06.008.

- Oebius, H.U., Becker, H.J., Rolinski, S., Jankowski, J.A., 2001. Parametrization and evaluation of marine environmental impacts produced by deep-sea manganese nodule mining. *Deep-Sea Res. Part II Top. Stud. Oceanogr.* 48, 3453–3467. doi:10.1016/S0967-0645(01)00052-2.
- Paul, S.A.L., Gaye, B., Haeckel, M., Kasten, S., Koschinsky, A., 2018. Biogeochemical Regeneration of a Nodule Mining Disturbance Site: Trace Metals, DOC and Amino Acids in Deep-Sea Sediments and Pore Waters. *Front. Mar. Sci.* 5. doi: 10.3389/fmars.2018.00117.
- Pearson, K., 1895. Notes on regression and inheritance in the case of two parents. *Proc. Royal Soc. London* 58, 240–242.
- Purser, A., Marcon, Y., Hoving, H.-J.T., Vecchione, M., Piatkowski, U., Eason, D., Bluhm, H., Boetius, A., 2016. Association of deep-sea incirrate octopods with manganese crusts and nodule fields in the Pacific Ocean. *Curr. Biol.* 26, R1268–R1269. doi:10.1016/j.cub.2016.10.052, 2016.
- Radziejewska, T., 2002. Response of deep-sea meiobenthic communities to sediment disturbance simulating effects of polymetallic nodule mining. *Int. Rev. Hydrobiol.* 87, 457–477.
- Ramirez-Llodra E., Tyler P.A., Baker M.C., Bergstad O.A., Clark M.R., Escobar, E., Levin, L.A., Menot, L., Rowden, A.A., Smith, C.R., Van Dover, C.L., 2011. Man and the Last Great Wilderness: Human Impact on the Deep Sea. *PLoS ONE* 6, e22588. doi:10.1371/journal.pone.0022588.
- Redfield, A.C., 1934. On the proportions of organic derivations in sea water and their relation to the composition of plankton. In: *James Johnstone Memorial Volume* (ed. Daniel, R.J.). University Press of Liverpool, pp. 176–192.
- Rühlemann, C., Kuhn, T., Wiedicke, M., Kasten, S., Mewes, K., Picard, A., 2011. Current status of manganese nodule exploration in the German license area. *Proc. of the 9th ISOPE Conference*, Maui, 168–173.
- Rühlemann, C., Albers, L., Briand, P., Brulport, J.-P., Cosson, R., Dekov, V.M., Galéron, J., Goergens, R., Gueguen, B., Hansen, J., Kaiser, S., Kefel, O., Khrpounoff, A., Kuhn, T., Larsen, K., Menot, L., Mewes, K., Miljutin, D., Mohrbeck, I., Nealova, L., Perret-Gentil, L., Regocheva, A., Wegorzewski, A., Zoch, D., 2012. BIONOD Cruise report, p. 299.
- Scott, S.D., 1987. Seafloor Polymetallic Sulfides: Scientific Curiosities or Mines of the Future? In: *Marine Minerals* (eds. Teleki, P.G., Dobson, M.R., Moore, J.R., von Stackelberg, U.). NATO ASI Series (Series C: Mathematical and Physical Sciences), 194, Springer, Dordrecht.
- Sharma, R., 2001. Indian Deep-sea Environment Experiment (INDEX):: An appraisal. *Deep-Sea Res. Part II Top. Stud. Oceanogr.* 48, 3295–3307. doi:10.1016/S0967-0645(01)00041-8.
- Smith, C.R., Levin, L.A., Koslow, A., Tyler, P.A., Glover, A.G., 2008. The near future of the deep seafloor ecosystems. In: *Aquatic Ecosystems: Trends and Global Prospects* (ed. Polunin, N.V.C.). Cambridge University Press, 334–353. doi: 10.1017/CBO9780511751790.030.
- Smith, K.L., White, G.A., Laver, M.B., 1979. Oxygen uptake and nutrient exchange of sediments measured in situ using a free vehicle grab respirometer. *Deep Sea Res. Part II* 26, 337–346. doi:10.1016/0198-0149(79)90030-X.

- Soetaert, K., Meysman, F., 2012. Reactive transport in aquatic ecosystems: Rapid model prototyping in the open source software R. *Environ. Model. Softw.* 32, 49–60. doi:10.1016/j.envsoft.2011.08.011.
- Spickermann, R., 2012. Rare Earth Content of Manganese Nodules in the Lockheed Martin Clarion-Clipperton Zone Exploration Areas. *Proc. Off. Technol. Conf.* Houston Texas.
- Stratmann, T., Lins, L., Purser, A., Marcon, Y., Rodrigues, C.F., Ravara, A., Cunha, M.R., Simon-Lledó, E., Jones, D.O.B., Sweetman, A.K., Köser, K., van Oevelen, D., 2018. Abyssal plain faunal carbon flows remain depressed 26 years after a simulated deep-sea mining disturbance. *Biogeosciences* 15, 4131–4145. doi.org/10.5194/bg-15-4131-2018.
- Thiel, H., and Forschungsverband Tiefsee-Umweltschutz, 2001. Evaluation of the environmental consequences of polymetallic nodule mining based on the results of the TUSCH Research Association. *Deep-Sea Res. Part II Top. Stud. Oceanogr.* 48, 3433–3452. doi:10.1016/S0967-0645(01)00051-0.
- Trueblood, D.D., Ozturgut, E., 1997. The benthic impact experiment: A study of the ecological impacts of deep seabed mining on abyssal benthic communities. *Proc. of the 7th ISOPE Conference*, Honolulu, Hawaii.
- Van Dover, C.L., 2011. Tighten regulations on deep-sea mining. *Nature* 470, 31–33. doi: 10.1038/470031a.
- Vanreusel, A., Hilario, A., Ribeiro, P.A., Menot, L., Arbizu, P.M., 2016. Threatened by mining, polymetallic nodules are required to preserve abyssal epifauna. *Sci. Rep.* 6, 26808, doi:10.1038/srep26808.
- Volz, J.B., Liu, B., Köster, M., Henkel, S., Koschinsky, A., Kasten, S., under review. Post-depositional manganese mobilization during the last glacial period in sediments of the eastern Clarion-Clipperton Zone, Pacific Ocean. *Earth Planet. Sci. Lett.*
- Volz, J.B., Mogollón, J.M., Geibert, W., Martínez Arbizu, P., Koschinsky, A., Kasten, S., 2018. Natural spatial variability of depositional conditions, biogeochemical processes and element fluxes in sediments of the eastern Clarion-Clipperton Zone, Pacific Ocean. *Deep-Sea Res. Part I* 140, 159–172.
- Wedding, L.M., Reiter, S.M., Smith, C.R., Gjerde, K.M., Kittinger, J.N., Friedlander, A.M., Gaines, S.D., Clark, M.R., Thurnherr, A.M., Hardy, S.M., Crowder, L.B., 2015. Managing mining of the deep seabed. *Science* 349, 144–145.
- Widmann, P., 2015. Enrichment of mobilizable manganese in relation to manganese nodules abundance, Master thesis, Eberhard Karls Universität Tübingen and the Federal Institute for Geoscience and Resources, Hannover, 182 p.
- Ziebis, W., McManus, J., Ferdelman, T., Schmidt-Schierhorn, F., Bach, W., Muratli, J., Edwards, K.J., Villinger, H., 2012. Interstitial fluid chemistry of sediments underlying the North Atlantic gyre and the influence of subsurface fluid flow. *Earth Planet. Sci. Lett.* 323-324, 79–91. doi:10.1016/j.epsl.2012.01.018.
- Zonneveld, K., Versteegh, G., Kasten, S., Eglinton, T.I., Emeis, K.-C., Huguet, C., Koch, B.P., de Lange, G.J., de Leeuw, J.W., Middelburg, J.J., Mollenhauer, G., Prahl, F., Rethemeyer, J., Wakeham, S., 2010. Selective preservation of organic matter in marine environments; processes and impact on the sedimentary record. *Biogeosciences* 7, 483–511.

CHAPTER VI:

Conclusions and Perspectives

In this cumulative PhD thesis, we present a complementary study on the natural spatial and temporal variation of the sediment geochemistry in the CCZ and the assessment of the potential impact of deep-sea mining in different European areas for the exploration of polymetallic nodules. We used the great potential of combining comprehensive pore-water and solid-phase analyses with numerical transport-reaction modelling. This approach revealed that the flux of organic matter to the seafloor and the rate of sediment accumulation ultimately determine the rates of biogeochemical processes and the development of the redox zonation in the sediments. While aerobic respiration represents the most dominant biogeochemical process, denitrification and manganese(IV) reduction consume only a small fraction of the organic matter delivered to the seafloor (Fig. 1A). Spatial variations in the meter-scale upper oxic zone are mostly associated with a lateral gradient in fluxes of organic matter to the seafloor. Further inter-areal variability is reflected by the depth distribution of REY in the sediments, which are predominantly bound to calcium phosphates. The oxidation of pore-water manganese at depth in several European contract areas indicates that upward diffusing oxygen from the basaltic crust appears to be a widespread phenomenon in the area of the CCZ (Fig. 1A). This finding has strong implications for the heat extraction of the oceanic crust and for biogeochemical processes and microbial communities at depth. The results of this first baseline study lead to the recommendation for the International Seabed Authority (ISA) that one of the protected Area of Particular Environmental Interest (APEI) located north of the CCZ does not represent the depositional and geochemical conditions found in the European contract areas.

The findings of this first baseline study led to the investigation of temporal variations in geochemical conditions in the sediments of the CCZ as a result of postulated climatically-driven lower oxygen concentrations in Pacific bottom waters during the last glacial period. Solid-phase manganese maxima in the surface sediments suggest that the redox zonation was more condensed during the last glacial period during which diagenetically redistributed manganese re-precipitated in the upper few centimeters of the sediments and was continuously mixed into subsequently depositing Holocene sediments (Fig. 1A). These findings have strong implications for paleoceanographic conditions in the Pacific Ocean, biogeochemical processes and redox conditions in the deep-sea sediments as well as the growth of polymetallic nodules in the CCZ. The results of this study further demonstrate that the APEI area located north of

the CCZ differs from the European contract areas as the redox zonation was not as compressed during the last glacial period in the APEI area due to considerably lower carbon burial rates.

As proposed in a previous study, the depth distribution of solid-phase manganese in the surface sediments of the CCZ provides a reliable tool for monitoring the disturbance depth of deep-sea mining (Fig. 1A). The removal of the surface sediments is associated with the loss of the reactive labile organic carbon fraction driving early diagenetic processes in the sediments. As a consequence of lower oxygen consumption rates after the sediment removal, the upper oxic zone extends deeper into the sediment, mostly inhibiting denitrification and manganese(IV) reduction and compressing the suboxic zone at depth (Fig. 1B). While the establishment of bioturbation plays a crucial role for the geochemical re-equilibration in the sediments after the disturbance, the depth of the disturbance as well as the carbon burial rate ultimately determine the geochemical re-equilibration in the sediments. While the reactive surface layer is mostly re-established within 10^3 years after the disturbance, the new geochemical equilibrium in the sediments is reached 10^4 – 10^5 years after the disturbance once the surface sediment layer is fully re-established (Fig. 1C).

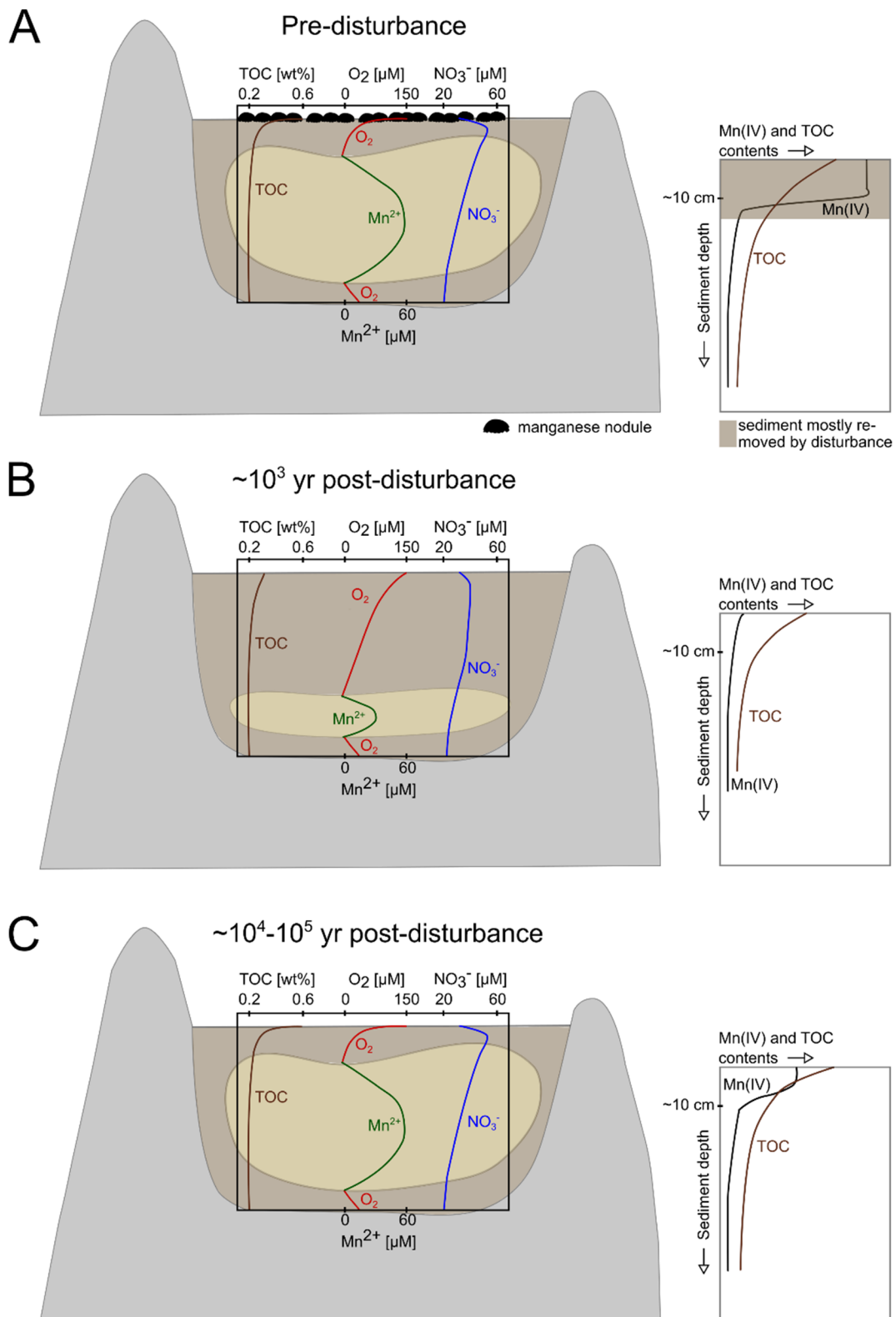


Figure 1: Schematic illustration of the geochemical conditions in the sediments of the CCZ before (A) and after (B, C) anthropogenic disturbances (compare Figure 5 in CHAPTER I: Introduction). (A): Undisturbed sediment redox zonation and solid-phase Mn and TOC maxima in the surface sediments. The uppermost 15 cm of the sediments are most likely removed by anthropogenic disturbances. (B) Redox zonation in the sediments 10^3 years after the surface sediment removal with an extended upper oxic zone and a compressed suboxic zone below. (C) Pre-disturbance redox conditions and the removed sediment surface layer are re-established 10^4 – 10^5 years after the disturbance (Depth distribution of Mn(IV) is roughly estimated).

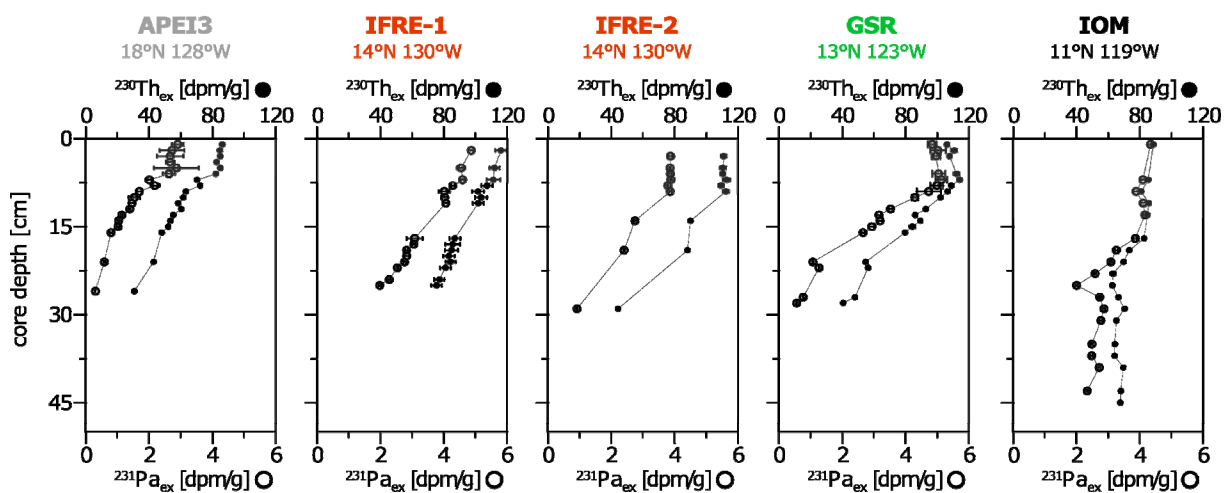
In the framework of this PhD project, data have been produced advancing the knowledge in Pacific paleoceanography, deep-sea sediment geochemistry and the environmental consequences of potential future deep-sea mining activities. Although the baseline studies presented in this thesis fill some knowledge gaps, deep-sea ecosystems are still insufficiently studied and the environmental consequences of deep-sea mining activities are poorly conceived. The results of this PhD project produced in the framework of the Joint Programming Initiative Healthy and Productive Seas and Oceans (JPI Oceans) pilot action “Ecological Aspects of Deep-Sea Mining (MiningImpact)” may provide fundamental information for the recently launched JPI Oceans follow-up project “MiningImpact 2”. During this new European project, the environmental consequences of an industrial component trial of a nodule collector system by the Belgian contractor DEME-GSR will be monitored by an independent scientific community.

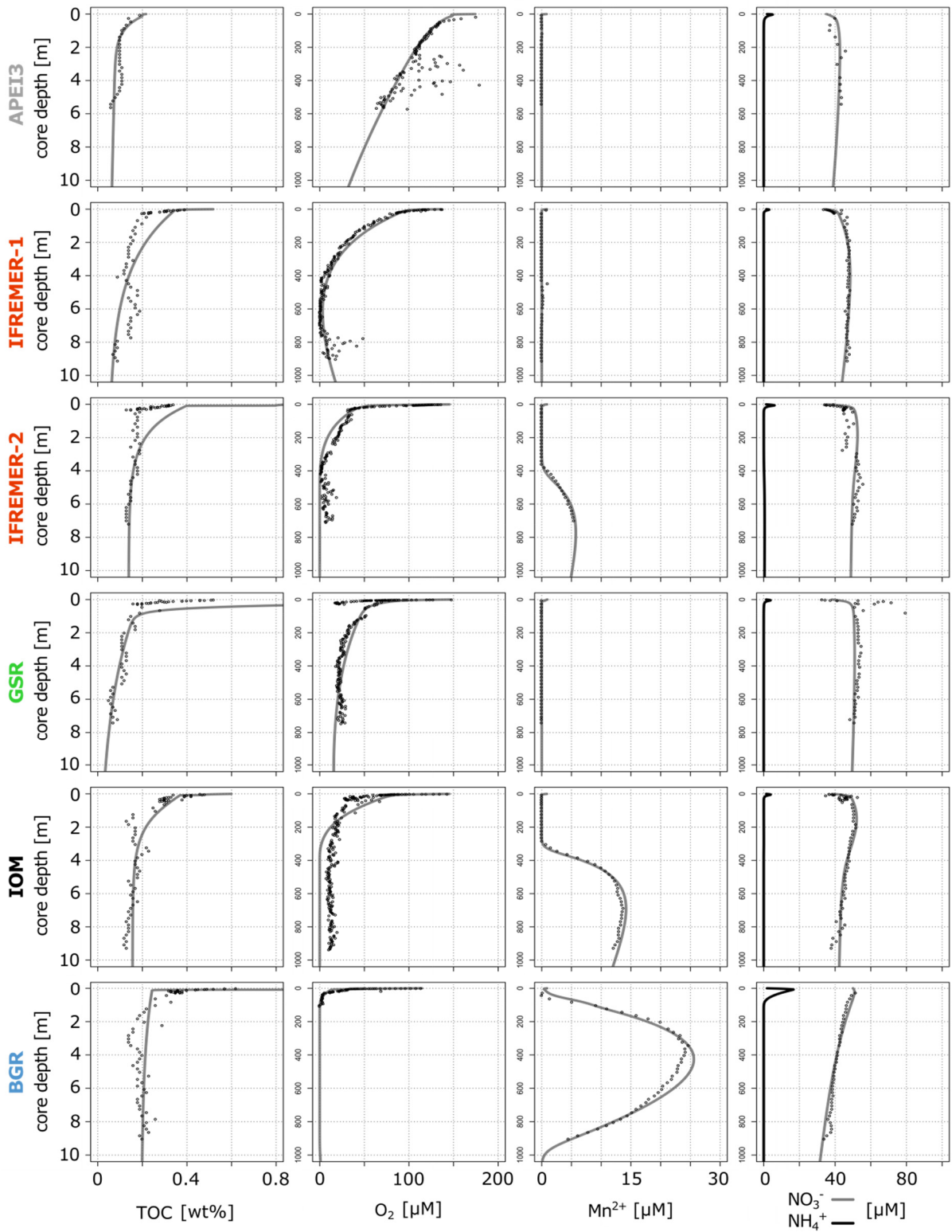
APPENDIX

APPENDIX I

Supplementary material to **CHAPTER II: Natural spatial variability of depositional conditions, biogeochemical processes and element fluxes in sediments of the eastern Clarion-Clipperton Zone, Pacific Ocean**

Supplementary Figure 1: $^{230}\text{Th}/^{231}\text{Pa}$ activity ratios for the uppermost 50 cm of the sediments of the APEI3, IFREMER, GSR and IOM sites. Only below the bioturbated layer (lower boundary indicated by dotted line) the activity ratio increases with depth as a result of radioactive decay.



Supplementary Figure 2: Model fits for all sites including TOC, oxygen, Mn^{2+} , nitrate and ammonia.

Supplementary Table 1: Electron-equivalent redox reactions and associated expressions and units used in the numerical diagenetic model.

| Reaction name | Reaction | Rate expression | Rate unit [yr ⁻¹] |
|--------------------------------|----------------|--|-------------------------------|
| Aerobic respiration | R ₁ | $(\sigma_1 C_{TOC1} + \sigma_2 C_{TOC2} + \sigma_3 C_{TOC3}) \frac{C_{O_2}}{C_{O_2} + h_1}$ | mM C ^a |
| Heterotrophic denitrification | R ₂ | $(\sigma_1 C_{TOC1} + \sigma_2 C_{TOC2} + \sigma_3 C_{TOC3}) \gamma \frac{C_{NO_3^-}}{C_{NO_3^-} + h_2}$ | mM C ^a |
| Dissimilatory Mn(IV) reduction | R ₃ | $(\sigma_1 C_{TOC1} + \sigma_2 C_{TOC2} + \sigma_3 C_{TOC3}) \gamma \frac{h_2}{C_{NO_3^-} + h_2}$ | mM C ^a |
| Mn ²⁺ oxidation | R ₄ | $k_4 C_{O_2} C_{Mn^{2+}}$ | μM O ₂ |
| Nitrification | R ₅ | $k_5 C_{O_2} C_{NH_4^+}$ | μM N |
| Mn-annamox | R ₆ | $k_6 C_{NH_4^+} C_{MnO_2} \gamma \frac{h_2}{C_{NO_3^-} + h_2}$ | μM Mn |

^a dry bulk sediment

$$\gamma = \frac{h_1}{(h_1 + C_{O_2})}$$

Supplementary Table 2: Species, parameter values and boundary conditions (BC) used in the reaction-transport model.

| | Symbol | Unit | BGR | IOM | GSR | IFRE-1 | IFRE-2 | APEI3 |
|--|------------------|--------------------------------------|---------|---------|---------|---------|---------|---------|
| <i>Species and boundary conditions</i> | | | | | | | | |
| Porosity at SWI | φ_0 | | 0.82 | 0.8 | 0.8 | 0.83 | 0.82 | 0.58 |
| Porosity at compaction | φ_∞ | | 0.69 | 0.67 | 0.65 | 0.67 | 0.66 | 0.47 |
| Sedimentation rate | ω_i | cm kyr ⁻¹ | 0.65 | 1.15 | 0.21 | 0.64 | 0.48 | 0.2 |
| Oxygen _{bw} | O_2 | μM | 120 | 150 | 150 | 140 | 150 | 170 |
| Ammonium _{bw} | NH_4^+ | μM | 1 | 1 | 1 | 1 | 1 | 1 |
| Nitrate _{bw} | NO_3^- | μM | 50 | 38 | 38 | 34 | 35 | 35 |
| Dissolved reduced manganese _{bw} | Mn^{2+} | μM | 1 | 1 | 1 | 1 | 1 | 1 |
| <i>Fitted parameters</i> | | | | | | | | |
| Sediment thickness | | m | 20 | 83 | 77 | 20 | 102 | 93 |
| Labile C _{org} | TOC_1 | mol m ⁻² yr ⁻¹ | 6.0E-02 | 4.5E-02 | 4.3E-02 | 4.4E-02 | 4.5E-02 | 3.2E-02 |
| Metabolizable C _{org} | TOC_2 | mol m ⁻² yr ⁻¹ | 1.2E-04 | 1.1E-03 | 2.9E-03 | 7.0E-04 | 5.1E-04 | 2.5E-04 |
| Refractory C _{org} | TOC_3 | mol m ⁻² yr ⁻¹ | 5.0E-04 | 7.8E-04 | 1.7E-04 | 1.2E-04 | 2.6E-04 | 1.5E-04 |
| Oxygen _{bas} | O_2 | μM | 18 | 55 | 150 | 90 | 15 | 25 |
| Ammonium _{bas} | NH_4^+ | μM | 1 | 1 | 1 | 1 | 1 | 1 |
| Nitrate _{bas} | NO_3^- | μM | 19 | 30 | 20 | 30 | 35 | 30 |
| Dissolved reduced manganese _{bas} | Mn^{2+} | μM | 1 | 1 | 1 | 1 | 1 | 1 |
| 1 st order deg. coeff. TOC_1 | σ_1 | yr ⁻¹ | 1.0E-03 | 1.0E-02 | 2.0E-02 | 3.0E-02 | 2.5E-03 | 1.0E-01 |
| 1 st order deg. coeff. TOC_2 | σ_2 | yr ⁻¹ | 1.0E-06 | 5.5E-06 | 7.0E-06 | 1.0E-06 | 1.7E-06 | 2.5E-06 |
| 1 st order deg. coeff. TOC_3 | σ_3 | yr ⁻¹ | 2.0E-09 | 2.5E-09 | 2.0E-07 | 5.0E-09 | 1.0E-11 | 4.0E-08 |
| Bioturbation coefficient | B_0 | cm ² yr ⁻¹ | 0.5 | 0.2 | 0.5 | 0.1 | 0.5 | 0.3 |
| Biomixing half depth | z_{mix} | cm | 7.0 | 7.0 | 7.0 | 7.0 | 7.0 | 13.0 |
| Biomixing attenuation | zz_{att} | cm | 0.1 | 0.1 | 0.01 | 0.1 | 0.1 | 0.1 |
| Bioirrigation coefficient | α_0 | yr ⁻¹ | 0.65 | 2.0 | 5.0 | 0.1 | 1.0 | 2.0 |
| O ₂ inhibition concentration for R ₁ | h_1 | μM | 0.008 | 0.006 | 5 | 0.5 | 0.5 | 0.001 |
| NO ₃ ⁻ inhibition concentration for R ₂ | h_2 | μM | 45 | 25 | 40 | 5 | 50 | 30 |
| R ₄ rate constant | k_4 | μM ⁻¹ yr ⁻¹ | 0.1 | 0.1 | 0.1 | 0.1 | 0.1 | 0.1 |
| R ₅ rate constant | k_5 | μM ⁻¹ yr ⁻¹ | 0.005 | 0.1 | 0.1 | 0.1 | 0.1 | 0.01 |
| R ₆ rate constant | k_6 | μM ⁻¹ yr ⁻¹ | 0.001 | 0.001 | 0 | 0 | 0 | 0 |

APPENDIX II

Supplementary material to **CHAPTER III: Calcium phosphate control of REY patterns of siliceous-ooze-rich deep-sea sediments from the central equatorial Pacific**

Supplementary Table EA1: Replicate analyses of NIST-2702 certified reference material (CRM) during ICP-OES measurements (n=12 digested samples; 14 measurements in 5 ICP-OES runs).

| LOQ [#] [mg/L] | Element | NIST-2702 certified [mg/kg] | NIST-2702 measured [mg/kg] | Accuracy (%) | Precision (%) |
|-------------------------|-----------------|-----------------------------|----------------------------|--------------|---------------|
| 30-120 | Al | 84100±2200 | 79735±1525 | -5 | 2 |
| 8.5-118 | Ca ^a | 3430±240 | 3486±69 | 2 | 2 |
| 6.5-103.5 | Fe | 79100±2400 | 76739±2430 | -3 | 3 |
| 60.5-951 | K | 20540±720 | 19500±386 | -5 | 2 |
| 0.5-17.1 | Mn | 1757±58 | 1728±41 | -2 | 2 |
| 169-2983 | Na | 6810±200 | 6485±568 | -5 | 9 |
| 7.5-45 | P | 1552±66 | 1537±39 | -1 | 3 |
| 8.5-148 | S ^b | 15000 | 16001±314 | 7 | 2 |
| 4.7-18.5 | Ti | 8840±820 | 8302±189 | -6 | 2 |

[#] LOQ: limit of quantification; 10*standard deviation of acid blanks for each run

^a reference value

^b information value

Supplementary Table EA2: Replicate analyses of NIST-2702 CRM during ICP-MS measurements (n=10 digested samples; 26 measurements in 2 ICP-MS runs). Accuracy and precision calculated from averages of each digested sample.

| Average LOQ [#] [mg/kg] | Element | NIST-2702 certified [mg/kg] | NIST-2702 measured [mg/kg] | Accuracy (%) | Precision (%) |
|----------------------------------|-----------------|-----------------------------|----------------------------|--------------|---------------|
| 0.122 | Ba | 397.4±3.2 | 393±27.4 | -1 | 7 |
| 0.074 | Y | --- | 36.8±2.1 | | 6 |
| 0.030 | La | 73.5±4.2 | 71.6±4.4 | -3 | 6 |
| 0.030 | Ce | 123.4±5.8 | 125.5±8.2 | 2 | 7 |
| 0.043 | Pr | --- | 16.5±1.0 | | 6 |
| 0.051 | Nd ^b | 56 | 61±3.5 | 9 | 6 |
| 0.050 | Sm ^b | 10.8 | 11.4±0.7 | 6 | 6 |
| 0.050 | Eu | --- | 2.0±0.1 | | 5 |
| 0.041 | Gd | --- | 9.0±0.5 | | 5 |
| 0.042 | Tb | --- | 1.3±0.1 | | 5 |
| 0.036 | Dy | --- | 7.4±0.4 | | 6 |
| 0.033 | Ho | --- | 1.4±0.1 | | 5 |
| 0.029 | Er | --- | 4.0±0.2 | | 5 |
| 0.023 | Tm | --- | 0.6±0.0 | | 5 |
| 0.017 | Yb | --- | 3.7±0.2 | | 5 |
| 0.018 | Lu | --- | 0.5±0.0 | | 4 |

[#] LOQ: limit of quantification; 10*standard deviation of acid blanks for each run

^b information value

Supplementary Table EA3: Replicate analyses of BHVO-2 CRM during ICP-MS measurements (n=1 digested sample; 2 measurements during 1 ICP-MS run). Accuracy and precision calculated from multiple measurements of 1 digested sample.

| Average LOQ [#] [mg/kg] | Element | BHVO-2 recommended [mg/kg] | BHVO-2 measured [mg/kg] | Accuracy (%) | Precision (%) |
|----------------------------------|-----------------|----------------------------|-------------------------|--------------|---------------|
| 0.122 | Ba | 130±13 | 129±6.1 | -1 | 5 |
| 0.074 | Y | 26±2 | 24.5±0.4 | -6 | 2 |
| 0.030 | La | 15±1 | 15.5±0.8 | 3 | 5 |
| 0.030 | Ce | 38±2 | 39±2 | 3 | 5 |
| 0.043 | Pr | --- | 5.4±0.28 | | 5 |
| 0.051 | Nd | 25.0±1.8 | 24.8±1.1 | -1 | 4 |
| 0.050 | Sm ^b | 6.2±0.4 | 6.3±0.3 | 1 | 5 |
| 0.050 | Eu | --- | 2.1±0.08 | | 4 |
| 0.041 | Gd ^b | 6.3±0.2 | 6.3±0.2 | 1 | 4 |
| 0.042 | Tb ^b | 0.9 | 0.9±0.03 | 2 | 4 |
| 0.036 | Dy | --- | 5.4±0.3 | | 5 |
| 0.033 | Ho ^b | 1.04±0.04 | 0.98±0.03 | -4 | 3 |
| 0.029 | Er | --- | 2.6±1.12 | | 5 |
| 0.023 | Tm | --- | 0.3±0.01 | | 3 |
| 0.017 | Yb ^b | 2.0±0.2 | 2.0±0.07 | 1 | 4 |
| 0.018 | Lu ^b | 0.28±0.01 | 0.28±0.01 | -2 | 4 |

[#] LOQ: limit of quantification; 10*standard deviation of acid blanks for each run

^b information value

APPENDIX II

Supplementary data 3: Salt-corrected major element contents and Fe/Al and Mn/Al ratios in CCZ sediment samples. All concentrations given in wt% (Al, Ca, Fe, K, Mn, Na) or ppm (Ba, P, S, Ti).

| Sample ID | Al | Ca | Fe | K | Mn | Na | Ba | P | S | Ti | Fe/Al | Mn/Al |
|--------------|------|------|-------|------|------|------|-------|------|------|------|-------|-------|
| SO239- | | | | | | | | | | | | |
| 87GC-35cm | 6.71 | 0.84 | 4.54 | 2.25 | 0.33 | 4.87 | 11747 | 1030 | 5386 | 3288 | 0.68 | 0.05 |
| 87GC-123cm | 7.51 | 0.91 | 5.05 | 2.4 | 0.14 | 3.83 | 11070 | 1226 | 5172 | 3678 | 0.67 | 0.02 |
| 87 GC-163cm | 7.5 | 0.95 | 4.84 | 2.42 | 0.58 | 4.05 | 12549 | 1347 | 5660 | 3615 | 0.65 | 0.08 |
| 87 GC-203cm | 7.3 | 0.85 | 4.82 | 2.37 | 0.09 | 3.82 | 14579 | 1075 | 5868 | 3586 | 0.66 | 0.01 |
| 87 GC-243cm | 7.96 | 0.97 | 5.28 | 2.58 | 0.06 | 4.02 | 10556 | 1370 | 5001 | 3911 | 0.66 | 0.01 |
| 87 GC-283cm | 7.58 | 0.95 | 4.99 | 2.4 | 0.08 | 3.87 | 11338 | 1224 | 4999 | 3736 | 0.66 | 0.01 |
| 87 GC-343cm | 7.38 | 0.98 | 4.84 | 2.33 | 0.13 | 3.92 | 12973 | 1479 | 5242 | 3570 | 0.66 | 0.02 |
| 87 GC-383cm | 7.16 | 0.96 | 4.65 | 2.28 | 0.24 | 3.87 | 12332 | 1423 | 5378 | 3484 | 0.65 | 0.03 |
| 87 GC-443cm | 7.39 | 1.03 | 5.08 | 2.42 | 0.07 | 3.89 | 10457 | 1709 | 5010 | 3547 | 0.69 | 0.01 |
| 87 GC-483cm | 7.11 | 1 | 4.91 | 2.36 | 0.17 | 3.74 | 16073 | 1713 | 5945 | 3409 | 0.69 | 0.02 |
| 87 GC-607cm | 7.19 | 1 | 5.24 | 2.33 | 0.06 | 3.59 | 14798 | 1599 | 5871 | 3594 | 0.73 | 0.01 |
| 87 GC-667cm | 7.22 | 0.96 | 4.89 | 2.3 | 0.06 | 3.41 | 12948 | 1484 | 5294 | 3471 | 0.68 | 0.01 |
| 87 GC-727cm | 6.93 | 1.15 | 4.94 | 2.21 | 0.24 | 3.50 | 10602 | 2229 | 4872 | 3366 | 0.71 | 0.03 |
| 87 GC-767cm | 7.11 | 1.3 | 5.18 | 2.25 | 0.89 | 3.59 | 13043 | 2690 | 5426 | 3482 | 0.73 | 0.12 |
| 87 GC-827cm | 6.92 | 1.3 | 4.81 | 2.1 | 0.9 | 3.59 | 13614 | 2708 | 5423 | 3455 | 0.7 | 0.13 |
| 87 GC-887cm | 6.84 | 1.37 | 4.87 | 2.13 | 0.92 | 3.39 | 13207 | 3100 | 5108 | 3423 | 0.71 | 0.13 |
| 165 GC-47cm | 7.84 | 0.75 | 4.94 | 2.59 | 0.26 | 3.31 | 5139 | 944 | 3241 | 3911 | 0.63 | 0.03 |
| 165 GC-127cm | 8.24 | 0.74 | 5.16 | 2.69 | 0.48 | 3.43 | 4646 | 850 | 3248 | 4100 | 0.63 | 0.06 |
| 165 GC-187cm | 7.94 | 0.74 | 5.03 | 2.6 | 0.58 | 3.64 | 5084 | 833 | 3511 | 3921 | 0.63 | 0.07 |
| 165 GC-267cm | 7.9 | 0.85 | 5.02 | 2.6 | 0.43 | 3.47 | 5610 | 1282 | 3497 | 3949 | 0.64 | 0.05 |
| 165 GC-367cm | 7.95 | 0.77 | 4.98 | 2.67 | 0.61 | 3.50 | 5146 | 1019 | 3349 | 4009 | 0.63 | 0.08 |
| 165 GC-407cm | 6.61 | 0.83 | 3.98 | 2.28 | 6.63 | 3.53 | 5910 | 804 | 3125 | 3485 | 0.60 | 1.00 |
| 165 GC-467cm | 7.92 | 0.72 | 5.08 | 2.61 | 0.11 | 3.49 | 6522 | 810 | 3736 | 3960 | 0.64 | 0.01 |
| 165 GC-517cm | 8.02 | 0.76 | 5.16 | 2.63 | 0.05 | 3.42 | 5366 | 916 | 3323 | 3934 | 0.64 | 0.01 |
| 165 GC-612cm | 8.08 | 0.76 | 5.24 | 2.6 | 0.05 | 3.43 | 4756 | 915 | 3217 | 3988 | 0.65 | 0.01 |
| 165 GC-672cm | 7.83 | 0.84 | 5.17 | 2.52 | 0.27 | 3.46 | 5856 | 1316 | 3631 | 3779 | 0.66 | 0.03 |
| 165 GC-732cm | 7.84 | 0.88 | 5.17 | 2.52 | 0.16 | 3.59 | 6342 | 1471 | 3803 | 3758 | 0.66 | 0.02 |
| 165 GC-792cm | 6.17 | 1.8 | 6.86 | 2.21 | 0.68 | 4.79 | 14757 | 4726 | 7035 | 2667 | 1.11 | 0.11 |
| 165 GC-832cm | 5.69 | 1.89 | 7.22 | 2.33 | 1.56 | 5.10 | 14560 | 5112 | 7237 | 2377 | 1.27 | 0.27 |
| 165 GC-912cm | 5.14 | 2.04 | 7.46 | 2.14 | 1.08 | 5.15 | 14305 | 6149 | 7300 | 2110 | 1.45 | 0.21 |
| 194 GC-5cm | 8.77 | 0.78 | 5.41 | 3.03 | 0.54 | 2.33 | 3275 | 961 | 1943 | 4762 | 0.62 | 0.06 |
| 194 GC-85cm | 8.74 | 0.73 | 5.48 | 3.06 | 0.6 | 2.38 | 3027 | 920 | 1887 | 4792 | 0.63 | 0.07 |
| 194 GC-157cm | 8.61 | 0.72 | 5.27 | 3.03 | 0.53 | 2.38 | 3626 | 972 | 2027 | 4713 | 0.61 | 0.06 |
| 194 GC-201cm | 8.48 | 0.72 | 5.24 | 3.02 | 0.64 | 2.23 | 3587 | 1001 | 1906 | 4579 | 0.62 | 0.08 |
| 194 GC-261cm | 8.45 | 0.76 | 5.35 | 3 | 0.78 | 2.24 | 3771 | 1074 | 1884 | 4695 | 0.63 | 0.09 |
| 194 GC-321cm | 8.45 | 0.78 | 5.29 | 2.98 | 0.85 | 2.18 | 3911 | 1181 | 2006 | 4550 | 0.63 | 0.1 |
| 194 GC-381cm | 8.64 | 0.8 | 5.6 | 3.05 | 0.93 | 2.28 | 3976 | 1244 | 2047 | 4750 | 0.65 | 0.11 |
| 194 GC-461cm | 8.24 | 0.88 | 5.43 | 2.97 | 1.2 | 2.38 | 3383 | 1497 | 1874 | 4604 | 0.66 | 0.15 |
| 194 GC-521cm | 8.49 | 1.73 | 4.87 | 3 | 0.77 | 3.30 | 3305 | 3004 | 2134 | 4088 | 0.57 | 0.09 |
| 194 GC-561cm | 6.8 | 1.71 | 11.77 | 2.76 | 2.08 | 3.33 | 3106 | 5110 | 2554 | 3024 | 1.73 | 0.31 |

APPENDIX II

Supplementary data 3 (continued): Salt-corrected REY concentrations in CCZ sediment samples. All concentrations given in ppm.

| Sample ID | La | Ce | Pr | Nd | Sm | Eu | Gd | Tb | Dy | Y | Ho |
|--------------|-------|-------|------|-------|------|------|------|------|------|-------|------|
| SO239- | | | | | | | | | | | |
| 87GC-35cm | 38.7 | 72 | 11.1 | 47.6 | 11.6 | 2.5 | 11.6 | 1.8 | 10.9 | 52.4 | 2.1 |
| 87GC-123cm | 55.6 | 91.6 | 16.8 | 70.7 | 17.3 | 3.64 | 17.1 | 2.58 | 15.5 | 76.3 | 2.97 |
| 87 GC-163cm | 58.6 | 93.7 | 17.6 | 73.1 | 17.9 | 3.68 | 17.7 | 2.65 | 16.2 | 81.1 | 3.19 |
| 87 GC-203cm | 54 | 96 | 16.1 | 67.1 | 16.4 | - | 16.4 | 2.55 | 15.1 | 74.5 | 2.9 |
| 87 GC-243cm | 63.3 | 106 | 19.2 | 79.5 | 19.4 | 4.27 | 19.5 | 2.95 | 17.9 | 86.6 | 3.46 |
| 87 GC-283cm | 59.6 | 98.6 | 17.9 | 74.7 | 18.3 | 4 | 18.4 | 2.8 | 17 | 83.9 | 3.25 |
| 87 GC-343cm | 70.9 | 110 | 21.6 | 90.6 | 22.6 | 4.82 | 22.5 | 3.41 | 20.8 | 102 | 4.06 |
| 87 GC-383cm | 64.5 | 95.7 | 20.3 | 85.4 | 21.2 | 4.56 | 21.1 | 3.25 | 19.4 | 95.1 | 3.84 |
| 87 GC-443cm | 67.9 | 90.5 | 20.5 | 85.3 | 21.1 | 4.73 | 22 | 3.36 | 20.2 | 100 | 3.97 |
| 87 GC-483cm | 75.2 | 104 | 23 | 96 | 23.5 | 4.98 | 24.3 | 3.69 | 22.5 | 107 | 4.32 |
| 87 GC-607cm | 71.2 | 99.8 | 22.3 | 92.2 | 23.1 | 4.95 | 23.7 | 3.6 | 21.4 | 107 | 4.08 |
| 87 GC-667cm | 73.3 | 104 | 23.5 | 97.8 | 24.5 | 5.32 | 24.9 | 3.82 | 22 | 106 | 4.23 |
| 87 GC-727cm | 99.2 | 103 | 31.5 | 134 | 33.6 | 7.81 | 34.4 | 5.15 | 30.8 | 148 | 5.91 |
| 87 GC-767cm | 114 | 109 | 34.2 | 146 | 36.1 | 8.18 | 38.2 | 5.64 | 34.1 | 177 | 6.78 |
| 87 GC-827cm | 117 | 110 | 36 | 153 | 36.8 | 8.65 | 40 | 5.92 | 36.4 | 191 | 7.26 |
| 87 GC-887cm | 130 | 113 | 39.4 | 168 | 40.5 | 9.4 | 43.4 | 6.5 | 39.7 | 208 | 7.73 |
| 165 GC-47cm | 45.1 | 98.1 | 12.5 | 49.8 | 11.7 | 2.5 | 10.9 | 1.8 | 10.3 | 54.9 | 2.04 |
| 165 GC-127cm | 46.0 | 101.6 | 12.7 | 50.3 | 11.8 | 2.5 | 11.0 | 1.7 | 10.2 | 51.7 | 1.98 |
| 165 GC-187cm | 46.9 | 103.2 | 13.3 | 52.3 | 12.1 | 2.6 | 11.4 | 1.7 | 10.6 | 53.4 | 2.03 |
| 165 GC-267cm | 55.3 | 105.6 | 15.5 | 63.1 | 15.0 | 3.3 | 15.1 | 2.3 | 14.2 | 74.2 | 2.75 |
| 165 GC-367cm | 53.5 | 108.1 | 15.1 | 60.4 | 14.5 | 3.1 | 13.8 | 2.2 | 13.0 | 64.9 | 2.49 |
| 165 GC-407cm | 51.0 | 100.6 | 15.0 | 60.9 | 14.7 | 3.2 | 13.8 | 2.2 | 12.7 | 59.9 | 2.41 |
| 165 GC-467cm | 44.3 | 103.0 | 12.6 | 50.2 | 12.0 | 2.5 | 11.2 | 1.7 | 10.5 | 52.8 | 2.03 |
| 165 GC-517cm | 48.7 | 99.5 | 13.9 | 55.6 | 13.1 | 2.8 | 12.5 | 1.9 | 11.7 | 57.8 | 2.26 |
| 165 GC-612cm | 48.3 | 100.6 | 14.1 | 55.9 | 13.5 | 3.0 | 13.0 | 2.0 | 12.1 | 60.4 | 2.33 |
| 165 GC-672cm | 56.3 | 99.2 | 16.5 | 68.9 | 16.7 | 3.8 | 16.7 | 2.5 | 15.7 | 82.0 | 3.05 |
| 165 GC-732cm | 63.7 | 110.8 | 19.3 | 79.3 | 19.4 | 4.4 | 19.4 | 3.0 | 18.1 | 90.2 | 3.45 |
| 165 GC-792cm | 110 | 75.1 | 29.5 | 125 | 28.0 | 6.0 | 30.2 | 4.4 | 27.7 | 155 | 5.58 |
| 165 GC-832cm | 107 | 77.6 | 30.1 | 127 | 28.9 | 6.3 | 30.5 | 4.4 | 27.8 | 149 | 5.54 |
| 165 GC-912cm | 127 | 75.0 | 33.0 | 140 | 30.4 | 6.8 | 33.8 | 4.8 | 30.9 | 184 | 6.42 |
| 194 GC-5cm | 52.0 | 123.7 | 13.6 | 53.1 | 11.9 | 2.5 | 10.6 | 1.7 | 10.0 | 54.7 | 2.0 |
| 194 GC-85cm | 51.7 | 124.8 | 13.8 | 54.1 | 12.3 | 2.7 | 11.1 | 1.7 | 10.4 | 54.5 | 2.0 |
| 194 GC-157cm | 54.6 | 127.1 | 14.7 | 57.1 | 12.8 | 2.8 | 12.0 | 1.8 | 11.1 | 56.0 | 2.1 |
| 194 GC-201cm | 55.6 | 129.6 | 15.3 | 61.1 | 14.0 | 3.0 | 12.9 | 1.9 | 12.1 | 60.9 | 2.3 |
| 194 GC-261cm | 62.8 | 146.1 | 17.4 | 69.2 | 16.0 | 3.5 | 14.9 | 2.2 | 13.7 | 68.0 | 2.6 |
| 194 GC-321cm | 61.2 | 138.6 | 17.8 | 72.1 | 17.2 | 3.8 | 16.2 | 2.4 | 14.7 | 75.0 | 2.9 |
| 194 GC-381cm | 66.9 | 141.9 | 19.5 | 78.6 | 18.6 | 4.2 | 17.8 | 2.7 | 16.0 | 81.3 | 3.1 |
| 194 GC-461cm | 77.5 | 157.3 | 23.3 | 95.7 | 22.8 | 5.3 | 22.2 | 3.3 | 20.1 | 99.4 | 3.8 |
| 194 GC-521cm | 94.7 | 122.9 | 28.5 | 118.8 | 28.1 | 6.6 | 28.6 | 4.2 | 25.5 | 136.3 | 5.0 |
| 194 GC-561cm | 138.0 | 137.0 | 38.8 | 163.1 | 36.7 | 8.7 | 37.9 | 5.5 | 34.1 | 187.2 | 6.8 |

APPENDIX II

Supplementary data 3 (continued): Salt-corrected REY concentrations in CCZ sediment samples. All concentrations given in ppm.

| Sample ID | Er | Tm | Yb | Lu | ΣREY | Ce/Ce* | Y/Ho | HREE/ LREE | MREE/ MREE* |
|--------------|------|-----|------|-----|-------|--------|------|---------------|----------------|
| SO239- | | | | | | | | | |
| 87GC-35cm | 6.0 | 0.8 | 5.6 | 0.8 | 276.0 | 0.8 | 24.9 | 0.090 | 0.104 |
| 87GC-123cm | 8.4 | 1.2 | 7.7 | 1.1 | 388.0 | 0.7 | 25.7 | 0.091 | 0.110 |
| 87 GC-163cm | 8.9 | 1.2 | 8.0 | 1.2 | 405.0 | 0.7 | 25.4 | 0.093 | 0.109 |
| 87 GC-203cm | 8.2 | 1.1 | 7.5 | 1.1 | - | 0.8 | 25.7 | 0.090 | 0.099 |
| 87 GC-243cm | 9.8 | 1.4 | 9.0 | 1.3 | 444.0 | 0.7 | 25.1 | 0.093 | 0.109 |
| 87 GC-283cm | 9.3 | 1.3 | 8.6 | 1.3 | 419.0 | 0.7 | 25.8 | 0.095 | 0.110 |
| 87 GC-343cm | 11.6 | 1.6 | 10.8 | 1.6 | 498.0 | 0.6 | 25.1 | 0.101 | 0.115 |
| 87 GC-383cm | 10.7 | 1.5 | 9.8 | 1.4 | 458.0 | 0.6 | 24.7 | 0.102 | 0.119 |
| 87 GC-443cm | 11.4 | 1.6 | 10.4 | 1.5 | 465.0 | 0.6 | 25.3 | 0.109 | 0.122 |
| 87 GC-483cm | 12.4 | 1.7 | 11.2 | 1.7 | 515.0 | 0.6 | 24.8 | 0.105 | 0.120 |
| 87 GC-607cm | 11.7 | 1.6 | 10.3 | 1.5 | 498.0 | 0.6 | 26.1 | 0.102 | 0.122 |
| 87 GC-667cm | 11.8 | 1.6 | 10.3 | 1.5 | 515.0 | 0.6 | 25.1 | 0.099 | 0.123 |
| 87 GC-727cm | 16.4 | 2.2 | 14.1 | 2.1 | 668.0 | 0.4 | 25.0 | 0.111 | 0.137 |
| 87 GC-767cm | 18.9 | 2.6 | 16.3 | 2.4 | 749.0 | 0.4 | 26.1 | 0.116 | 0.136 |
| 87 GC-827cm | 19.9 | 2.8 | 17.7 | 2.5 | 785.0 | 0.4 | 26.3 | 0.121 | 0.137 |
| 87 GC-887cm | 21.6 | 2.9 | 18.7 | 2.7 | 851.0 | 0.4 | 26.9 | 0.119 | 0.138 |
| 165 GC-47cm | 5.8 | 0.8 | 5.5 | 0.8 | 312.5 | 0.9 | 26.9 | 0.073 | 0.084 |
| 165 GC-127cm | 5.6 | 0.8 | 5.2 | 0.8 | 313.9 | 1.0 | 26.1 | 0.068 | 0.083 |
| 165 GC-187cm | 5.8 | 0.8 | 5.3 | 0.8 | 322.2 | 1.0 | 26.3 | 0.068 | 0.083 |
| 165 GC-267cm | 8.0 | 1.1 | 7.3 | 1.1 | 384.0 | 0.8 | 27.0 | 0.084 | 0.096 |
| 165 GC-367cm | 7.1 | 1.0 | 6.5 | 1.0 | 366.7 | 0.9 | 26.1 | 0.076 | 0.091 |
| 165 GC-407cm | 6.9 | 1.0 | 6.4 | 0.9 | 351.5 | 0.8 | 24.8 | 0.078 | 0.095 |
| 165 GC-467cm | 6.0 | 0.8 | 5.3 | 0.8 | 315.6 | 1.0 | 26.0 | 0.071 | 0.084 |
| 165 GC-517cm | 6.5 | 0.9 | 5.9 | 0.9 | 334.0 | 0.9 | 25.6 | 0.076 | 0.090 |
| 165 GC-612cm | 6.7 | 0.9 | 6.2 | 0.9 | 340.0 | 0.9 | 25.9 | 0.078 | 0.092 |
| 165 GC-672cm | 8.8 | 1.2 | 8.1 | 1.2 | 400.7 | 0.7 | 26.9 | 0.093 | 0.105 |
| 165 GC-732cm | 10.0 | 1.4 | 9.1 | 1.4 | 453.0 | 0.7 | 26.1 | 0.093 | 0.108 |
| 165 GC-792cm | 16.1 | 2.3 | 14.0 | 2.1 | 631.3 | 0.3 | 27.9 | 0.118 | 0.127 |
| 165 GC-832cm | 15.9 | 2.2 | 13.8 | 2.0 | 628.4 | 0.3 | 26.9 | 0.115 | 0.128 |
| 165 GC-912cm | 18.3 | 2.5 | 15.8 | 2.3 | 710.8 | 0.3 | 28.7 | 0.121 | 0.127 |
| 194 GC-5cm | 5.7 | 0.8 | 5.2 | 0.8 | 348.2 | 1.1 | 27.4 | 0.060 | 0.071 |
| 194 GC-85cm | 5.8 | 0.8 | 5.3 | 0.8 | 351.9 | 1.1 | 27.3 | 0.060 | 0.074 |
| 194 GC-157cm | 6.1 | 0.9 | 5.7 | 0.8 | 365.7 | 1.0 | 26.1 | 0.062 | 0.075 |
| 194 GC-201cm | 6.7 | 0.9 | 6.1 | 0.9 | 383.3 | 1.0 | 26.0 | 0.065 | 0.079 |
| 194 GC-261cm | 7.5 | 1.0 | 6.8 | 1.0 | 432.8 | 1.0 | 25.8 | 0.065 | 0.080 |
| 194 GC-321cm | 8.0 | 1.1 | 7.1 | 1.0 | 439.3 | 1.0 | 26.1 | 0.070 | 0.088 |
| 194 GC-381cm | 8.8 | 1.2 | 7.8 | 1.1 | 469.5 | 0.9 | 26.0 | 0.072 | 0.090 |
| 194 GC-461cm | 10.6 | 1.5 | 9.3 | 1.4 | 553.3 | 0.8 | 26.0 | 0.075 | 0.097 |
| 194 GC-521cm | 14.3 | 2.0 | 12.6 | 1.8 | 629.9 | 0.5 | 27.2 | 0.098 | 0.116 |
| 194 GC-561cm | 19.7 | 2.7 | 16.9 | 2.5 | 835.6 | 0.4 | 27.3 | 0.102 | 0.117 |

APPENDIX II

Supplementary data 3 (continued): Salt-corrected major element contents and REY concentrations for leached CCZ sediment samples. All concentrations given in ppm.

| Sample ID | Fe | Mn | P | La | Ce | Pr | Nd | Sm | Eu |
|-----------------------|-------|-------|-------|-------|-------|--------|-------|--------|-------|
| Na acetate 87_163 | 17.6 | 80.6 | 1122 | 37.2 | 13.1 | 13.2 | 57.8 | 15.3 | 3.85 |
| Na acetate 87_827 | 3.2 | 570 | 3247 | 117 | 34.4 | 37.9 | 168 | 42.6 | 10.7 |
| Na acetate 165_407 | 5.87 | 457 | 623 | 22 | 4.75 | 8.52 | 37.6 | 10.2 | 2.55 |
| Na acetate 165_812 | 21.7 | 112 | 4662 | 96 | 9.52 | 27.9 | 122 | 28.3 | 6.96 |
| Na acetate 194_157 | 9.08 | 8.28 | 576 | 20.5 | 4.3 | 7.42 | 32.9 | 8.67 | 2.17 |
| Na acetate 194_561 | 3 | 6.37 | 2748 | 73.9 | 1.3 | 22.8 | 108 | 27.2 | 6.69 |
| 0.1M HA 87_163 | 355 | 4999 | nm | 1.25 | 3.55 | 0.422 | 1.81 | 0.461 | 0.123 |
| 0.1M HA 87_827 | 290 | 8553 | nm | 4.22 | 5.96 | 1.38 | 5.89 | 1.47 | 0.37 |
| 0.1M HA 165_407 | 568 | 55286 | nm | 1.49 | 6.69 | 0.476 | 1.99 | 0.476 | 0.123 |
| 0.1M HA 165_812 | 1686 | 15842 | nm | 5.87 | 15.3 | 1.64 | 6.37 | 1.34 | 0.315 |
| 0.1M HA 194_157 | 1180 | 4530 | nm | 0.943 | 6.66 | 0.31 | 1.27 | 0.315 | 0.075 |
| 0.1M HA 194_561 | 4792 | 17706 | nm | 16 | 30.9 | 4.24 | 16.1 | 2.97 | 0.641 |
| 1M HA 87_163 | 2032 | 827 | 68 | 3.33 | 42.1 | 0.897 | 3.31 | 0.712 | 0.164 |
| 1M HA 87_827 | 1776 | 1936 | 130 | 9.97 | 62.5 | 2.7 | 9.63 | 2.05 | 0.488 |
| 1M HA 165_407 | 1977 | 4225 | 109 | 3.46 | 39.9 | 0.932 | 3.45 | 0.788 | 0.17 |
| 1M HA 165_812 | 6302 | 2287 | 144 | 8.17 | 40.9 | 2 | 6.67 | 1.21 | 0.247 |
| 1M HA 194_157 | 3658 | 666 | 87 | 4.09 | 53.1 | 1.07 | 3.9 | 0.845 | 0.17 |
| 1M HA 194_561 | 22188 | 2487 | 692 | 36 | 82.6 | 9.45 | 32.1 | 5.98 | 1.27 |
| Na-dithionite 87_163 | 6371 | 81.3 | < LOQ | 0.469 | 2.4 | < LOQ | 0.303 | < LOQ | < LOQ |
| Na-dithionite 87_827 | 6563 | 192 | < LOQ | 0.889 | 4.19 | < LOQ | 0.626 | < LOQ | - |
| Na-dithionite 194_561 | 56683 | 209 | < LOQ | 2.27 | 6.62 | 0.575 | 2.07 | 0.399 | < LOQ |
| NH4 oxalat 87_163 | 2664 | 34 | < LOQ | 0.601 | 1.21 | 0.129 | 0.484 | 0.0859 | < LOQ |
| NH4 oxalat 87_827 | 3213 | 114 | < LOQ | 1.07 | 2.09 | 0.248 | 0.864 | 0.151 | 0.03 |
| NH4 oxalat 165_407 | 2271 | 42.7 | < LOQ | 0.614 | 1.26 | 0.134 | 0.49 | 0.0843 | < LOQ |
| NH4 oxalat 165_812 | 4054 | 18.9 | < LOQ | 0.218 | 0.61 | 0.0481 | 0.19 | 0.0312 | - |
| NH4 oxalat 194_157 | 2883 | 19.4 | < LOQ | 0.882 | 1.83 | 0.206 | 0.719 | 0.129 | < LOQ |
| NH4 oxalat 194_561 | 3956 | 18.7 | < LOQ | 0.399 | 0.876 | 0.0929 | 0.322 | 0.0634 | < LOQ |
| Na-dithionite 87_163 | 6371 | 81.3 | < LOQ | 0.469 | 2.4 | < LOQ | 0.303 | < LOQ | < LOQ |
| Na-dithionite 87_827 | 6563 | 192 | < LOQ | 0.889 | 4.19 | < LOQ | 0.626 | < LOQ | - |
| Na-dithionite 165_407 | 5813 | 237 | < LOQ | 0.491 | 2.65 | < LOQ | 0.349 | - | - |
| Sum leaching | | | | | | | | | |
| 87_163 | | | 1190 | 42.9 | 62.4 | 14.6 | 63.7 | 16.6 | 4.1 |
| 87_827 | | | 3377 | 133.1 | 109.1 | 42.2 | 185.0 | 46.3 | 11.6 |
| 165_407 | | | 732 | 28.1 | 55.3 | 10.1 | 43.9 | 11.5 | 2.8 |
| 165_812 | | | 4806 | 110.6 | 68.2 | 31.6 | 135.5 | 30.9 | 7.5 |
| 194_157 | | | 663 | 27.1 | 69.5 | 9.0 | 39.2 | 10.0 | 2.4 |
| 194_561 | | | 4703 | 128.6 | 122.3 | 37.2 | 158.6 | 36.6 | 8.6 |

nm: not measured

APPENDIX II

Supplementary data 3 (continued): Salt-corrected major element contents and REY concentrations for leached CCZ sediment samples. All concentrations given in ppm.

| Sample ID | Gd | Tb | Dy | Y | Ho | Er | Tm | Yb |
|-----------------------|-----------|-----------|-----------|----------|-----------|-----------|-----------|-----------|
| Na acetate 87_163 | 16.8 | 2.52 | 15 | 79.9 | 2.87 | 8.02 | 1.08 | 7.1 |
| Na acetate 87_827 | 47.6 | 6.98 | 42.3 | 235 | 8.2 | 23.1 | 3.1 | 19.7 |
| Na acetate 165_407 | 10.7 | 1.59 | 9.42 | 43.9 | 1.73 | 4.81 | 0.637 | 4.16 |
| Na acetate 165_812 | 31.4 | 4.58 | 28 | 153 | 5.55 | 15.9 | 2.12 | 13.3 |
| Na acetate 194_157 | 9.25 | 1.39 | 8.01 | 42.5 | 1.54 | 4.24 | 0.567 | 3.59 |
| Na acetate 194_561 | 31 | 4.4 | 26.8 | 152 | 5.36 | 14.9 | 1.93 | 11.9 |
| 0.1M HA 87_163 | 0.468 | 0.0694 | 0.422 | 2.16 | 0.079 | 0.228 | 0.0281 | 0.208 |
| 0.1M HA 87_827 | 1.56 | 0.226 | 1.4 | 7.15 | 0.256 | 0.736 | 0.1 | 0.683 |
| 0.1M HA 165_407 | 0.469 | 0.074 | 0.451 | 1.67 | 0.0842 | 0.251 | 0.0343 | 0.259 |
| 0.1M HA 165_812 | 1.31 | 0.193 | 1.18 | 6.33 | 0.23 | 0.683 | 0.0942 | 0.63 |
| 0.1M HA 194_157 | 0.324 | 0.0498 | 0.293 | 1.43 | 0.0551 | 0.165 | < LOQ | 0.146 |
| 0.1M HA 194_561 | 2.69 | 0.394 | 2.39 | 12.3 | 0.469 | 1.4 | 0.202 | 1.33 |
| 1M HA 87_163 | 0.663 | 0.102 | 0.609 | 2.79 | 0.111 | 0.333 | 0.0456 | 0.358 |
| 1M HA 87_827 | 2 | 0.326 | 1.97 | 9.77 | 0.361 | 1.05 | 0.155 | 1.08 |
| 1M HA 165_407 | 0.671 | 0.113 | 0.658 | 2.27 | 0.118 | 0.356 | 0.0537 | 0.387 |
| 1M HA 165_812 | 1.03 | 0.166 | 1.04 | 4.99 | 0.2 | 0.596 | 0.0887 | 0.619 |
| 1M HA 194_157 | 0.747 | 0.118 | 0.693 | 2.84 | 0.127 | 0.383 | 0.0582 | 0.402 |
| 1M HA 194_561 | 5.02 | 0.88 | 5.42 | 23.6 | 1.04 | 3.14 | 0.486 | 3.34 |
| Na-dithionite 87_163 | - | < LOQ | - | 0.3 | < LOQ | - | < LOQ | < LOQ |
| Na-dithionite 87_827 | < LOQ | < LOQ | < LOQ | 0.598 | < LOQ | < LOQ | < LOQ | < LOQ |
| Na-dithionite 194_561 | 0.369 | < LOQ | 0.461 | 2.15 | < LOQ | 0.294 | < LOQ | 0.386 |
| NH4 oxalat 87_163 | 0.0679 | < LOQ | 0.05 | 0.202 | < LOQ | < LOQ | < LOQ | - |
| NH4 oxalat 87_827 | 0.123 | < LOQ | 0.104 | 0.377 | < LOQ | 0.04 | < LOQ | 0.04 |
| NH4 oxalat 165_407 | 0.0711 | < LOQ | 0.0467 | 0.192 | < LOQ | - | < LOQ | 0.0219 |
| NH4 oxalat 165_812 | 0.0262 | < LOQ | < LOQ | < LOQ | < LOQ | - | < LOQ | < LOQ |
| NH4 oxalat 194_157 | 0.104 | < LOQ | 0.0768 | 0.291 | < LOQ | 0.0345 | < LOQ | 0.0313 |
| NH4 oxalat 194_561 | 0.0566 | < LOQ | 0.0568 | 0.208 | < LOQ | 0.0264 | < LOQ | 0.0269 |
| Na-dithionite 87_163 | - | < LOQ | - | 0.3 | < LOQ | - | < LOQ | < LOQ |
| Na-dithionite 87_827 | < LOQ | < LOQ | < LOQ | 0.598 | < LOQ | < LOQ | < LOQ | < LOQ |
| Na-dithionite 165_407 | < LOQ | < LOQ | - | 0.308 | < LOQ | - | < LOQ | - |
| Sum leaching | | | | | | | | |
| 87_163 | 18.0 | 2.7 | 16.1 | 85.4 | 3.1 | 8.6 | 1.2 | 7.7 |
| 87_827 | 51.3 | 7.5 | 45.8 | 252.9 | 8.8 | 24.9 | 3.4 | 21.5 |
| 165_407 | 11.9 | 1.8 | 10.6 | 48.3 | 1.9 | 5.4 | 0.7 | 4.8 |
| 165_812 | 33.8 | 4.9 | 30.2 | 164.6 | 6.0 | 17.2 | 2.3 | 14.5 |
| 194_157 | 10.4 | 1.6 | 9.1 | 47.6 | 1.7 | 4.8 | 0.6 | 4.2 |
| 194_561 | 39.1 | 5.7 | 35.1 | 190.3 | 6.9 | 19.8 | 2.6 | 17.0 |

nm: not measured

APPENDIX II

Supplementary data 3 (continued): Salt-corrected major element contents and REY concentrations for leached CCZ sediment samples. All concentrations given in ppm.

| Sample ID | Lu | Ce/Ce* | Y/Ho | HREE/ LREE | MREE/ MREE* |
|-----------------------|--------|--------|------|---------------|----------------|
| Na acetate 87_163 | 1.06 | 0.13 | 27.8 | 0.166 | 0.189 |
| Na acetate 87_827 | 2.95 | 0.12 | 28.7 | 0.160 | 0.181 |
| Na acetate 165_407 | 0.612 | 0.08 | 25.4 | 0.164 | 0.203 |
| Na acetate 165_812 | 1.97 | 0.04 | 27.6 | 0.152 | 0.169 |
| Na acetate 194_157 | 0.535 | 0.08 | 27.6 | 0.161 | 0.195 |
| Na acetate 194_561 | 1.79 | 0.01 | 28.4 | 0.174 | 0.199 |
| 0.1M HA 87_163 | 0.0257 | 1.11 | 27.3 | 0.081 | 0.102 |
| 0.1M HA 87_827 | 0.0973 | 0.56 | 27.9 | 0.107 | 0.130 |
| 0.1M HA 165_407 | 0.0347 | 1.81 | 19.8 | 0.062 | 0.070 |
| 0.1M HA 165_812 | 0.0878 | 1.13 | 27.5 | 0.059 | 0.070 |
| 0.1M HA 194_157 | < LOQ | 2.80 | 26.0 | 0.040 | 0.055 |
| 0.1M HA 194_561 | 0.183 | 0.86 | 26.2 | 0.053 | 0.064 |
| 1M HA 87_163 | 0.0474 | 5.60 | 25.1 | 0.018 | 0.022 |
| 1M HA 87_827 | 0.146 | 2.77 | 27.1 | 0.033 | 0.039 |
| 1M HA 165_407 | 0.0553 | 5.11 | 19.2 | 0.020 | 0.025 |
| 1M HA 165_812 | 0.0763 | 2.33 | 25.0 | 0.027 | 0.031 |
| 1M HA 194_157 | 0.0538 | 5.85 | 22.4 | 0.016 | 0.020 |
| 1M HA 194_561 | 0.449 | 1.03 | 22.7 | 0.053 | 0.055 |
| Na-dithionite 87_163 | < LOQ | | | | |
| Na-dithionite 87_827 | < LOQ | | | | |
| Na-dithionite 194_561 | < LOQ | | | 0.059 | 0.050 |
| NH4 oxalat 87_163 | < LOQ | 1.00 | | | 0.042 |
| NH4 oxalat 87_827 | < LOQ | 0.94 | | 0.019 | 0.046 |
| NH4 oxalat 165_407 | < LOQ | 1.01 | | 0.009 | 0.040 |
| NH4 oxalat 165_812 | < LOQ | 1.37 | | 0.000 | 0.027 |
| NH4 oxalat 194_157 | < LOQ | 0.99 | | 0.018 | 0.042 |
| NH4 oxalat 194_561 | < LOQ | 1.05 | | 0.032 | 0.051 |
| Na-dithionite 87_163 | < LOQ | | | | |
| Na-dithionite 87_827 | < LOQ | | | | |
| Na-dithionite 165_407 | < LOQ | | | | |
| Sum leaching | | | | | |
| 87_163 | 1.1 | | | | |
| 87_827 | 3.2 | | | | |
| 165_407 | 0.7 | | | | |
| 165_812 | 2.1 | | | | |
| 194_157 | 0.6 | | | | |
| 194_561 | 2.4 | | | | |

nm: not measured

APPENDIX II

Supplementary data 3 (continued): Leached percentages of major elements and REY for CCZ sediment samples.

| Sample ID | P | La | Ce | Pr | Nd | Sm | Eu | Gd | Tb | Dy | Y | Ho |
|--------------------------|------|-------|-------|------|-------|------|------|------|------|------|-------|------|
| Na acetate 87_163 | 83 | 63 | 14 | 75 | 79 | 85 | 105 | 95 | 95 | 93 | 99 | 90 |
| Na acetate 87_827 | 120 | 100 | 31 | 105 | 110 | 116 | 124 | 119 | 118 | 116 | 123 | 113 |
| Na acetate 165_407 | 77 | 43 | 5 | 57 | 62 | 70 | 80 | 77 | 74 | 74 | 73 | 72 |
| Na acetate 165_812 | 97 | 87 | 13 | 95 | 98 | 101 | 115 | 104 | 103 | 101 | 98 | 100 |
| Na acetate 194_157 | 59 | 38 | 3 | 51 | 58 | 68 | 78 | 77 | 77 | 72 | 76 | 72 |
| Na acetate 194_561 | 54 | 54 | 1 | 59 | 66 | 74 | 77 | 82 | 80 | 79 | 81 | 78 |
| 0.1M HA 87_163 | | 2 | 4 | 2 | 2 | 3 | 3 | 3 | 3 | 3 | 3 | 2 |
| 0.1M HA 87_827 | | 4 | 5 | 4 | 4 | 4 | 4 | 4 | 4 | 4 | 4 | 4 |
| 0.1M HA 165_407 | | 3 | 7 | 3 | 3 | 3 | 4 | 3 | 3 | 4 | 3 | 3 |
| 0.1M HA 165_812 | | 5 | 20 | 6 | 5 | 5 | 5 | 4 | 4 | 4 | 4 | 4 |
| 0.1M HA 194_157 | | 2 | 5 | 2 | 2 | 2 | 3 | 3 | 3 | 3 | 3 | 3 |
| 0.1M HA 194_561 | | 12 | 23 | 11 | 10 | 8 | 7 | 7 | 7 | 7 | 7 | 7 |
| 1M HA 87_163 | 5 | 6 | 45 | 5 | 5 | 4 | 4 | 4 | 4 | 4 | 3 | 3 |
| 1M HA 87_827 | 5 | 9 | 57 | 8 | 6 | 6 | 6 | 5 | 6 | 5 | 5 | 5 |
| 1M HA 165_407 | 14 | 7 | 40 | 6 | 6 | 5 | 5 | 5 | 5 | 5 | 4 | 5 |
| 1M HA 165_812 | 3 | 7 | 54 | 7 | 5 | 4 | 4 | 3 | 4 | 4 | 3 | 4 |
| 1M HA 194_157 | 9 | 7 | 42 | 7 | 7 | 7 | 6 | 6 | 7 | 6 | 5 | 6 |
| 1M HA 194_561 | 14 | 26 | 60 | 24 | 20 | 16 | 15 | 13 | 16 | 16 | 13 | 15 |
| Na-dithionite 87_163 | | 1 | 3 | | 0 | | | | | | 0 | |
| Na-dithionite 87_827 | | 1 | 4 | | 0 | | | | | | 0 | |
| Na-dithionite 165_407 | | 1 | 3 | | 1 | | | | | | 1 | |
| Na-dithionite 165_812 | | 0 | 2 | | 0 | | | | | | 0 | |
| Na-dithionite 194_157 | | 1 | 3 | | 1 | | | | | | 1 | |
| Na-dithionite 194_561 | 25 | 2 | 5 | 1 | 1 | 1 | | 1 | | 1 | 1 | |
| NH4 oxalat 87_163 | | 1 | 1 | 1 | 1 | 0 | | 0 | | 0 | 0 | |
| NH4 oxalat 87_827 | | 1 | 2 | 1 | 1 | 0 | 0 | 0 | | 0 | 0 | |
| NH4 oxalat 165_407 | | 1 | 1 | 1 | 1 | 1 | | 1 | | 0 | 0 | |
| NH4 oxalat 165_812 | | 0 | 1 | 0 | 0 | 0 | | 0 | | | | |
| NH4 oxalat 194_157 | | 2 | 1 | 1 | 1 | 1 | | 1 | | 1 | 1 | |
| NH4 oxalat 194_561 | | 0 | 1 | 0 | 0 | 0 | | 0 | | 0 | 0 | |
| Bulk content | | | | | | | | | | | | |
| 87_163 | 1347 | 58.6 | 93.7 | 17.6 | 73.1 | 17.9 | 3.68 | 17.7 | 2.65 | 16.2 | 81.1 | 3.19 |
| 87_827 | 2708 | 117 | 110 | 36 | 153 | 36.8 | 8.65 | 40 | 5.92 | 36.4 | 191 | 7.26 |
| 165_407 | 804 | 51.0 | 100.6 | 15.0 | 60.9 | 14.7 | 3.2 | 13.8 | 2.2 | 12.7 | 59.9 | 2.4 |
| 165_812 (REY from 792cm) | 4793 | 110 | 75.1 | 29.5 | 125 | 28.0 | 6.0 | 30.2 | 4.4 | 27.7 | 155 | 5.58 |
| 194_157 | 972 | 54.6 | 127.1 | 14.7 | 57.1 | 12.8 | 2.8 | 12.0 | 1.8 | 11.1 | 56.0 | 2.1 |
| 194_561 | 5110 | 138.0 | 137.0 | 38.8 | 163.1 | 36.7 | 8.7 | 37.9 | 5.5 | 34.1 | 187.2 | 6.8 |

Supplementary data 3 (continued): Leached percentages of major elements and REY for CCZ sediment samples.

| Sample ID | Er | Tm | Yb | Lu |
|--------------------------|-----------|-----------|-----------|-----------|
| Na acetate 87_163 | 90 | 89 | 89 | 90 |
| Na acetate 87_827 | 116 | 112 | 111 | 118 |
| Na acetate 165_407 | 70 | 66 | 65 | 65 |
| Na acetate 165_812 | 99 | 94 | 95 | 95 |
| Na acetate 194_157 | 69 | 63 | 63 | 65 |
| Na acetate 194_561 | 76 | 72 | 70 | 73 |
| 0.1M HA 87_163 | 3 | 2 | 3 | 2 |
| 0.1M HA 87_827 | 4 | 4 | 4 | 4 |
| 0.1M HA 165_407 | 4 | 4 | 4 | 4 |
| 0.1M HA 165_812 | 4 | 4 | 5 | 4 |
| 0.1M HA 194_157 | 3 | | 3 | |
| 0.1M HA 194_561 | 7 | 7 | 8 | 7 |
| 1M HA 87_163 | 4 | 4 | 4 | 4 |
| 1M HA 87_827 | 5 | 6 | 6 | 6 |
| 1M HA 165_407 | 5 | 6 | 6 | 6 |
| 1M HA 165_812 | 4 | 4 | 4 | 4 |
| 1M HA 194_157 | 6 | 7 | 7 | 6 |
| 1M HA 194_561 | 16 | 18 | 20 | 18 |
| Na-dithionite 87_163 | | | | |
| Na-dithionite 87_827 | | | | |
| Na-dithionite 165_407 | | | | |
| Na-dithionite 165_812 | | | | |
| Na-dithionite 194_157 | | | | |
| Na-dithionite 194_561 | 1 | | 2 | |
| NH4 oxalat 87_163 | | | | |
| NH4 oxalat 87_827 | 0 | | 0 | |
| NH4 oxalat 165_407 | | | 0 | |
| NH4 oxalat 165_812 | | | | |
| NH4 oxalat 194_157 | 1 | | 1 | |
| NH4 oxalat 194_561 | 0 | | 0 | |
| Bulk content | | | | |
| 87_163 | 8.94 | 1.22 | 8.01 | 1.18 |
| 87_827 | 19.9 | 2.76 | 17.7 | 2.51 |
| 165_407 | 6.9 | 1.0 | 6.4 | 0.9 |
| 165_812 (REY from 792cm) | 16.11 | 2.25 | 13.97 | 2.07 |
| 194_157 | 6.1 | 0.9 | 5.7 | 0.8 |
| 194_561 | 19.7 | 2.7 | 16.9 | 2.5 |

No bulk REY data for 165GC 812 cm. To calculate the approximate % that was leached, REY data from 792 cm was used. REY concentrations in this layer are similar to the next sampled layers below 812 cm and it can therefore be assumed that the REY content is representative.

Supplementary data 3 (continued): Pore-water REY concentrations from 194GC. All concentrations given in mg/kg.

| Sample ID | 194GC 511 cm | 194GC 551 cm | 194GC 571 cm | Average Blank |
|------------|--------------|--------------|--------------|---------------|
| La | 3.20E-04 | 5.52E-05 | 7.57E-05 | 6.64E-06 |
| Ce | 4.85E-05 | 5.63E-05 | 3.86E-05 | 3.06E-05 |
| Pr | 8.55E-05 | 1.23E-05 | 1.79E-05 | 2.51E-06 |
| Nd | 3.96E-04 | 6.62E-05 | 7.81E-05 | 9.83E-06 |
| Sm | 8.83E-05 | 1.50E-05 | 1.58E-05 | 6.61E-06 |
| Eu | | | | 3.21E-06 |
| Gd | 1.04E-04 | 1.22E-05 | 1.58E-05 | 6.23E-06 |
| Tb | | | | 5.53E-06 |
| Dy | 9.47E-05 | 1.21E-05 | 1.56E-05 | 2.52E-06 |
| Y | 6.35E-04 | 7.93E-05 | 1.17E-04 | 8.04E-06 |
| Ho | 2.01E-05 | | | 1.52E-06 |
| Er | 5.44E-05 | | 1.01E-05 | 2.49E-06 |
| Tm | 6.22E-06 | | | 9.72E-07 |
| Yb | 4.68E-05 | 4.22E-06 | 8.14E-06 | 2.52E-06 |
| Lu | 5.66E-06 | | | 1.66E-06 |
| Ce/Ce* | 0.07 | 0.50 | 0.24 | |
| Y/Ho | 3.16E+01 | | | |
| HREE/LREE | 0.157 | 0.022 | 0.087 | |
| MREE/MREE* | 0.146 | 0.101 | 0.103 | |

APPENDIX III

Supplementary material to **CHAPTER IV: Post-depositional manganese mobilization during the last glacial period in sediments of the eastern Clarion-Clipperton Fracture Zone, Pacific Ocean****S1. Model setup and parameterization**

The reactive transport-reaction was slightly modified after the steady state transport-reaction model presented in Volz et al. (2018) including all parameters. It consists of 5 species (O_2 , Mn^{2+} , labile C_{org} , metabolizable C_{org} , refractory C_{org} ; Supplementary Table S1) and 3 redox reactions using the advection-transport-reaction equation (e.g., Mewes et al., 2016; Mogollón et al., 2016; Volz et al., 2018) for dissolved species (Eq. S1) and solid species (Eq. S2):

$$\varphi_i \frac{\partial C_{i,j}}{\partial t} = \frac{\partial}{\partial z} \left(\varphi_i \left(\frac{D_{i,j}}{\theta^2} + D_{b,i} \right) \frac{\partial C_{i,j}}{\partial z} \right) - \frac{\partial \varphi_i v_i C_{i,j}}{\partial z} + \alpha_i \varphi_i (C_{0,j} - C_{i,j}) + \varphi_i \sum R_{i,j} \quad (S1)$$

$$(1 - \varphi_i) \frac{\partial G_{i,j}}{\partial t} = \frac{\partial}{\partial z} \left(D_{b,i} (1 - \varphi_i) \frac{\partial G_{i,j}}{\partial z} \right) - \frac{\partial (1 - \varphi_i) w_i G_{i,j}}{\partial z} + (1 - \varphi_i) \sum R_{i,j} \quad (S2)$$

where t is time, z is sediment depth and i, j represent subscripts depicting depth and species-dependence, respectively; φ is the porosity; C and G are the concentrations of the aqueous phase and the solid phase, respectively; D is the diffusion coefficient; θ^2 is the tortuosity ($(\theta^2 = 1 - 2 \ln \varphi)$; Boudreau, 1996); D_b is the bioturbation coefficient; α is the bioirrigation coefficient; v, w are the burial velocity of the aqueous phase and the solid phase, respectively; $\sum R_{i,j}$ is the sum of the reactions affecting the given species j (see Supplementary Table S2).

Porosity data were fit for each station and showed an exponential decrease with depth typical of compacting sediment and were fit with the following equation:

$$\varphi = \varphi_\infty + (\varphi_0 - \varphi_\infty) \exp(-\beta z) \quad (S3)$$

where φ_∞ is the porosity at compaction; φ_0 is the porosity at the sediment-water interface (SWI), and β is the depth-attenuation coefficient.

Based on the assumption of steady state sediment compaction, the burial velocities of the aqueous phase (v) and the solid phase (w) follow the conservation law:

$$v = \omega \frac{\varphi_{\infty}}{\varphi} \quad (\text{S4})$$

$$w = \omega \frac{1-\varphi_{\infty}}{1-\varphi} \quad (\text{S5})$$

where ω is the compacted burial velocity of the sediments at depth obtained from $^{230}\text{Th}/^{231}\text{Pa}$ -based sedimentation rate determined by Volz et al. (2018) and the porosity correction.

Bioturbation-induced mixing profiles were assumed to follow a modified logistic function with the break attenuation depths after Mogollón et al. (2016) and Volz et al. (2018):

$$D_b = D_b^0 \exp\left(\frac{z_{mix}-z}{z_{att}}\right) / \left(1 + \exp\left(\frac{z_{mix}-z}{z_{att}}\right)\right) \quad (\text{S6})$$

where D_b^0 is constant, representing the maximum bioturbation coefficients at the SWI; z_{mix} is the depth, where D_b^0 becomes half their value and z_{att} is the attenuation of the biogenically induced mixing with depth. The bioirrigation coefficient α for the dissolved phases is approximated (Boudreau, 1997a):

$$\alpha = \alpha_0 \exp(-z/z_{irr}) \quad (\text{S7})$$

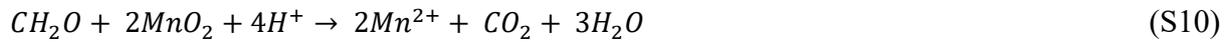
where α_0 and z_{irr} describe the bioirrigation intensity at the SWI and its depth attenuation, respectively. The effect of low O_2^{bw} on bioturbation was assumed to logistically alleviate the bioturbation coefficient D_b^0 within a relatively narrow range of O_2^{bw} (Katsev et al., 2007; Supplementary Fig. S1A):

$$D_b^0 = D_{b_{ref}}^0 (1 - \eta) \frac{1}{1 + \exp(-\tau(O_2^{bw} - O_2^{thr}))} + \eta D_{b_{ref}}^0 \quad (\text{S8})$$

where $O_2^{thr} = 62.5 \mu\text{M}$ is the threshold concentration after Katsev et al. (2007), below which the bioturbation is reduced due to the onset of benthic hypoxia (e.g., Diaz and Rosenberg, 1995; Supplementary Fig. S1A); τ characterizes D_b^0 as a function of O_2^{bw} and was chosen as $\tau = 0.3 \mu\text{M}^{-1}$ (Katsev et al., 2007); $D_{b_{ref}}^0$ is the bioturbation coefficient at current O_2^{bw} of $\sim 150 \mu\text{M}$, while the dimensionless parameter η represents the residual bioturbation in less oxygenated sediments (Katsev et al., 2007). Based on a sensitivity test of the residual bioturbation η as a function of O_2^{bw} using the threshold concentration of $62.5 \mu\text{M}$ proposed by Katsev et al. (2007), we have set the residual bioturbation factor η to 0.000125 (Supplementary

Fig. S1; Supplementary Table 2). The bioirrigation coefficient α_0 at the SWI is considered to have the same logistic dependency on O_2^{bw} as D_b^0 .

The redox reactions include aerobic respiration (Eq. S9), the dissimilatory reduction of Mn (oxyhydr)oxides (Eq. S10) and the oxidation of pore-water Mn^{2+} (Eq. S11) adapted from Burdige and Gieskes (1983). As pore-water Mn^{2+} concentrations are below detection limit throughout all investigated MUC sediment cores (Table 1), we have used pore-water oxygen and Mn^{2+} data and contents of organic matter (CH_2O) from GC sediment cores presented by Volz et al. (2018) with:



The organic matter degradation rate (R_{TOC}) was modeled by using a 3-G model to account for the heterogeneity of organic matter and its evolution during burial (Arndt et al., 2013). The 3-G model is based on the assumption that organic matter is composed in three discrete compound classes (labile C_{org}^1 , metabolizable C_{org}^2 and refractory C_{org}^3), each characterized by a specific degradability σ_1 - σ_3 . (Supplementary Table 2). The degradation coefficients σ_1 - σ_3 were adapted from Volz et al. (2018) in order to fit the depth profiles of Mn^{2+} and O_2 . The apparent reactivity of the bulk organic matter and its evolution during burial is related to the reactivity of each class by $R_{TOC} = -\sum_{i=1}^3 \sigma_i C_{org}^i$ (Arndt et al., 2013).

The rate expressions R_1 - R_3 for the organic matter degradation pathways and the oxidation of pore-water Mn^{2+} are given with the saturation constants (h_1 - h_4) taken from Mogollón et al. (2016) and Volz et al. (2018). The saturation constants (h_1 - h_4) are assumed to be equal to the inhibition constants, which characterize the reagent concentration above which the less energetically favorable reagents are inhibited (Boudreau, 1997b) with:

$$R_1 = R_{TOC} \times \frac{C_{O_2}}{C_{O_2} + h_1} \quad (S12)$$

$$R_2 = R_{TOC} \times \frac{h_1}{C_{O_2} + h_1} \times \frac{C_{MnO_2}}{C_{MnO_2} + h_2} \quad (S13)$$

$$R_3 = k_1 \times \frac{C_{O_2}}{C_{O_2} + h_3} \times \frac{C_{Mn^{2+}}}{C_{Mn^{2+}} + h_4} \quad (S14)$$

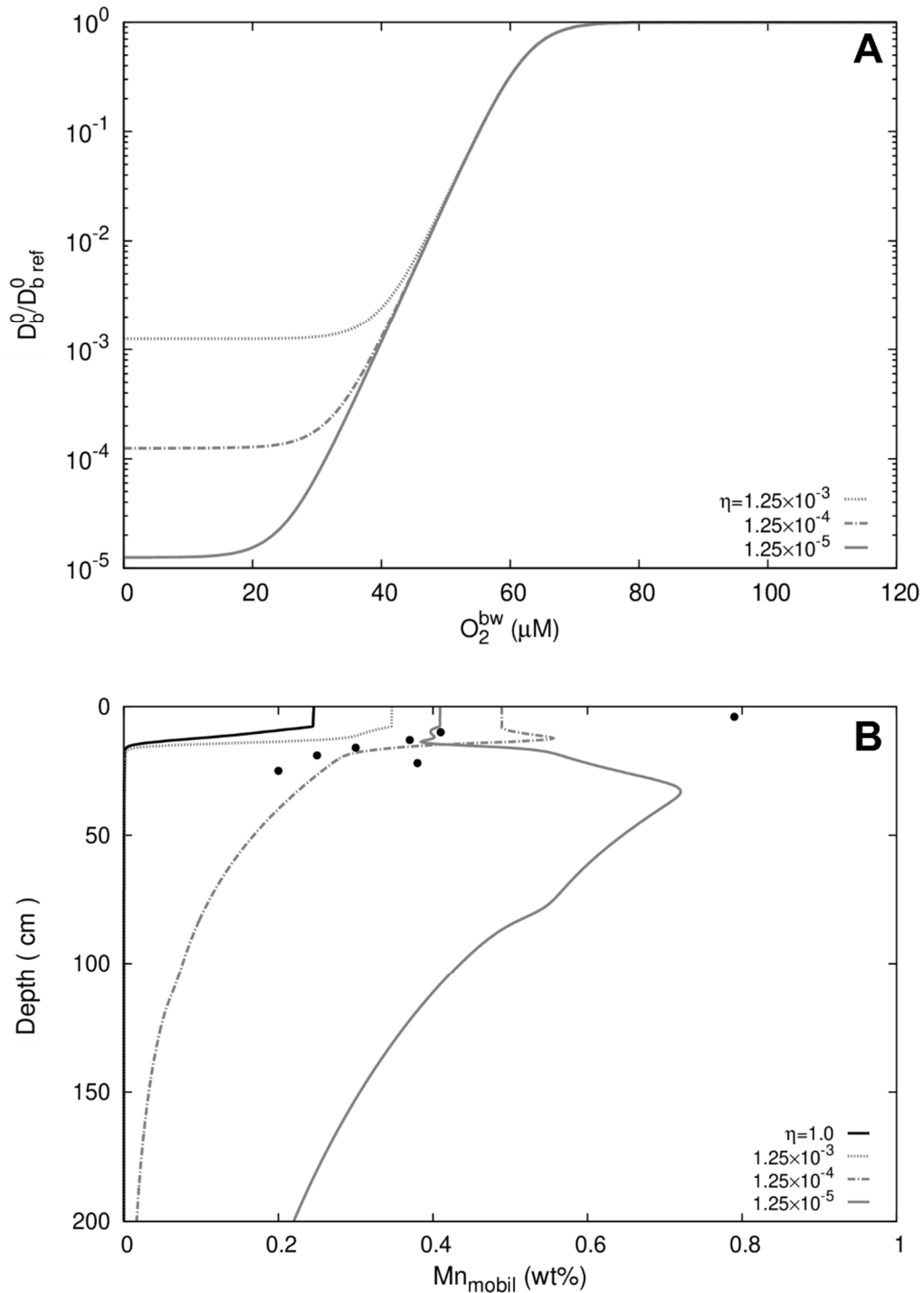
The formulation of Eq. S12 ensures that when oxygen becomes limited, aerobic mineralization is reduced. If oxygen concentrations are "high", i.e. $C_{O_2} \gg h_1$, the rate R_1 becomes independent of the oxygen concentration. Conversely, when $C_{O_2} \ll h_1$ the reaction rate R_1 becomes linearly

dependent on the oxygen concentration. Similarly, the expression R_2 in Eq. S13 incorporates the saturation constant h_2 once MnO_2 is used as oxidant. This implies that the organic matter consumption by the other successive oxidant such as Fe(III) and SO_4^{2-} (R_{other}) can be expressed as $R_{other} = R_{TOC} - R_1 - R_2$. The expression R_3 in Eq. S14 is the manganese oxidation rate where the parameters h_3 and h_4 are the saturation constants for oxygen and Mn^{2+} , respectively.

The boundary conditions at the SWI are imposed concentrations and fluxes for the aqueous and solid species, respectively, while a no-gradient boundary condition is used for all species at the bottom of the domain. Katsev et al. (2007) introduced the recycling coefficient ε , which considers that upward diffusing aqueous species released into the bottom water are re-precipitated. The recycling coefficient ε is defined as $\frac{F_{rec}}{F_{out}}$, where F_{out} is the total molar flux into the bottom water and F_{rec} is the molar flux that is recycled by oxidation. We have integrated the recycling coefficient ε_{Mn} for Mn after Katsev et al. (2007) assuming that 60% of the total molar flux F_{out}^{Mn} is recycled and immediately precipitated as an authigenic Mn(IV) phase.

The model was coded in R (version 3.2.4) using the ReacTran package (Soetaert and Meysman, 2012) to solve Eq. S1 and S2 and the marelac package (Soetaert et al., 2010) to solve the molecular diffusion coefficients for the modeled species (D_0). The advective velocities of solid phases and pore-water species were solved using the compact grid function within the ReacTran package, which takes sediment compaction into account.

Supplementary Figure S1: (A) Sensitivity test of the residual bioturbation η in dependency of bottom-water oxygen concentrations (O_2^{bw}) using the threshold concentration of $62.5 \mu\text{M}$ for the onset of benthic hypoxia after Katsev et al. (2007). (B) Impact of different residual bioturbation factors η in the transient transport-reaction model on the depth distribution of authigenic Mn(IV) in the sediments of the BGR-RA site. The bioturbation factor $\eta = 1$ represents the current bioturbation activity at O_2^{bw} of $150 \mu\text{M}$ which has been assumed in the steady state model after Volz et al. (2018) and does not reproduce the depth distribution of authigenic Mn(IV).



Supplementary Table S1: Species, parameter values and boundary conditions used in the one-dimensional steady state transport-reaction model and transient transport-reaction model for the BGR-RA, IFRE-2 and APEI3 sites.

| | Symbol | Unit | BGR-RA | IFRE-2 | APEI3 |
|--|--------------------|---|----------|----------|----------|
| Species and boundary conditions | | | | | |
| Porosity at SWI | φ_0 | | 0.82 | 0.82 | 0.58 |
| Porosity at compaction | φ_∞ | | 0.69 | 0.66 | 0.47 |
| Sedimentation rate | ω | cm kyr ⁻¹ | 0.65 | 0.48 | 0.2 |
| Oxygen _{bw} | O_2^{bw} | μM | 35-120 | 35-150 | 35-160 |
| Dissolved reduced manganese _{bw} | Mn^{2+} | μM | 0 | 0 | 0 |
| Fitted parameters | | | | | |
| Sediment thickness | | cm | 200 | 750 | 600 |
| Labile C _{org} | TOC_1 | mol m ⁻² yr ⁻¹ | 6.0E-02 | 4.5E-02 | 3.2E-02 |
| Metabolizable C _{org} | TOC_2 | mol m ⁻² yr ⁻¹ | 1.2E-04 | 6.0E-04 | 2.5E-04 |
| Refractory C _{org} | TOC_3 | mol m ⁻² yr ⁻¹ | 5.0E-04 | 2.0E-04 | 1.5E-04 |
| 1 st order deg. coeff. TOC ₁ | σ_1 | yr ⁻¹ | 5.0E-04 | 2.0E-04 | 1.0E-03 |
| 1 st order deg. coeff. TOC ₂ | σ_2 | yr ⁻¹ | 5.0E-06 | 1.0E-06 | 2.5E-06 |
| 1 st order deg. coeff. TOC ₃ | σ_3 | yr ⁻¹ | 7.0E-07 | 5.0E-8 | 4.0E-08 |
| MnO ₂ sedimentation rate | F_{MnO_2} | μg Mn cm ⁻² yr ⁻¹ | 1.2 | 0.5 | 1 |
| Bioturbation coeff. | D_{bref}^0 | cm ² yr ⁻¹ | 0.5 | 0.5 | 0.3 |
| Biomixing half depth | z_{mix} | cm | 7.0 | 7.0 | 13.0 |
| Biomixing attenuation | z_{zatt} | cm | 0.1 | 0.1 | 0.1 |
| Bioirrigation coeff. | α_{bref}^0 | yr ⁻¹ | 0.65 | 1.0 | 0.3 |
| Biomixing attenuation | z_{irr} | cm | 1.0 | 1.0 | 1.0 |
| Residual of bioturbation factor | η | - | 0.000125 | 0.000125 | 0.000125 |
| Threshold O ₂ concentration | O_2^{thr} | μM | 62.5 | 62.5 | 62.5 |
| D_b^0 steepness attenuation | τ | μM ⁻¹ | 0.3 | 0.3 | 0.3 |
| Mn recycling coefficient | ε_{Mn} | - | 0.6 | 0.6 | 0.6 |
| O ₂ inhibition concentration for R ₁ | h_1 | μM | 0.008 | 0.008 | 0.008 |
| MnO ₂ inhibition concentration for R ₂ | h_2 | mM | 100 | 1200 | 100 |
| R ₃ rate constant | k_1 | mM ⁻¹ yr ⁻¹ | 0.1 | 0.1 | 0.1 |
| O ₂ inhibition concentration for R ₃ | h_3 | μM | 0.008 | 0.008 | 0.008 |
| MnO ₂ inhibition concentration for R ₃ | h_4 | mM | 0.1 | 0.1 | 0.1 |

SWI: sediment-water interface

bw: bottom water

deg. coeff: degradation coefficient

Supplementary Table S2: Reaction term for species used in the model.

| Species | Symbol | Unit | Reaction term $\sum R_{i,j}$ |
|----------------------|-----------|---------------|------------------------------|
| Total organic carbon | CH_2O | μM | $-R_{TOC}$ |
| Oxygen | O_2 | μM | $-f_c R_1 - R_3$ |
| Dissolved manganese | Mn^{2+} | μM | $2f_c R_2 - 2R_3$ |
| Manganese oxide | MnO_2 | μM | $-R_2 + \frac{2R_3}{f_c}$ |

Conversion factor: $f_c = \frac{1-\varphi}{\varphi}$

Supplementary Table 1: Species, parameter values and boundary conditions used in the one-dimensional steady state transport-reaction model and transient transport-reaction model.

| | Symbol | Unit | BGR-RA | IFRE-2 |
|---|--------------------|--------------------------------------|---------|---------|
| <i>Species and boundary conditions</i> | | | | |
| Porosity at SWI | φ_0 | | 0.82 | 0.82 |
| Porosity at compaction | φ_∞ | | 0.69 | 0.66 |
| Sedimentation rate | ω_i | cm kyr ⁻¹ | 0.65 | 0.48 |
| Oxygen _{bw} | O_2^{bw} | μM | 35-120 | 35-150 |
| Dissolved reduced manganese _{bw} | Mn^{2+} | μM | 0 | 0 |
| <i>Fitted parameters</i> | | | | |
| Sediment thickness | | cm | 200 | 750 |
| Labile C _{org} | TOC_1 | mol m ⁻² yr ⁻¹ | 6.0E-02 | 4.5E-02 |
| Metabolizable C _{org} | TOC_2 | mol m ⁻² yr ⁻¹ | 1.2E-04 | 6.0E-04 |
| Refractory C _{org} | TOC_3 | mol m ⁻² yr ⁻¹ | 5.0E-04 | 2.0E-04 |
| 1 st order deg. coeff. TOC ₁ | σ_1 | yr ⁻¹ | 5.0E-04 | 2.0E-04 |
| 1 st order deg. coeff. TOC ₂ | σ_2 | yr ⁻¹ | 5.0E-06 | 1.0E-06 |
| 1 st order deg. coeff. TOC ₃ | σ_3 | yr ⁻¹ | 7.0E-07 | 5.0E-8 |
| MnO ₂ sedimentation rate | F_{MnO_2} | μg cm ⁻² yr ⁻¹ | 1.2 | 0.5 |
| Bioturbation coeff. | D_{bref}^0 | cm ² yr ⁻¹ | 0.5 | 0.5 |
| Biomixing half depth | z_{mix} | cm | 7.0 | 7.0 |
| Biomixing attenuation | z_{att} | cm | 0.1 | 0.1 |
| Bioirrigation coeff. | α_{bref}^0 | yr ⁻¹ | 0.65 | 1.0 |
| Biomixing attenuation | z_{irr} | cm | 1.0 | 1.0 |
| Residual of bioturbation factor | η | - | 0.00125 | 0.00125 |
| Threshold O ₂ concentration | O_2^{thr} | μM | 62.5 | 62.5 |
| D_b^0 steepness attenuation | τ | μM ⁻¹ | 0.3 | 0.3 |
| Mn recycling coefficient | ε_{Mn} | - | 0.6 | 0.6 |
| O ₂ inhibition concentration for R _{1a} | h_1 | μM | 0.008 | 0.008 |
| MnO ₂ inhibition concentration for R _{2a} | h_2 | mM | 100 | 1200 |
| R _{3a} rate constant | k_1 | mM ⁻¹ yr ⁻¹ | 0.1 | 0.1 |
| O ₂ inhibition concentration for R _{3a} | h_3 | μM | 0.008 | 0.008 |
| MnO ₂ inhibition concentration for R _{3a} | h_4 | mM | 0.1 | 0.1 |

SWI: sediment-water interface

bw: bottom water

deg. coeff: degradation coefficient

APPENDIX IV

Supplementary material to **CHAPTER V: Impact of small-scale disturbances on geochemical conditions, biogeochemical processes and element fluxes in sediments of the eastern Clarion-Clipperton Zone, Pacific Ocean**

Supplementary Table 1: Electron-equivalent redox reactions used in the transient transport-reaction model for the 1-day old EBS disturbance in the BGR-RA area and for the 20-year old IOM-BIE disturbance in the IOM area.

| Reaction name | Reaction | Redox reaction |
|--------------------------------|----------------|---|
| Aerobic respiration | R ₁ | $(CH_2O)(NH_4^+)_{\frac{16}{106}} + O_2 \rightarrow CO_2 + \frac{16}{106}NH_4^+ + H_2O$ |
| Heterotrophic denitrification | R ₂ | $5(CH_2O)(NH_4^+)_{\frac{16}{106}} + 4NO_3^- + 4H^+ \rightarrow 2N_2 + 5CO_2 + 5\frac{16}{106}NH_4^+ + 7H_2O$ |
| Dissimilatory Mn(IV) reduction | R ₃ | $(CH_2O)(NH_4^+)_{\frac{16}{106}} + 2MnO_2 + 4H^+ \rightarrow 2Mn^{2+} + CO_2 + \frac{16}{106}NH_4^+ + 3H_2O$ |
| Mn ²⁺ oxidation | R ₄ | $2Mn^{2+} + O_2 + 2H_2O \rightarrow 2MnO_2 + 4H^+$ |
| Nitrification | R ₅ | $NH_4^+ + 2O_2 \rightarrow NO_3^- + 2H^+ + H_2O$ |
| Mn-anammox | R ₆ | $3MnO_2 + 2NH_4^+ + 4H^+ \rightarrow 3Mn^{2+} + N_2 + 6H_2O$ |

Supplementary Table 2: Species, parameter values and boundary conditions used in the transient transport-reaction models for the 1-day old EBS disturbance in the BGR-RA area and the 20-year old IOM-BIE disturbance in the IOM area.

| | Symbol | Unit | BGR | IOM |
|--|------------------|--------------------------------------|---------|---------|
| <i>Species and boundary conditions</i> | | | | |
| Porosity at SWI | φ_0 | | 0.82 | 0.8 |
| Porosity at compaction | φ_∞ | | 0.69 | 0.67 |
| Sedimentation rate | ω_i | cm kyr ⁻¹ | 0.65 | 1.15 |
| Oxygen _{bw} | O_2 | μM | 120 | 150 |
| Ammonium _{bw} | NH_4^+ | μM | 1 | 1 |
| Nitrate _{bw} | NO_3^- | μM | 50 | 38 |
| Dissolved reduced manganese _{bw} | Mn^{2+} | μM | 1 | 1 |
| <i>Fitted parameters</i> | | | | |
| Sediment thickness | | m | 10 | 10 |
| Removed sediment thickness | | cm | 10 | 7 |
| Labile C _{org} | TOC_1 | mol m ⁻² yr ⁻¹ | 6.0E-02 | 4.5E-02 |
| Metabolizable C _{org} | TOC_2 | mol m ⁻² yr ⁻¹ | 1.2E-04 | 1.1E-03 |
| Refractory C _{org} | TOC_3 | mol m ⁻² yr ⁻¹ | 5.0E-04 | 7.8E-04 |
| Oxygen _{bas} | O_2 | μM | 18 | 55 |
| Ammonium _{bas} | NH_4^+ | μM | 1 | 1 |
| Nitrate _{bas} | NO_3^- | μM | 19 | 30 |
| Dissolved reduced manganese _{bas} | Mn^{2+} | μM | 1 | 1 |
| 1 st order deg. coeff. TOC ₁ | σ_1 | yr ⁻¹ | 1.0E-03 | 1.0E-02 |
| 1 st order deg. coeff. TOC ₂ | σ_2 | yr ⁻¹ | 1.0E-06 | 5.5E-06 |
| 1 st order deg. coeff. TOC ₃ | σ_3 | yr ⁻¹ | 2.0E-09 | 2.5E-09 |
| Bioturbation coefficient | B_0 | cm ² yr ⁻¹ | 0.5 | 0.2 |
| Biomixing half depth | z_{mix} | cm | 7.0 | 7.0 |
| Biomixing attenuation | zz_{att} | cm | 0.1 | 0.1 |
| Bioirrigation coefficient | α_0 | yr ⁻¹ | 0.65 | 2.0 |
| O ₂ inhibition concentration for R ₁ | h_1 | μM | 0.008 | 0.006 |
| NO ₃ ⁻ inhibition concentration for R ₂ | h_2 | μM | 45 | 25 |
| R ₄ rate constant | k_4 | μM ⁻¹ yr ⁻¹ | 0.1 | 0.1 |
| R ₅ rate constant | k_5 | μM ⁻¹ yr ⁻¹ | 0.005 | 0.1 |
| R ₆ rate constant | k_6 | μM ⁻¹ yr ⁻¹ | 0.001 | 0.001 |

Supplementary Table 3: Electron-equivalent redox reactions and associated expressions used in the numerical diagenetic model.

| Reaction name | Reaction | Rate expression |
|--------------------------------|----------------|--|
| Aerobic respiration | R ₁ | $(\sigma_1 C_{TOC1} + \sigma_2 C_{TOC2} + \sigma_3 C_{TOC3}) \frac{C_{O_2}}{C_{O_2} + h_1}$ |
| Heterotrophic denitrification | R ₂ | $(\sigma_1 C_{TOC1} + \sigma_2 C_{TOC2} + \sigma_3 C_{TOC3}) \gamma \frac{C_{NO_3^-}}{C_{NO_3^-} + h_2}$ |
| Dissimilatory Mn(IV) reduction | R ₃ | $(\sigma_1 C_{TOC1} + \sigma_2 C_{TOC2} + \sigma_3 C_{TOC3}) \gamma \frac{h_2}{C_{NO_3^-} + h_2}$ |
| Mn ²⁺ oxidation | R ₄ | $k_4 C_{O_2} C_{Mn^{2+}}$ |
| Nitrification | R ₅ | $k_5 C_{O_2} C_{NH_4^+}$ |
| Mn-annamox | R ₆ | $k_6 C_{NH_4^+} C_{MnO_2} \gamma \frac{h_2}{C_{NO_3^-} + h_2}$ |

$$\gamma = \frac{h_1}{(h_1 + C_{O_2})}$$

DANKSAGUNG

An erster Stelle möchte ich meiner Doktormutter Prof. Dr. Sabine Kasten für ihr Vertrauen und die Betreuung meiner Arbeit danken. Über die Jahre haben mich ihre unermüdliche Begeisterung, Unterstützung und konstruktive Kritik stets begleitet, motiviert und geprägt. Mein Dank gebührt Prof. Dr. Andrea Koschinsky für die vertrauensvolle Zusammenarbeit und permanente Unterstützung. Weiterhin möchte ich Prof. Dr. Anton Eisenhauer herzlich für seine Bereitschaft und Funktion als Zweitgutachter danken.

Meinen besonderen Dank möchte ich an Prof. Dr. Gerhard Bohrmann, Dr. Timothy G. Ferdelman und Dr. Matthias Haeckel richten, die sich umstandslos dazu bereit erklärt haben, meinem PhD Komitee anzugehören und mich bei meiner Promotion zu unterstützen. Die lebendigen und fruchtbaren Diskussionsrunden waren stets konstruktiv und zielführend. Herzlichen Dank an Dr. Laura Haffert, Dr. Sophie Paul, Dr. Gerard Versteegh, Dr. Walter Geibert, Dr. Thomas Kuhn, Dr. Natascha Riedinger und Dr. Susann Henkel für zahlreiche intensive Diskussionen und Denkanstöße. Für die angenehme Arbeitsatmosphäre, die einzigartigen Momente in der roten Ecke und die Aufnahme in den Pilzclub Krause Unke n.e.V. danke ich den Mitgliedern der Sektion Marine Geochemie. Für die tatkräftige Unterstützung bei Laborarbeiten und Analysen bedanke ich mich vor allem bei Ingrid Stimac, Ingrid Dohrmann, Olaf Kreft, Dennis Köhler, Dr. Gerhard Kuhn, Ruth Cordelair, Rita Fröhlking-Teichert und Susanne Wiebe. Vielen Dank an Dr. Autun Purser und Male Köster für das Korrekturlesen der vorliegenden Arbeit.

Ich danke meinen Mit-Doktoranden, Büro-Kollegen und Freunden Male Köster, Ole Valk, Eva Kirschenmann, Anne-Christin Melcher, Josefa Verdugo und Manuel Ruben für die gegenseitigen Ermutigungen und geschätzte Gesellschaft bei regelmäßigen Kaffee-Pausen und langatmigen Zugfahrten. Vielen Dank an Sabine Haalboom und an meine lieben Freunde Lili, Thea, Barbara, Franzi, Musti, Isa, Pai, Itxi, JC, Annika, Flo, Coralie, Nicole und Moni für den Zuspruch.

Mein tiefster Dank gilt meinen Eltern Evelyn und Martin Volz und meiner Großmutter Elfriede Volz für ihr Wohlwollen, ihre Unterstützung und den beständigen Halt.